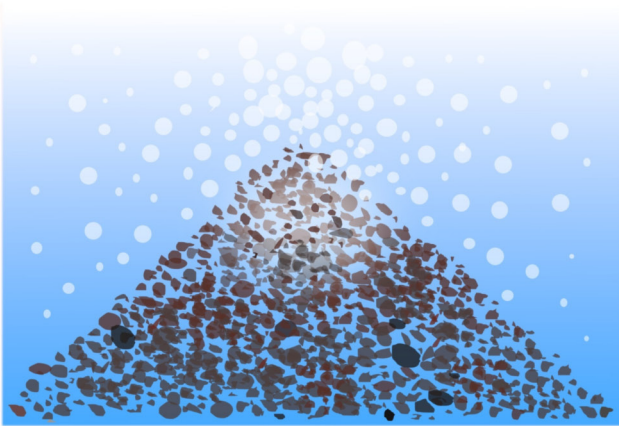
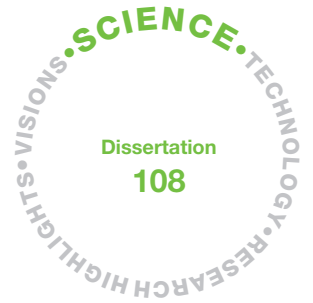
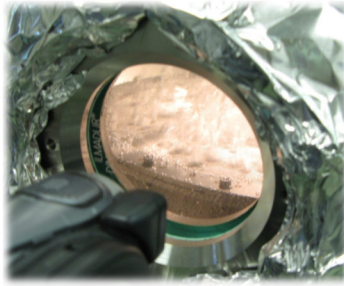


11010  
010110  
10100  
00110



# Coolability of porous core debris beds

Effects of bed geometry and multi-dimensional flooding

Eveliina Takasuo



# Coolability of porous core debris beds

Effects of bed geometry and multi-dimensional flooding

---

Eveliina Takasuo

VTT Technical Research Centre of Finland Ltd

*Thesis for the degree of Doctor of Science (Technology) to be presented with due permission for public examination and criticism in auditorium 1382 at Lappeenranta University of Technology, Finland, on the 23rd of October 2015, at 12 noon.*



ISBN 978-951-38-8344-7 (Soft back ed.)

ISBN 978-951-38-8345-4 (URL: <http://www.vttresearch.com/impact/publications>)

VTT Science 108

ISSN-L 2242-119X

ISSN 2242-119X (Print)

ISSN 2242-1203 (Online)

<http://urn.fi/URN:ISBN:978-951-38-8345-4>

Copyright © VTT 2015

JULKAISIJA – UTGIVARE – PUBLISHER

Teknologian tutkimuskeskus VTT Oy

PL 1000 (Tekniikantie 4 A, Espoo)

02044 VTT

Puh. 020 722 111, faksi 020 722 7001

Teknologiska forskningscentralen VTT Ab

PB 1000 (Teknikvägen 4 A, Esbo)

FI-02044 VTT

Tfn +358 20 722 111, telefax +358 20 722 7001

VTT Technical Research Centre of Finland Ltd

P.O. Box 1000 (Tekniikantie 4 A, Espoo)

FI-02044 VTT, Finland

Tel. +358 20 722 111, fax +358 20 722 7001

# Coolability of porous core debris beds

Effects of bed geometry and multi-dimensional flooding

Eveliina Takasuo. Espoo 2015.

## Abstract

This thesis addresses the coolability of porous debris beds in the context of severe accident management of nuclear power reactors. In a hypothetical severe accident at a Nordic-type boiling water reactor, the lower drywell of the containment is flooded, for the purpose of cooling the core melt discharged from the reactor pressure vessel in a water pool. The melt is fragmented and solidified in the pool, ultimately forming a porous debris bed that generates decay heat. The properties of the bed determine the limiting value for the heat flux that can be removed from the debris to the surrounding water without the risk of re-melting.

The coolability of porous debris beds has been investigated experimentally by measuring the dryout power in electrically heated test beds that have different geometries. The geometries represent the debris bed shapes that may form in an accident scenario. The focus is especially on heap-like, realistic geometries which facilitate the multi-dimensional infiltration (flooding) of coolant into the bed. Spherical and irregular particles have been used to simulate the debris. The experiments have been modeled using 2D and 3D simulation codes applicable to fluid flow and heat transfer in porous media. Based on the experimental and simulation results, an interpretation of the dryout behavior in complex debris bed geometries is presented, and the validity of the codes and models for dryout predictions is evaluated.

According to the experimental and simulation results, the coolability of the debris bed depends on both the flooding mode and the height of the bed. In the experiments, it was found that multi-dimensional flooding increases the dryout heat flux and coolability in a heap-shaped debris bed by 47–58% compared to the dryout heat flux of a classical, top-flooded bed of the same height. However, heap-like beds are higher than flat, top-flooded beds, which results in the formation of larger steam flux at the top of the bed. This counteracts the effect of the multi-dimensional flooding. Based on the measured dryout heat fluxes, the maximum height of a heap-like bed can only be about 1.5 times the height of a top-flooded, cylindrical bed in order to preserve the direct benefit from the multi-dimensional flooding.

In addition, studies were conducted to evaluate the hydrodynamically representative effective particle diameter, which is applied in simulation models to describe debris beds that consist of irregular particles with considerable size variation. The results suggest that the effective diameter is small, closest to the mean diameter based on the number or length of particles.

**Keywords** nuclear energy, severe accident, corium coolability, debris bed, two-phase flow, thermal-hydraulic experiment, porous medium, numerical modeling

## Huokoisen sydänromukeon jäähdytettävyyys

Tutkimus keon muodon ja moniulotteisen virtauksen vaikutuksista

Eveliina Takasuo. Espoo 2015.

### Tiivistelmä

Tämä väitöskirja käsittelee sydänmateriaalin jäähdytettävyyttä vakavien ydinvoimalaitosonnettomuuksien hallinnassa. Pohjoismaisten kiehtusvesilaitosten sujarakennuksen alakuivatila tulvitetaan reaktorisydämen sulamiseen johtavassa onnettomuustilanteessa. Toimenpiteen tavoitteena on muodostaa vesiallas, minne sydänsula fragmentoituu ja jäähtyy reaktoripainesäiliön rikkoutumisen jälkeen. Vesialtaaseen muodostuu huokoinen, sydänromusta koostuva partikkelipeti, joka tuottaa fissiotuotteiden hajoamisesta aiheutuvaa jälkilämpötehoa, joka poistuu petiä ympäröivään vesialtaaseen. Huokoisen pedin virtaus- ja lämmönsiirto-ominaisuudet määräävät, kuinka suuri jälkilämpöteho on mahdollista poistaa, jotta materiaalin uudelleen sulaminen estyisi.

Työssä on tutkittu huokoisen partikkelipedin jäähdytettävyyttä kokeellisesti mittaamalla kuivumiseen johtava lämpöteho erilaisissa partikkelipetigeometrioissa, jotka edustavat sulapurkauksessa muodostuvia huokoisen pedin muotoja. Erityisesti kekomaiset, realistiset partikkelipedit, joissa jäähdytteen virtaus petiin on selkeästi moniulotteinen, on otettu huomioon. Kokeet on mallinnettu käyttämällä kaksi- ja kolmiulotteisia laskentamalleja, jotka simuloivat kaksifaasivirtausta huokoisessa väliaineessa. Koe- ja mallinnustulosten avulla esitetään tulkinta partikkelipetien kuivumiskäyttäytymisestä sekä arvioidaan mallien soveltuvuutta jäähdytettävyyssarviointiin.

Kokeiden ja laskentamallien tulosten mukaan kuivumislämpövuoto riippuu virtausmekanismista ja pedin korkeudesta. Kokeissa havaittiin, että moniulotteinen virtaus parantaa kekomaisen petien jäähdytettävyyttä. Kuivumislämpövuoto on 47–58 % suurempi kuin päältä jäähdytettävässä pedissä. Kekomainen peti on kuitenkin korkeampi kuin tilavuudeltaan vastaava tasaisesti jakautunut, päältä jäähdytettävä peti, mikä kasvattaa höyryvuotoa kekomaisen pedin yläosassa ja huonontaa jäähdytettävyyttä. Kuivumislämpövuodon perusteella pedin korkeus saa olla vain noin puolitoistakertainen tasaisesti jakautuneeseen petiin verrattuna, jotta moniulotteisesta virtauksesta saatava suora hyöty säilyisi.

Lisäksi työssä arvioitiin hydrodynaamisesti edustavaa efektiivistä partikkelikokoa, jota mallinnuksessa sovelletaan kuvaamaan epäsäännöllisistä ja vaihtelevan kokoisista partikkeleista koostuvaa petiä. Tulokset viittaavat siihen, että efektiivinen koko tulee valita kokojakauman pienempien partikkelien joukosta, mahdollisesti käyttäen partikkelien lukumäärän tai pituuden mukaan painotettua keskikokoa.

**Avainsanat** ydinenergia, vakava ydinvoimalaitosonnettomuus, jäähdytettävyyys, huokoinen aine, partikkelipeti, kokeellinen termohydrauliikka, kaksifaasivirtaus, laskentamalli

## Academic dissertation

Supervisors	Professor Juhani Hyvärinen LUT School of Energy Systems Lappeenranta University of Technology Finland
	Professor Riitta Kyrki-Rajamäki LUT School of Energy Systems Lappeenranta University of Technology Finland
Reviewers	Professor Sevostian Bechta Division of Nuclear Power Safety KTH Royal Institute of Technology Sweden
	Professor Ville Alopaeus Chemical Engineering Department of Biotechnology and Chemical Technology Aalto University Finland
Opponent	Doctor Alexei Miassoedov Institute for Nuclear and Energy Technologies Karlsruhe Institute of Technology Germany

## Preface

The focus of this thesis is on a specific topic in a diverse field of applied sciences where safety issues cannot be overlooked: nuclear energy research. The organizations, groups and individuals whose contributions are described below have, thus far, made it possible for me to "do my bit" in this important field and to undertake the journey towards a doctoral degree which is now, after some intensive months at the writing desk, close to completion.

The research work presented has been conducted within the frameworks of SAFIR2010 and SAFIR2014, the Finnish National Programmes on Nuclear Power Plant Safety. In addition, support has been received from the Nordic Nuclear Safety platform NKS and from the Severe Accident Research Network of Excellence (SARNET-2) in the 7th Framework Programme by the European Union. The finalization phase of the thesis was funded by the YTERA doctoral school, for which I wish to thank the YTERA Board.

I wish to express my sincere gratitude to my supervisors, Prof. Juhani Hyvärinen and Prof. Riitta Kyrki-Rajamäki, for their guidance and support and to the reviewers, Prof. Ville Alopaeus and Prof. Sevostian Bechta, for their extremely valuable comments on the manuscript. I also wish to thank VTT Nuclear Energy and its Technology manager, Dr. Timo Vanttola, and my colleagues for creating an easy-going environment in the office and for the opportunity to work independently on various interesting projects.

I am greatly indebted to the COOLOCE project team and to the several professionals involved in the experimental work from the days of the STYX downcomer experiments in 2008 to the last COOLOCE experiment in the fall of 2014. Especially, the efforts by Mr. Tuomo Kinnunen and Ms. Taru Lehtikuusi, who solved all the technical problems encountered in operating the test facility, are appreciated. Dr. Stefan Holmström and Mr. Pekka H. Pankakoski had a crucial role in the original planning of the whole test programme, and in introducing me to the world of experimental research.

Another half of the project team, the experts of two-phase flow and CFD modeling, consisted of Mr. Ville Hovi, Mr. Veikko Taivassalo and Mr. Mikko Ilvonen, who performed the implementation (programming, that is) of the debris coolability models into the CFD simulation codes and whose contributions are gratefully acknowledged.

I would not have been able to conduct such an in-depth assessment of the debris bed dryout behavior alone.

The debris coolability experiments at VTT would probably not have reached their final extent without the many ideas proposed by Assoc. Prof. Pavel Kudinov from the Royal Institute of Technology (KTH). I wish to thank him and his research team for the insightful and productive co-operation in the DECOSE project. The MEWA code was licensed to Finland by Institut für Kernenergetik und Energiesysteme (IKE) at Stuttgart University, for which I express my sincere thanks Dr. Michael Buck, Dr. Georg Pohlner and Dr. Saidur Rahman. I am also grateful to the many colleagues at European research organizations for their co-operation in SARNET-2.

Finally, I would like to thank the personnel at LUT Nuclear Engineering for making me feel very welcome at Lappeenranta University of Technology during the finalization phase of the thesis. Heartfelt thanks are extended to Dr. Vesa Tanskanen for his constant support during my research and studies, and for all the things we have shared over the years.

With deepest appreciation – and her hardworking but ever-optimistic attitude in mind – I dedicate this thesis to the loving memory of my mother.

Espoo, August 2015

Eveliina Takasuo

## List of publications

This thesis is mainly based on the following original publications which are referred to in the text as I–V. The publications are reproduced with kind permission from the publishers.

- I Takasuo, E., Holmström, S., Kinnunen, T., Pankakoski, P.H., Hosio, E., Lindholm, I. 2011. The effect of lateral flooding on the coolability of irregular core debris beds. *Nuclear Engineering and Design* (241), 1196–1205.
- II Takasuo, E., Holmström, S., Kinnunen, T., Pankakoski, P.H. 2012. The COOLOCE experiments investigating the dryout power in debris beds of heap-like and cylindrical geometries. *Nuclear Engineering and Design* (250), 687–700.
- III Takasuo, E., Hovi, V., Ilvonen, M., Holmström, S. 2012. Modeling of Dryout in Core Debris Beds of Conical and Cylindrical Geometries. 20th International Conference on Nuclear Engineering collocated with the ASME 2012 Power Conference. July 30–August 3, 2012, Anaheim, California, USA. ICONE20-POWER2012-54159. 10 p.
- IV Takasuo, E., Hovi, V., Ilvonen, M. 2012. Applications and Development of the PORFLO 3D Code in Nuclear Power Plant Thermal Hydraulics. 20th International Conference on Nuclear Engineering collocated with the ASME 2012 Power Conference. July 30–August 3, 2012, Anaheim, California, USA. ICONE20-POWER2012-54161. 10 p.
- V Chikhi, N., Coindreau, O., Li, L.X., Ma, W.M., Taivassalo, V., Takasuo, E., Leininger, S., Kulenovic, R., Laurien, E. 2014. Evaluation of an effective diameter to study quenching and dry-out of complex debris bed. *Annals of Nuclear Energy* (74), 24–41.

## **Author's contributions**

The author had the main responsibility for the planning and analysis of the experimental work and she performed the majority of the numerical simulations presented in this thesis. The author's contribution to the publications I–V is described below.

### **Publication I**

The author participated in the planning of the coolability experiments, interpreted the experimental data, carried out the numerical simulations modeling the experiments and wrote the paper taking into account the comments by the co-authors.

### **Publication II**

The author planned the experimental facility and conducted the experiments together with the co-authors, and supervised the work in the role of project manager. The author interpreted and analyzed the experimental data, carried out the numerical simulations and wrote the paper, taking into account the comments by the co-authors.

### **Publications III–IV**

The author initiated the development of the CFD modeling approach for the coolability application, performed the 2D simulations with related data analyses and carried out part of the 3D simulations. The author wrote the papers together with the POR-FLO code developers and the other co-authors.

### **Publication V**

The author performed the analyses and the interpretation of the experimental data in the part of this joint publication that describes the research performed at VTT together with the co-author at VTT, wrote this part of the paper and provided comments to the other authors.

## Other publications

In addition to Publications I–V, the author has written several technical reports and contributed to other papers on core debris coolability. These publications are listed below. Some of the results presented in this thesis are based on technical reports 1–5.

1. Takasuo, E., Kinnunen, T., Holmström, S., Lehtikuusi, T. 2013a. COOLOCE coolability experiments with a cylindrical debris bed and lateral flooding: COOLOCE-10. Research Report VTT-R-0463-13, VTT Technical Research Centre of Finland.
2. Takasuo, E., Kinnunen, T., Holmström, S., Lehtikuusi, T. 2013b. COOLOCE debris bed coolability experiments with an agglomerate simulant: Test series 11. Research Report VTT-R-03316-13, VTT Technical Research Centre of Finland.
3. Takasuo, E., Kinnunen, T., Lehtikuusi, T. 2013c. COOLOCE-12 debris bed coolability experiment: Cone on a cylindrical base. Research Report VTT-R-07967-13, VTT Technical Research Centre of Finland.
4. Takasuo, E., Taivassalo, V., Hovi, V. 2014. A study on the coolability of debris bed geometry variations using 2D and 3D models. Research Report VTT-R-00676-14, VTT Technical Research Centre of Finland.
5. Takasuo, E., Taivassalo, V., Kinnunen, T., Lehtikuusi, T. 2015. Coolability analyses of heap-shaped debris bed. Research Report VTT-R-00367-15, VTT Technical Research Centre of Finland.
6. Takasuo, E., Holmström, S., Hovi, V., Rahman, S., Bürger, M., Buck, M., Pohlner, G. 2012. Experimental and Computational Studies of the Coolability of Heap-like and Cylindrical Debris Beds. The 5th European Review Meeting on Severe Accident Research (ERMSAR-2012), Cologne, Germany, March 21–23, 2012.
7. Pohlner, G., Buck, M., Meignen, R., Kudinov, P., Ma, W., Polidoro, F., Takasuo, E. 2014. Analyses on ex-vessel debris formation and coolability in SARNET frame. *Annals of Nuclear Energy* (74), 50–57.

# Contents

<b>Preface</b>	<b>9</b>
<b>List of publications</b>	<b>11</b>
<b>Author's contributions</b>	<b>12</b>
<b>Nomenclature</b>	<b>17</b>
<b>1 Introduction</b>	<b>21</b>
1.1 Scientific value of this study . . . . .	23
<b>2 Coolability of porous debris beds – overview</b>	<b>25</b>
2.1 The flooding modes . . . . .	26
2.2 What is known of debris bed geometry? . . . . .	29
2.3 Heat flux in conical and cylindrical beds . . . . .	30
<b>3 Experimental approach and the early results</b>	<b>33</b>
3.1 Determination of dryout . . . . .	34
3.2 Experiments with irregular particles . . . . .	34
3.2.1 The effect of lateral flooding . . . . .	37
3.2.2 Behavior of the fine particle layer . . . . .	39
3.2.3 Measurement errors . . . . .	40
<b>4 Debris bed geometry experiments</b>	<b>43</b>
4.1 Flooding mode experiments . . . . .	47
4.1.1 Dryout heat flux . . . . .	49
4.1.2 Dryout locations . . . . .	55
4.1.3 Effect of bed height . . . . .	57
4.2 Pool subcooling experiments . . . . .	59
4.3 Measurement errors . . . . .	61
4.3.1 Condensate flow and heat losses . . . . .	62
4.4 Discussion . . . . .	63

<b>5</b>	<b>Simulations</b>	<b>65</b>
5.1	Modeling principles . . . . .	66
5.1.1	Drag force models . . . . .	67
5.1.2	Heat transfer models . . . . .	69
5.2	Simulation set-up . . . . .	71
5.3	Applicability of drag force models . . . . .	73
5.4	Results and discussion on dryout characteristics . . . . .	74
5.4.1	Conical and cylindrical beds . . . . .	74
5.4.2	Dryout heat flux . . . . .	78
5.4.3	Post-dryout conditions . . . . .	79
5.4.4	Non-uniform heating . . . . .	80
5.4.5	Geometry variations . . . . .	81
5.4.6	Free-flow water pool . . . . .	86
5.5	Extension to reactor scale . . . . .	88
<b>6</b>	<b>Effective particle size</b>	<b>93</b>
6.1	Research methods . . . . .	94
6.2	Results . . . . .	97
6.3	Discussion . . . . .	99
<b>7</b>	<b>Conclusions</b>	<b>101</b>
	<b>References</b>	<b>105</b>
	<b>Appendices</b>	
	Publications I–V	

# Nomenclature

## Latin letters

$A$	Area	$m^2$
$a$	Interfacial area density	$m^2/m^3$
$d$	Diameter	$m$
$F$	Volumetric drag force	$N/m^3$
$g$	Acceleration of gravity	$m/s^2$
$h$	Specific enthalpy	$J/kg$
$j$	Superficial velocity	$m/s$
$K$	Permeability	$m^2$
$K_r$	Relative permeability	-
$m$	Empirical constant (relative permeability)	-
$n$	Empirical constant (relative passability)	-
Nu	Nusselt number	-
$p$	Pressure	Pa
$Q$	Power density, volumetric heat flux	$W/m^3$
$q$	Heat flux	$W/m^2$
$r$	Radius	$m$
Re	Reynolds number	-
$T$	Temperature	K
$t$	Time	s
$V$	Volume	$m^3$
$v$	Phase velocity	$m/s$
$W$	Specific heat	$W/kg$
$z$	Height	$m$

## Greek letters

$\alpha$	Void fraction	-
$\alpha_i$	Fraction of phase i	-
$\varepsilon$	Porosity	-
$\eta$	Passability	$m$

$\eta_r$	Relative passability	-
$\Gamma$	Mass transfer rate	$\text{kg}/(\text{m}^3 \cdot \text{s})$
$\kappa$	Heat transfer coefficient	$\text{W}/(\text{m}^2 \cdot \text{K})$
$\lambda$	Thermal conductivity	$\text{W}/(\text{m} \cdot \text{K})$
$\mu$	Dynamic viscosity	$\text{Pa} \cdot \text{s}$
$\rho$	Density	$\text{kg}/\text{m}^3$
$\tau$	Viscous stress	$\text{N}/\text{m}^2$

### Subscripts

cone	Conical
cyl	Cylindrical
decay	Decay heat
do	Dryout
eff	Effective
g	Gas
h	Heater
i	Interfacial
l	Liquid
p	Particle
s	Solid
sat	Saturated fluid

### Abbreviations

BWR	Boiling water reactor
CCM	Test facility, fuel-coolant interaction
CFD	Computational fluid dynamics
CHF	Maximum coolable heat flux
COOLOCE	Test facility, debris coolability
DEFOR	Debris Bed Formation test facility
DHF	Dryout heat flux
FARO	Test facility, fuel-coolant interaction
FCI	Fuel-coolant interaction
IKE	Institut für Kernenergetik und Energiesysteme
IRSN	Institut de Radioprotection et de Sûreté Nucléaire
KROTOS	Test facility, fuel-coolant interaction
KTH	Kungliga Tekniska Högskolan
LOCA	Loss of coolant accident
LWR	Light water reactor
MEWA	MEIt and WAtEr, simulation code by Stuttgart University
MTD	Modified Tung and Dhir drag force model
NPP	Nuclear power plant
POMECO	Test facility, debris coolability

PORFLO	Two-phase flow simulation code by VTT
RPV	Reactor pressure vessel
SARNET	Severe Accident Research NETwork of excellence
STYX	Test facility, debris coolability
TC	Thermocouple
TROI	Test for Real cOrium Interaction with water
VTT	VTT Technical Research Centre of Finland Ltd

# 1. Introduction

The utilization of nuclear energy for power generation is a safety critical activity due to the large amount of radioactive materials contained in the nuclear reactor core. In the design of modern power reactors, the possibility of a severe accident that results in damage to the reactor core, or even melting, has to be taken into account. One of the main questions in the management and mitigation of the consequences of a severe accident is how to cool and stabilize the molten corium. The goal is to avoid the potential threat to the structural integrity of the containment and, ultimately, to prevent the release of radioactive materials into the environment and the risk to public health and safety.

Different severe accident management strategies have been adopted depending on the reactor type (Sehgal, 2012). In light-water reactors (LWRs), these strategies rely on terminating the progress of the accident in the reactor pressure vessel (RPV) and maintaining the RPV integrity, or ex-vessel if the RPV failure cannot be ruled out. In some of the Generation III power reactor designs, the ex-vessel corium is cooled in a core catcher, a system specially designed for this purpose.

At the time of the construction of the older Generation II power plants built in the 70s and 80s and currently in operation, severe accident systems as known today were not installed because large-break loss of coolant accident (LOCA) was considered as the worst-case scenario. Safety systems, including the leak-tight containment, designed for large-break LOCA and other accidents and transients specified as a design basis, were considered adequate for preventing the development of an accident into a severe accident resulting in radioactive releases. The potentially catastrophic consequences of a hypothetical core melt accident were, however, already recognized in early studies (U.S. Atomic Energy Commission, 1957; U.S. Nuclear Regulatory Commission, 1975) and taken into account in the planning of nuclear power plant siting and protection zones around the sites.

The accidents at Three Mile Island in 1979, at Chernobyl in 1986 and at Fukushima Daiichi in 2011 showed that severe accidents, even though unlikely, can occur in the real world regardless of the multiple safety systems for managing design-basis accidents. The Three Mile Island accident can be seen as a turning point in the history of commercial nuclear power plants that initiated the research programs of severe accident phenomenology and the technical preparation for the core melt

## 1. Introduction

management measures (Sehgal, 2012).

In this thesis, the focus is on stabilizing the corium in the form of a particle bed (debris bed) which is volumetrically heated by the decay heat. Core melt management as solidified debris is applied in the operating Finnish and Swedish boiling water reactors where severe accident systems have been retrofitted to the plant design. In a severe accident situation in these reactors, the cavity below the RPV, called the lower drywell, is flooded from the condensation pool by operator action. The molten corium, which may have a temperature close to three thousand degrees Celsius, discharges from the RPV into the about 10 m deep water pool where it is fragmented and solidified. During and after the initial cooling in the pool, the solidified particles settle to the floor of the containment and form a porous debris bed.

The containment of the BWRs located at Olkiluoto in Finland is shown in Figure 1.1. The power plant site has two reactor units supplied by Asea-Atom with 880 MW electrical and 2500 MW thermal power. An illustration of the corium in the flooded lower drywell is shown in the figure.

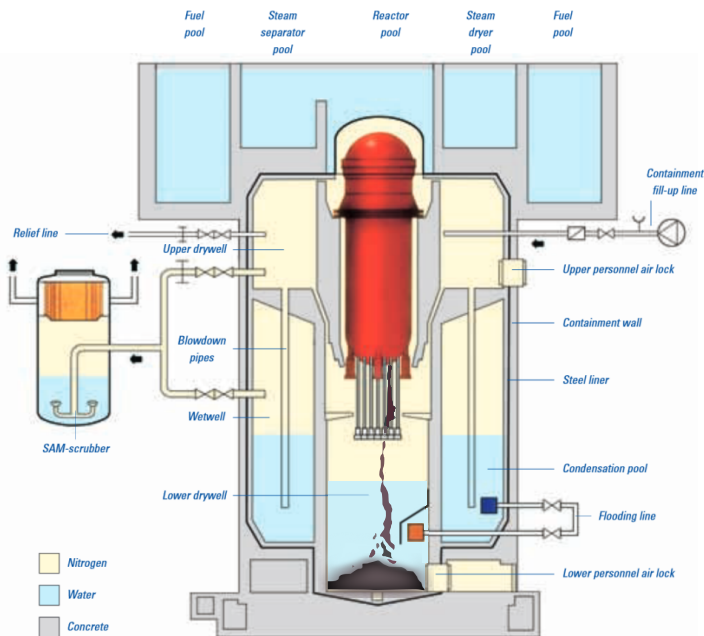


**Figure 1.1.** Containment of the Olkiluoto 1 and 2 nuclear power plants (TVO, 2008), corium illustration by the author.

The debris bed generates residual heat due to the radioactive decay of the fission products. The decay power depends on the thermal power of the reactor: it is about seven per cent of the total power during reactor operation and starts to decrease

instantly after shutdown (Lamarsh, 1983, p. 350). After one hour from shutdown, the decay power is about one per cent of the operation power and, after one week, the power has fallen to around 0.2%.

In the time frame of the debris bed formation and cooling, the decay power is great enough to result in re-melting of the debris and a potential threat to the containment structures, unless it is effectively transferred from the debris particles. Sufficiently large heat removal rate is achieved by boiling the water in the pool. Then, the key question becomes how to ensure that an adequate amount of water may infiltrate into the debris bed to replace the mass transfer by boiling.

The question of debris coolability is addressed in the present thesis by (1) experimental investigations of dryout power in thermal-hydraulic test facilities tailored for this purpose, and (2) numerical simulations of two-phase flows and heat transfer in the debris bed. Firstly, the experimental facilities and results are described, and the significance of the results from the safety point of view is discussed. Then, the simulation models and their implementation into the 2D and 3D two-phase flow codes are described, and the simulation results are assessed against the experimental data.

### **1.1 Scientific value of this study**

This thesis presents the first debris bed coolability study that experimentally addresses the issue of the geometry (spatial distribution) of an ex-vessel debris bed, and accounts for the heap-like shapes that are considered realistic in severe accident scenarios. In addition, the coolability has been measured for several variations of the cylindrical debris bed geometry, which has produced new data on the effectiveness of the different modes of water infiltration (flooding) into the debris bed. It is shown that the coolability depends on the flooding mode and the height of the bed.

The main practical application of the study is the ex-vessel coolability of the Nordic BWRs. However, the considerations related to the multi-dimensional phenomena in the water infiltration are rather general and can be extended to other types of debris beds. The experimental results have been utilized in the modeling work and the validation of severe accident simulation codes within the author's organization and in other European research organizations (Rahman, 2013, p. 44–47; Kudinov et al., 2014, p. 89–95). Nuclear power utilities and safety authorities can utilize the results in assessing and developing severe accident management and mitigation measures. The study has been an integral part of the corium coolability research conducted in the framework of the European Severe Accident Research Network of Excellence, SARNET-2 (Pohlner et al., 2014; Takasuo et al., 2012a).

The analytical part of the study presents an assessment of the experiments and the debris bed dryout behavior by applying 2D and 3D simulation codes. The implementation of the porous media models into the computational fluid dynamics codes and the subsequent simulation work was the first research effort in public literature that applies the full CFD solution of the two-phase flow equations to the problem of debris coolability. The simulations provide a detailed insight into the dryout mechanisms of debris beds with different flooding modes, and yield realistic results of the

## 1. Introduction

two-phase flows in the water pool – debris bed system. The main benefit of testing several simulation approaches is that, by comparing the results, the most suitable methods for assessing the debris coolability as a part of safety analyses can be identified.

## 2. Coolability of porous debris beds – overview

The long-term coolability of the core debris depends on the properties of the debris bed and the ambient pressure. The bed properties include porosity, particle size, particle morphology and the overall geometry of the debris bed. The bed geometry largely determines what type of two-phase flow is formed to cool the debris. The particle size and shape as well as porosity have an effect on coolability mainly through the frictional forces between the solid particles and the gas and liquid phases.

It is well known that bed porosity and particle diameter are highly influential from the coolability point of view. The effect of particle diameter was studied in several experiments in the early 1980s e.g. by Barleon and Werle (1981) and Trenberth and Stevens (1980), summaries of which are given by Schmidt (2004) and Bürger et al. (2006). For larger particles, the surface area is reduced compared to smaller particles, which means that the frictional forces between the particles and the fluid phases are smaller, and the flow resistance is reduced. This improves the capability of the porous medium to remove heat. Larger porosity allows greater liquid content in the pores of the debris, yielding increased water reservoir for boiling, and it also reduces the particle-fluid friction. Thus, large particle size and large porosity are favorable for coolability.

The ambient pressure affects the coolability through the material properties of steam. In greater pressures the steam density is larger, and the volume occupied by steam in the pores of the bed is smaller. Since the mass of steam in the bed is directly connected to heat generation and the boiling rate, larger rates of heat removal can be achieved with denser steam because more pore volume is then available for the coolant. Most of the experiments described in this thesis consider the pressure range from atmospheric to 7 bar, which covers the pressure range expected in the containment of a Finnish BWR during a severe accident. The early studies investigating the effect of pressure on dryout include those by Squarer et al. (1982) and Miyazaki et al. (1986), who noticed that the dryout heat flux increased with increasing pressure. The decrease in the latent heat of vaporization as a function of pressure counteracts the effect of the increased density but, for containment-relevant pressures, density increase is the dominant effect.

The aforementioned studies addressing the fundamental properties which influence the heat removal capability of the porous bed form the basis for the present-

## 2. Coolability of porous debris beds – overview

day coolability investigations. Experimental programs on debris coolability and the reflooding of hot dry debris have continued throughout the 2000s. Meanwhile, the test arrangements have evolved to consider more and more realistic conditions. The recent studies include investigations with larger scales, various particle sizes and shapes, different flooding modes and volumetric heating arrangements by Konovlikhin (2001), Atkhen and Berthoud (2006), Rashid et al. (2008), Repetto et al. (2011), Li et al. (2012) and other researchers.

### 2.1 The flooding modes

The geometry, or the spatial distribution, of the debris bed affects the flooding mode. This may have a key role in whether the debris bed is coolable or not. The flooding mode can be described as the direction and the flow pattern of the water infiltration from the surrounding water pool into the debris bed. Here, the flooding modes are divided to top flooding, lateral flooding and multi-dimensional flooding. For instance, in the case of a conical bed, the flooding mode is multi-dimensional because water can infiltrate into the porous bed through the full surface of the cone. The cylindrical bed with closed walls is top-flooded because only the top surface is permeable to fluid flow. The debris bed geometries and flooding modes are illustrated in Figure 2.1 which shows principal sketches of the six test beds in the COOLOCE experiments described in this thesis.

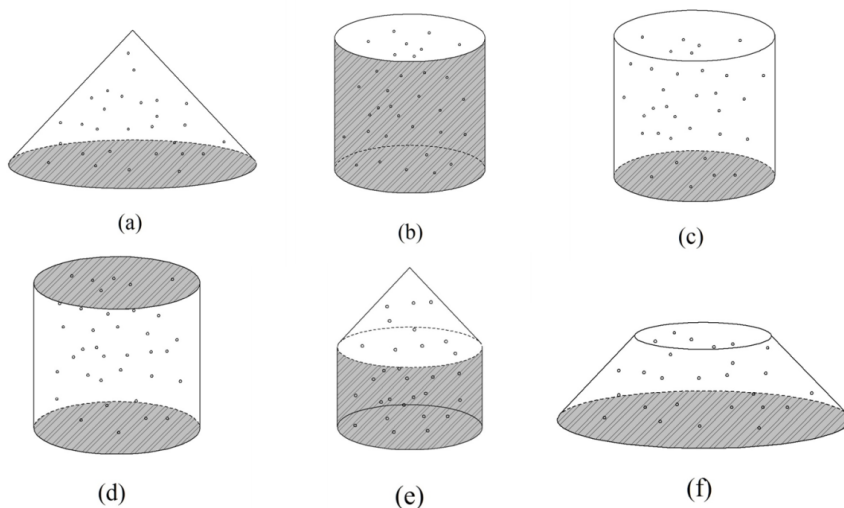


**Figure 2.1.** Sketches of the test bed geometries in the COOLOCE experiments:(a) conical, (b) top-flooded cylinder, (c) fully-flooded cylinder (open walls), (d) cylinder with lateral flooding, (e) cone on a cylindrical base, and (f) truncated cone. The shaded areas are impermeable walls; other surfaces are open for fluid flow.

## 2. Coolability of porous debris beds – overview

A top-flooded bed such as the one in Figure 2.1(b) is formed if the debris is evenly distributed into the corium spreading area, bound by its walls. Heap-shaped beds, for instance the beds in Figures 2.1(a), (c) and (f), can be formed in the corium discharge and settling if the particles are not effectively spread by the flows in the water pool. It is also possible that the debris settles partially against the wall while the top part of the bed has a conical shape, as in Figure 2.1(e). The cylinder with lateral flooding in Figure 2.1(d) has an impermeable top. The top simulates a layer of solid but non-fragmented corium on an otherwise multi-dimensionally flooded bed.

Top-flooded beds are in general more difficult to cool than multi-dimensionally flooded beds. This is due to differences in the flooding mode. In the top-flooded bed, the water and steam flow in opposite directions in counter-current mode, and dryout occurs when the steam flux that exits the bed is large enough to prevent the water from flooding the bed interior. This type of flooding is effectively one-dimensional since there are no changes in radial direction. In the case of multi-dimensional flooding, the water and steam may flow co-current, at least in parts of the bed. Dryout is reached when the mass flux of steam is large enough to fully replace the water, either locally or in a full cross-section of the debris bed. The flow patterns of water and steam expected in top-flooded and multi-dimensional configurations are illustrated in Figure 2.2.

A specific case of one-dimensional flooding is bottom flooding. In this flooding mode, the bottom of the debris bed is permeable to water infiltration and either forced or natural flow of water is conducted through it. In this configuration it is theoretically possible to achieve fully co-current flow of water and steam. Studies have shown that bottom flooding and multi-dimensional flooding are clearly more effective in removing heat than top flooding (Hofmann, 1984; Rashid et al., 2011; Rashid et al., 2012; Atkhen and Berthoud, 2006; Thakre et al., 2014) though few of these studies have been conducted in set-ups which truly allow flooding through large non-horizontal surfaces. Instead, the lateral component of the flow is usually achieved by a downcomer, which provides coolant to the lower parts of the bed. (In fact, there is some ambiguity between the concepts of bottom flooding, multi-dimensional flooding and lateral flooding.)

Publication I of this thesis presents dryout measurements of the effects of lateral flooding achieved with downcomers combined to flooding from the top. In Publication II the study is extended to account for the bed geometry by using a pool-type test facility COOLOCE in which the test beds are removable and modifiable. With this set-up, the multi-dimensional flooding is a result of the geometry, rather than an additional construct to an initially one-dimensional arrangement of the classical experiments. A total of six test bed geometries corresponding to those in Figure 2.1 have been examined.

In addition to the flooding mode, the geometry is related to another factor of key importance: the debris bed height. Due to gravity and buoyancy, steam flows upwards and water downwards. For a bed with uniform internal heat generation, or constant power density, the mass flux of steam increases along with the height of the bed. Thus, for beds with greater height, greater steam mass fluxes can be achieved, and

## 2. Coolability of porous debris beds – overview

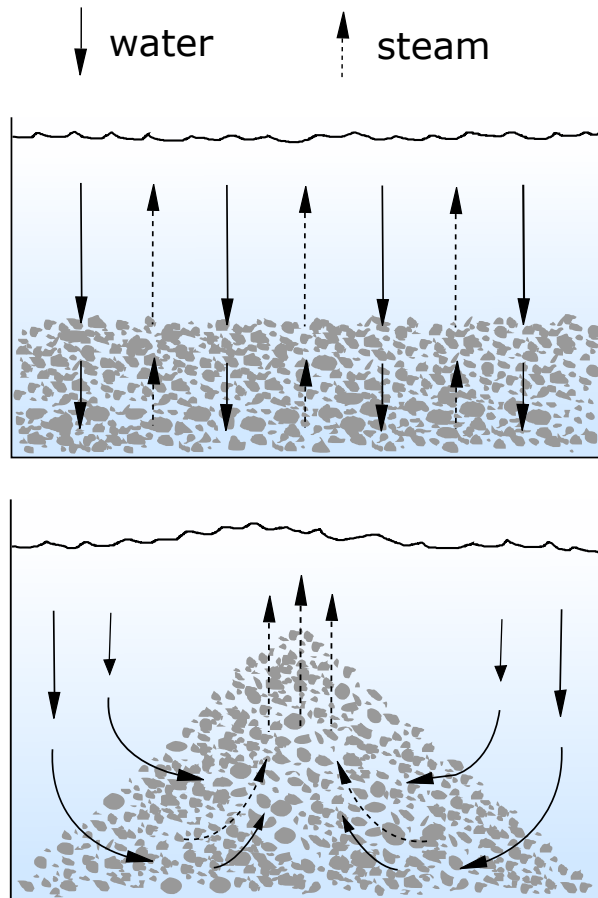


**Figure 2.2.** Top-flooded debris bed (top) and conical bed with multi-dimensional flooding.

greater chances of dryout when the steam at certain critical flux prevents water from accessing the bed.

The enthalpy of the steam flow that exits from the bed averaged over the cross-sectional surface area is the heat flux ( $W/m^2$ ). The *dryout heat flux*, usually abbreviated as DHF, corresponds to the mass flux at which the water infiltration is no longer capable of replacing the evaporating water, and dryout is reached in some part of the debris bed interior. Dryout is defined as the increase of void fraction  $\alpha$  in the pores of the bed to one, or the decrease of liquid saturation  $(1 - \alpha)$  to zero. In classical analyses, dryout heat flux is the coolability limit. If the heat flux by decay power generation is below this limit, stable coolable conditions are achieved for the corium.

### 2.2 What is known of debris bed geometry?

Knowledge of the debris bed properties has been obtained from fuel-coolant interaction (FCI) experiments, which include FARO (Magallon and Huhtiniemi, 2001), CCM (Spencer et al., 1994), KROTOS (Huhtiniemi and Magallon, 2001; Magallon, 2006), TROI (Song et al., 2003) and COTELS (Kato et al., 1999) conducted with  $\text{UO}_2 - \text{ZrO}_2$  corium, and the newer DEFOR (Kudinov et al., 2013) with simulant materials such as  $\text{Bi}_2\text{O}_3 - \text{WO}_3$ . The data from these types of experiments is extremely valuable since core melt accidents – quite obviously – cannot be tested with real-life NPPs.

It is important to note that the debris bed properties depend on the melt discharge process, the properties of which (e.g. melt jet diameter) depend on the in-vessel progression of the accident and the RPV failure mechanism. The chain of events leading to the formation of the porous bed is highly complex, and it would be practically impossible to take all possibilities into account in experimental studies, or even in numerical modeling. Moreover, the melt discharge from the RPV, the droplet solidification and the particle settling are stochastic processes which always include some randomness. Because of this, exact predictions of the debris properties cannot be made. This leads to the fact that uncertainties must be considered when assessing the reliability of debris cooling strategies.

In the present thesis, the emphasis is on the effects of the spatial distribution and the geometrical shape of the debris bed. Regardless of the uncertainties in the debris bed formation, the most probable geometry appears to be the conical shape with some irregularity and a round-shaped top. This is a plausible assumption, since the pouring of granular material on a vertical surface forms a conical pile due to the friction between the particles as witnessed in geotechnics (sand piles, etc.)

It is possible that the real, irregular debris bed is not axially symmetric and/or has non-homogenous internal structure. Here, the possible non-symmetry has been excluded from the studies, since it would have required significant extensions to the test program, after tackling the problem of selecting representative non-symmetric geometries for the experiments. Also, the effects of internal non-homogeneity, for instance, regions of higher porosity in the bed, have not been included in the research objectives (although the effects of local test bed heating will be discussed).

In most of the FCI experiments, the geometry of the debris bed resulting from the melt pour has not been documented. This is probably due to this being beyond the scope of the studies and the difficulty in drawing conclusions from the limited amount of experiments. Some mentions of debris bed shape can be found in the literature. In the CCM experiments, heap-like and uneven shapes were observed in CCM-4–CCM-6, which are described by Spencer et al. (1994) as a "central tapered mass of material" and having the greatest depth near the centre. The DEFOR debris beds resulting from the pour of simulant materials are clearly heap-like as reported by Karbojian et al. (2009). An example of a DEFOR debris bed is shown in Figure 2.3.

The steepness of a conical pile resulting from the pour of materials is given by the angle of repose. This is the maximum slope angle of a pile of granular material at which the material is at rest. Typically, the angle of repose varies between  $25^\circ$

## 2. Coolability of porous debris beds – overview



**Figure 2.3.** Fully fragmented non-homogenous debris bed formed in the DEFOR-E7 experiment (Karbojian et al., 2009).

and  $45^\circ$ , depending on e.g. the surface roughness (Kleinhans et al., 2011; Pohlman et al., 2006). In principle, studies of the angle of repose of soils and gravel materials could be used as guidelines for estimating the slope angle of the debris bed. However, it is possible that the convective flows in the water pool, caused by the hot debris, spread the particles more effectively than pouring through air or cool water. This is expected to flatten the conical bed towards a cylindrical form. The spreading by the two-phase flow is called self-leveling and it has been examined by Basso et al. (2014), Cheng et al. (2014) and Zhang et al. (2011). Even though typical slope angles for core debris beds cannot be derived based on existing data, about  $45^\circ$  appears as a reasonable maximum steepness for the debris bed.

The majority of previous debris coolability experiments have been performed in pipe-like test sections with either top or bottom flooding. These type of experiments offer only a limited possibility to examine the effect of multi-dimensional flooding, and the actual geometry of the debris bed is not considered at all. The present COOLOCE geometry variations in a pool-type facility are unique and serve as a step towards more reactor prototypic debris beds due to the consideration of the heap-like geometries: the fully conical bed and the truncated cone (see Figure 2.1). The drawback is that the experiments cannot be made on a realistic scale but, even on a laboratory scale, the experiments provide information on the relative effectiveness of the flooding modes and a basis for the validation and development of simulation codes applied in analyzing the issue on a reactor scale.

### 2.3 Heat flux in conical and cylindrical beds

The coolability of the fully conical debris bed is compared to the fully cylindrical bed in Publication II. The cylindrical bed is top-flooded because it is assumed to settle against the walls of the spreading area. Considering the reactor scale assessment,

## 2. Coolability of porous debris beds – overview

the geometry comparisons have to be made for the same amount of debris, and also independently of the other parameters that influence the dryout power. (The amount of debris in the flooded drywell may depend on the accident scenario and vary as a function of time, but it would hardly make sense to vary the corium mass simultaneously with the geometry).

In addition to the mass of the debris, it is useful to apply a constant volume to the debris bed by assuming that porosity is constant. This is necessary in order to rule out the effect of porosity on coolability but also on the dimensions of the debris bed. The debris bed coolability depends on the height of the bed as already mentioned in Section 2. Let us consider a top-flooded cylindrical bed as in Figure 2.1(b). For this geometry, the dryout heat flux DHF is calculated as the total dryout power of the bed  $P_{do}$  (W) divided by the area  $A$  (m<sup>2</sup>) of the bed top surface:

$$\text{DHF} = \frac{P_{do}}{A} \quad (2.1)$$

The heat flux  $q$  (W/m<sup>2</sup>) for any horizontal cross-section at height  $z$  in the bed interior can be calculated by dividing the integral power below this cross-section by its area  $A$ , whether or not dryout is reached:

$$q = \frac{P}{A} \quad (2.2)$$

For a cylindrical bed, the areas of the top surface and any horizontal cross-section are, naturally, the same. For a homogeneously heated bed, the heat flux at height  $z$  can be expressed with the power density  $Q$ , which is the power generation per unit volume (W/m<sup>3</sup>). Then the equation for heat flux is

$$q = \frac{QV}{A} = Qz \quad (2.3)$$

With the above expression, the heat flux at any height  $z$  can be defined without consideration of the cross-sectional area  $A$  when the volumetric heat generation is known. This is used in comparing the coolability of the different geometries, some of which do not have a clearly defined top surface comparable to the cylindrical bed. Another way to express the heat flux independently of the area, and also of volume, is by using the power per unit mass of the solid material  $W$  (W/kg):

$$q = \rho(1 - \varepsilon)Wz \quad (2.4)$$

where  $\rho$  is solid density (kg/m<sup>3</sup>) and  $\varepsilon$  is porosity, i.e. the fraction of the pore volume in the total volume.

In the case of the Finnish BWRs, the assumption that the debris is evenly distributed against the walls and has a fairly small porosity of 40%, results in a wide but rather shallow cylindrical bed. The height of the bed is approximately 0.6 m. If the same amount of debris settles in a conical configuration so that the bottom of the cone is spread against the walls of the drywell, the cone is 1.8 m in height. Assuming that the cylinder and the cone are equal in volume ( $V$ ) and bottom radius

## 2. Coolability of porous debris beds – overview

( $r$ ), it follows directly from the geometry that the cone is three times higher than the cylinder:

$$V = \frac{1}{3}\pi r^2 z_{\text{cone}} = \pi r^2 z_{\text{cyl}} \quad (2.5)$$

$$\Rightarrow z_{\text{cone}} = 3z_{\text{cyl}} \quad (2.6)$$

Then, if the power density is the same in the two beds, the heat flux at the top boundary of the cone is always three times higher than that of the cylinder according to Equation 2.3:

$$q_{\text{cone}} = 3Qz_{\text{cyl}} \quad (2.7)$$

It is expected that the multi-dimensional flooding facilitated by the conical shape of the bed increases the dryout power and coolability compared to the flat, top-flooded cylinder, but the increased height counteracts this effect because it facilitates the formation of greater heat flux near the top of the bed. When considering the coolability in realistic containment geometries, the dimensions of the debris bed cannot be ignored. The main objective of the study in Publication II was to find out how significant the effect of multi-dimensional flooding is compared to the effect of the debris bed height, and what its significance to the overall coolability is.

It must be mentioned that the heat flux discussed above is by definition a surface-related variable which is directly applicable only for one-dimensional flow in which the steam flow is directed upwards. In the conical bed, no top surface exists that would be directly comparable to that of the cylinder. However, the heat flux at the highest point of the cone and other geometries illustrated in Figure 2.1 can be calculated with Equation 2.3 using the power density. This makes it possible to compare the coolability of the different geometries, as will be discussed later in the thesis.

### 3. Experimental approach and the early results

The experiments addressing the effect of multi-dimensional flooding were conducted using the STYX and the COOLOCE test facilities. The STYX experiments described in Publication I were a continuation of the series of tests which investigated the coolability of test beds with irregularly-shaped particles with a particle size distribution based on FCI experiments (Lindholm et al., 2006; Holmström et al., 2005). Particle size stratification by means of a layer of fine particles on top of the debris bed was also examined to account for the presence of small, thoroughly fragmented particles formed in a possible steam explosion.

The STYX test set-up is close to the classical test facilities due to its cylindrical shape and the flooding through the top surface. As described in Publication I, the cylindrical test facility was equipped with downcomers that facilitated a type of combination flooding through the permeable top and the downcomers attached to the sides of the cylinder near the bottom of the test bed. The COOLOCE facility described in Publication II differs from the STYX facility and other classical facilities, because the test bed section is modifiable so that measurements can be performed for differently-shaped test beds. In this arrangement, it is not necessary to apply downcomers to produce different flooding modes. Instead, the test bed itself can be changed, which yields more freedom in the dimensions of the test bed, making the set-up more realistic.

In addition to the multi-dimensional flooding investigations, the effect of the simulant material has been considered in some of the COOLOCE experiments. These results are included in Publication V, which presents several studies on the effects of the size and morphology of the debris particles, conducted by different European laboratories involved in the SARNET network (van Dosselaere and Paci, 2014). The objective was to form a better understanding of the applicability of the effective particle diameter as a representative measure for the irregularly-shaped and -sized particles of realistic debris beds. The concept of effective particle diameter cannot be avoided in connection with the models developed for predicting dryout in the porous bed. This is because the multitude of possible particle shape and size variations have to be described in an averaged manner.

In this chapter, the experimental methods are described, followed by the description of the STYX facility and the review and summary of the experimental results.

### 3. Experimental approach and the early results

Chapter 4 is dedicated to the COOLOCE experiments. The studies of the effective particle diameter are presented in Chapter 6 following the discussion about the simulation models, because these studies applied both experiments and simulations.

#### 3.1 Determination of dryout

Both COOLOCE and STYX facilities apply electrical resistance heating to simulate decay heat. The formation of dryout is detected based on the sustained increase of temperature from the saturation temperature. In principle, the experimental procedure is similar in the two facilities. The test run is initiated with a heat-up sequence during which the facility is pressurized and the temperature is increased up to the saturation temperature (at the pressure of the intended experiment) and steady-state boiling is developed. During this phase, the air possibly trapped in the pores of the bed exits from the bed.

The heat-up sequence is followed by the test sequence which consists of stepwise increases of heating power until temperature excursion from the saturation temperature is indicated by one or more of the temperature sensors installed into the test bed. This indicates dryout at the sensor location(s). To allow the development of dryout, a waiting time of 20–30 minutes is applied at each power level, between the power steps.

The result of the measurement is a pair of powers: the maximum power at which the bed is in a coolable steady state and the minimum power at which local dryout is reached. The minimum power at which local dryout is reached is taken as the dryout power. The heat flux corresponding to the dryout power is abbreviated as DHF and the maximum coolable power as CHF. The size of the power steps in both STYX and COOLOCE experiments was typically 1 kW or 2 kW, and the measured dryout power was between 15 kW and 55 kW. The maximum operating temperature prior to dryout was about 165 °C, which is the saturation temperature at 7 bar.

#### 3.2 Experiments with irregular particles

The main components of the STYX test facility are the pressure vessel which contains the test bed, the feed water and steam removal systems, and the process control and data acquisition systems. The principal measurements are temperature, pressure and the input power of the heating elements. The schematic of the pressure vessel including downcomers, and a photograph of the particle bed housed in an inner cylinder are illustrated in Figure 3.1. The test bed is 300 mm in diameter and 600 mm in height. Three symmetrical downcomer tubes at 120° intervals connect the pool on top of the bed to inlets near the bottom of the inner cylinder.

The debris bed consists of alumina ( $\text{Al}_2\text{O}_3$ ) gravel with a particle size range of 0.25–10 mm. The size distribution of the particles was initially chosen based on the measured size distributions in FCI experiments, resulting in a distribution close to the one in the FARO-L31 test (Lindholm et al., 2006). The size distribution was re-examined by sieve analysis while the test series was ongoing (Holmström et al.,

### 3. Experimental approach and the early results

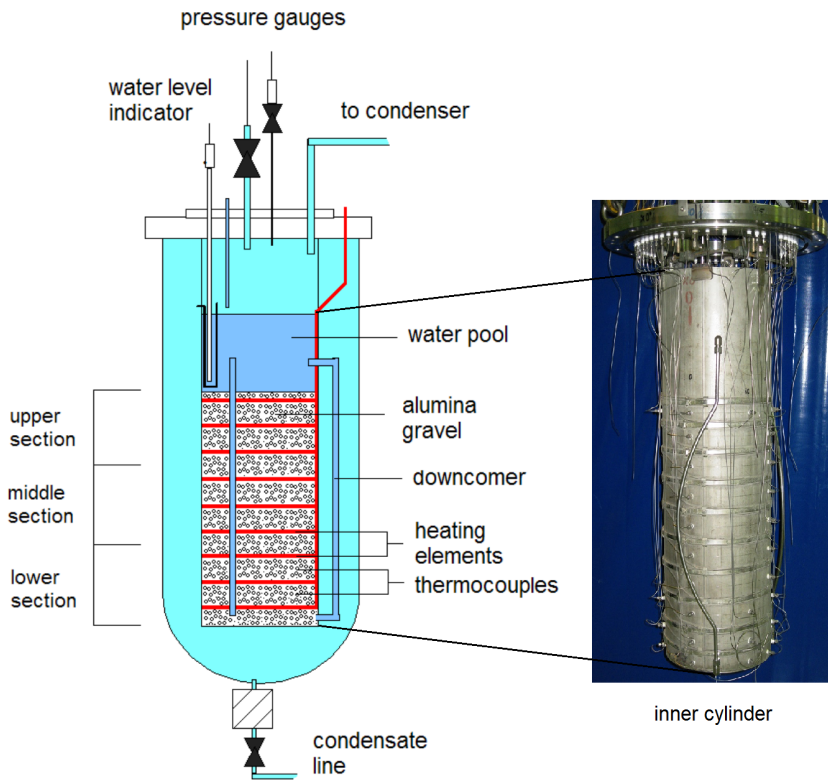


**Figure 3.1.** Schematic of the STYX test vessel and a photo of the inner cylinder.

2005) and later in connection with the COOLOCE-8 experiment in which the same material was used (Takasuo et al., 2012b). The size distributions are presented in Figure 3.2. The layer of fine particles applied in some of the tests is not accounted for in the distribution. However, the very small particles with the diameter less than 0.25 mm, found in COOLOCE-8 but absent in STYX-1, might be traces of the fine layer mixed into the bed of coarser particles.

The porosity of the test bed has been estimated to be 34–37% (Lindholm et al., 2006). The bed was built by carefully placing small batches of gravel into the test cylinder, aiming for a uniform mixing of the different-sized particles. This probably resulted in somewhat looser packing and greater porosity than the densest possible packing for the material, at least initially. The test bed was not systematically emptied and rebuilt between the test runs, and there is no data considering the repeatability of the test bed packing.

In general, the irregular shapes of the gravel particles resemble the shapes found in FCI experiments by e.g. Kudinov et al. (2013), which means that the gravel particles can be considered to be realistic. Porosity, on the other hand, may be greater in

### 3. Experimental approach and the early results

real debris beds even with irregularly-shaped particles. Porosities of 46–71% were found in the DEFOR experiments (Kudinov et al., 2010) and large porosities of 53% and 65% were also reported in the CCM-1 and CCM-3 experiments (Spencer et al., 1994).

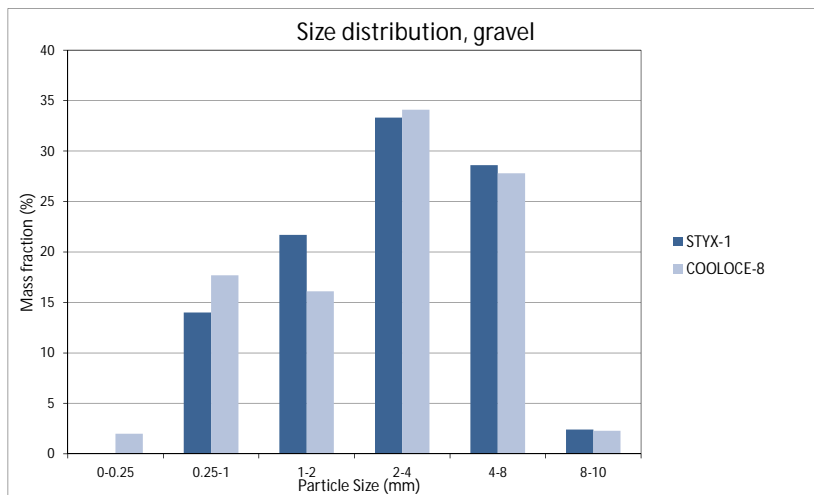


**Figure 3.2.** Size distribution of the alumina gravel in the STYX and COOLOCE-8 experiments.

The heating arrangement consists of resistance wire elements with a width of 10 mm that are distributed within the 600 mm test bed at nine horizontal levels, at 67 mm distance from each other. The maximum power output of the facility is 87 kW. K type thermocouples (TCs) were installed between the heaters so that nine levels of TCs were at equal distances between the heaters. In order to determine the dryout location accurately in the horizontal direction, each of the levels contained four to eight sensors.

The unheated volume between the heating elements is relatively large, which results in high local power density in the vicinity of the heaters. This might lead to local dryout near the heater surfaces at comparatively low power. On the other hand, the determination of dryout is based on TCs located in the unheated volume, 33 mm from the heaters, which means that no data is recorded at the heater locations. It can be assumed that the steam generated by the heaters is distributed into the unheated volume, so that each of the nine heater level produces additional steam into the unheated volume above it, and thus the test bed approximates homogenous heating (constant power density). The COOLOCE experiments that will be described in the next chapter rely on a similar approach to manage the possible effect of local heating, and the consequently large local power densities, even though the heater type and

### 3. Experimental approach and the early results

orientation are different in COOLOCE.

In addition to the porous bed, thermocouples were placed on the inner and outer pressure vessel walls and in the water reservoir above the bed. Two pressure gauges were used: one for controlling the pressure in the test vessel and one for monitoring it. A water level measurement controls the water level on top of the test bed.

The experiments with downcomers consisted of four test series with and without the fine particle layer, listed in Table 3.1. These test series are numbered 10–14 and they follow the test series 1–9 which consisted of pure top-flooding experiments using the same simulant material. In the test series 10–14, dryout was measured for the pressures of 2, 5 and 7 bar (absolute) with two sizes of small downcomers, 5 mm and 8 mm in diameter (each of the three downcomers had the same size). STYX-11 was a top-flooding experiment with plugged downcomers, performed to produce comparison data for the other tests. For the homogenous test bed of STYX-13, comparison data is obtained from an older top-flooding experiment STYX-8 described in detail by Holmström et al. (2005).

**Table 3.1.** The STYX experiments with and without downcomers.

Experiment	Bed height and type	Pressure [bar]	Downcomer diameter [mm]
STYX-8	600 mm homogenous	2, 5, 7	-
STYX-10	600 mm with 60 mm fine layer	2, 5, 7	5
STYX-11	600 mm with 60 mm fine layer	2, 5, 7	-
STYX-12	600 mm with 60 mm fine layer	2, 5, 7	8
STYX-13	600 mm homogenous	2, 5, 7	8

#### 3.2.1 The effect of lateral flooding

For the test bed without the fine particle layer, the effect of the multi-dimensional flooding was clear and consistent towards increased dryout heat flux and better coolability. The DHF increased by 22–25% with the 8 mm downcomers (STYX-13) compared to the STYX-8 experiment without the downcomers. The measured DHFs for the different pressure levels are shown in Figure 3.3. The effect of the downcomers in the case of the bed with the stratification layer was not as clear and consistent. The DHFs for this bed are shown in Figure 3.4.

The maximum DHF of 523 kW/m<sup>2</sup> was obtained for the homogenous bed with downcomers at 7 bar. The corresponding dryout power was 37.0 kW. The stratified bed with no downcomers at 2 bar pressure had the lowest DHF, 235 kW/m<sup>2</sup>, and the lowest dryout power, 16.6 kW.

It was seen that dryout occurred first near the top of the bed at 533 mm TC level in the homogenous bed with downcomers (STYX-13), while without downcomers (STYX-8), the location was in the lowermost parts of the 60-cm-deep test bed. This

### 3. Experimental approach and the early results

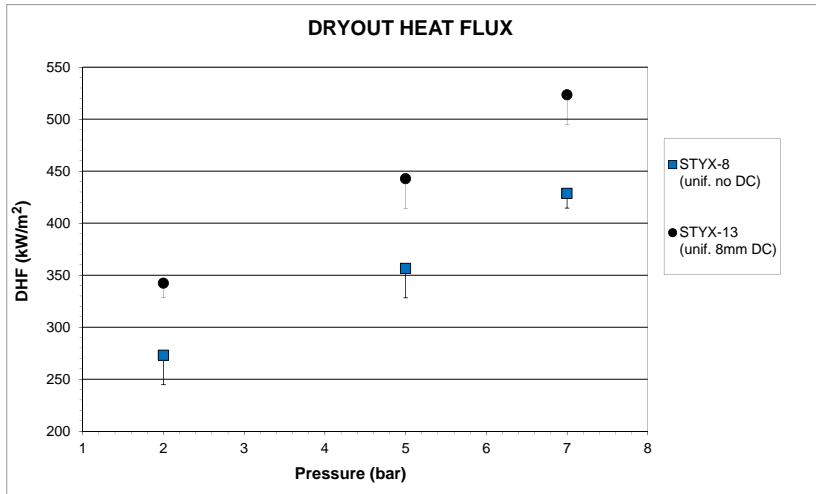


**Figure 3.3.** Dryout heat flux in the homogenous STYX test bed with and without downcomers.

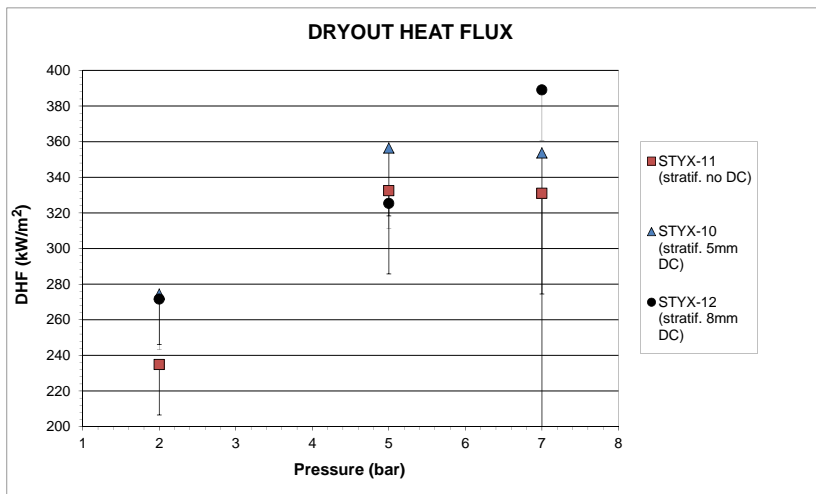


**Figure 3.4.** Dryout heat flux in the stratified STYX test bed with and without downcomers.

is in accordance with the theoretical expectations and earlier results concerning the dryout development in top- and bottom-fed beds (Hofmann, 1987; Schmidt, 2004) as

### 3. Experimental approach and the early results

will be discussed in detail in Section 5.4.1. The dryout locations suggest that even though the downcomers are small (their area is only 0.03% of the surface area of the cylinder sidewall) and the test bed is relatively wide, the downcomers are capable of providing co-current flow in the bed interior, transferring the dryout location from the lowest TC levels to the top and yielding a notable coolability increase.

For the stratified beds, the DHF increase by the downcomers was small and the results were, in general, not as clear as in the homogenous cases. The 2 bar tests with downcomers of both sizes (STYX-10 and STYX-12) showed a 16-17% increase in the dryout power compared to the top-flooded test (STYX-11). At 5 bar pressure, the test with 5 mm downcomers showed a 5% increase, and the test with 8 mm downcomers showed a small decrease. In the 7 bar experiment using the 8 mm downcomers, an increase of 18% was seen while, for the smaller 5 mm downcomers (STYX-10), the increase remained below 10%. The increases for 2 and 5 bar points were only marginally greater than the uncertainty. In the stratified test beds, the initial dryout location varied. In the 5 mm downcomer tests, dryout was observed in the middle section of the test bed. With the 8 mm downcomers, dryout was first seen near the lowermost TC levels and at the 267 mm level.

The results also show that the stratified test bed has a 10–30% lower DHF than the homogenous bed. This is approximately similar to the difference seen in the earlier STYX experiments (Lindholm et al., 2006). Even lower DHFs could be expected for a bed with a fixed layer of small particles based on experiments (Hofmann and Barleon, 1986) and commonly used simulation models as discussed in Publication I. It has been concluded that the fine layer has not been stable in the STYX experiments. Instead, according to post-test inspections, it has been fluidized under the forces caused by the steam flow which causes the relatively good coolability.

#### 3.2.2 Behavior of the fine particle layer

Questions of interest in the experiments with the stratified bed include why the DHF did not notably increase through the use of downcomers, or even through the increase of pressure from 5 bar to 7 bar as seen in Figure 3.4. It must be mentioned that the 7 bar tests in STYX-10 and -11 did not follow the normal stepwise test procedure because the maximum coolable power was not measured. This explains the large error margin for the 7 bar points in Figure 3.4. However, since the measured DHF is a roof value that cannot deviate upwards, the result concerning the unexpectedly low DHF is valid. The apparent loss of pressure dependency was already observed by Holmström et al. (2005) when testing different bed depths and fine particle layers but not analyzed.

The small particles in the fine layer are more easily fluidizable than the larger main bed particles. For fluidization, the flow velocity has to exceed the minimum fluidization velocity, which means that the fluidization is only relevant near the top of the bed. The minimum fluidization velocity can be estimated using the well-known Ergun equation (Ergun, 1952) by assuming that the pressure loss due to drag force equals the weight of the particles. The obtained velocity is compared to the steam velocity

### 3. Experimental approach and the early results

at the top of the bed which is calculated from the boiling mass flow rate. Assuming that the effective particle diameter of the fine layer is of the order of 0.12 mm, as estimated by Kokkonen (2004), the superficial velocity (the flow rate divided by the flow area) of steam may have exceeded the fluidization velocity of the fine particles for all the pressure levels.

However, the velocity comparison does not reveal why the behavior is different depending on the pressure. The minimum fluidization velocity decreases if the ambient pressure is increased (Yang, 2003), which should increase the coolability, rather than decrease it. In general, the three-phase fluidization of particles in gas and liquid flow is a complicated phenomenon in which e.g. the bed expansion and bubble size variation (as a function of pressure) may play a role, and based on only the DHF data the mechanism explaining the behavior of the stratified test bed might be impossible to detect.

The material comparison experiments carried out with the COOLOCE facility shed some light on the behavior of the gravel bed (Takasuo et al., 2012b; Takasuo, 2013). It was seen that the DHF increase as a function of pressure measured with the alumina gravel was not as steep as with the spherical beads, or as predicted by models. The packing of the gravel bed was left loose by careful mixing of the particles, and did not initially reach the minimum porosity. During the experiments, the bed is subjected to mechanical stresses caused by the boiling mass flow and, also, the small particles may gradually be shifted between the larger ones. It seems plausible that the packing of the test bed changed in some manner during the test runs towards smaller porosity, but the change was not large enough to be seen as a reduced test bed height.

In general, the experiments were conducted starting from the low or medium pressure levels. Thus, before the 7 bar test run, the bed had already undergone several boiling, dryout and reflooding sequences, which could have caused changes in porosity. This effect might have been enhanced in the stratified bed due to the gradual mixing of the fine particles into the coarser debris. On the other hand, some repeatability experiments were conducted with the gravel bed, which did not show notable differences between older and newer test results.

In any case, the fluidization effects of the fine particle layer with possible changes in bed porosity have such a large and poorly predictable effect on the DHF that the contribution of the downcomers is indistinguishable. Finally, it can be stated that the fluidization and mixing of the finer and lighter particles cannot be considered non-prototypical to reactor conditions because the steam flow may indeed fluidize the particles and cause the bed to spread by self-leveling as mentioned in Section 2.2. This might occur even though corium is heavier than the simulant particles, having a density more than twice that of gravel.

#### 3.2.3 Measurement errors

The largest error source in the dryout heat flux experiments in both the STYX and COOLOCE facilities is the method of finding the dryout power using stepwise in-

### 3. Experimental approach and the early results

put power increases. The magnitudes of the power steps between the maximum coolable and minimum dryout powers are indicated by the error bars in Figures 3.3 and 3.4. The exact value of the DHF is between these two power levels. A 2 kW increase of the total power corresponds to a maximum error of about 30 kW/m<sup>2</sup>, which yields a relative error of 5–10%, depending on the pressure level.

The error caused by the inaccuracies of the power meter and the manual power control were estimated to be at most  $\pm 15$  kW/m<sup>2</sup>. In the STYX downcomer experiments, a temperature increase of at least 5 °C from the saturation temperature was considered to be an indication of dryout. Thus, the dryout measurement is not influenced by minor temperature changes due to pressure fluctuations or the thermocouple accuracy. A more detailed discussion of the measurement errors is presented in Section 4.3 in connection with the COOLOCE experiments, which utilized the same power source as the STYX experiments.

## 4. Debris bed geometry experiments

The COOLOCE facility, which was designed to investigate the effect of the test bed geometry, utilizes the same power source and feed water and steam removal systems as STYX. The pressure vessel with the test bed section and its instrumentation, however, were rebuilt for the COOLOCE experiments. The test bed is housed in a relatively large stainless steel pressure vessel that has an outer diameter of 613 mm and a volume of 270 dm<sup>3</sup>. The arrangement of heaters and TCs is somewhat different from that of STYX. The resistance wires were not technically practical in a conical test bed, and they were replaced with cartridge heaters which are inserted into the bed through tapered holes in the bottom of the pressure vessel. Similarly, the temperature sensors are connected through the bottom.

The conical bed has 137 heaters (6 mm diameter) and 68 thermocouples (3 mm diameter) between the heaters at different heights. The heaters are installed into the bottom plate of the pressure vessel into a "square mesh" at a distance of 30 mm from each other. The cylindrical bed has 69 heaters and 60 TCs. Depending on the experiment, one to three of the TCs were multi-point thermocouples that had ten sensor points. In the conical test bed, one sensor covers the volume of 69 cm<sup>3</sup> near the center of the test bed. In the cylindrical test bed, there is one sensor for 97 cm<sup>3</sup>. The schematic of the test facility with the conical test bed installed is shown in Figure 4.1 and the heater and thermocouple arrangements are shown in Figure 4.2.

With cartridge heaters of different lengths and constant nominal power per length, a volumetrically even and dense power distribution was achieved. The maximum power output varies depending on the test bed; for the conical bed it is about 55 kW. It was acknowledged that the vertical orientation of the heaters and TCs can result in increased artificial channeling of the flows in the bed due to the increased porosity near the surface of the vertical structures. However, because the main objective was to study the differences in the flooding mode and all the experiments were planned to be conducted with similar heating arrangement, this was not considered to be a critical issue that would reduce the comparability of the results. In addition, the temperature sensors for dryout detection are located in the porous medium between the heaters, not next to the heater surfaces where the possible local effects are realized.

Spherical ceramic beads (mixture of ZrO<sub>2</sub> and SiO<sub>2</sub>) were used as the particle ma-

#### 4. Debris bed geometry experiments

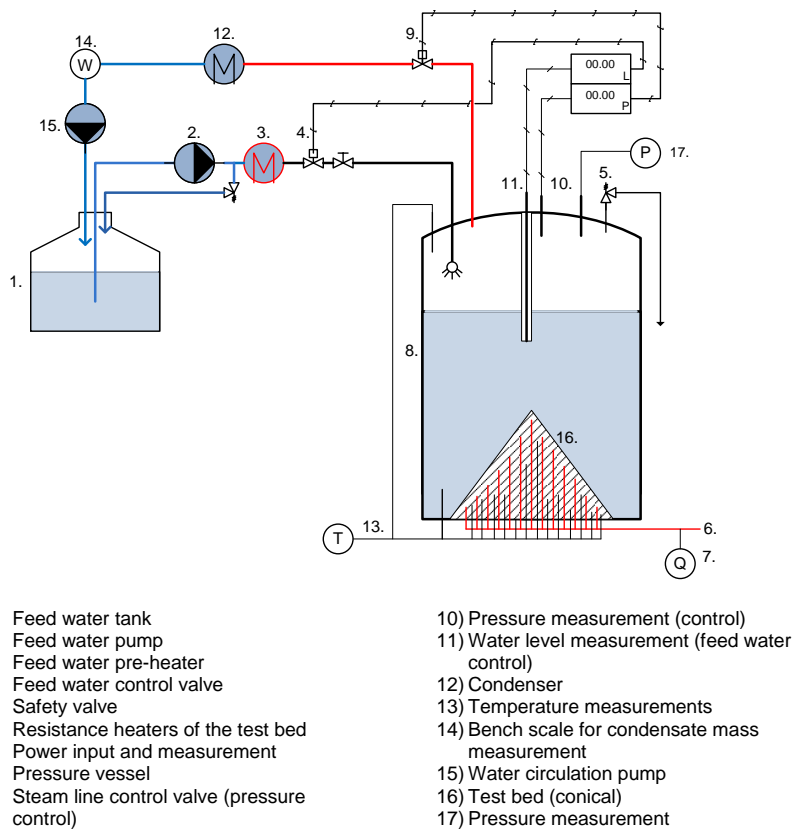
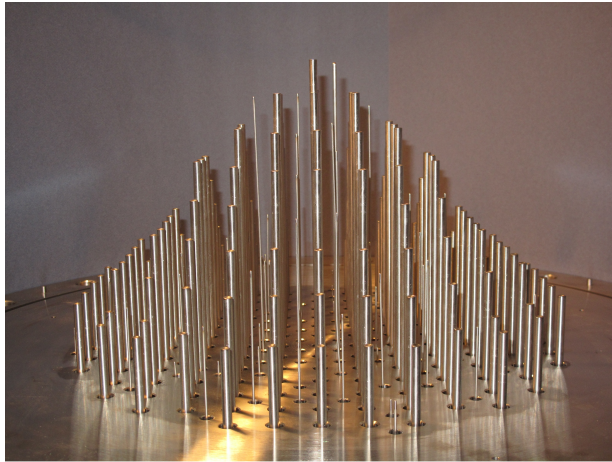


**Figure 4.1.** Schematic of the COOLOCE test facility.

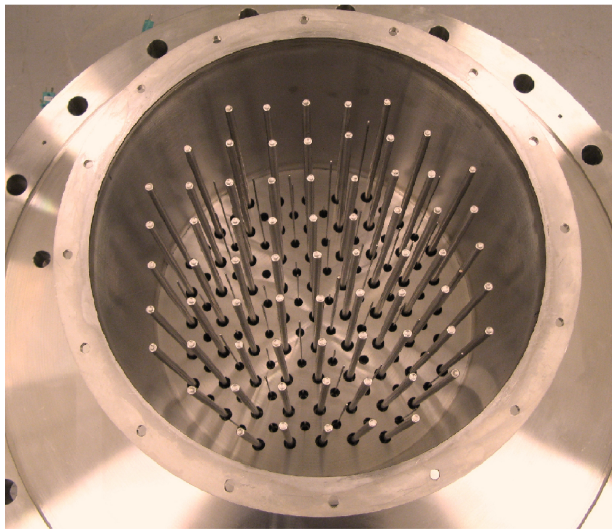
material for the geometry comparison experiments. The material is not prototypic like the alumina gravel but, due to the more uniform size and the simpler packing mechanism of spherical particles, it provides well-defined conditions for distinguishing the effect of the multi-dimensional flooding by reducing the uncertainties related to the bed packing. The particle size was measured to be in the range of 0.815 – 1.126 mm by image processing analysis of a sample of 1000 particles. The arithmetic mean diameter was 0.97 mm. The size distribution was further verified by a laser diffraction analyzer (Malvern, 2015), which showed results close to the image analysis.

The test matrix is presented in Table 4.1. The table shows with which geometry, flooding mode and particle material each test has been conducted. There is some variation in the pressure range of the experiments because in some cases the dry-out power was greater than the maximum power of the facility (mainly in the higher pressures).

#### 4. Debris bed geometry experiments



(a)



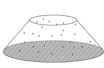
(b)

**Figure 4.2.** The heater and thermocouple arrangements of (a) the conical test bed and (b) the cylindrical test bed.

Of the different test series, the effect of the flooding mode is examined in COOLOCE-3-5, COOLOCE-6-7 and COOLOCE-10-13. COOLOCE-8 was conducted with the alumina gravel to obtain comparison data for the experiments with the ceramic beads. COOLOCE-9 was conducted with initially subcooled water in

#### 4. Debris bed geometry experiments

**Table 4.1.** The COOLOCE experiments.

Experiment	Flow configuration	Test bed	Simulant material	Pressure range [bar]
COOLOCE-1 – 2	Conical, multi-dimensional flooding		Spherical beads (ZrO <sub>2</sub> , SiO <sub>2</sub> )	1.6-2.0
COOLOCE-3 – 5	Cylindrical, top flooding			1.1-7.0
COOLOCE-6 – 7	Conical, multi-dimensional flooding			1.1-3.0
COOLOCE-8	Cylindrical, top flooding		Irregular gravel (Al <sub>2</sub> O <sub>3</sub> )	1.1-7.0
COOLOCE-9	Cylindrical, top flooding (initially subcooled)			1.0
COOLOCE-10	Cylindrical, lateral and top flooding		Spherical beads (ZrO <sub>2</sub> , SiO <sub>2</sub> )	1.3-2.9
COOLOCE-11	Cylindrical, lateral flooding			1.1-6.9
COOLOCE-12	Cone on a cylindrical base, flooding through conical part			1.1-3.8
COOLOCE-13	Truncated cone, multi-dimensional flooding			1.3

order to scope the effect of the pool subcooling that might be expected in the case of a real accident. The first tests, COOLOCE-1–2, were preliminary experiments with the conical test bed, the results of which are not considered as reliable as those from the later experiments as explained in Publication II. (In the first tests, the temperature increase was not very clear and measurements above 2 bar were not successful.) The repeatability of the dryout power was verified by one additional measurement in three test set-ups, COOLOCE-3, -4 and -8. The results of the first and the repeated experiments differed by less than 1 kW. The test beds were not disassembled and re-packed between the measurements.

In addition to the data contained in Publications I, II and V and the following sections, detailed descriptions of the COOLOCE-3–13 experiments including the time evolutions of the heating power and temperatures during the test runs have been published in technical reports of the test series (Takasuo et al., 2011b; Takasuo et al., 2011c; Takasuo et al., 2012b; Takasuo et al., 2013a; Takasuo et al., 2013b; Takasuo et al., 2013c and Takasuo et al., 2015).

#### 4.1 Flooding mode experiments

The effect of the flooding mode was investigated by using the six debris bed geometry variations which were illustrated in Figure 2.1 and Table 4.1. Photographs of the test beds are shown in Figure 4.3. The volumes and diameters of the test beds are indicated on the figure. The height of all test beds is 270 mm with the exception of the truncated cone, the height of which is 160 mm. The slope angle (the presumed angle of repose) of the cone, the truncated cone and the top part of the cone on a cylindrical base is  $47^\circ$ .

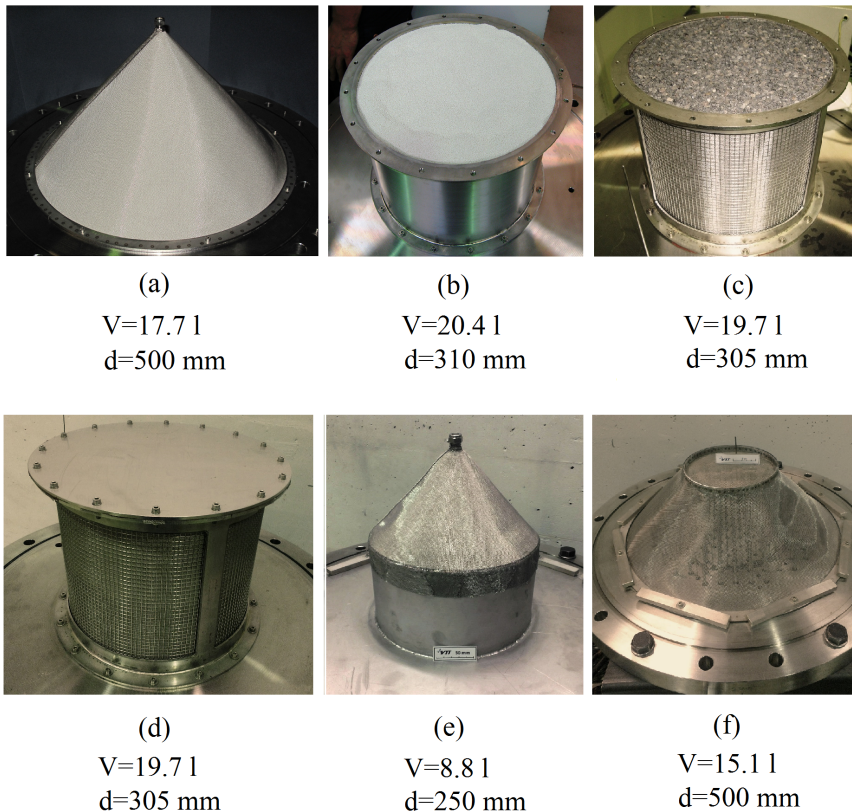


**Figure 4.3.** The COOLOCE test beds: (a) conical, (b) top-flooded cylinder, (c) fully-flooded cylinder (open walls), (d) cylinder with lateral flooding, (e) cone on a cylindrical base, and (f) truncated cone.

The conical bed and the truncated cone which approximates a round-shaped heap are representative of reactor scenarios as reviewed in Section 2.2. The top-flooded cylinder is also a prototypic form, presuming that the debris is evenly spread in a flat layer. The fully flooded cylinder which allows water infiltration through all surfaces

#### 4. Debris bed geometry experiments

(except the bottom) is an approximation of the heap-shaped bed. This test bed was modified from the top-flooded bed by replacing the steel cylinder with a wire net. Later it was decided to equip the fully conical arrangement with shorter heaters to achieve the truncated cone geometry which, in retrospect, is the most prototypic shape. The cone on a cylindrical base considers the case in which the bottom part of the debris is spread evenly but the top part retains the conical shape. This combination shape is also possible in a reactor scenario, though the width-to-height ratio would be larger on a realistic scale.

The experiment with the laterally flooded cylinder having an impermeable top was motivated by the possibility of particle agglomeration. Partially molten particles may attach to each other to form agglomerates impermeable to fluid flow. Even large regions of solid "cakes" have been observed in experiments (Kudinov et al., 2013). It must be stated that a cake region that would fully cover the top of the debris bed is not a particularly probable configuration. However, its advantage compared to some completely arbitrary form of agglomerate is that it gives clearly defined conditions for experimentally testing the lateral flooding and evaluating the capabilities of simulation models to predict the dryout behavior if the fraction of lateral flow is large.

The porosity of each test bed was estimated by weighting the particles when building the test beds. For the top-flooded cylinder, porosity was also measured by filling the ready test bed with water and measuring the water volume. The volumes of the heaters and TCs, which is approximately 2% of the total volume, are subtracted from the total volume in the porosity estimates. The porosities for the ceramic beads were as follows:

- Cylindrical beds 0.39-0.392
- Conical bed 0.40
- Cone on a cylindrical base 0.375
- Truncated cone 0.354

For the truncated cone, the measured porosity of 35.4% is so low that the value is probably erroneous. The maximum random packing of spherical particles corresponds to a porosity of about 36.6% (Song et al., 2008). The small porosity might be due to the stretching of the wire net, which would increase the amount of particles that can be fitted into the test bed. The wire net is a flexible structure, which means that the dimensions of the test beds supported by the net are more uncertain than those of the top-flooded cylinder constrained by a solid wall. For analytical purposes, it is reasonable to assume that the porosity of the truncated cone is approximately the same as the conical bed porosity. The measurement by filling the cylindrical test bed with water yielded a somewhat smaller porosity, 38.1%.

Due to technical reasons, there is variation in the test bed volumes (see Figure 4.3). Thus, the total dryout power which is recorded by the data acquisition system is not a very useful variable for comparing the flooding effectiveness, because it depends on the volume. Power density is more useful in assessing the relative

coolability because it is independent of the dimensions. Dryout heat flux is practical because, for a homogeneously heated bed, it is independent of the bed height. Here, the flooding mode comparisons are presented using the dryout heat flux at the top boundary. The effect of the test bed height is treated separately by converting the dryout heat fluxes measured for the top-flooded cylinder back to power density. The independence of DHF from the bed height makes this comparison possible so that the "absolute" coolabilities (in  $\text{W/m}^3$ ) of the flat-shaped cylindrical bed and the tall, conical beds may be compared.

### 4.1.1 Dryout heat flux

The dryout heat flux for the top-flooded cylinder is calculated from the power recorded by the data acquisition system and the top surface area according to Equation 2.1. It may also be calculated using the power density using Equation 2.3.

The heat flux is primarily applicable to the effectively one-dimensional bed, such as the top-flooded cylinder, that has a surface area through which the energy is transferred in the form of the enthalpy flux corresponding to the mass flux of steam flowing through it. The conical bed does not have a comparable surface because the highest location of the cone is a point, not a surface. The steam flow, of course, escapes from the cone through the fully open surface but the average heat flux through the large, inclined surface is not a very useful variable because it is not directly comparable to the horizontal surface of the top-flooded bed. In fact, the average DHF calculated using the cone surface would neglect the increase of heat flux with increasing height since also the lowest, perimeter regions of the cone would be integrated into the DHF. In the cylinder with lateral flooding only, the top is impermeable and there is no steam flux through it. Instead, steam is forced to escape through the sidewall which, again, is not comparable to the heat flux through the top.

The problem of finding a suitable DHF definition for the comparisons is solved as follows. It has been shown in several numerical simulations in Publications III and IV and other works by the author (Takasuo et al., 2014; Takasuo et al., 2015) and others (Yakush et al., 2012) that the steam flow is practically always directed upwards in terms of the superficial velocity near the central axis of the conical bed, and even in the bed with impermeable top, the vertical steam flow turns lateral only just before the impermeable part. Then, Equation 2.3 can be applied to calculate the local heat flux for the highest point of the geometry by multiplying the power density by the maximum height of the bed. This heat flux calculation makes no difference whether the maximum height is represented by a planar surface or a point (an infinitesimally small surface). For instance, the 1D cylindrical bed has a heat flux (in  $\text{W/m}^2$ ) through any of its highest points (that form the planar top surface) which is equal to the heat flux through the top surface. The effectiveness of the different geometry-related flooding modes can easily be compared by comparing the DHFs at the maximum height of the bed, without considering the surface areas.

The dryout heat fluxes for the six geometry variations are presented in Figure 4.4–Figure 4.9. Each pressure level is shown in a separate chart. The ratio of the

#### 4. Debris bed geometry experiments

DHF of each geometry to the DHF<sub>0</sub> of the "base case", the top-flooded cylinder, is shown on top of the bars in the charts. This ratio indicates the relative increase of coolability compared to the top-flooded cylinder. The most informative pressure levels are 1 bar and 2 bar because, above these pressures, the dryout power gradually became greater than the maximum output of the facility for most geometries. At 5 and 7 bar only two measurements were possible (with the two beds that had poorest coolability).

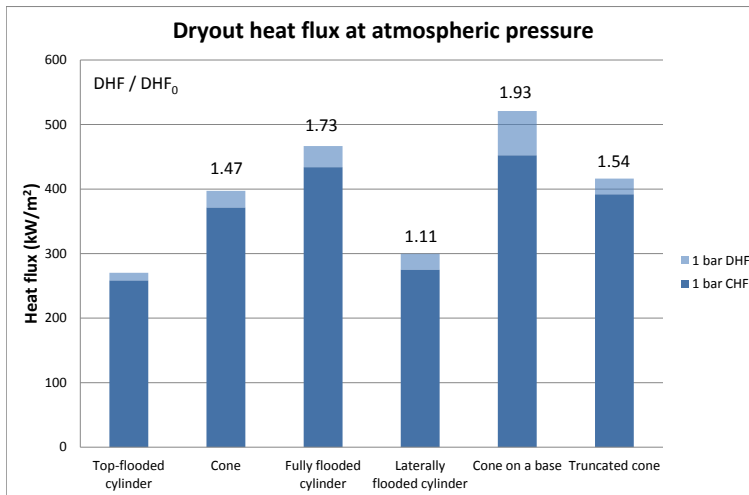


**Figure 4.4.** The dryout heat flux (DHF) at atmospheric pressure. CHF is the maximum coolable power and the light blue zone at the top is the error margin DHF–CHF.

All the COOLOCE geometries are included in the DHF comparison in Figure 4.4. The tests were performed at the atmospheric pressure or close to that (1.1 – 1.3 bar), depending on the accuracy of the pressure control. The largest DHFs were obtained for the cone on a cylindrical base, the fully flooded cylinder and the fully conical bed, and also for the truncated cone. The DHF increase for these geometries compared to the top-flooded cylinder was 47–93%. At 2 and 3 bar, the increase was 50–73%.

The larger variation in the DHF/DHF<sub>0</sub> ratio at 1 bar is explained by the pressure variation. Experiments at atmospheric pressure had more pressure fluctuations than experiments with a pressurized test vessel. A test run at atmospheric pressure requires that the control valve at the steam line is fully open. It was noticed during the tests that if the operating power and the consequent steam flow rate are very high, which is the case in the well coolable test beds, the flow resistance in the steam line builds counter-pressure that causes the vessel pressure to increase, even though the steam valve is fully open. In the conical bed test series, the attempt to measure at atmospheric conditions first lead to an increase of up to 1.6 bar. Then, the control

#### 4. Debris bed geometry experiments

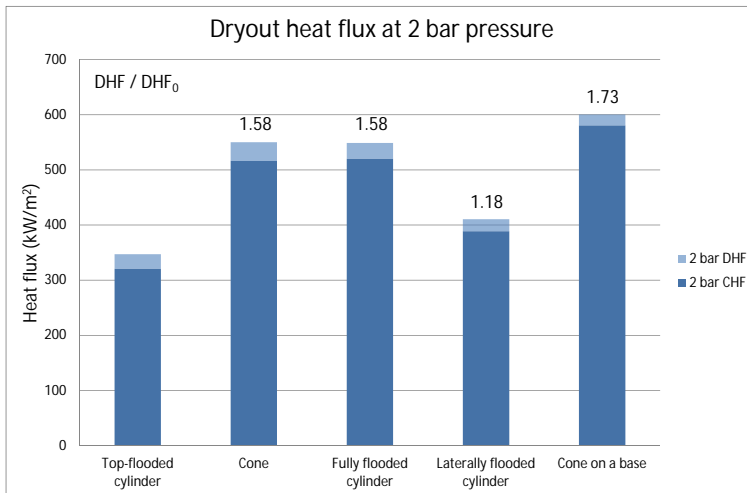


**Figure 4.5.** The dryout heat flux (DHF) at 2 bar pressure. CHF is the maximum coolable power and the light blue zone at the top is the error margin DHF–CHF.

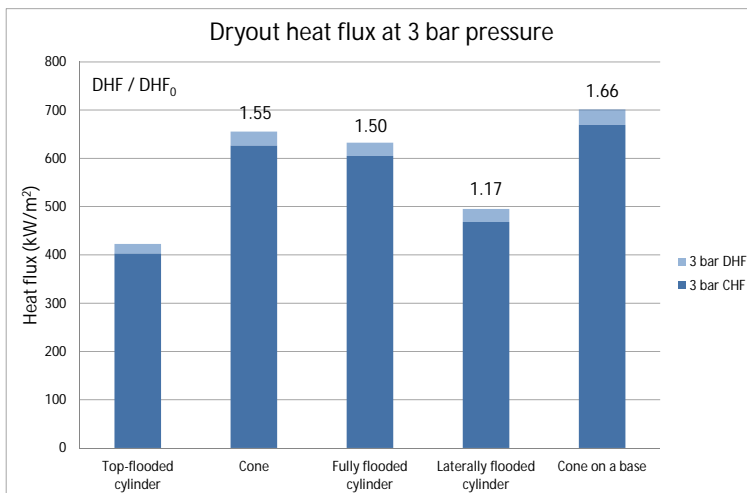


**Figure 4.6.** The dryout heat flux (DHF) at 3 bar pressure. CHF is the maximum coolable power and the light blue zone at the top is the error margin DHF–CHF.

#### 4. Debris bed geometry experiments

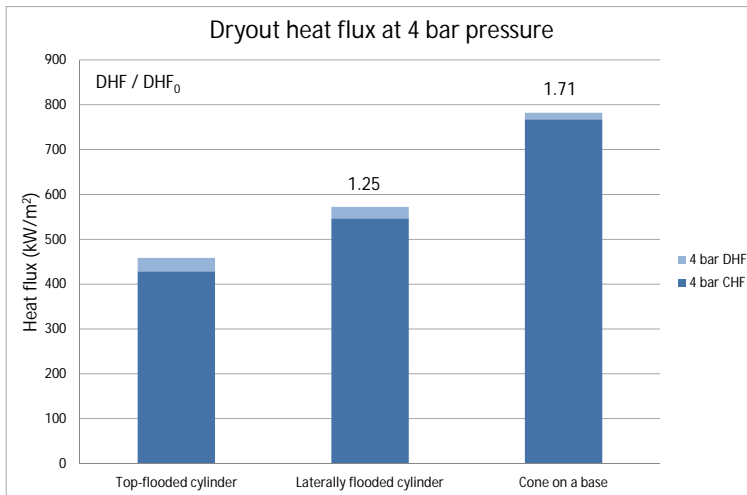


**Figure 4.7.** The dryout heat flux (DHF) at 4 bar pressure. CHF is the maximum coolable power and the light blue zone at the top is the error margin DHF–CHF.

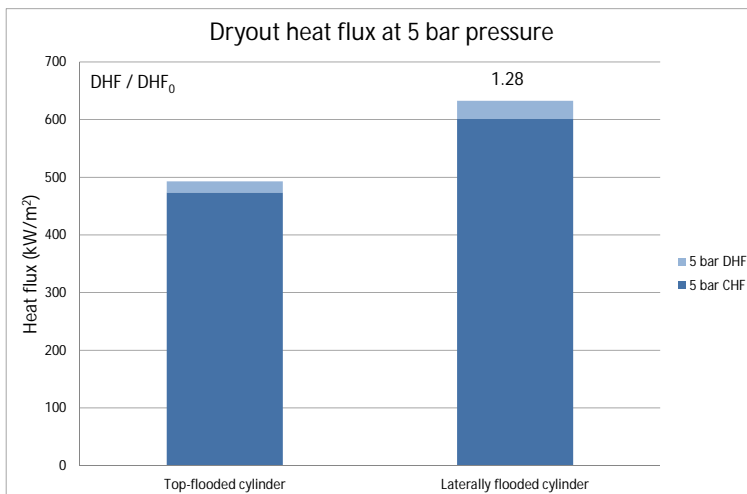


**Figure 4.8.** The dryout heat flux (DHF) at 5 bar pressure. CHF is the maximum coolable power and the light blue zone at the top is the error margin DHF–CHF.

#### 4. Debris bed geometry experiments

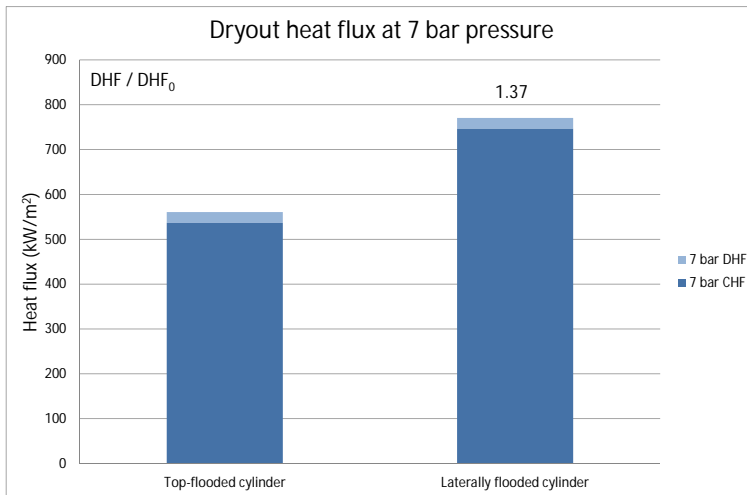


**Figure 4.9.** The dryout heat flux (DHF) at 7 bar pressure. CHF is the maximum coolable power and the light blue zone at the top is the error margin  $DHF-CHF$ .

valve was completely removed from the steam line which allowed a measurement at 1.1 bar. The 1.6 bar measurement was later utilized by measuring the same pressure point for the top-flooded cylinder.

Due to the pressure build-up, the dryout pressures for the fully flooded cylinder and the truncated cone were greater by 0.15 –0.2 bar than in the other experiments in which the average pressure at the dryout power was 1.1 bar. This explains the relatively high DHF in Figure 4.4 for the fully flooded cylinder while, for greater pressures, the DHF for this geometry is practically equal to that of the conical geometry. For the truncated cone no high-pressure comparison data exists, but the elevated pressure suggests that the DHF also for this geometry is "too high" by a small amount.

The effect of pressure on the DHF and the relative coolabilities for all geometries are shown in Figure 4.10, which includes the 1.6 bar points. It is seen that the pressure dependency is quite consistent for the different geometries and flooding modes. In general, the variation in the dryout heat flux is large, ranging from 270 kW/m<sup>2</sup> in the top-flooded cylinder at 1.1 bar bar to 782 kW/m<sup>2</sup> in the cone on a base at 4 bar. The latter is just slightly higher than the 7 bar DHF for the laterally flooded cylinders.

Common to the geometries with high DHF is that some form of multi-dimensional infiltration of water is present: water can flood the bed through lateral surfaces to replace steam, which exits upwards through the top of the bed. An interesting observation is that the best coolability was found for the combination flooding: the cone on a cylindrical base. At 1 bar level, the error due to the size of the power step is large – the CHF is only marginally greater than the CHF of the fully flooded cylinder

#### 4. Debris bed geometry experiments

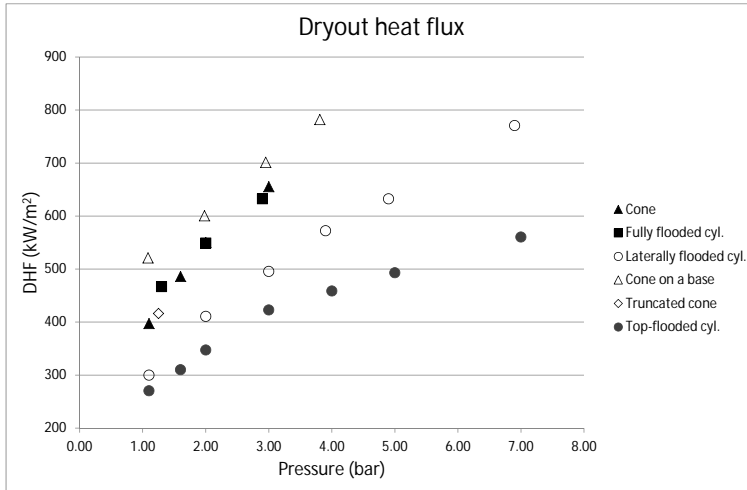


**Figure 4.10.** The dryout heat flux as a function of pressure in the COOLOCE experiments.

– but the trend of this geometry having the greatest DHF (as well as CHF) continues systematically up to 4 bar pressure.

The result was somewhat surprising since the fully conical and the top-flooded cylindrical geometries were assumed to be the easiest and the most difficult to cool, respectively. Apparently, the dryout behavior is governed by flooding through the conical part. The mass flux of steam accumulated in the outer – and the lowest – region of the test bed is small enough to allow water to infiltrate downwards through this region. Concerning the dryout zone, it is not important whether the bottom region of the test bed receives coolant through the inclined surface of the full cone, or through the flow downwards near the perimeter of the cylindrical part in the cone on a base. Both geometries are capable of providing water into the bottom region. This explains why the cone on a base configuration has as good coolability as the fully conical bed, but not why it should be even better coolable.

Taking into account that the  $DHF/DHF_0$  ratio of 1.93 at 1 bar is likely to be too high due to a large power step between CHF and DHF, the difference is rather marginal. Then, possible causes might be related to the slightly different volumetric distribution of heating power, minor differences in the packing of the material, or even inaccuracies in the test bed dimensions which affect volume in the calculation of the heat flux.

The lowest dryout heat fluxes were seen for the top-flooded cylinder and the cylinder with lateral flooding only. In the case of the top-flooded cylinder, this is explained by the fact that the two phases have to flow in counter-current mode: water can infiltrate only through the top surface against the upwards flowing steam. In the case of

the laterally flooded cylinder which has a solid top plate, both water and steam have to infiltrate and exit through the open lateral surface. The top plate forces the steam to escape through the side of the bed instead of the top surface, which makes the top part below the plate vulnerable to dryout.

At 1.1 bar pressure, the  $DHF/DHF_0$  ratio of 1.11 shows that the two modes are equally efficient (or inefficient) at removing the heat generated by the test bed. However, for the greater pressures, the lateral flooding apparently becomes more beneficial, with the ratio of 1.37 at 7 bar (in Figure 4.9). Based on the available data, the increase of DHF as a function of pressure for the laterally flooded cylinder is similar to the other multi-dimensionally flooded geometries. However, above 3 bar the DHF increase for the top-flooded cylinder is not as steep as for the laterally flooded case, which explains the large  $DHF/DHF_0$  ratios at 4 bar and beyond.

The increase of DHF with pressure is mainly caused by the increased steam density, resulting in smaller void fractions in the bed at constant power. The density at 1 bar is about  $0.6 \text{ kg/m}^3$  and  $3.7 \text{ kg/m}^3$  at 7 bar. The DHF increase for the top- and laterally flooded beds in Figure 4.10 resembles the one in the STYX experiments without downcomers (Lindholm et al., 2006). For the other geometries, the pressure dependency appears to be linear. The differences in the DHF curves suggests that the pressure dependency of DHF is not independent of the flooding mode. The experimental data of the higher pressure levels, however, is too scarce to make definite conclusions about this issue.

### 4.1.2 Dryout locations

In addition to the DHFs, the measured locations of the incipient dryout are of interest since they yield information about the dryout mechanisms. In many of the experiments with the ceramic beads, no spreading of dryout was seen, even in the case of the top-flooded cylinder. This is probably due to the heating and TC arrangement which favors local dryout. The dryout locations are illustrated in Figure 4.11 by the red areas, which indicate successfully measured dryout points, including all pressure levels for the test bed shown. The locations are approximate and based on the temperature sensor data.

The exact dryout locations are given in Table 4.2, which lists the locations of the TCs that indicated dryout. The presented coordinates are height from the bed bottom, the radial distance from the bed center and the direction angle of the sensor relative to the other sensors ( $0^\circ$  is the direction of a multi-point sensor near the bed center that has ten measurement points). The radial distance of 21.2 mm where most of the dryouts were measured indicates the innermost TCs in the test bed. The center point (0.0 mm) is occupied by a heating cartridge.

It was found that the two variations of the cylindrical bed, the fully flooded and the laterally flooded bed, and the truncated cone dried out near the top. The cone on a cylindrical base developed dryout above the junction of the conical and cylindrical parts (upper central region). The fully conical bed also showed dryout in the upper central region, with some variation depending on the test run. The top-flooded bed

#### 4. Debris bed geometry experiments

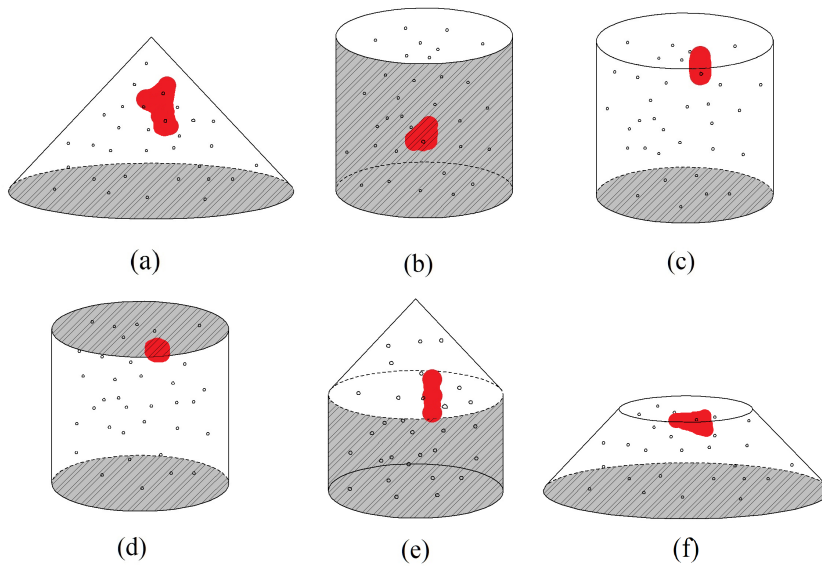


**Figure 4.11.** Approximate dryout locations in the COOLOCE experiments.

**Table 4.2.** Exact dryout locations in the COOLOCE experiments.

Geometry	Height (mm)	Radius from the center (mm)	Direction (°)
(a)	150, 170, 200	21.2	90
	170	21.2	0
	140	21.2	270
	180	21.2	180
(b)	120, 150	21.2	0
	110	21.2	180
	110	48.5	243
(c)	200, 220	21.2	0
(d)	220	21.2	45
(e)	120, 150, 170	21.2	90
(f)	110	48.5	63
	120	21.2	90
	130	21.2	0

indicated dryout in the lower central part. In the radial direction, dryouts were near the center of the test bed, not near the perimeter.

Publication II discusses the dryout locations of the fully conical bed and the top-flooded cylinder by comparing them to the locations predicted by a 2D simulation model. In the model predictions, dryout is formed in the tip of the cone (the highest point) and in the bottom of the cylinder (the lowest point) in principle in a similar manner as in the STYX tests with and without the lateral flooding by downcomers. This behavior is not reproduced accurately in the experiments because, firstly, capturing the exact dryout power would need a measurement with almost infinite accuracy and, secondly, because the internal non-homogeneity of the test beds causes some 3D effects not present in the idealized debris bed model. The descriptions of the dryout mechanisms as predicted by simulation models are given in Sections 5.4.1 and 5.4.5.

It must be mentioned that in Publication II, it is erroneously stated that the percentage of the dryout volume to the total bed volume in the conical and cylindrical test beds is 4–20%. The correct percentage is 0.4–2%. The dryout zone volumes given in deciliters in Table 2 of Publication II are correct.

#### 4.1.3 Effect of bed height

The examination of the coolability problem on a realistic scale requires that the dimensions of the debris beds are accounted for. For beds with a complex shape, the dryout heat flux is not a suitable measure for the overall coolability, since it does not state the total power that can be compared to the decay heat generation. According to Equation 2.6, the conical geometry is three times higher than the cylindrical one if the volumes and radii are equal. Such beds are illustrated in Figure 4.12 showing the dimensions of the COOLOCE cone and a flat-shaped cylinder with the same volume.

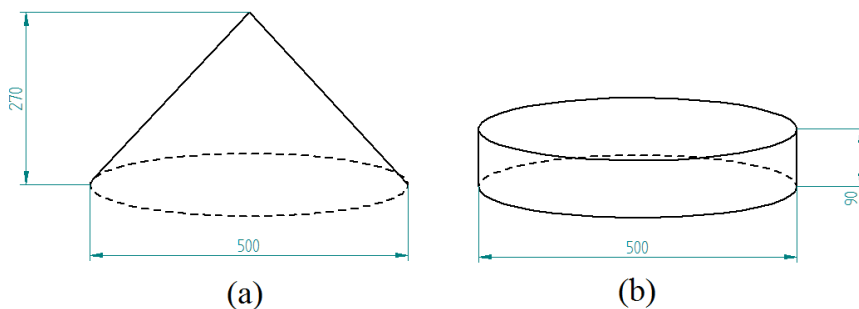


**Figure 4.12.** (a) Conical and (b) cylindrical beds of equal volume and radius.

#### 4. Debris bed geometry experiments

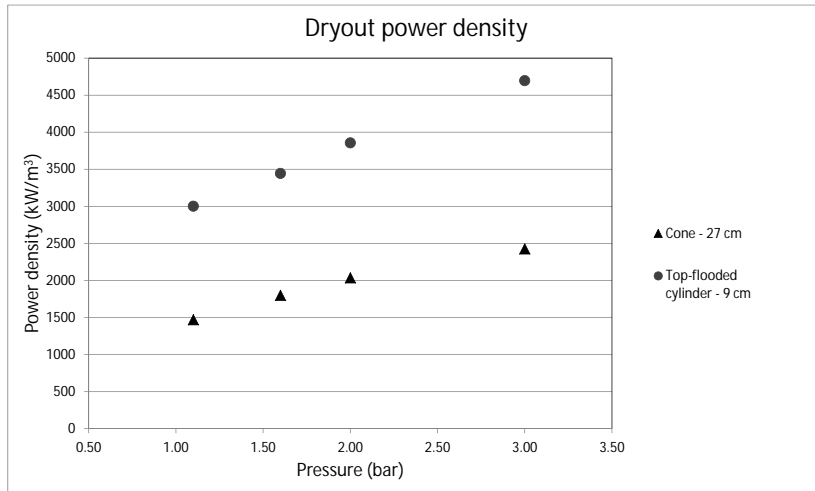


**Figure 4.13.** Dryout power densities as a function of pressure for the conical test bed and the flat-shaped cylinder. The values for the cylindrical bed are obtained by scaling from the cylindrical bed experiments.

The previous section presented DHFs for the cylindrical and conical beds. Figure 4.13 shows the dryout power density which is obtained from the measured DHF by inserting it into Equation 2.3 and assuming that the debris bed height is 270 mm for the cone and 90 mm for the cylinder, as in Figure 4.12. Now, it is seen that the dryout power density is greater for the cylindrical bed at all pressures by 89–100%. The total power that would be required for dryout in a 90 mm cylinder increases by the same ratio because the volumes are assumed to be equal. It is clear that the benefit achieved by the multi-dimensional flooding is not sufficient to compensate for the effect of the increased height. The multi-dimensional flooding yielded 1.5–1.6 times greater DHFs compared to top-flooding but, at the top boundary of the cone, the calculated heat flux is 3.0 times that of the cylinder.

The problem may be seen as the heap-shaped debris bed having a maximum height that is allowed in order to maintain improved coolability compared to the top-flooded bed. Theoretically, the height difference should not exceed the  $DHF/DHF_0$  ratio that describes the effectiveness of the lateral flooding. In this case, this means that the height of the conical bed should not be greater than 130–140 mm.

In Figure 4.13, the total power for the cone is exactly as measured in the experiments but not for the cylinder, due to the scaling of the height to 90 mm. A direct way to measure the height-dependent overall coolability would have been to construct the flat-shaped cylinder for the experiments. However, this would not have made sense because the 90 mm cylinder would have been impractically low (even to the

extent of possibly causing notable boundary layer effects between the pool and the bed) and would have required too high heating power compared to the capacity of the facility (as already observed in the first pre-test simulations used as a basis for technical design).

The other geometries of the COOLOCE experiments are not easily scalable to the reactor scenario due to the variable width to height ratios and the multi-dimensional flooding. This is true also for the STYX downcomer experiments: the 1D flooding without downcomers is easy to extend to account for the full width of the spreading area as there are no changes in the radial direction, but the downcomers immediately change the conditions to 3D, so that the lateral distance becomes meaningful. Obviously, the radius of only 300 mm is then too small compared to the realistic bed height of 600 mm.

Nevertheless, the effect of the bed height was clearly observed in certain other experiments. In the case of the truncated cone, the DHF was relatively high but the power density and total power required for dryout were notably higher than for the other geometries. The fully conical bed showed dryout at about  $1470 \text{ kW/m}^3$  at 1.1 bar and the total power was 26.0 kW. The truncated cone required  $2601 \text{ kW/m}^3$  at 1.25 bar, corresponding to 39.2 kW.

Again, the better overall coolability is caused by the lower height of the geometry. Dryout is reached when the accumulated mass flux (or volume flux) of upwards flowing steam is great enough to replace water, as elaborated in Section 2.1. This limit is given by the dryout heat flux. In a homogeneously heated debris bed, or in an experimental set-up which approximates homogenous heating, the mass flux increases with increasing height. Then, for the 160 mm truncated cone, the distance "available" for the steam flux increase to reach the critical level is less than for the 270 mm conical test bed, and the total power and power density must increase in order to produce the required DHF.

Indeed, the DHFs for the truncated cone and the full cone are within 5% of each other,  $416 \text{ kW/m}^2$  for the former and  $397 \text{ kW/m}^2$  for the latter. This suggests that the coolability difference between these geometries depends mainly on the debris bed height, and the flooding modes are equally efficient. Considering the analysis in Section 4.1.1, the truncated cone may be counted as one of the four debris bed shapes that favor coolability by the effectiveness of the flooding mode, along with the conical bed, the cone on a base and the fully flooded cylinder. Taking into account the pressure uncertainty, the measured DHFs are so close to each other that it can be concluded that the flooding modes of these four geometries are equally efficient. Consequently, the overall coolability of the heap-shaped beds with permeable tops depends on the bed height, which determines the maximum possible heat flux.

### 4.2 Pool subcooling experiments

The COOLOCE-9 experiment was conducted at an initially subcooled pool temperature. The motivation for this was to examine the possible coolability benefit gained from the initially cool water into which the corium is discharged. In this case, part of

#### 4. Debris bed geometry experiments

the heat generated by the debris is consumed by elevating the water temperature.

The water level in the test vessel is controlled automatically by the instrumentation system that injects feed water pre-heated to a temperature of about 80 °C. The arrangement does not include the possibility to cool or control the water temperature, which required a test procedure different from the other test runs. In the subcooled pool experiments, there was no heat-up sequence. At the beginning of the test runs, the power level was rapidly increased up to – or above – the level that was the expected dryout power in normal, saturated conditions. The power was held constant until dryout, and the time required for the development of dryout was measured.

The effect of the pool temperature may be estimated based on the dryout development time. The time depends on the excess power as described in the experimental study by Hu and Theofanous (1991), who found that the critical power "can be uniquely defined as an asymptotic limit (i.e. yielding dryout after an infinitely long delay), and that this limit can be conveniently, and accurately, inferred from a few experimental runs". In the case of top flooding, the dryout development time increases as the power gets closer to the exact critical power.

In the COOLOCE experiments, it was seen that the time to dryout varied depending on the heating power and on the amount of subcooling. The dryout development time as a function of subcooling (saturation temperature minus the measured pool temperature) is shown in Figure 4.14. The subcooling is the average value during the dryout development time.

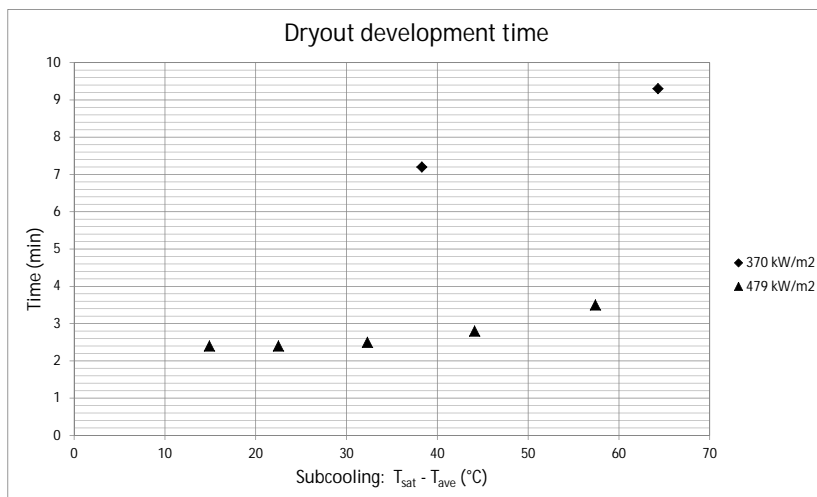


**Figure 4.14.** Dryout development times in COOLOCE-9.

The shortest times of 2.4–3.5 minutes were measured for the heat flux of 479 kW/m² corresponding to the power of 35 kW. For the heat flux of 370 kW/m²,

#### 4. Debris bed geometry experiments

the time was 7.2–9.3 minutes. For 274 kW/m<sup>2</sup>, the time was as long as 27 minutes. This heat flux is not shown in the figure because only one dryout time was measured for it before the pool temperature reached saturation. The decrease in the dryout development time for greater heat fluxes is in accordance with the observations of Hu and Theofanous (1991). The effect of the pool subcooling is small compared to the effect caused by the heat flux differences, but the trend towards increasing dryout time as a function of increasing subcooling is visible in Figure 4.14 in the range of 40 °C to 65 °C.

The effect of pool subcooling was also seen in the heat-up sequence of one of the previous test runs (COOLOCE-8a). In this test, the heat-up sequence was performed with a power that later turned out to exceed the dryout power, but the time to dryout was significantly longer than what it would have been in saturated initial conditions.

The results suggest that the pool subcooling has a measurable effect on the dryout power and at least a small coolability increase is achieved. However, the effect is not effectively quantifiable because of relatively few measurements and because the water temperature in the pool increased without the possibility to control it.

It was also seen that the dryout locations were closer to the top of the test bed than in the other experiments. This might suggest that the dryout mechanism is different with a subcooled pool, and possibly affected by thermal stratification in the water pool. Cooler water was located near the test bed bottom which created different heat transfer conditions for the bottom parts of the test bed. On the other hand, heating powers that exceed the dryout power can transfer the incipient dryout to the top region. This is because the point at which all the downwards flowing water is evaporated is shifted upwards in the bed.

#### 4.3 Measurement errors

The main error source in the experimental procedure is the power increase scheme. The exact dryout heat flux is between the reported DHF and CHF, which causes a relative error of 5–11% depending on the pressure. The largest error in the instrumentation system is that of the power measurement. This includes calibration error of the power analyzer, the voltage conversion error and the possible inaccuracy of the data logging system. Not all the errors in the power measurement chain are known but it is estimated that the maximum error contributed by the voltage conversion and the calibration inaccuracy is approximately  $\pm 0.3$  kW for power levels below 42 kW (applicable for 21 out of 26 measurements). For the power level of 50 kW, the inaccuracy is about  $\pm 0.6$  kW. The resulting maximum error in the dryout heat flux is  $\pm 9$  kW/m<sup>2</sup>.

In some tests, erroneous power peaks were recorded by the output module of the power analyzer. These were not detectable from the digital display of the power analyzer, and were removed from the final data. In addition, the control power does not remain completely stable throughout the experiments, and power fluctuations depending on e.g. the temperature dependence of the heater resistivity were seen. The fluctuations might have reached a maximum of a few hundred watts but it was not

#### 4. Debris bed geometry experiments

seen that these fluctuations would have caused or quenched a dryout. The reported values are based on power step averages that have been cross-checked against the values shown by the power analyzer display.

During experiments, the test vessel pressure fluctuates due to the insertion of cooler feed water. The accuracy of the pressure control is about  $\pm 0.1$  bar. The nominal accuracy of the thermocouples is  $\pm 1.5$  °C. The sensor-specific accuracy against the saturation temperature has been checked during test runs, and the fluctuations have been very small (a few tenths of a °C). The temperature closely followed the pressure fluctuations. The thermocouple error is not assumed to contribute to the dryout power measurement since dryout is registered only after a significant temperature increase.

The possible effect of the local heating and the reduced porosity near the heater surfaces was mentioned in the beginning of this chapter. The magnitude of this effect on the results (in case it is notable) is too complicated to be accounted for with normal error estimation. Instead, the local heating will be briefly considered in connection with the simulation cases in Section 5.4.4.

##### 4.3.1 Condensate flow and heat losses

The average condensate mass flow at the steam line exit was estimated by weighing the condensed water (see Publication II, Section 4.2). The average power and DHF were calculated from the mass flow rate by assuming that the flow rate equals to the evaporation rate by the heated test bed. The power obtained this way was lower than the control power reported in the previous sections by 7–20%. This is due to the heat losses from the facility, the energy consumed by heating the subcooled feed water, and the possible direct contact condensation in the vessel when the cooler feed water mixed into the water pool is in contact with the evaporating steam.

The difference between the power calculated from the condensate mass and the control power is largest at the high pressure levels. This is explained by the increased heat losses to the environment and the increased subcooling of the feed water (the saturation temperature increases but the feed water from the pre-heater is at about 80 °C). It was estimated that the heating of the feed water to the saturation temperature is the main source of the deviation between the control power and the estimated evaporation power.

The condensation phenomena in the test vessel cannot be reliably measured, and they are not considered to influence the comparative coolability of the different geometries (the DHF/DHF<sub>0</sub> ratios). However, the observed difference between the two powers introduce an uncertainty to the absolute value of DHF. As a consequence, the measured CHF<sub>s</sub> and DHF<sub>s</sub> may be greater than what they would be in a completely isolated test arrangement in thermal equilibrium in saturated conditions.

### 4.4 Discussion

From the safety point of view, the most important results of the COOLOCE experiments are the relative coolabilities of the different geometries and flooding modes, and the effect of the bed height. The relative coolability was evaluated by using the measured DHFs, and the effect of the bed height was analyzed by a simple DHF-based scaling of the dryout power density for a flat-shaped test bed. The bed height is part of the bed geometry and, as such, it is inseparable from the flooding mode in realistic debris beds which – in most cases – are allowed to settle into the spreading area without separate constructs or downcomers that would influence the final distribution of the debris. Both height and flooding mode have to be accounted for in the analyses.

The heap-like geometry, as compared to top-flooding in classical analysis, has a twofold effect on coolability: it increases the dryout power by facilitating multi-dimensional infiltration of water into the bed, and partial co-current flow of steam and water, but it also decreases the dryout power by having a greater height. Based on the present analysis, the effect of the increased height is easily substantial enough to exceed the effect of the multi-dimensional flooding. As a consequence, it is shown that multi-dimensionally flooded debris beds cannot be outright considered as the easiest to cool.

To gain understanding of the debris behavior in all conditions of interest, it is necessary to analyze the bed behavior during and after dryout, i.e. in post-dryout conditions. In the COOLOCE experiments, dryout was found to occur in a relatively small volume and its location varied depending on the geometry. This gives an indication of the differences in dryout behavior in the different flooding modes. While post-dryout states are mainly out of range of the test facility, simulation models offer a convenient way to examine the development after dryout. In the next chapter, simulation codes are utilized to analyze the geometry-specific dryout behavior and to extend the analysis to post-dryout conditions in order to examine how severe the increase of particle temperature is after the cooling by water has been locally lost.

## 5. Simulations

A wide range of models and correlations exists to predict the dryout heat flux. Early methods such as the correlations by Theofanous and Saito (1981) and Dhir and Catton (1976) and the 0D- and 1D models proposed by Lipinski (1982) are suitable for calculating the heat flux under the assumption of a 1D top-flooded bed. The state-of-the-art approach is to use two-phase flow simulation codes that consider the lateral flooding by 2D modeling approach. These codes include MEWA developed by the IKE Institute at Stuttgart University in Germany (Bürger et al., 2006; Rahman, 2013) and DECOSIM by the Royal Institute of Technology in Sweden (Kudinov et al., 2014). In addition, occasional studies using other multi-dimensional simulation codes that include a solver module for debris coolability have been reported (Berthoud, 2006; Bechaud et al., 2001).

Studies that truly apply 3D models to analyze debris coolability are almost non-existent in public literature. The advantage of 3D modeling is that, in principle, non-symmetric heap-like beds and otherwise highly irregular debris bed geometries can be accounted for. Drawbacks to the approach are its longer simulation time and the inherent difficulty in estimating which types of irregular configurations would be representative for reactor scenarios, and thus worthwhile for detailed modeling.

The 2D modeling of the STYX experiments by using the MEWA code is described in Publication I, and a brief comparison of the COOLOCE experimental results and MEWA simulations is presented in Publication II. More extensive simulation studies are described in Publications III and IV, which address the modeling of the experiments by using both 2D and 3D simulation approaches. The codes used in the 3D modeling were the in-house CFD code PORFLO by VTT (Hovi, 2008; Hovi, 2012; Ilvonen et al., 2014; Leppänen et al., 2015), and the commercial CFD solver Fluent by Ansys Inc. Prior to this work, PORFLO and Fluent did not include readily available physical models for solving two-phase flow and heat transfer in a porous bed. The models were incorporated into the codes as a part of the simulation efforts: in the case of PORFLO, the model implementation was done by directly editing the source code and, in Fluent, user-defined functions (UDFs) were used.

## 5. Simulations

### 5.1 Modeling principles

The multi-dimensional modeling of debris bed dryout is based on solving the two-phase flow conservation equations, namely the mass, momentum and energy conservation for the gas and liquid phases. The closure models that describe heat transfer and the frictional forces between the three phases of the debris bed – gas, liquid and solid – are well-known models suitable for flows in porous media. The general form of the basic conservation equations is given below. The mass conservation is

$$\frac{\partial}{\partial t}(\varepsilon\alpha_i\rho_i) + \nabla \cdot (\varepsilon\alpha_i\rho_i\vec{v}_i) = \Gamma \quad (5.1)$$

where  $\varepsilon$  is porosity (-),  $\alpha_i$  is the volume fraction of the fluid phase  $i$  (for gas  $i=g$ , for liquid  $i=l$ ),  $\rho_i$  is the density of phase  $i$  ( $\text{kg/m}^3$ ),  $\vec{v}_i$  is the velocity of phase  $i$  ( $\text{m/s}$ ) and  $\Gamma$  is the source term due to evaporation ( $\text{kg/m}^3/\text{s}$ ). The momentum equation is

$$\frac{\partial}{\partial t}(\varepsilon\alpha_i\rho_i\vec{v}_i) + \nabla \cdot (\varepsilon\alpha_i\rho_i\vec{v}_i\vec{v}_i) = -\varepsilon\alpha_i\nabla p + \varepsilon\alpha_i\rho_i\vec{g} + \nabla \cdot (\varepsilon\alpha_i\vec{\tau}_i) + \vec{F}_{s,i} + \vec{F}_i \quad (5.2)$$

where  $p$  is pressure (Pa),  $\vec{\tau}_i$  is the viscous stress tensor ( $\text{N/m}^2$ ),  $\vec{F}_{s,i}$  is the drag force between the solid particles and the fluid phase  $i$  ( $\text{N/m}^3$ ) and  $\vec{F}_i$  is the interfacial drag (gas-liquid drag) on the phase  $i$  ( $\text{N/m}^3$ ). The energy conservation equation for the fluid phases is

$$\frac{\partial}{\partial t}(\varepsilon\alpha_i\rho_i h_i) + \nabla \cdot (\varepsilon\alpha_i\rho_i\vec{v}_i h_i) = \nabla \cdot (\lambda_{\text{eff},i}\nabla T_i) + Q_{s,i} + Q_{\text{evap},i} \quad (5.3)$$

where  $h_i$  is the specific enthalpy of phase  $i$  ( $\text{J/kg}$ ),  $T_i$  is the phase temperature (K),  $Q_{s,i}$  is the heat flux from the solid phase to the fluid ( $\text{W/m}^3$ ) and  $Q_{\text{evap},i}$  is the heat flux by evaporation ( $\text{W/m}^3$ ). The effective thermal conductivity  $\lambda_{\text{eff},i}$  ( $\text{W/m/K}$ ) is calculated from the phase thermal conductivity,  $\lambda_{\text{eff},i} = (\lambda_i\varepsilon\alpha_i)$ .

For the solid phase, the mass and momentum equations are not solved, but the energy equation is needed to model the heat transfer in the solid matrix. For the moment, only one decay-heated solid phase (the porous matrix) is considered, denoted by the subscript  $s$ . The energy equation for the solid is

$$\frac{\partial}{\partial t}((1-\varepsilon)\rho_s h_s) = \nabla \cdot (\lambda_{\text{eff},s}\nabla T_s) + Q_{s,\text{decay}} - Q_{s,\text{sat}} - Q_{s,g} - Q_{s,l} \quad (5.4)$$

where  $Q_{s,\text{decay}}$  is the internal heat source of the material (decay heat or test facility heaters),  $Q_{s,\text{sat}}$  is the heat flux directed to evaporation and  $Q_{s,g}$  and  $Q_{s,l}$  are the heat fluxes from the solid particles directly to the fluid phases.  $Q_{s,g}$  is important mainly in dryout conditions and  $Q_{s,l}$  if the liquid phase is subcooled. To calculate the effective thermal conductivity of the porous medium  $\lambda_{\text{eff},s}$ , models for convection and radiation in the porous medium can be applied, e.g. based on the models by Imura and Takegoshi (1974) and Vortmeyer (1978).

### 5.1.1 Drag force models

The frictional forces between the solid and the fluid phases can be expressed as functions of superficial phase velocities  $j_i$  by using the concepts of permeability  $K$  and passability  $\eta$ , and relative permeability  $K_r$  and relative passability  $\eta_r$ . The equations for the drag forces between the solid and the liquid and gas phases are

$$\vec{F}_{s,l} = \varepsilon(1 - \alpha) \left( \frac{\mu_l}{K K_{rl}} \vec{j}_l + \frac{\rho_l}{\eta \eta_{rl}} |\vec{j}_l| \vec{j}_l \right) \quad (5.5)$$

$$\vec{F}_{s,g} = \varepsilon\alpha \left( \frac{\mu_g}{K K_{rg}} \vec{j}_g + \frac{\rho_g}{\eta \eta_{rg}} |\vec{j}_g| \vec{j}_g \right) \quad (5.6)$$

where the phase fractions in the pores  $\alpha_i$  have been written using the void fraction ( $\alpha = \alpha_g$ ). The relation between the superficial velocity and the (physical) phase velocity is

$$\vec{j}_l = \varepsilon(1 - \alpha) \vec{v}_l \quad (5.7)$$

$$\vec{j}_g = \varepsilon\alpha \vec{v}_g \quad (5.8)$$

Permeability and passability, which describe the capability of porous medium to transmit fluid, depend on porosity  $\varepsilon$  and particle diameter  $d$ . According to Ergun (1952) they are expressed as

$$K = \frac{\varepsilon^3 d^2}{150(1 - \varepsilon)^2} \quad (5.9)$$

$$\eta = \frac{\varepsilon^3 d}{1.75(1 - \varepsilon)} \quad (5.10)$$

The extension to two-phase flow is done by the relative permeability and passability which are functions of the void fraction:

$$K_{rl} = (1 - \alpha)^n \quad (5.11)$$

$$K_{rg} = \alpha^n \quad (5.12)$$

$$\eta_{rl} = (1 - \alpha)^m \quad (5.13)$$

$$\eta_{rg} = \alpha^m \quad (5.14)$$

The exponents of relative permeability and passability are empirical constants which vary depending on the literature source. For the relative permeability,  $n = 3$  is typically used. For the relative passability, Lipinski (1982) suggested  $m = 3$ . Reed (1982) suggested  $m = 5$ , which yields a somewhat increased friction and was later used also by Lipinski (1984). Later, Hu and Theofanous (1991) proposed  $m = 6$ . These three models that differ from each other only in the relative passability are the "classical" models used without the consideration of the interfacial drag. However,

## 5. Simulations

since the empirical models aim to describe the total pressure loss, the gas-liquid drag is implicitly included in the models.

In the modeling options that account for the interfacial drag term  $\vec{F}_i$ , there are two alternative approaches. Schulenberg and Müller (1986) proposed an empirical correlation for the interfacial drag based on pressure loss measurements. Tung and Dhir (1988) developed a more detailed model in which the drag coefficients are expressed separately for the flow regimes of bubbly, slug and annular flows. The Tung and Dhir model was later modified by Schmidt (2004) and Rahman (2013) to increase the capability of the model to predict dryout heat flux in both top and bottom flooding conditions.

One main difference between the CFD codes and MEWA is that MEWA uses a simplified form of the momentum equations (Schmidt, 2004), which is obtained by neglecting the viscous stresses, momentum transfer due to convection and the time derivatives of Equation 5.2. Assuming no (explicit) interfacial drag, the momentum equations can be written as follows in one-dimensional form:

$$-\frac{dP}{dz} - \rho_l g = \frac{\mu_l}{K K_{r1}} j_l + \frac{\rho_l}{\eta \eta_{r1}} |j_l| j_l \quad (5.15)$$

$$-\frac{dP}{dz} - \rho_g g = \frac{\mu_g}{K K_{rg}} j_g + \frac{\rho_g}{\eta \eta_{rg}} |j_g| j_g \quad (5.16)$$

In all the simulations of this study, it is assumed that the phases have the same pressure  $p$ . Thus, surface tension effects, such as the residual hold-up of liquid in the bed pores, are considered negligible in the dryout formation process. The simplified momentum equations are analogous to the general law for pressure loss in porous media which, for single-phase flow, is

$$\frac{dp}{dz} = \frac{\mu}{K} j + \frac{\rho}{\eta} |j| j \quad (5.17)$$

The total pressure loss consists of the linear term representing the viscous losses (first term on the right-hand side) and the quadratic term (second term on the right-hand side) representing the inertial losses. The linear relation between the pressure and flow velocity was first established by Darcy (1856), and the quadratic term, named after Forchheimer (1901), was included later into Equation 5.17 to account for high-velocity flows for which the pressure loss deviates from the linear Darcy's law. Probably the most widely used model for the permeability  $K$  and passability  $\eta$  in the viscous and inertial terms is that of Ergun (1952), which was presented in Equations 5.9 and 5.10.

Criticism related to interpreting the Forchheimer term as representative of inertial forces (and the level of turbulence in the flow) has been presented by Lage (1998) since there is no momentum change in steady, fully developed flow and, rather, the quadratic term is a form drag. In the present work, however, the question of interest is the applicability of the well-known models described in this chapter for predicting the pressure loss and, most importantly, the dryout heat flux in the porous particle

bed. The fundamental physics and terminology is left to experts of the porous media transport theory.

### 5.1.2 Heat transfer models

In coolable steady state and even in post-dryout conditions, if the dry zone is small and highly localized, the heat is transferred from the debris mainly by the phase change of water to steam. The boiling rate  $\Gamma$  is calculated by dividing the heat flux  $Q_{s,sat}$  from the solid with the latent heat of evaporation:

$$\Gamma = \frac{Q_{s,sat}}{h_{g,sat} - h_{l,sat}} \quad (5.18)$$

The heat flux  $Q_{s,sat}$  is calculated as

$$Q_{s,sat} = a_{s,sat} \kappa_{s,sat} (T_s - T_{sat}) \quad (5.19)$$

To calculate the heat transfer coefficient  $\kappa_{s,sat}$  (W/m<sup>2</sup>/K) for boiling, the Rohsenow correlation (Rohsenow, 1952) is applied to the nucleate pool boiling regime and the Lienhard correlation (Lienhard, 2012) to the film boiling regime, with a transition zone between the two regimes calculated by an interpolation function. The interfacial area density  $a_{s,sat}$  is obtained from porosity and the particle diameter  $d$ :

$$a_{s,sat} = \frac{6 \cdot (1 - \varepsilon)}{d} F(\alpha_1) \quad (5.20)$$

where

$$F(\alpha_1) = \begin{cases} 1 & \text{if } \alpha_1 \geq 0.3 \\ \frac{\alpha_1}{0.3} & \text{if } \alpha_1 < 0.3 \end{cases} \quad (5.21)$$

The calculation of  $a_{s,sat}$  by Equation 5.20 assumes that steam appears in the form of spherical bubbles with a diameter equal to the particle diameter  $d$ . The heat transfer from the solid particles to steam becomes significant in near-dryout conditions, and especially after dryout has been reached and the temperature of the solid starts to increase. Heat transfer from solid to steam is assumed to occur when the solid temperature is above saturation temperature and the gas fraction is 0.7 or greater. For this case, the heat flux  $Q_{s,g}$  is calculated as

$$Q_{s,g} = a_{s,g} \kappa_{s,g} (T_s - T_g) \quad (5.22)$$

where  $\kappa_{s,g}$  is the solid to gas heat transfer coefficient. The interfacial area density is calculated as a function of the void fraction

$$a_{s,g} = \frac{6 \cdot (1 - \varepsilon)}{d} F(\alpha_g) \quad (5.23)$$

## 5. Simulations

where

$$F(\alpha_g) = \begin{cases} 0 & \text{if } \alpha_g < 0.7 \\ \frac{\alpha_g - 0.7}{0.3} & \text{if } \alpha_g \geq 0.7 \end{cases} \quad (5.24)$$

The heat transfer coefficient from solid to steam is

$$\kappa_{s,g} = \frac{\text{Nu}_{s,g} \lambda_g}{d} \quad (5.25)$$

The Nusselt number is calculated according to the correlation of Ranz and Marshall (1952):

$$\text{Nu}_{s,g} = 2 + 0.6 \sqrt{\text{Re}_g} \cdot \sqrt[3]{\text{Pr}_g} \quad (5.26)$$

where the Reynolds number is

$$\text{Re}_g = \frac{|\rho_g \vec{v}_g d|}{\mu_g} \quad (5.27)$$

In addition, MEWA calculates the heat flux between the solid and liquid phases  $Q_{s,l}$  in case the water is subcooled and the continuous phase (Rahman, 2013). Because the three phases are initially at saturation temperature in the simulations discussed here, the heat transfer from subcooled water is not important.

A schematic that illustrates all the heat fluxes  $Q$  calculated in the MEWA and PORFLO models is presented in Figure 5.1. The MEWA solution has one solid phase for which the heat transfer is calculated. In PORFLO it was decided to include the test facility heaters in the model by the calculation of heat fluxes from the heaters to the fluid phases  $Q_{h,i}$  and to the phase change by boiling  $Q_{h,\text{sat}}$ , and the solid to solid conduction  $Q_{h,s}$  from the heaters to the bed particles. Thus, the PORFLO solution considers two solid phases denoted  $s$  and  $h$  in Figure 5.1 and, in MEWA, only the heat fluxes related to solid  $s$  are included. In practice, the heat generation in MEWA is then assumed to occur in the single solid phase, regardless of whether it is produced by heaters adjacent to the porous medium or by internal volumetric heating. The other heat fluxes in the figure calculated as described in Equations 5.18–5.27 are taken into account in both codes.

In addition to the heat flux from the solid and heaters, the PORFLO model considers the contributions of the fluid phases (bubbles and droplets) to the boiling rate by using the correlation of Lee and Ryley (1968). These are shown in Figure 5.1 as  $Q_{i,\text{sat}}$ . The decision to include these models into the code by VTT was supported by some of the earlier versions of MEWA which also included them (Buck et al., 2012). The implementation of the heat transfer and drag force models is described in a technical report (Takasuo et al., 2011a) including preliminary comparisons of PORFLO and MEWA results. The code generated for the PORFLO model was used as a basis for the implementation of the models to Fluent using user-defined functions.

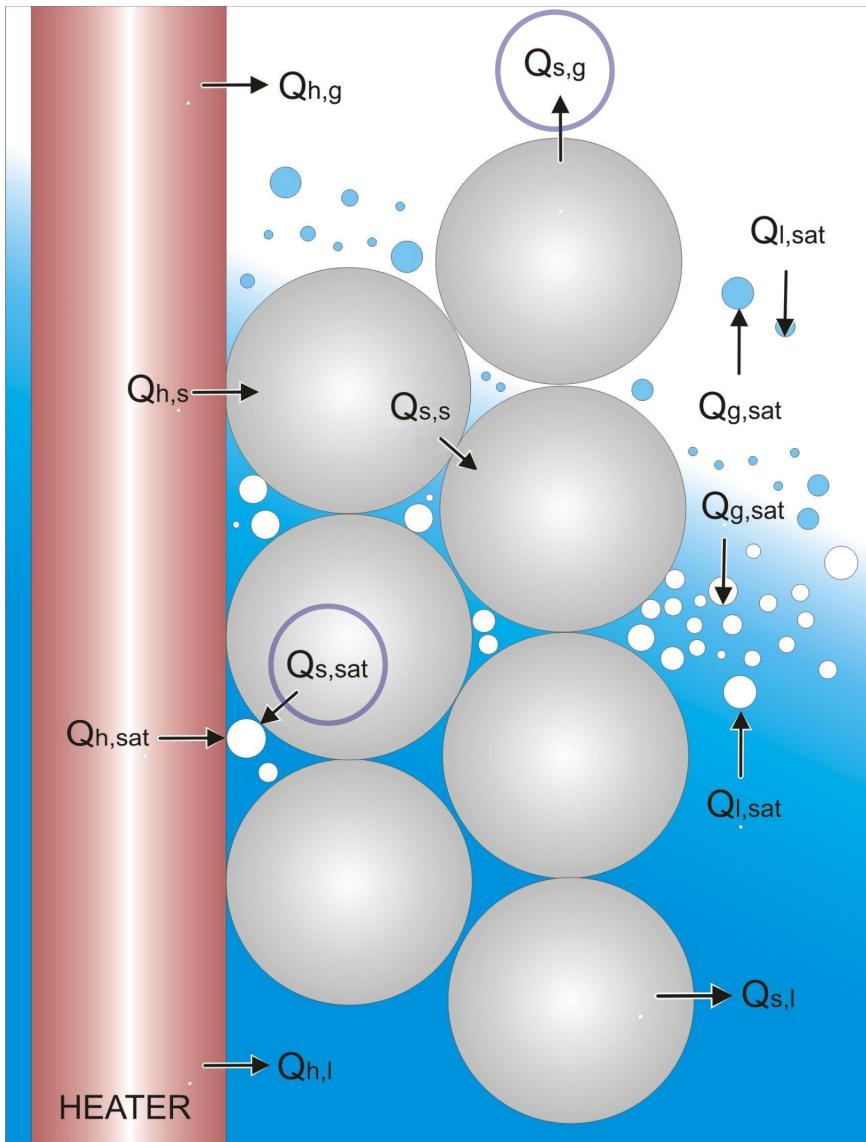


**Figure 5.1.** Heat fluxes in the porous medium with two-phase flow and heaters. The most important heat transfers  $Q_{s,sat}$  (Equation 5.19) and  $Q_{s,g}$  (Equation 5.22) in the present applications are circled.

## 5.2 Simulation set-up

The main objective of the simulations was to evaluate the dryout power. In principle, this was done in a similar manner to the experiments: by finding out the minimum

## 5. Simulations

power level that leads to dryout (DHF) and the maximum power level at which the particle bed just remains in a coolable steady state (CHF). It is worth mentioning that the aim of the simulations was not to repeat the stepwise power increase exactly as it was conducted in the laboratory, because coolable conditions are dominated by steady-state boiling, and the recorded data then mainly consists of the saturation temperature in the test vessel. Instead, the CHF and DHF conditions just before and after dryout are of interest since they reveal how accurately the dryout heat flux is predicted by the simulation codes and what type of flow patterns are associated with the dryout formation.

The cylindrical symmetry of the experimental geometry was utilized in the MEWA simulations by using an axisymmetric 2D grid for the spatial discretization. The relatively small size of the test beds and the fast 2D solver made it possible to decrease the grid cell size to 2.5 x 2.5 mm. In the PORFLO model, structured 3D grids with the cell size of 15 mm in the porous zone were applied. The iterative numerical solution method of the conservation equations in both MEWA and PORFLO is based on the SIMPLE algorithm by Patankar (1980). The boundary conditions for the computational domain were as follows:

- Top: pressure boundary, saturated liquid inflow
- Bottom and sidewalls: Adiabatic frictionless walls, no flow-through

By default, homogenous heating similar to a decay-heated bed is assumed in the simulations. An exception to this is a variation of the PORFLO model in which the heating power is concentrated on the grid cells that contain the heaters. This results in a grid in which every other vertical cell column has zero power density, while every other cell has high power density (to achieve the same total power as the homogeneously heated model). The purpose of this locally heated model was to evaluate the possible effect of the heating arrangement, and to estimate whether the arrangement would cause non-prototypic behavior concerning the overall coolability. The heaters were also accounted for in the average porosity, yielding smaller porosity for the cells that contain the solid heaters.

In Publications II–III the bed porosity selected for the MEWA simulations was 0.38 and the particle diameter was 0.9 mm. The particle diameter was taken as the middle point of the range provided by the particle manufacturer, 0.8 – 1.0 mm, and the porosity was based on the measurement by filling the test bed with water. Note that the verification of the particle size distribution by the laser diffraction and image analyses mentioned in Chapter 4 was conducted for the effective particle diameter studies in Publication V and the comparative analyses between COOLOCE and POMECCO experiments (Takasuo et al., 2014), and the precision mean values for the diameter were not available at the time of writing of Publications II–IV.

Concerning porosity, the value of 0.38 is expected to yield more conservative results (lower dryout heat flux) than the porosity of 0.39–0.40 that was measured by weighing the particles in the conical and cylindrical test beds. On the other hand, the conservative porosity is countered by the effect of the particle diameter as the

effective diameter is probably even smaller than 0.9 mm for the porosity of 0.39–0.40 as will be shown in Chapter 6.

### 5.3 Applicability of drag force models

The role of interfacial drag force in two-phase flow has been investigated by measuring the pressure gradient in porous beds (Tutu et al., 1984; Schulenberg and Müller, 1986; Bürger et al., 2006). It has been established that the models with implicit consideration of interfacial drag, namely the Lipinski (1982), Reed (1982) and Hu and Theofanous (1991) models, are not adequate for modeling debris beds with multi-dimensional flooding. This is based on the observations that the models do not predict the pressure gradient correctly, and the classical models typically underestimate dryout heat flux measured for bottom-flooding conditions (Schmidt, 2004; Bürger et al., 2006; Rahman, 2013). It has been postulated (Schmidt, 2004; Bürger et al., 2006) that the interfacial drag force has opposite effects on the magnitude of the dryout heat flux in top-flooded and bottom-flooded configurations: in purely counter-current flows in top-flooded beds, the gas-liquid drag hinders the water infiltration into the bed against the steam flow. In co-current flow, the gas-liquid drag enhances the coolability because it acts to increase the liquid flow from bottom through interaction with the upwards flowing steam.

The aim of the modified Tung and Dhir (MTD) model by the IKE Institute at Stuttgart University was to develop a model that would be applicable to top- and bottom flooding as well as multi-dimensional flooding (Rahman, 2013). The modifications to the original model were adjustments to the flow regime limits and to the fluid-particle and interfacial friction coefficients, mainly to make the approach better suited for small particles ( $d < 6$  mm). In the MTD model, the transition to annular, channel-like flow occurs earlier. For instance, in case of 1 mm particles the flow is purely annular if the void fraction is greater than 0.2 and the bubbly flow regime is non-existent (Rahman, 2013, p. 31). In the original Tung and Dhir model, the bubble diameter would be larger than the pore diameter for the small particles, which directly shows a deficiency in the original model (Schmidt, 2004).

For pure counter-current flow, the classical models with implicit interfacial drag have been found to be applicable and good results have been obtained, especially with the Reed model (Schmidt, 2004; Li and Ma, 2011). For these reasons, it was chosen to use the MTD model as a default to simulate the cases with multi-dimensional flooding and the Reed model for the top-flooded cylinder. In addition, other drag force models have been tested in the case of some examined geometries, motivated by the lack of previous data on the models' applicability to complex flooding modes.

During the present work, it was also found that the Reed model, due to its simplicity, is computationally fast and easy to implement into simulation codes. The programming and the model verification process is less tedious compared to the MTD model, which necessitates the inclusion of several drag coefficients expressed separately for the different flow regimes (and transition zones). By using the classi-

## 5. Simulations

cal models, it is also possible to find an analytical solution to the DHF in 1D flooding, which is utilized, for example, in the probabilistic safety studies by KTH (Yakush et al., 2013; Yakush et al., 2012).

The friction force models describe the flow in the debris bed (porous zone). In addition to the porous zone, the simulation models have to account for the water pool in which the bed is submerged. The pool is a free-flow zone for which the models for the porous medium are not in principle applicable. MEWA and PORFLO, however, do not include separate models for the pool zone. Instead, the zone is modeled as a high-porosity porous medium that serves as a water reservoir whose function is simply to replace the evaporated liquid in the porous zone without having a presumed effect on the overall coolability. In selected Fluent simulations, the pool was taken into account in a more realistic manner by modeling it as a free-flow zone using the interfacial drag force model by Schiller and Naumann (1935) and the standard  $k-\epsilon$  turbulence model (Wilcox, 2006).

### 5.4 Results and discussion on dryout characteristics

In this section, the simulation results are summarized and assessed against the experimental findings. Model-to-model comparisons between MEWA and the CFD models are included and, based on the detailed view of the two-phase flow provided by the simulations, an interpretation of the dryout behavior in multi-dimensionally flooded debris beds is presented. This approach yields a more comprehensive picture of the dryout behavior than the one that would be achievable based on the experiments only. Guidelines for the validation of simulation codes by means of the different results and comparisons are emphasized in the discussions.

First, the differences in the dryout process in the top-flooded cylinder and the multi-dimensionally flooded cone are examined. The experimental and simulated DHFs in these geometries are then compared. Subsection 5.4.3 addresses the development of particle temperature after dryout has been reached based on the simulations, and it also considers some experimental observations of post-dryout steady states. The results of the locally heated model are described in Subsection 5.4.4, including discussion on the effects of the non-homogenous heating on the experimental results. The modeling of the non-conventional debris bed geometries, namely the fully and laterally flooded cylinder, the cone on a cylindrical base and the truncated cone are presented in Subsection 5.4.5, after which the effect of the pool modeling approach (highly porous or free-flow zone) is discussed. The concluding section of this chapter presents examples and discussion on the multi-dimensional flooding on the scale of a BWR.

#### 5.4.1 Conical and cylindrical beds

The simulations revealed that the dryout process is fundamentally different in the conical and cylindrical debris beds as a result of the differences in the flooding mode. In the cylindrical debris bed, the counter-current flow limitation determines whether

liquid water reaches the bottom of the bed before it evaporates. The bottom part of the bed is completely dried out in the horizontal direction, which is sometimes called global dryout. In the conical debris bed, coolant infiltrates through the sidewall of the cone, driven by the lateral pressure difference caused by evaporation deeper in the bed. The bottom part remains coolable while local dryout is formed near the tip of the cone where the accumulated steam flux which, at the dryout power, is large enough to replace water.

The dryout conditions are illustrated in Figure 5.2 and Figure 5.3, which show the distributions of void fraction (gas volume fraction) in the conical and cylindrical beds just after dryout has been reached. The vectors of superficial liquid velocity are shown on the saturation maps. The vector arrows are scaled and their number is less than the amount of grid cells for clear visualization.

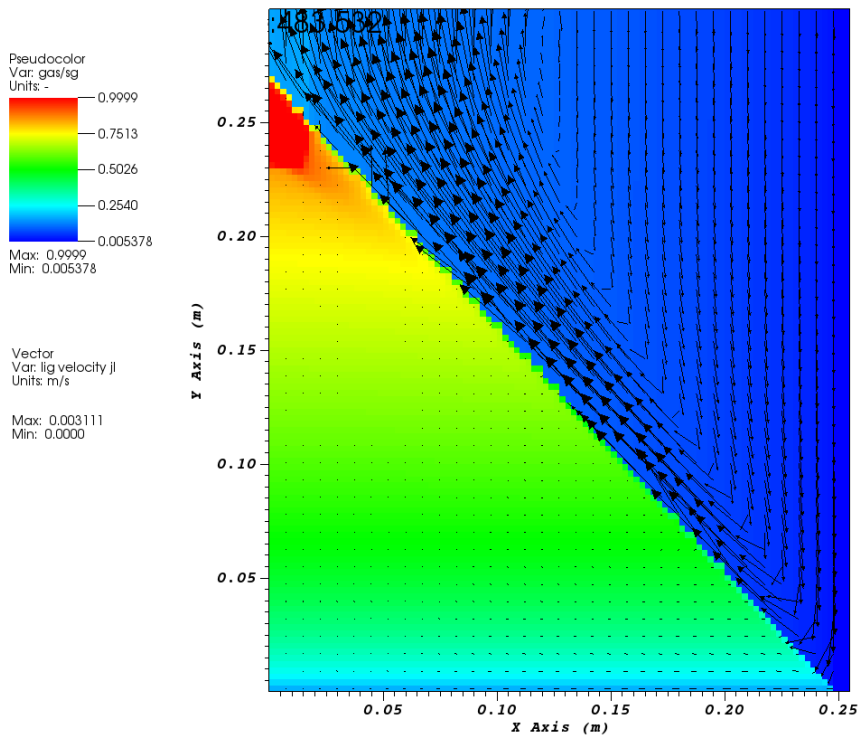


**Figure 5.2.** Void distribution (gas volume fraction) in MEWA simulation of the conical bed with vectors of superficial liquid velocity.

Qualitatively similar dryout behavior was achieved by using PORFLO, which is illustrated in Figure 5.4. In the cylindrical bed simulations, the location of the incipient dryout is slightly elevated from the bottom of the bed and a layer of liquid water is present in the bottom. This indicates that the heating power in the simulations

## 5. Simulations

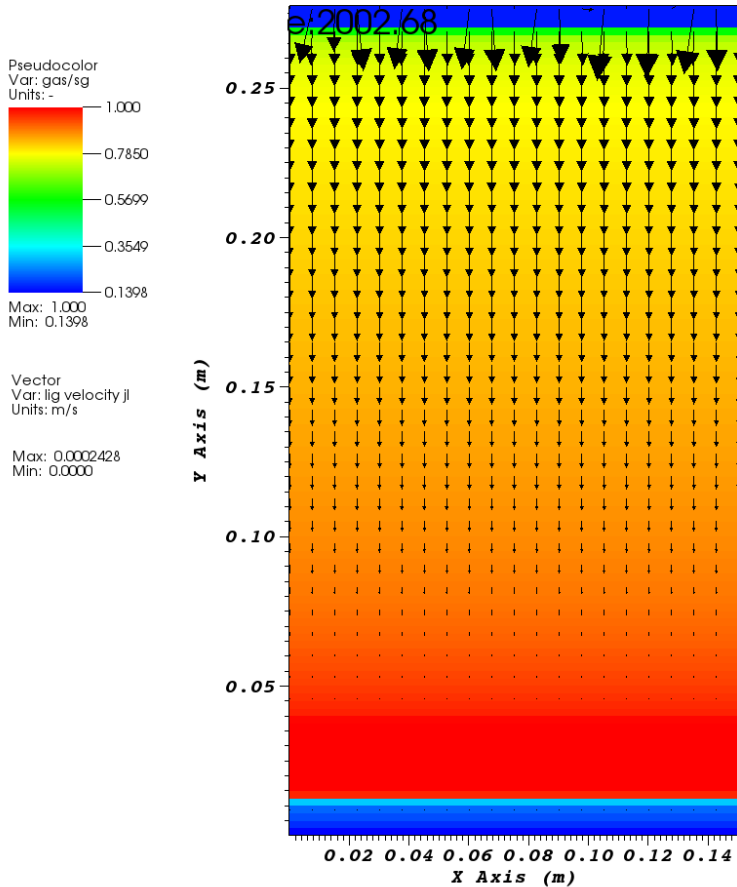


**Figure 5.3.** Void distribution (gas volume fraction) in MEWA simulation of the cylindrical bed with vectors of superficial liquid velocity.

slightly exceeds the critical power at which the bed just reaches the onset of dryout development. In fact, even in these types of simulations it would be impossible to capture the exact DHF because this would require infinite waiting time for the dryout development as formulated by Hu and Theofanous (1991).

The flow pattern in the conical bed and in the surrounding pool is illustrated in Figure 5.5, which shows the velocity vectors for the liquid and gas phases in a PORFLO simulation. Near the outer perimeter of the pool, in the cool region, the water flow is directed downwards and, in the hot region of the circulation loop, the water either infiltrates laterally into the porous bed or is accelerated upwards at the surface of the cone. The steam flow is directed upwards in almost every location and is fastest near the center. In the simulations of the cylindrical bed, the model predicts pure counter-

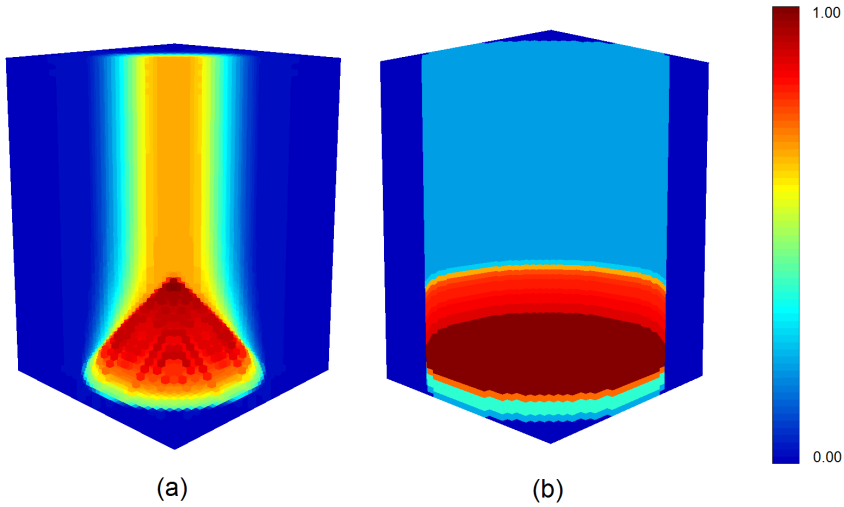


**Figure 5.4.** Distributions of void fraction in PORFLO simulations of (a) conical bed and (b) cylindrical bed.

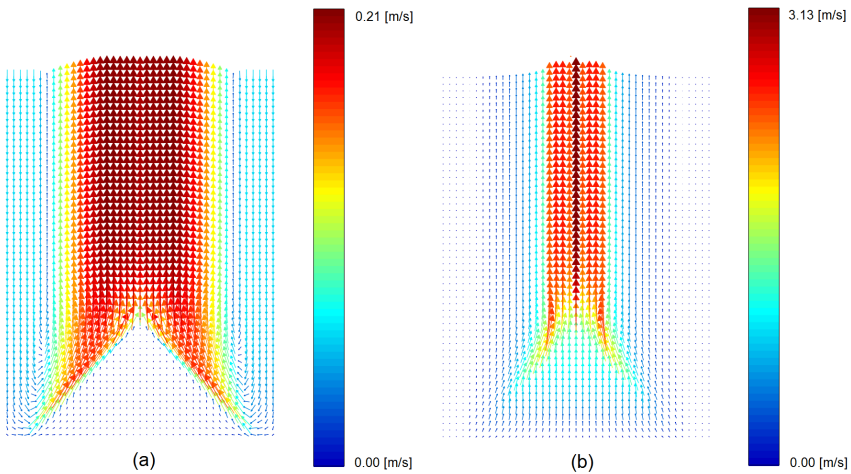


**Figure 5.5.** Vectors of (a) liquid and (b) gas phase velocities in the conical debris bed.

current flow in which the steam flows directly upwards and water downwards. The flow velocities are strongly dependent on the heating power, and Figure 5.5 is only an example of the results. However, the flow directions in the circulation loop are independent of the power in coolable steady state or near-DHF conditions, and also

## 5. Simulations

of pressure and the properties of the debris bed such as porosity. The MEWA simulations generally show similar circulation loops for liquid and gas as PORFLO.

It should be kept in mind that the pool zone is not modeled mechanistically as a free-flow zone. The pool is treated as a highly permeable porous zone as will be further discussed in Section 5.4.6. This explains the large slip velocity (velocity difference between gas and liquid), which can be as high as several meters per second in the simulations.

The saturation profiles at different simulation times presented in Publication II show that, for the cylindrical bed, the dryout is formed after a saturation transient during which the point of minimum dryout is transferred towards the bed bottom. This type of interpretation for the dryout in bed bottom was already presented by e.g. Hofmann (1984) and seen in other MEWA simulations (Bürger et al., 2010; Sehgal, 2012, p. 341). For the conical bed, the saturation profile in the bed undergoes only minor changes which are connected to the power increases, and the point of maximum saturation is near the top of the bed, where the steam flux is at its greatest. The difference in the flow behavior explains the long dryout development time required for top-flooded beds and why the holding time between the power steps is important in top-flooded experiments to obtain an accurate DHF. In the conical bed, the dryout formation is expected sooner after the power increase.

### 5.4.2 Dryout heat flux

In general, the dryout power and the DHF were accurately predicted for the cylindrical beds with homogenous heating but, for the conical cases, the experimental dryout power was somewhat underestimated by the simulation model. In the experiments, the ratio of the heat fluxes in the conical and cylindrical beds  $DHF/DHF_0$  was 1.47–1.58 (see Figures 4.4–4.6), while in the MEWA simulations it was 1.36–1.52. The DHF ratios as a function of pressure in the experiments and simulations are shown in Figure 5.6. Note that the differences between the drag force models of Reed and MTD are carried over to the simulation results, due to the modeling choice of using the "best" available models based on existing literature.

Simulations of a flat-shaped 90 mm cylinder (illustrated in Figure 4.12) are also presented in Publication III. The predicted dryout heat flux was the same as for the tall cylinder, and the dryout power density increased proportionally to the decrease in bed height as stated by Equation 2.3.

The comparatively small heat flux in the conical bed simulations is likely explained by the inherently smaller dryout zone compared to the cylindrical bed and the limited accuracy in the experimental determination of dryout location. Contrary to the simulations, it is not possible to capture extremely small steam pockets that might be present in between the TCs in the test bed. As the discussion on the dryout formation process showed, the dryout zone resists spreading unless heating power is increased. This means that an undetectable small dryout zone may exist in the bed without any practical effect on the bed temperature.

Also, the cylindrical geometry shows some discrepancy between the experimental

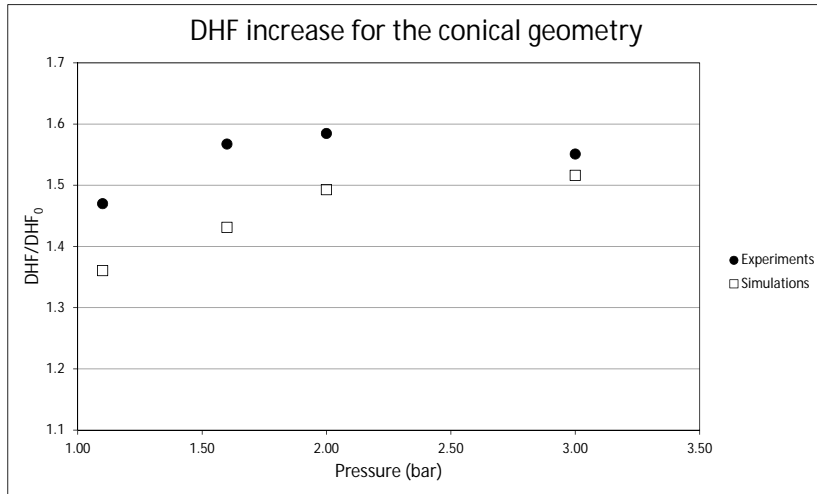


**Figure 5.6.** Relative increase of DHF in the conical debris bed compared to the cylindrical bed in experiments and MEWA simulations.

and simulation results in the location of dryout. In the experiments, the dryout was located higher in the bed and showed no significant lateral spreading as indicated in Figure 4.11. The difference is probably caused by the non-uniform heating that leads to local changes in porosity and power distribution. However, the general agreement between the experimental and simulated DHF increases the confidence that the test design can be used for reliable measurements of overall coolability.

Concerning the absolute DHF in the simulations, presented as power density in Publication III (Figures 5 and 6), it must be kept in mind that the simulation results are sensitive to the model parameters, especially porosity and particle diameter. Even small modifications in these parameters can notably affect the permeability and passability of the bed and thus the predicted DHF. A sensitivity study based on variations of porosity and particle size is reported in Takasuo (2013), which considers parameter combinations in the ranges of 0.37–0.40 for porosity and 0.8–0.97 mm for the particle size. For instance, the increase of porosity from 0.37 to 0.40 for 0.97 mm particles yielded an average increase of 28% in DHF.

### 5.4.3 Post-dryout conditions

The post-dryout conditions in cylindrical and conical beds were investigated in Publication II by examining the liquid saturation and solid temperature behavior in the simulations of COOLOCE-4b (cylindrical bed) and -7b (conical bed). For the cylindrical bed, it was seen that the fluid flow is stagnant in the dryout zone due to lack of boiling. This leads to the formation of a relatively large dryout zone, and a rapid

## 5. Simulations

increase of solid temperature.

In the case of the conical bed, the dryout zone remained small, even at a power level that was elevated from the dryout power by 12.5%, and the solid temperature stabilized to form a post-dryout steady state. Contrary to the bottom dryout in the top-flooded bed, the top dryout zone is exposed to steam flow from evaporation in the bed below (and surrounded by the large water reservoir above the bed), which enhances the convective heat transfer from the solid. This causes the temperature to stabilize at least for small excess power levels. In addition, the top dryout zone is not in direct contact with the floor of the spreading area, which improves the overall scenario by preventing (or at least delaying) the increased thermal loading to the containment structures.

The formation of post-dryout steady states was somewhat expected. The potential for the cooling by steam flow has been suggested by Zeisberger and Mayinger (2006), Atkhen and Berthoud (2006) and Bürger et al. (2006) and the early studies by Rivard (1978). A study specifically concentrated on the numerical simulations of post-dryout cooling was recently published by Yakush and Kudinov (2014).

The post-dryout conditions are difficult to study experimentally using resistance heating, since this causes overheating and damage to the heaters much sooner than in normal experiments. However, some evidence of temperature stabilization was seen in the experiment with the truncated cone in which the temperature increase at the measured DHF stabilized at about 10 °C above the saturation temperature. An apparently continuous increase was seen when the power was 2 kW (5%) above the DHF. In the SILFIDE experiments heated by an induction coil, temperature stabilization was seen for temperatures up to 200 °C above the saturation temperature (Atkhen and Berthoud, 2006). The experimental evidence of post-dryout steady states is not comprehensive but it supports the simulations and analytical studies which are rather consistent in stating this phenomenon as favorable for achieving stabilized conditions for the corium.

The post-dryout behavior in multi-dimensional flooding suggests that the coolability criterion based on the formation of the first dry zone is overly conservative. It is worth considering defining the coolability limit using the solid temperature, rather than the void fraction. Ultimately, it is the high temperature that threatens the containment integrity, not the phase fraction.

### 5.4.4 Non-uniform heating

The results of the locally heated PORFLO model were described in Publication III. In this case, dryout was formed in the uppermost parts of the channels that were heated. This occurred at low total power compared to the homogenous model because of the localized heating and the porosity difference between the heated and non-heated cells. The question of interest is whether this type of behavior is present in the experimental beds. Due to the local heating, steam flow may be directed upwards at the heater surfaces, yielding high void and early dryout in these regions.

Dryout in the experiments is only detected based on sensors between the heaters,

not on temperature at the heater surfaces. This aims to rule out the non-uniformity by the local heating in the final measured values. According to the simulations, the regions containing the sensors remained coolable when the heater cells were already in dryout and overheated. On the other hand, the non-homogenous model with the averaged porosity is not fully representative of the local heating since it does not actually model the solid heaters, or the porosity variation due to particle packing against them. In the model, porosity is decreased in the heated channels due to the large volume of the solid heaters but, in reality, the bed porosity (in the radial direction) first increases near the heater surfaces and then falls to zero in the location of the heaters. This variation of porosity could be taken into account with a refined grid for which the porosity is specified separately for each cell, but it is likely that the real near-wall behavior would only be captured by a structure-fitted CFD model.

A comparison of the top-flooding DHFs measured with the COOLOCE and POMECO-HT facilities at KTH suggest that the COOLOCE facility tends to overestimate the DHF, rather than underestimate it, at least compared to one other facility. This is described in Chapter 6 of the report Takasuo et al. (2014), in which it was found that the unexplained difference in the results is about 20%. The sensor locations make sure that dryout is not measured at a too low power, but it might be measured at a too great power, because the steam flow favors the high-porosity channels near the heaters. In this case, the excess power would be needed to spread the dryout from the heater surfaces to the TC locations. There is no definite answer to the question of local void fraction and temperature in the experimental bed, but the comparison suggests that the error caused by the heating arrangement acts towards increased coolability. This does not contradict the simulation that showed early dryout only in the heater cells.

Finally, it must be noted that also other factors may influence the discrepancy in the results between COOLOCE and POMECO-HT. In the former, the test beds are immersed into a relatively large pool, but the latter is a more typical pipe-like test design. The DHFs in the COOLOCE results are based on the input power, which includes the measurement errors described in Section 4.3. If the power calculated from the condensate mass flow rate (see Section 4.3.1), which was 7-20% smaller than the input power, was used in the comparisons, the COOLOCE results would be in closer agreement with those of POMECO-HT.

#### 5.4.5 Geometry variations

The previous sections presented MEWA and PORFLO simulations of the classical top-flooded cylinder and the more realistic conical bed. The four other COOLOCE geometries have also been modeled using MEWA, but the applied CFD code was Fluent instead of PORFLO. These simulations have been described in research reports (Takasuo et al., 2014; Takasuo et al., 2015) but not yet published as scientific articles. The shift of focus in the CFD simulations from PORFLO to Fluent was due to the orientation of the PORFLO development towards generic improvements to the solution algorithms, and coupling the code to reactor dynamics and neutronics codes.

## 5. Simulations

In this section, it is examined whether the dryout conditions for the non-conventional bed geometries can be reproduced by the simulation models.

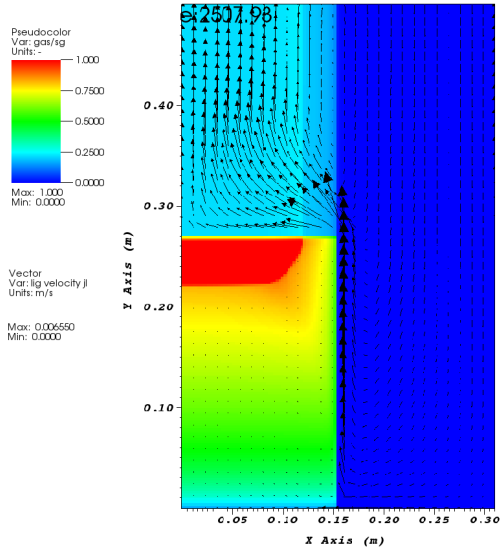
The void fraction fields in dryout conditions for the test bed geometries of the fully and laterally flooded cylinders are illustrated in Figure 5.7, and for the cone on a cylindrical base and the truncated cone in Figure 5.8. The vectors of superficial liquid velocity indicate the direction of the coolant flow. The Reed drag force model with implicit interfacial drag was applied in the simulations. For the effective particle diameter, the value of 0.84 mm was chosen, with the bed of porosity of 0.39. This is one of the parameter combinations found representative as will be discussed in Chapter 6). Note that these are slightly different from the modeling options in Publications II–IV.

All the cases, with the exception of the cylinder with impermeable top in Figure 5.7(b), show quasi-steady-state conditions in which the phase fractions and temperatures in the bed zone have been stabilized, but minor fluctuations in the phase velocities are present in the pool. The simulated conditions – pressure and heating power – are those of the experiments COOLOCE-10–13 at near-atmospheric pressure.

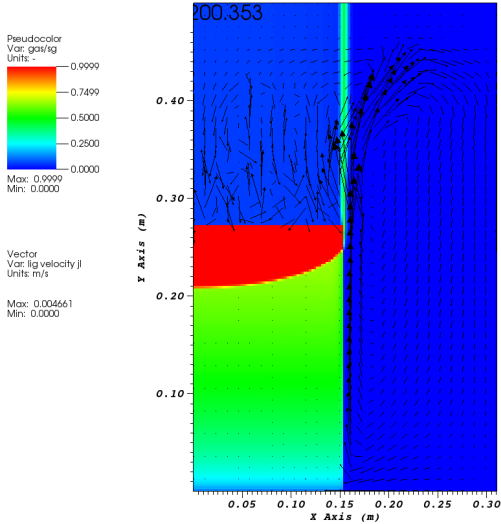
In comparison to the experiments, the Reed model results appear plausible for the fully flooded cylinder, the cone on a cylindrical base and the truncated cone. In the fully flooded cylinder and the cone on a base, the dryout zone is rather large which indicates that the excess power (the difference between the exact DHF and the observed DHF) is greater. In the case of truncated cone in Figure 5.8(b), local dryout spots are seen at the top of the geometry which will form a dried-out layer similarly to the fully flooded cylinder if the power is increased. The difference to the other geometries suggests that either the model overestimates coolability, or the dryout power measured in the experiment is, for some reason, low compared to the other geometries.

A problem with small local dryouts is that they might be impossible to capture using thermocouples distributed into the bed. The dryout zones in Figures 5.7 and 5.8 are large enough to be seen with the COOLOCE arrangement which, indeed, they were since the heating power in the simulations was taken as the DHF power in the experiments. The truncated cone with the local dry spots is closer to the limit where dryout might not be noticed with the test arrangement. As the heaters and the TC structures are not included in the simulation model, their effect on the local void fraction is not predicted. Thus, it is unlikely that the predicted and simulated dry spots, in terms of size and location, would be in exact agreement for this geometry. The effects of the heat transfer properties of the heaters (such as internal conduction) and TCs are also not considered, but it can be assumed that they are insignificant as error sources compared to the size of the power step, at least for the time scale of the experiments in which the post-dryout overheating for each test run is short.

In the cylinder with lateral flooding only, Figure 5.7(b), a large steam "bubble" is formed directly under the top plate. This occurs already at low power and is practically independent of the applied drag force model as similar fast dryout was obtained with the TD and MTD models. In the experiments, the behavior of this bed was closer



(a)



(b)

**Figure 5.7.** Void fraction fields calculated with MEWA 2D: (a) fully-flooded cylinder, 452 kW/m<sup>2</sup>, and (b) laterally-flooded cylinder, 300 kW/m<sup>2</sup>. Case (a) is in steady state, case (b) is transient with increasing solid temperature.

## 5. Simulations

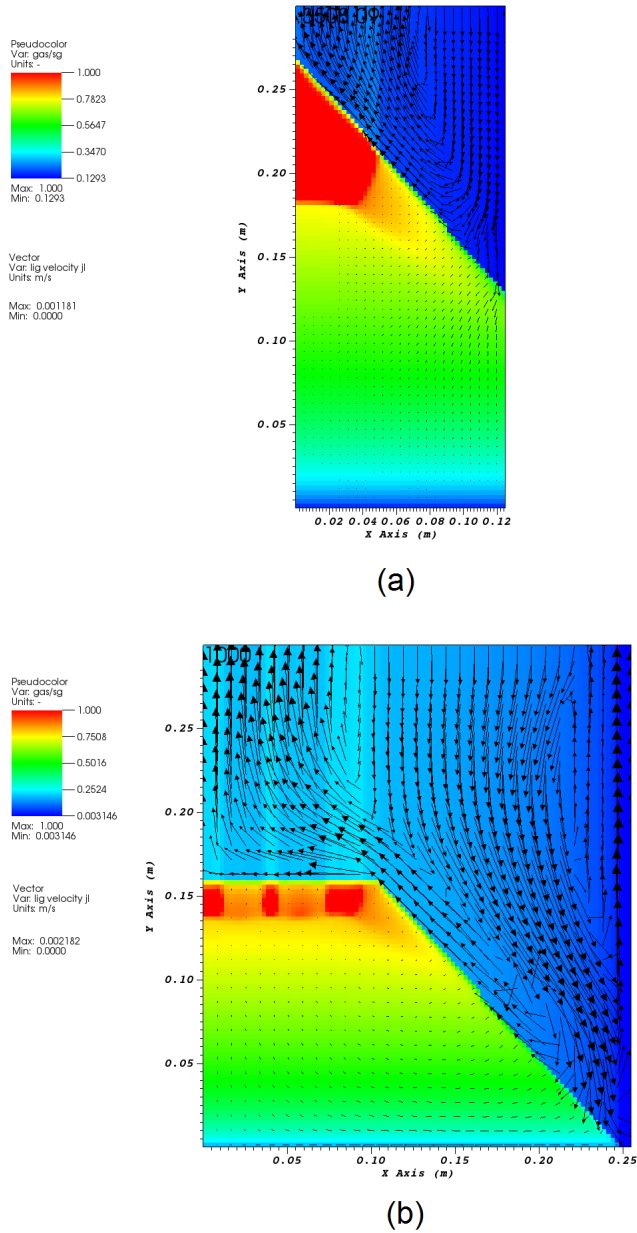


**Figure 5.8.** Void fraction fields calculated with MEWA: (a) cone on a cylindrical base, 521 kW/m<sup>2</sup>, and (b) truncated cone, 416 kW/m<sup>2</sup>. The cases are in steady state.

to the other multi-dimensionally flooded geometries: dryout did not spread and the measured DHF was even greater than in the top-flooded cylinder. A sensitivity test revealed that if a 10 mm gap with large porosity and no heating was assumed below the impermeable plate, the dryout with the same heat flux of  $300 \text{ kW/m}^2$  was limited to a small, flat volume below the top plate. This type of effect might explain the good coolability in the experimental set-up, where the porosity increases near the top plate and the heaters do not reach the top.

For the fully flooded cylinder in Figure 5.7(a), the predicted dryout behavior depended on the applied model to a greater extent than in the other geometries, as reported in Takasuo et al. (2014). A good agreement with the experimental DHF was initially obtained with the Reed model, which does not include explicit interfacial drag. The TD and MTD models, with the explicit interfacial drag, resulted in localized dryout at greater power compared to the experiments. In the cases of the other geometries with lateral flooding, the Reed model underestimated the DHF.

For the cone on a cylindrical base, the results were consistent with the fully conical geometry, and the dryout power and location were the same as in the fully conical bed. A good prediction of DHF was achieved by the MTD model with explicit gas-liquid drag (Takasuo et al., 2014). On the other hand, there is again some uncertainty in the correct effective particle diameter and the accuracy of the measured porosity. The result using the MTD model was obtained with the particle diameter and porosity of 0.97 mm and 0.38, respectively, but also the case in Figure 5.8(a) with the Reed model shows a rather good result with 0.84 mm particle diameter and 0.39 porosity. The latter case has a large dryout zone as seen in Figure 5.8(a), whereas the former only shows dryout at the tip (Takasuo et al., 2014, p. 18), signifying that the power is close to the exact DHF. In the case of the MTD model, it must be also stated that the model as well as the MEWA solver have been under active development in recent years, and some results specific to the code version have been found as presented in Takasuo et al. (2015).

The MTD model includes a relatively complicated calculation of the drag coefficients, which is based on the two-phase flow regimes and particle size (Rahman, 2013). Even though the Reed model does not explicitly account for the interfacial drag term at all, as described in Section 5.1.1, the results in Figures 5.7 and 5.8 suggest that, in practice, the general dryout behavior can be simulated using this model, even for the multi-dimensionally flooded geometries. Regardless of this, some of the simulations raise questions about the applicability of the models to all conditions. The non-consistent drag force model behavior in the case of the fully flooded cylinder, as well as the difficulties in reproducing the characteristic behavior of the laterally flooded cylinder, suggest that the models are not completely reliable if the role of lateral flooding is significant. The model development is based on experiments with vertical flows controlled by gravity and buoyancy. Against this background, it is not surprising that model deficiencies or unexpected results are seen in connection with complex flooding modes.

The comparisons of the MEWA and Fluent results of the different test bed geometries have shown that the qualitative agreement between the results is relatively

## 5. Simulations

good (Takasuo et al., 2014; Takasuo et al., 2015). Differences related to the numerical solution methods and different computational grids were seen. In the case of the conical bed, the tip of the cone was more vulnerable to dryout in the Fluent simulations than in MEWA. On the other hand, the temperature excursions in the Fluent simulations in dryout conditions, with moderate excess power, were limited and the dryout was somewhat sensitive to the pool model.

The CFD results illustrate that defining a coolability limit for multi-dimensionally flooded beds is not a straightforward task. The occurrence of local dryout may depend on the solver options, and the level of detail in the modeling (such as grid density). As a result, the dryout heat flux is sensitive to the advanced model and solver options, and not only to the model parameters that describe the highly influential properties of the bed, such as porosity. Thus, a relatively large uncertainty is present in the prediction of the dryout power and location if the coolability limit is set strictly to the increase of the local void fraction to one (in any cell of the computational model). This supports the conclusion that a more reasonable approach would be to determine the long-term coolability based on the temperature (and volume) of the dryout zone.

### 5.4.6 Free-flow water pool

The pool region is often modeled as a porous zone with large porosity and large particles (e.g. 0.9 and 10 mm). The frictional forces are calculated according to the model which is applied in the porous bed. In order to study the significance of these modeling assumptions, an alternative approach was tested in which a turbulent multiphase flow was assumed for the open pool. The two-phase flow drag force model by Schiller and Naumann (1935) and the  $k-\varepsilon$  turbulence model were applied. The models are available within the standard package of Fluent. It is worth mentioning that the free-flow model would be the primary choice for the pool zone in normal CFD modeling because it cannot be expected that the porous zone approach would produce the "correct" flow behavior. The porous zone approach in the Fluent simulations was selected primarily to make the results easily comparable to the MEWA results.

Some apparent differences were observed between the free-flow pool and the porous pool model results. In the case of the conical bed, the tip of the cone remained more effectively coolable when dryout had just been reached with the free-flow pool models. This was connected to the greater liquid velocity and pressure just above the cone, and the consequently enhanced flow downwards from the pool at the tip. Then, the heat transfer from the particles at the zone which is most vulnerable to reach dryout is increased, which limits the solid temperature increase. The difference in solid temperature was almost 100 °C between the simulations, with only a few degrees increase from saturation temperature in the free-flow pool case.

The liquid saturation fields shown in Figure 5.9 for the conical bed illustrate the effect of the pool model. The saturation fields (and the void fraction) are clearly different in the pool but less so in the debris bed zone. The region that has dried out is

almost the same size in both cases but the maximum solid temperatures are different: 105 °C in case (a) and 197 °C in case (b). The heating power in the simulations is the experimental dryout power of the conical bed at 1.1 bar pressure.

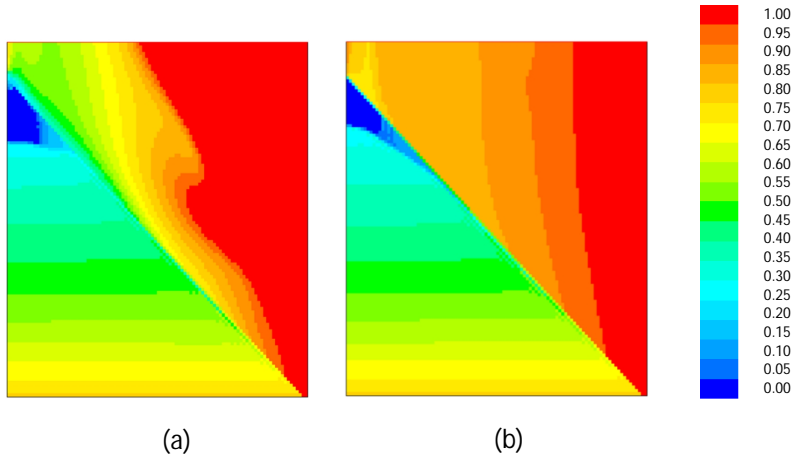


**Figure 5.9.** Liquid volume fraction calculated with (a) free-flow pool model and (b) porous pool model. The MTD drag force model is applied in the bed zone and in the pool zone in case (b).

Another difference was the decrease of the slip velocity. In the porous zone pool assumption, the steam velocity may increase up to several m/s in the pool, while the water velocity remains below 0.1 m/s. With the free-flow pool model, the liquid accelerates and the maximum slip velocity is the order of 0.5 m/s, which is still somewhat large compared to typical terminal velocities of bubbles in two-phase flow but has the correct order of magnitude (Wallis, 1969, p. 248).

In addition, the porous pool model assumes that there is a small fraction of solid particles in the pool zone. Then, in the case of solid temperature increase, solid-to-solid conduction may occur between the bed and the pool zones, creating somewhat peculiar additional heat transfer. Obviously, this type of effect is not present in the free-flow pool.

The main effects of the pool model selection were, indeed, limited to the pool zone. The pool model did not have drastic effects on the predicted saturation/void fraction distributions in the bed zone, and it is generally adequate to use the porous zone pool assumption. For the conical case, the limited local effects of the pool model on the debris bed increased the predicted coolability. Thus, the porous pool assumption tends to yield more conservative results. The descriptions of the Fluent models and the detailed results with and without the free-flow pool model can be found in Takasuo et al. (2014) and Takasuo et al. (2015).

## 5. Simulations

### 5.5 Extension to reactor scale

Assuming that the debris is evenly distributed as a flat-shaped cylinder, the STYX experiments with top flooding are directly scalable to the dimensions of the Nordic BWR. The particle size is realistic, the diameter of the test bed is large enough to rule out possible boundary effects and, in the case of top flooding, there are no pressure, velocity or temperature gradients expected in the radial direction. This makes it possible to make direct comparisons of the level of decay heat to the experimental dryout heat flux. However, this is not the case in the downcomer experiments in which the flooding is multi-dimensional. For a debris bed with a large diameter, the lateral distance to the center of the bed is great compared to height, and the inflow from the small downcomers probably would not effectively cool the center of the bed.

For the COOLOCE test beds, the height and width are both smaller compared to the reactor scale. The conical test bed is about 1:7 in height and 1:18 in diameter compared to a debris bed of about 200 metric tons of corium and 40% porosity. On a realistic scale, the angle of repose in the conical test bed is also smaller due to the lower height-to-width ratio: For a conical debris bed whose base reaches the walls of the flooded lower drywell, the angle of repose would be approximately  $22^\circ$ , in comparison to the  $47^\circ$  of the COOLOCE test bed.

The steam generation in the realistic debris as a whole is, of course, greater than in the test bed. The effect of the height scaling is seen in the Reynolds number (Equation 5.27), which depends on the flow velocity, particle size, density and viscosity. Keeping in mind that the steam flux increases with height and power density, the steam phase achieves greater velocity in a real debris bed compared to the test bed. For a bed consisting of fine debris, the gravel particles applied in STYX and COOLOCE are a good approximation of realistic particles considering the particle size. With greater flow velocity and the same particle size, the Reynolds number increases, which suggests that the steam flow is more turbulent.

From the equation of the gas phase drag (Equation 5.6) it is seen that the inertial (quadratic) component of the pressure loss is greater on the large scale than on the laboratory scale due to the velocity increase. This also suggests that the flow instabilities are greater. Note that the scale differences are pronounced in the upper parts of the bed where the length of the steam flow path is greatest. In principle, the simulation models are capable of taking this transition towards higher velocities into account.

A more difficult question to answer is whether the different height-to-width ratio affects the effectiveness of the lateral flooding. There is no experimental data of multi-dimensional flooding in different scales, and the extension to large scale has to be done by the simulation models. An example of a BWR calculation with MEWA is shown in Figure 5.10, which illustrates the void fraction and temperature distributions for a debris bed consisting of about 200 metric tons of solidified corium. The angle of repose has been conservatively set to  $42^\circ$  in order to create a tall, fully conical bed. The containment pressure in the simulation is 5.5 bar and the applied drag force model is MTD. The decay power has been adjusted to just exceed the dryout power.

It is seen that the large-scale bed behaves quite similarly to the conical test beds

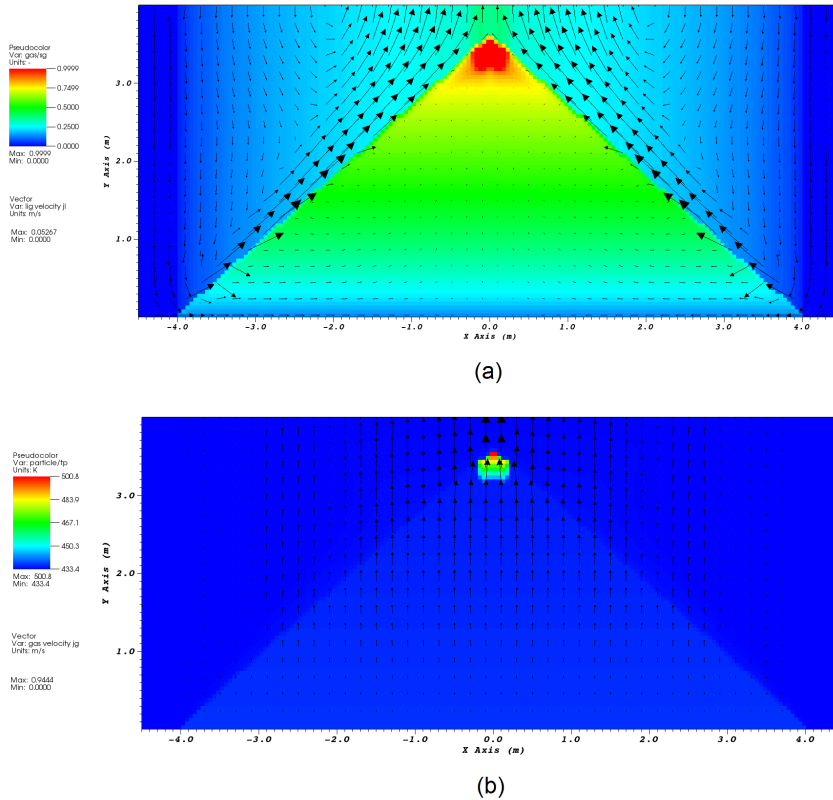


**Figure 5.10.** (a) Void fraction and (b) solid temperature in a MEWA simulation of the conical debris bed ( $42^\circ$  slope angle) on a realistic scale. The dryout power is just exceeded. Vectors of superficial velocity are shown in (a) for liquid and (b) for gas.

in Figures 5.2 and 5.5. The steam flow is directed almost directly upwards, and the water flow forms a convection loop in which it travels laterally into the bed interior through the conical surface and turns upwards with the steam flow in the center of the bed. The solid temperature has stabilized to  $228^\circ\text{C}$ , about  $70^\circ\text{C}$  above the saturation temperature in the bottom of the pool. The results, especially the similar steam flow pattern, suggest that the coolability is strongly dependent on the bed height on the reactor scale.

The size of the dryout zone in the simulation in Figure 5.10 does not increase and the temperature remains clearly below the re-melting temperature, unless the heating power is further increased. In the case of only a small increase, the system finds a new steady state with greater solid temperature and slightly larger dryout zone size. This is shown in Figure 5.11, which illustrates the void fraction and solid temperature in the same simulation case as in Figure 5.10 with the heating power

## 5. Simulations

increased by 10%. Now, the solid temperature is stabilized at 289 °C, which is still an order of magnitude smaller than the temperature of fully molten corium. The melting point of uranium dioxide is approximately 2850 °C (IAEA, 2006).

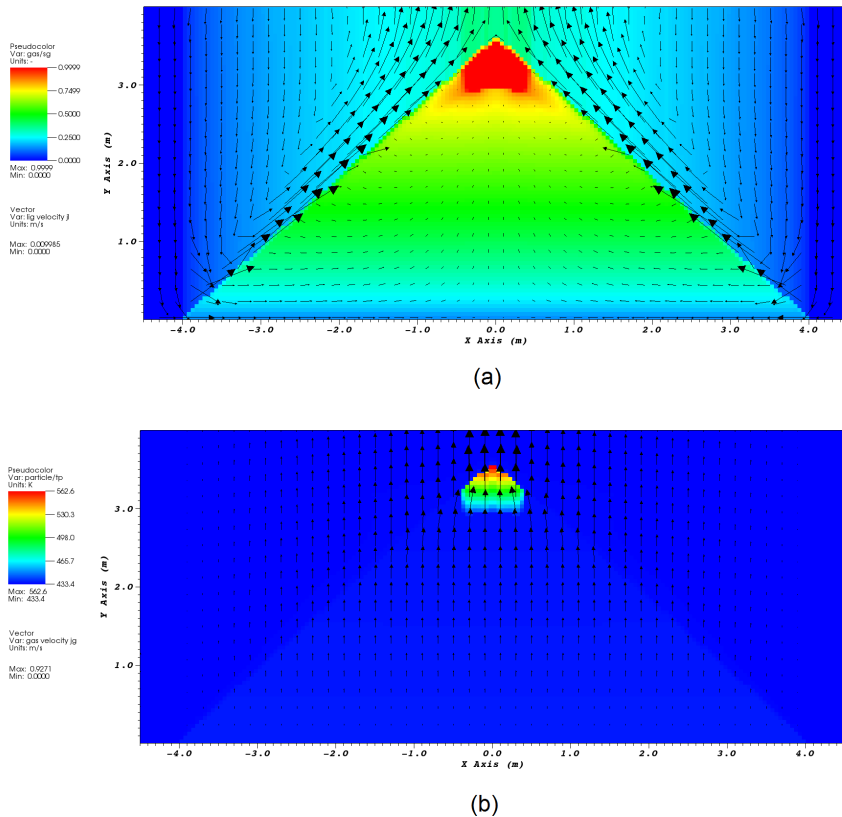


**Figure 5.11.** (a) Void fraction and (b) solid temperature in a MEWA simulation of the conical debris bed (42° slope angle) on a realistic scale. The dryout power is exceeded by 10%. Vectors of superficial velocity are shown in (a) for liquid and (b) for gas.

The co-current flooding pattern and the steam flow that passes through the dry zone cannot sustain the steady conditions if the heat generation is excessively high. When the power increases to a critical level, the convection by steam flow is no longer capable of removing the heat from the particles effectively and the temperature increases until the corium starts to re-melt. (Re-melting can result, for instance, in a molten pool lower in the bed, which is insulated from the surrounding debris

by a solidified layer called crust.) A significant contributor to the loss of cooling by steam flow is the reduction in the evaporating steam flow rate; when the size of the dry zone increases by spreading downwards, the water reservoir below the dry zone that provides the steam flow becomes smaller.

The data available of the maximum excess power and the critical size of the dryout zone at which steady states can be formed are scarce. The studies concerning the post-dryout behavior were listed in Section 5.4.3. One of these studies (Yakush and Kudinov, 2014) makes an effort to quantify the maximum permitted size of the dryout zone using the DECOSIM code which, in general, utilizes an approach similar to MEWA. According to the study, the dryout zone might spread to cover more than 50% of the bed height until temperature stabilization is no longer possible. However, no experimental data exists to verify this behavior.

Concerning the modeling of heat transfer, the properties of the experimental materials, ceramic beads and alumina gravel differ from that of corium (e.g. their thermal conductivity is lower). This may play a role in the behavior of post-dryout temperatures, even though it is not apparent based on the simulations which apply realistic material properties for the corium. In addition, it should be pointed out that the validation of the heat transfer models for prediction of the post-dryout temperature increase is another topic beyond the scope of this work. It is recommended to review the available heat transfer models and their validity in different configurations prior to the application of the temperature-based criterion for coolability.

In the dryout zones, adverse effects might also result from the exothermic reaction of zirconium oxidation at temperatures above 1000 °C (IAEA, 2011). This reaction, which is responsible of the hydrogen generation in a severe accident, produces additional heat (and a source of hydrogen) that may have poorly predictable effects on the debris re-melting behavior. Then, the maximum "safe" temperature applied in coolability simulations could be based on the start of the high-temperature zirconium oxidation, instead of the onset of debris re-melting.

## 6. Effective particle size

An almost obvious assumption in the modelling of real debris beds – a reactor scenario or an experimental bed – is that the internal structure of the bed is homogenous and isotropic. This means that the bed properties such as porosity, particle size, permeability and passability are independent of the examined location and direction. It is assumed that single representative values for particle diameter and porosity are applicable throughout the bulk of the bed as if it consisted of uniform spherical particles.

In reality, the jet fragmentation of corium and the settling of quenched particles is likely to produce a bed with a complex internal structure, consisting of a mixture of particles of various sizes and shapes. It is not possible to account for all debris bed configurations that can result from the corium discharge. Moreover, even if the internal structure of some highly non-homogenous beds were known in detail, its detailed modeling would be impractical because capturing flows at the pore level would require structure-fitted grids, advanced two-phase flow models, and excessive amounts of CPU times. Thus, some extent of averaging of the bed properties is always present in modeling.

It is important that the representative particle diameter for the bed, namely the *effective diameter*, is selected in such a way that it yields accurate predictions of the dryout behavior. The question of how to find a representative effective diameter is addressed in Publication V. This paper provides a large review of the particle sizes and porosities expected for in-vessel and ex-vessel debris, and collects results from experimental activities in different European laboratories.

The particle materials in the effective diameter experiments included e.g. glass spheres, prisms, steel cylinders and screws and gravels. Two approaches were used to determine the effective particle diameter. In the first approach the effective diameter was derived by combining experimental data and models so that the diameter which yielded the best correlation between model and experiment was taken as the effective diameter. The second approach was to compare beds consisting of irregular particles to beds consisting of uniform spherical particles. The advantage of this method is that it is independent of any modeling assumption but, in practice, it is difficult to find out which uniform particles correspond to the irregular bed in question and a large number of tests may be needed.

## 6. Effective particle size

In the concise summary presented here, the focus is on the findings obtained with the debris materials of the Finnish facilities COOLOCE and STYX. Many of the works in Publication V can be viewed as fundamental studies addressing the properties of complex porous media. From the point of view of the thesis, the orientation is towards the practical problem of finding a useful effective particle diameter for coolability simulations dealing with realistic conditions, i.e. with random, probably irregular particles. The considerable amount of research of the other laboratories is not repeated in detail, but those interested may find more information in Publication V and its list of literature references.

### 6.1 Research methods

The first approach – the combination of experimental data and models – was applied in the investigations conducted with the alumina gravel ( $\text{Al}_2\text{O}_3$ ) and the ceramic beads ( $\text{ZrO}_2 - \text{SiO}_2$ ) of the STYX and COOLOCE experiments. For these materials, the effective particle diameter was estimated by (1) measuring the single-phase pressure loss and fitting the data to the Ergun equation (Ergun, 1952) and (2) utilizing the DHFs measured in the COOLOCE experiments and fitting the data to the predictions of dryout models. The dryout models are based on the extension of the Ergun equation to two-phase flow as described in Chapter 5. The effective particle diameters obtained from the DHF and pressure loss measurements were compared to the mean values calculated from the particle size distributions.

The pressure gradient measurements to determine the effective particle diameter were performed at KTH with the POMECO-FL facility. Isothermal air or water single-phase flows were used in the measurements. The schematic of the facility is shown in Figure 6.1. The test section consists of a Plexiglas pipe with 90 mm inside diameter and 635 mm height. The pressure gradient is measured by high-accuracy differential pressure transmitters and the flow rate is measured by seven rotameter-type flow meters (Li and Ma, 2011). The particles were well mixed prior to the experiments and the test bed was flooded with a low flow rate to make sure that the bed was fully saturated with the fluid, and there were no changes in the bed height. During the measurements, constant single-phase flow was supplied through the porous medium for about half an hour in order to establish a steady state for which the flow rate and pressure gradient data was recorded. This procedure was repeated for all the intended flow rates. Qualifications of the test arrangement were made also by pressure gradient measurements using a bed of single-sized glass spheres, and comparing them to the predictions by the Ergun equation (Thakre et al., 2013).

The DHF-based estimate was performed using the COOLOCE data, namely, the results of the COOLOCE-3 and COOLOCE-8 tests with the cylindrical bed described in Chapter 4. No new DHF data was produced for the effective diameter studies. The method is similar to predicting the DHF from known particle size and porosity by applying the simulation models but the process is reversed. Instead of predicting the DHF with the particle diameter as an input, DHF is taken as a known parameter and the particle diameter is fitted into the DHF measurement, assuming that the

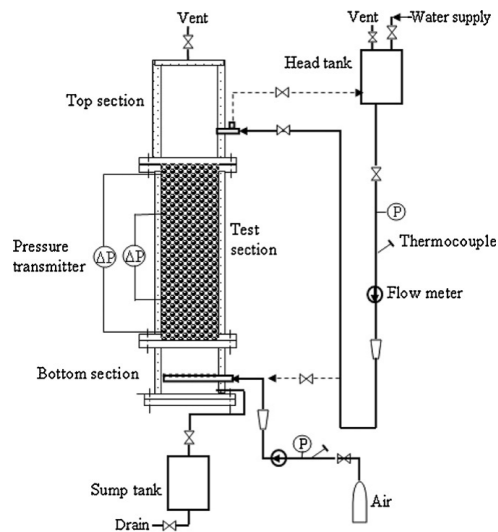


**Figure 6.1.** The POMECO-FL apparatus for pressure loss measurements in porous media (image by KTH).

two-phase models, such as the Reed model, are valid.

Particle size distributions were measured and verified for calculating the weighted average diameters, which are usually considered to be representative of differently sized granular materials. These diameters are count, length, surface area and volume (mass) mean diameters. The equations for calculating the mean diameters from the weighted or counted particle sizes are given in Table 2 of Publication V. For the gravel, the size distribution was estimated by sieve analysis during the STYX and COOLOCE experiments, and the latest measured size distribution (illustrated in Figure 3.2), was applied in the study.

In contrast to the gravel, the ceramic particles are smooth, spherical and comparatively uniform in size. Because of this, it was expected that finding out a suitable effective diameter for the beads would be much easier than for the irregular gravel. However, as the beads are not high-precision particles, there is variation in their diameter and roundness. The size distribution of the beads was measured by image processing and by a laser diffraction analyzer (Malvern, 2015) designed for the sizing of powder-like materials. According to a sample of about 1000 beads that were photographed, the size range was 0.82–1.11 mm, with the arithmetic mean of 0.97 mm.

The volume-based laser diffraction analysis (not the same samples) showed that the volume-weighted average diameter is 0.975 mm and the surface mean calculated from the volume-based data is 0.960 mm. Small, trace amounts of particles (0.03–0.12%) were even found to be smaller than 0.666 mm and larger than 1.430 mm but it seems likely that these extreme values are caused by occasional impurities in the sample, or the conglomeration of several particles. The size distribution obtained

## 6. Effective particle size

by the laser diffraction analysis is shown in Figure 6.2. Figure 6.3 shows the normal distribution of the particle size (within the measured size range), calculated from the sizes obtained with the image processing software.

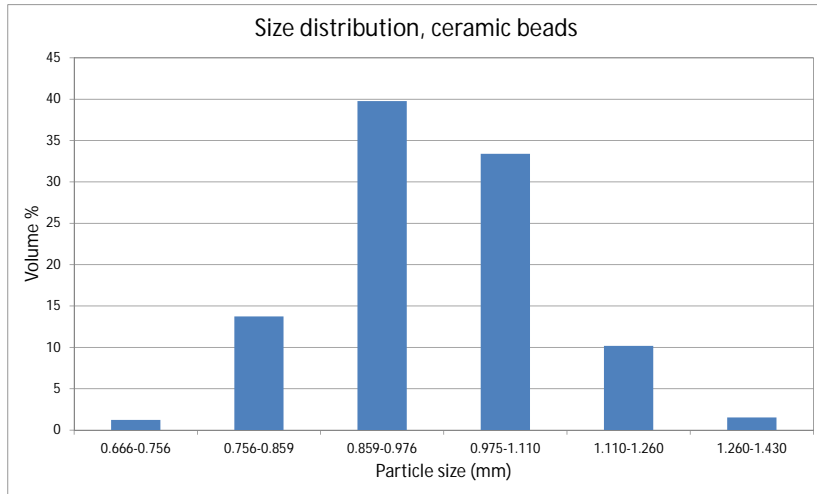


**Figure 6.2.** Size distribution of the ceramic beads in the COOLOCE experiments (laser diffraction analysis).



**Figure 6.3.** Normal distribution of the ceramic bead size in the COOLOCE experiments (image analysis).

## 6.2 Results

The effective diameters obtained from the pressure loss and DHF measurements and the average diameters obtained from the particle size distributions for the gravel and beads are presented in Table 6.1. Since the pressure loss is dependent on both particle size and porosity, the only way to distinguish the contribution of particle diameter in the pressure loss is to carefully measure the porosity of the bed for which the effective particle diameter is measured. This also implies that the effective diameter is not universally valid for all beds consisting of the same material but coupled with porosity. Because of this, the bed porosities for which the effective diameters were obtained are given in the table.

**Table 6.1.** Mean and effective particle diameters for the debris simulant materials.

Calculation method	Diameter [mm]	
Count mean	0.725	 <p>Size range: 0.25-10 mm</p>
Length mean	0.969	
Surface mean	1.77	
Mass mean	3.32	
Effective, $\Delta p$ ( $\epsilon=0.408$ )	0.65	
Effective, DHF ( $\epsilon=0.408$ )	0.65	
Effective, DHF ( $\epsilon=0.392$ )	0.70	
Count mean	0.970	 <p>Size range: 0.82-1.11 mm</p>
Length mean	0.974	
Surface mean	0.978	
Volume mean	0.983	
Effective, $\Delta p$ ( $\epsilon=0.399$ )	0.8	
Effective, DHF ( $\epsilon=0.400$ )	0.8	
Effective, DHF ( $\epsilon=0.370$ )	0.97	
Effective, DHF ( $\epsilon=0.390$ )	0.84	

According to the pressure loss measurements, the effective particle diameter of the gravel was 0.65 mm for the bed porosity of 0.408. It was found that the DHF predicted with the Reed model using this diameter and porosity was in good agreement with the experimental results, yielding the same effective particle diameter for both pressure loss and DHF-based estimates. However, the COOLOCE gravel bed had a porosity of 0.392 which is marginally lower than the porosity of the POMECO-FL

## 6. Effective particle size

bed. For this porosity, the effective diameter would have to be slightly larger to yield the measured pressure gradient and also DHF. Then, the effective diameter based on pressure loss would be 0.70 mm.

A small effective diameter was also obtained for the beads, 0.80 mm for a bed porosity of 0.399 in the pressure loss test. These values yielded rather accurate predictions of the measured DHF. However, the porosity of the COOLOCE test bed for the DHF measurement was again estimated to be marginally lower, 0.39. For this porosity, the effective diameter that yields the same pressure loss and DHF is about 0.84 mm. The mean diameter of 0.97 mm corresponds to the porosity of about 0.37 which is approximately the minimum porosity achievable for randomly packed spherical particles and, for the larger surface and volume means, the porosity would be even smaller. Again, the DHF based effective diameter relies on the Reed model in the extension of the analysis from single-phase to two-phase flow.

For the ceramic beads, the calculated means are close to each other (within 1%) due to the narrow size distribution and, due to the sphericity of the beads, the means were expected to describe the particle properties well. However, the estimated effective diameter of 0.80 mm for 0.40 porosity is close to the lowest limit of the size distribution, being even slightly smaller than the minimum size present in the image analysis sample (but within the range by the laser diffraction analysis). For the maximum random packing of spherical particles with 0.37 porosity, the effective diameter increases to the count mean of 0.97 mm. There is some uncertainty in porosity which affects the particle diameter (and its error), but even so it can be deduced that the effective diameter lies within the lower half of the size distribution for realistically packed spheres (with 0.37–0.40 porosity).

It must be noted that the DHF-based analysis cannot be more accurate than the measured DHF. In COOLOCE, the total error in the measured dryout power may cause an error between +0.01 mm and -0.1 mm in effective diameter (the one-sidedness of the error is caused by the CHF/DHF power stepping method). For the gravel bed, the error is acceptable but for the ceramic beads with the small size range, finding out the effective diameter within the size range is not reliable using this method.

It was also seen that the pressure dependency predicted by the simulation models did not exactly correspond to the measured one, as illustrated in Figure 7 of Publication V. This was especially true for the gravel bed in which the 7 bar and 5 bar DHFs were close to each other. For higher pressures, the Hu and Theofanous (1991) drag force model appeared to give somewhat better agreement than the Reed model. On the other hand, a plausible explanation to the lower DHFs at higher pressures is the possible shift in the bed porosity and packing during the test runs, discussed in Section 3.2.2. For the spherical particles, the simulated DHF at atmospheric pressure was slightly lower than the experimental DHF but, starting from 2 bar, the results are in good agreement.

### 6.3 Discussion

It was found that the effective diameters for particles that had complex shapes were comparatively small. This was seen in all the studies in Publication V which addressed both simple and complex particles. KTH found that, for sand particles resembling the alumina gravel in the VTT experiments, the effective diameter was between the length and count means but closer to the length mean (Publication V, Table 9). The IKE Institute observed that, for screws with different sizes and well-defined but complicated geometry, the length mean yielded the best agreement with the measured pressure gradient (Publication V, Figure 12). In the case of the VTT alumina gravel, the effective diameter was closest to the count mean, which is the smallest of the weighted mean diameters. The results suggest that the complicated morphology of particles provides increased fluid-particle drag, and that the average diameters based on the size distribution are of limited use in the case of irregular particles.

A curious result was obtained by IRSN: the Sauter mean diameter (equivalent to a sphere with the same volume-to-surface area ratio) yielded the best prediction for the pressure gradient but, when steam flow rates from different test beds were compared during quenching experiments (reflooding), the effective diameter decreased close to the count mean of the particles (Publication V, Figures 17 and 18). This result was obtained using mixtures of differently-sized spheres, cylinders and prisms. This result would suggest that the representative, effective diameter is different for mechanical and thermal properties of the bed. The authors of the study, however, acknowledge the need for repeatability experiments to confirm the results.

The overall conclusion from the European studies was positive towards determining the effective diameter for complex beds from simpler bed configurations. In the studies that examined pressure gradients in beds of single-sized spheres and non-spherical particles with well-defined geometries (cylinders and prisms), the Sauter mean diameter was found to be well representative. In the studies that applied more complicated thermal-hydraulic models or experiments – DHF and steam flow during quenching – it was more difficult to identify a representative diameter. In these cases that deal with two-phase flow, the complicated physical mechanisms and model uncertainties are larger. For instance, the calculated DHF depends on particle size and porosity but also on the model for relative permeability and passability. From the alternative drag force models (Reed, 1982; Lipinski, 1982; Hu and Theofanous, 1991), some yield greater DHFs than others, without full consistency of the best model. For irregular particles, porosity is difficult to measure with high precision (especially when the bed may shift under heavy steam flow) and to separate its contribution from the particle diameter. Then, the separation of at least three parameters, particle diameter, porosity and the empirical constants in the models becomes intractable.

A major issue in extending the studies to realistic debris beds is how to account for the gravel-type materials with large size, shape and porosity variation. Since the shape of the debris particles is not well-defined, the effective diameter obtained directly from pressure gradient measurements or other simple experiments is a reasonable approach. In addition, the particle count- and length-weighted means give

## 6. Effective particle size

fairly representative estimates of the effective diameter. It is an important notion that for these types of particles, the effective (hydrodynamically representative) diameter can be significantly smaller than the surface-weighted mean, which is often considered representative for fluid-particle drag forces.

Considering the large impact of the particle diameter on coolability, the correct choice of the effective diameter is crucial in analytical work and the modeling of accident scenarios. The effect of the particle diameter is seen in Figure 8 in Publication V which shows the DHF as a function of particle diameter for the porosities of 0.37, 0.39 and 0.41. If the particle diameter is increased from 0.80 mm to 1.0 mm (25%), the resulting increase in DHF is close to 40%. The DHF calculation in the figure is based on the analytical solution of the Reed model. For simulations that address realistic and fully fragmented debris beds, it is recommended to select the effective diameter based on pressure loss or one of the smallest mean diameters to avoid overestimating the coolability for coarse, irregular particles. In this case, the conservative choice is likely to be the most representative.

## 7. Conclusions

A study investigating the coolability of porous beds which simulate the debris bed consisting of solidified corium in the case of a postulated severe nuclear power plant accident has been performed. The focus was on the debris bed geometrical shape and its effect on coolability, which is defined by the maximum heat flux that can be removed from the bed without local dryout, or by the stabilization of solid temperature.

Realistic conical and heap-like shapes were examined by measuring the dryout heat fluxes in the laboratory-scale COOLOCE facility, and comparing them to the dryout heat flux of a one-dimensionally flooded cylindrical bed. The one-dimensional bed has been examined in many classical studies on the topic. The main difference between the classical assumption of an effectively one-dimensional bed and the present approach is that the realistic bed assumption allows multi-dimensional infiltration (flooding) of coolant into the bed interior, as a consequence of the complex shape of the bed.

Five different variations of the multi-dimensionally flooded beds were included in the experiments, in addition to a classical top-flooded cylinder and one configuration in which multi-dimensional flooding was achieved using downcomers. The actual dimensions of the debris beds were considered by emphasizing that a bed with a conical shape is three times higher than a cylindrical bed if the bed volume and radius are equal. In the case of volumetrically uniform power generation, this implies that the heat flux at the bed top is three times greater, since it increases proportionally to height. Then, the longer flow path makes the top of the conical geometry vulnerable to dryout.

The experiments directly showed that the multi-dimensional flooding increases the dryout heat flux and enhances coolability compared to top flooding by 47–73% if the beds are equal in height. One dryout heat flux experiment suggested an increase of 93%, but the maximum error in this measurement was rather large. For a conical bed and for a conical bed with flattened top, the increase was 47–58%. For a laterally flooded bed with an impermeable top (simulant of a solid particle agglomerate), the coolability was comparable to that of the top-flooded bed, or even slightly better, regardless of the fact that the steam flow could not escape through the top of the bed.

If the debris bed height and volume are taken into account, the coolabilities of the

## 7. Conclusions

heap-shaped beds and the top-flooded beds are reversed: the top-flooded cylindrical bed has better coolability than the conical bed. This is because the increase of *maximum heat flux* from the increased height is greater than the *dryout heat flux* increase achieved by the multi-dimensional flooding. The multi-dimensional flooding is directly beneficial only if the height increase due to the conical shape is below the measured dryout heat flux increase ratio, at most about 1.5–1.6 times the height of the top-flooded cylindrical bed. This result is valid if the formation of the first dry zone, even if highly local, is considered to be the coolability limit.

Numerical simulations that model the dryout behavior of the experimental test beds have been conducted using two-phase flow solvers. The applied codes included MEWA 2D developed by Stuttgart University, the in-house code PORFLO developed by VTT, and the generic commercial CFD code Fluent by Ansys Inc. The codes readily included suitable physical models for two-phase flows in porous media, or were implemented into the codes during the study described in this thesis.

In general, the MEWA code was able to predict the relative dryout heat flux increase resulting from the multi-dimensional flooding for the pressure range addressed in the experiments, 1–7 bar. Also, the absolute dryout heat fluxes may be predicted by the code. However, there is some uncertainty in the bed porosity and effective particle diameter, which have a significant impact on the predicted DHF, and some non-consistency between the results yielded by different drag force models. The void fractions and temperatures in the PORFLO and Fluent simulations were qualitatively similar to the MEWA results. The Fluent simulations also revealed possible local effects which might play a role in the formation of dryout in the conical bed.

The simulations provided insight into the details of the dryout development, and the fundamental differences between top flooding and multi-dimensional flooding. According to the simulations, dryout was a local phenomenon initially occurring in small volume in the upper parts of the multi-dimensionally flooded beds. Even with relatively large dryout zones, some simulation cases reached steady state in which the solid temperature was above saturation temperature but showed no further increase. This is in contrast to the top-flooded bed in which the bottom part of the bed was practically completely emptied from coolant by evaporation. The difference is mainly related to the steam flow that enhances the heat transfer in the dryout zone.

The simulations support the idea that the criterion that determines the coolability limit should be based on the particle temperature rather than on the local dryout. Then, the benefit gained from the multi-dimensional flooding would be greater than the aforementioned increase of 47–73%. The currently existing research, however, does not include conclusive information on how much the criterion could be modified to retain an adequate safety margin.

Finally, a study on the determination of a hydrodynamically and thermally representative effective particle diameter to be applied in modeling was presented. In realistic beds, the debris particles are expected to have complex shape (in addition to large size variation), for which the effective diameter might not be found based on the mean diameters derived from the size distribution, or a suitable shape factor can-

not be defined. In this study, the approach was to determine the effective diameter based on single-phase flow pressure loss measurements and the Ergun equation, which connects the pressure gradient to the diameter of the particles. Compared to the particle size range and distribution, the obtained effective diameter was rather small, closest to the mean diameter based on the length or the number of particles. Thus, for realistic beds consisting of irregular particles, the representative diameter can be notably smaller than, for instance, the surface area mean often considered representative for fluid-particle drag.

The experimental results of the study have provided new data for the validation of severe accident simulation codes. The existence of a comprehensive experimental database for this purpose is essential since the progress of accident scenarios on a realistic scale have been and will be analyzed with simulation codes. Understanding of the underlying mechanisms of the debris bed dryout behavior is required in reliably assessing which types of conditions are safe, and which might result in re-melting of the debris due to decay heat.

One of the findings of the simulation work was that the most advanced methods for dryout prediction, such as CFD and the complicated interfacial drag force models, are not always the most practical ones but, even when it is well-founded to use simple models, limitations of the models against the reality of the two-phase flow should be clear in mind. The experiments and simulations with multi-dimensional flooding have revealed a view into the behavior of realistically-shaped debris beds, which is quite distant from that of the one-dimensionally flooded bed, which has been the basis for all the classical analyses and model development. In particular, the results show that the multi-dimensionally flooded debris beds cannot be outright considered as the easiest to cool because these types of beds may have great height.

## References

- Atkhen, K. and Berthoud, G. (2006). SILFIDE experiment: Coolability in a volumetrically heated debris bed. *Nuclear Engineering and Design*, 236:2126–2134.
- Barleon, L. and Werle, H. (1981). Dependence of dryout heat flux on particle diameter for volume- and bottom-heated debris beds. Technical Report KfK 3138, Forschungszentrum Karlsruhe.
- Basso, S., Konovalenko, A., and Kudinov, P. (2014). Sensitivity and uncertainty analysis for prediction of particulate debris bed self-leveling in prototypic SA conditions. In *International Congress on Advances in Nuclear Power Plants (ICAPP)*, Charlotte, USA April 6–9, number 14329.
- Bechaud, C., Duval, F., Fichot, F., Quintard, M., and Parent, M. (2001). Debris Bed Coolability Using a 3-D Two Phase Model in a Porous Medium. In *9th International Conference on Nuclear Engineering. April 8–12, 2001, Nice, France*.
- Berthoud, G. (2006). Models and validation of particulate debris coolability with the code MC3D-REPO. *Nuclear Engineering and Design*, 236:2135–2143.
- Bürger, M., Buck, M., Pohlner, G., Rahman, S., Kulenovic, R., Fichot, F., Ma, W., Miettinen, J., Lindholm, I., and Atkhen, K. (2010). Coolability of particulate beds in severe accidents: Status and remaining uncertainties. *Progress in Nuclear Energy*, 52:61–75.
- Bürger, M., Buck, M., Schmidt, W., and Widmann, W. (2006). Validation and application of the WABE code: Investigations of constitutive laws and 2D effects on debris coolability. *Nuclear Engineering and Design*, 236:2164–2188.
- Buck, M., Pohlner, G., and Rahman, S. (2012). Documentation of the MEWA code. Unpublished draft. Stuttgart University.
- Cheng, S., Tagami, H., Yamano, H., Suzuki, T., Tobita, Y., Zhang, B., Matsumoto, T., and Morita, K. (2014). Evaluation of debris bed self-leveling behavior: A simple empirical approach and its validations. *Annals of Nuclear Energy*, 63(188–198).

## REFERENCES

- Darcy, H. (1856). *Les Fontaines Publiques de la Ville de Dijon*. Victor Dalmont, Paris.
- Dhir, V. and Catton, I. (1976). Prediction of Dryout Heat Fluxes in Bed of Volumetrically Heated Particles. In *International Meeting on Fast Reactor Safety and Related Physics, Chicago, Illinois, October 5–8, 1976*, number CONF-761001.
- Ergun, S. (1952). Fluid Flow Through Packed Columns. *Chemical Engineering Progress*, 48:89–94.
- Forchheimer, P. (1901). Wasserbewegung durch Boden. *Zeitschrift des Vereines Deutscher Ingenieuer*, 45:1782–1788.
- Hofmann, G. (1984). On the location and mechanisms of dryout in top-fed and bottom-fed particulate beds. *Nuclear Technology*, 65:36–45.
- Hofmann, G. (1987). Dryout in very deep particulate beds. *Nuclear Engineering and Design*, 99:177–185.
- Hofmann, G. and Barleon, L. (1986). Reduced coolability of particle beds as a result of capillary effects at horizontal phase boundaries. In *International ANS/ENS Topical Meeting on Thermal Reactor Safety, San Diego, CA, USA, February 1986*.
- Holmström, S., Pankakoski, P., and Hosio, E. (2005). STYX dry-out heat flux testing with different bed thicknesses. Part II. Homogenous and stratified tests with 600 mm and 400 mm test beds. Research Report BTUO74-051381, VTT Technical Research Centre of Finland.
- Hovi, V. (2008). *Calculations of Boiling Two-Phase Flow Using a Porous Media Model*. Master's thesis. Lappeenranta University of Technology.
- Hovi, V. (2012). New PORFLO version with unstructured mesh and parallelization. Technical Report VTT-R-01143-12, VTT Technical Research Centre of Finland.
- Hu, K. and Theofanous, T. (1991). On the measurement and mechanism of dryout in volumetrically heated coarse particle beds. *International Journal of Multiphase Flow*, 17.
- Huhtiniemi, I. and Magallon, D. (2001). Insight into steam explosions with corium melts in KROTOS. *Nuclear Engineering and Design*, 204:391–400.
- IAEA (2006). Thermophysical properties database of materials for light water reactors and heavy water reactors. Final report of a coordinated research project 1999–2005. IAEA-TECDOC-1496, International Atomic Energy Agency.
- IAEA (2011). Mitigation of Hydrogen Hazards in Severe Accidents in Nuclear Power Plants. Technical Report IAEA-TECDOC-1661, International Atomic Energy Agency.

- Iivonen, M., Hovi, V., and Taivassalo, V. (2014). 3D Core Thermal Hydraulics with the PORFLO Code - Turbulence Modeling and Porous Medium with Porosity Steps. In *22nd International Conference on Nuclear Engineering. July 7–11, 2014, Prague, Czech Republic*, number ICONE22-30731.
- Imura, S. and Takegoshi, E. (1974). Effect of Gas Pressure on the Effective Thermal Conductivity of Pack Beds. *Heat Transfer Japanese Research*, 3(4).
- Karbojian, A., Ma, W., Kudinov, P., and Dinh, T. (2009). A scoping study of debris bed formation in the DEFOR test facility. *Nuclear Engineering and Design*, 239:1653–1659.
- Kato, M., Nagasaka, H., Vasilyev, Y., Kolodeshnikov, A., and Zhdanov, V. (1999). Fuel coolant interaction tests under ex-vessel conditions. In *Proceedings of the OECD Workshop on Ex-vessel Debris Coolability, November 15–18, 1999, Karlsruhe, Germany*.
- Kleinhans, M., Markies, H., S.J. de Vet, S., in 't Veld, A., and Postema, F. (2011). Static and dynamic angles of repose in loose granular materials under reduced gravity. *Journal of Geophysical Research: Planets*, 116.
- Kokkonen, I. (2004). Permeability measurements for STYX-5 experiment. Technical Report TERMO-305, Fortum Nuclear Services Ltd.
- Konovalikhin, M. J. (2001). *Investigations on Melt Spreading and Coolability in a LWR Severe Accident*. Royal Institute of Technology. PhD thesis.
- Kudinov, P., Karbojian, A., Ma, W., and Dinh, T. (2010). The DEFOR-S experimental study of debris formation with corium simulant materials. *Nuclear Technology*, 170:219–230.
- Kudinov, P., Karbojian, A., Tran, C.-T., and Villanueva, W. (2013). Agglomeration and size distribution of debris in DEFOR-Experiments with Bi<sub>2</sub>O<sub>3</sub>–WO<sub>3</sub> corium simulant. *Nuclear Engineering and Design*, 263:284–295.
- Kudinov, P., Konovalenko, A., Grishchenko, D., Yakush, S., Basso, S., Lubchenko, N., and Karbojian, A. (2014). Analysis of Debris Bed Formation, Spreading, Coolability, and Steam Explosion in Nordic BWRs. Final Report from the NKS-R DE-COSE activity. NKS-317, Nordic Nuclear Safety Research.
- Lage, J. (1998). The fundamental theory of flow through permeable media from Darcy to turbulence. In Ingham, D. B. and Pop, I., editors, *Transport Phenomena in Porous Media*, Elsevier Science. Pergamon, 1st edition. ISBN-0-08-042843-6.
- Lamarsh, J. R. (1983). *Introduction to Nuclear Engineering*. Addison-Wesley Publishing Company, 2nd edition. ISBN 0-201-14200-7.
- Lee, K. and Ryley, D. (1968). The evaporation of water droplets in superheated steam. *Journal of Heat Transfer*, pages 445–451.

## REFERENCES

- Leppänen, J., Hovi, V., Ikonen, T., Kurki, J., Pusa, M., Valtavirta, V., and Viitanen, T. (2015). The Numerical Multi-Physics project (NUMPS) at VTT Technical Research Centre of Finland. *Annals of Nuclear Energy*, 84:55–62.
- Li, L. and Ma, W. (2011). Experimental characterization of the effective particle diameter of a particulate bed packed with multi-diameter spheres. *Nuclear Engineering and Design*, 241:1736–1745.
- Li, L., Ma, W., and Thakre, S. (2012). An experimental study on pressure drop and dryout heat flux of two-phase flow in packed beds of multi-sized and irregular particles. *Nuclear Engineering and Design*, 242:369–378.
- Lienhard, J. (2012). *A Heat Transfer Textbook*. Phlogiston Press, Cambridge, Massachusetts, USA, 4th edition.
- Lindholm, I., Holmström, S., Miettinen, J., Lestinen, V., Hyvärinen, J., Pankakoski, P., and Sjövall, H. (2006). Dryout heat flux experiments with deep heterogeneous particle bed. *Nuclear Engineering and Design*, 236:2060–2074.
- Lipinski, R. (1982). A Model for Boiling and Dryout in Particle Beds. Technical Report NUREG/CR-2646, SAND82-0765, US Nuclear Regulatory Commission.
- Lipinski, R. (1984). A coolability model for postaccident nuclear reactor debris. *Nuclear Technology*, 65:53–66.
- Magallon, D. (2006). Characteristics of corium debris bed generated in large-scale fuel-coolant interaction experiments. *Nuclear Engineering and Design*, 236:1998–2009.
- Magallon, D. and Huhtiniemi, I. (2001). Corium melt quenching tests at low pressure and subcooled water in FARO. *Nuclear Engineering and Design*, 204:369–376.
- Malvern (2015). Mastersizer 3000. <http://www.malvern.com/en/products/product-range/mastersizer-range/mastersizer-3000/default.aspx>. Retrieved on 29 April 2015.
- Miyazaki, K., Murai, K., Ohama, T., Yamaoka, N., and Inoue, S. (1986). Dryout Heat Flux for Core Debris Bed. *Nuclear Science and Technology*, 23:702–710.
- Patankar, S. (1980). *Numerical Heat Transfer and Fluid Flow*. Number ISBN 0-89116-552-3. Hemisphere Publishing Corporation, New York.
- Pohlman, N., Severson, B., Ottino, J. M., and Lueptow, R. (2006). Surface roughness effects in granular matter: Influence on angle of repose and the absence of segregation. *Physical Review E: Statistical, Nonlinear, and Soft Matter Physics*, 73(031304).
- Pohlner, G., Buck, M., Meignen, R., Kudinov, P., Ma, W., Polidoro, F., and Takasuo, E. (2014). Analyses on ex-vessel debris formation and coolability in SARNET frame. *Annals of Nuclear Energy*, 74:50–57.

- Rahman, S. (2013). *Coolability of Corium Debris under Severe Accident Conditions in Light Water Reactors*. PhD thesis, Insitut für Kernenergetik und Energiesysteme, University of Stuttgart. IKE 2-155.
- Ranz, W. and Marshall, W. (1952). Evaporation from drops. *Chemical Engineering Progress*, 48:141–146.
- Rashid, M., Chen, Y., Kulenovic, R., and Laurien, E. (2008). Experiments on the coolability of a volumetrically heated particle bed with irregularly shaped particles. In *7th International Meeting on Nuclear Reactor Thermal Hydraulics Operation and Safety, NUTHOS-7, Seoul, Korea, October 5–9, 2008*.
- Rashid, M., Kulenovic, R., and Laurien, E. (2012). Experimental results on the coolability of a debris bed with down comer configurations. *Nuclear Engineering and Design*, 249:104–110.
- Rashid, M., Kulenovic, R., Laurien, E., and Nayak, A. (2011). Experimental results on the coolability of a debris bed with multidimensional cooling effects. *Nuclear Engineering and Design*, 241:4537–4543.
- Reed, A. (1982). *The effect of channeling on the dryout of heated particulate beds immersed in a liquid pool*. Massachusetts Institute of Technology. PhD thesis.
- Repetto, G., Garcin, T., Eymery, S., and Fichot, F. (2011). Experimental program on debris reflooding (PEARL) – Results on PRELUDE facility. *Nuclear Engineering and Design*, 264:176–186.
- Rivard, J. (1978). Debris bed studies and experiments at Sandia. Technical Report SAND78-0299, Sandia National Laboratories.
- Rohsenow, W. (1952). A method of correlating heat transfer data for surface boiling of liquids. *Transactions of the ASME*, 74:969–976.
- Schiller, L. and Naumann, Z. (1935). A drag coefficient correlation. *Zeitschrift des Vereines Deutscher Ingenieur*, 77:318–325.
- Schmidt, W. (2004). *Influence of Multidimensionality and Interfacial Friction on the Coolability of Fragmented Corium*. Number IKE 2 - 149. PhD Thesis. Institut für Kernenergetik und Energiesysteme, University of Stuttgart.
- Schulenberg, T. and Müller, U. (1986). A refined model for the coolability of core debris with flow entry from the bottom. In *Proceedings of the Sixth Information Exchange Meeting on Debris Coolability. EPRI NP-4455. Los Angeles, March 1986*.
- Sehgal, B. R. (2012). *Nuclear Safety in Light Water Reactors. Severe Accident Phenomenology*. Number ISBN 978-0-12-388446-6. Elsevier.
- Song, C., Wang, P., and Makse, H. (2008). A phase diagram for jammed matter. *Nature*, 453:629–632.

## REFERENCES

- Song, J., Park, I., Shin, Y., Kim, J., Hong, S., Min, B., and Kim., H. (2003). Fuel coolant interaction experiments in TROI using a UO<sub>2</sub>/ZrO<sub>2</sub> mixture. *Nuclear Engineering and Design*, 222:1–15.
- Spencer, B., Wang, K., Blomquist, C., McUmbler, L., and Schneider, J. (1994). Fragmentation and Quench Behaviour of Corium Melt Streams in Water. Technical Report NUREG/CR-6133, ANL-93/32, US Nuclear Regulatory Commission.
- Squarer, D., Pieczynski, A. T., and Hochreiter, L. E. (1982). Effect of debris bed pressure, particle size and distribution on degraded nuclear reactor core coolant. *Nuclear Science and Engineering*, 80:2–13.
- Takasuo, E. (2013). Debris coolability simulations with different particle materials and comparisons to COOLOCE experiments. Research Report VTT-R-00257-13, VTT Technical Research Centre of Finland.
- Takasuo, E., Holmström, S., Hovi, V., Rahman, S., Bürger, M., Buck, M., and Pohlner, G. (2012a). Experimental and Computational Studies of the Coolability of Heap-like and Cylindrical Debris Beds. In *5th European Review Meeting on Severe Accident Research (ERMSAR-2012)*, Cologne, Germany, March 21–23, 2012.
- Takasuo, E., Hovi, V., and Ilvonen, M. (2011a). PORFLO modelling of the coolability of porous particle beds. Research Report VTT-R-09376-10, VTT Technical Research Centre of Finland.
- Takasuo, E., Kinnunen, T., and Holmström, S. (2012b). COOLOCE particle bed coolability experiments with a cylindrical test bed: Test series 8–9. Research Report VTT-R-07224-12, VTT Technical Research Centre of Finland.
- Takasuo, E., Kinnunen, T., Holmström, S., and Lehtikuusi, T. (2013a). COOLOCE coolability experiments with a cylindrical debris bed and lateral flooding: COOLOCE-10. Research Report VTT-R-0463-13, VTT Technical Research Centre of Finland.
- Takasuo, E., Kinnunen, T., Holmström, S., and Lehtikuusi, T. (2013b). COOLOCE debris bed coolability experiments with an agglomerate simulant: Test series 11. Research Report VTT-R-03316-13, VTT Technical Research Centre of Finland.
- Takasuo, E., Kinnunen, T., and Lehtikuusi, T. (2013c). COOLOCE-12 debris bed coolability experiment: Cone on a cylindrical base. Research Report VTT-R-07967-13, VTT Technical Research Centre of Finland.
- Takasuo, E., Kinnunen, T., Pankakoski, P. H., and Holmström, S. (2011b). The COOLOCE particle bed coolability experiments with a conical geometry: Test series 6 and 7. Research Report VTT-R-07097-11, VTT Technical Research Centre of Finland.

- Takasuo, E., Kinnunen, T., Pankakoski, P. H., and Holmström, S. (2011c). The COOLOCE particle bed coolability experiments with a cylindrical test bed: Test series 3-5. Research Report VTT-R-07099-11, VTT Technical Research Centre of Finland.
- Takasuo, E., Taivassalo, V., and Hovi, V. (2014). A study on the coolability of debris bed geometry variations using 2D and 3D models. Research Report VTT-R-00676-14, VTT Technical Research Centre of Finland.
- Takasuo, E., Taivassalo, V., Kinnunen, T., and Lehtikuusi, T. (2015). Coolability analyses of heap-shaped debris bed. Research Report VTT-R-00367-15, VTT Technical Research Centre of Finland.
- Thakre, S., Li, L., and Ma, W. (2014). An experimental study on coolability of a particulate bed with radial stratification or triangular shape. *Nuclear Engineering and Design*, 276:54–63.
- Thakre, S., Ma, W., Kudinov, P., and Bechta, S. (2013). Study on Effective Particle Diameters and Coolability of Particulate Beds Packed with Irregular Multi-size Particles. NKS-DECOSE Report-2/2012. NKS-288, Nordic Nuclear Safety Research.
- Theofanous, T. and Saito, M. (1981). An assessment of class 9 (core-melt) accidents for PWR dry-containment systems. *Nuclear Engineering and Design*, 66:301–332.
- Trenberth, R. and Stevens, G. (1980). An experimental study of boiling heat transfer and dryout in heated particulate beds. Technical report, UKAEA Atomic Energy Establishment, Winfrith.
- Tung, V. and Dhir, V. (1988). A Hydrodynamic Model for Two-Phase Flow through Porous Media. *International Journal of Multiphase Flow*, 14:47–65.
- Tutu, N., Ginsberg, T., and Chen, J. (1984). Interfacial drag for two-phase flow through high permeability porous beds. *Journal of Heat Transfer*, 106:865–870.
- TVO (2008). Nuclear power plant units Olkiluoto 1 and Olkiluoto 2. Eura Print.
- U.S. Atomic Energy Commission (1957). Theoretical Possibilities and Consequences of Major Accidents in Large Nuclear Power Plants. USAEC Report WASH-740.
- U.S. Nuclear Regulatory Commission (1975). Reactor Safety Study. An Assessment of Accident Risks in U.S. Commercial Nuclear Power Plants. WASH-1400, NUREG-75/014, USNRC.
- van Dosselaere, J.-P. and Paci, S. (2014). ERMSAR2013 conference of the SARNET network. *Annals of Nuclear Energy*, 74:1–3.
- Vortmeyer, D. (1978). Radiation in Packed Solids. In *6th International Heat Transfer Conference, Toronto, Canada*.

## REFERENCES

- Wallis, G. B. (1969). *One-dimensional Two-phase Flow*. McGraw-Hill Book Company.
- Wilcox, D. C. (2006). *Turbulence Modeling for CFD. Second edition*. DCW Industries.
- Yakush, S. and Kudinov, P. (2014). A model for prediction of maximum post-dryout temperature in decay-heated debris bed. In *22nd International Conference on Nuclear Engineering. July 7-11, 2014, Prague, Czech Republic*, number ICONE22-31214.
- Yakush, S., Kudinov, P., and Lubchenko, N. (2013). Coolability of heat-releasing debris bed. Part 2: Uncertainty of dryout heat flux. *Annals of Nuclear Energy*, 52:72–79.
- Yakush, S., Lubchenko, N., and Kudinov, P. (2012). Risk-Informed Approach to Debris Bed Coolability Issue. In *20th International Conference on Nuclear Engineering collocated with the ASME 2012 Power Conference. July 30–August 3, 2012, Anaheim, California, USA*, number ICONE20POWER2012-55186.
- Yang, W.-C., editor (2003). *Handbook of Fluidization and Fluid-Particle Systems*. Marcel Dekker.
- Zeisberger, A. and Mayinger, F. (2006). Heat transport and void fraction in granulated debris. *Nuclear Engineering and Design*, 236:2117–2123.
- Zhang, B., Harada, T., Hirahara, D., Matsumoto, T., Morita, K., Fukuda, K., Yamano, H., Suzuki, T., and Tobita, Y. (2011). Experimental investigation on self-leveling behavior in debris beds. *Nuclear Engineering and Design*, 241.

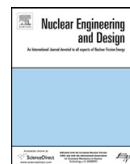
PUBLICATION I

**The effect of lateral flooding  
on the coolability of  
irregular core debris beds**

Nuclear Engineering and Design (241), 1196–1205.

Copyright 2011 Elsevier B.V.

Reprinted with permission from the publisher.



## The effect of lateral flooding on the coolability of irregular core debris beds

Eveliina Takasuo\*, Stefan Holmström, Tuomo Kinnunen, Pekka H. Pankakoski, Ensio Hosio, Ilona Lindholm

VTT Technical Research Centre of Finland, Finland

### ARTICLE INFO

#### Article history:

Received 27 January 2010

Received in revised form 23 April 2010

Accepted 26 April 2010

### ABSTRACT

The coolability of ex-vessel core debris is an important issue in the severe accident management strategy of, e.g. the Nordic boiling water reactors. In a core melt accident, the molten core material is expected to discharge into the containment and form a porous debris bed on the pedestal floor of a flooded lower drywell. The debris bed generates decay heat which must be removed by boiling in order to stabilize the debris bed and to prevent local dryout and possible re-melting of the material. The STYX test facility which consists of a cylindrical bed of irregular alumina particles has been used to investigate the effect of lateral coolant inflow on the dryout heat flux of the particle bed. The lateral flow was achieved by downcomers attached on the sides of the test rig. The downcomers provide coolant into the lower region of the bed by natural circulation. Both homogenous and stratified bed configurations have been examined. It was observed that the dryout heat flux is increased by 22–25% for the homogenous test bed compared to the case with no lateral flooding. For the stratified configuration with a fine particle layer on top of the bed, no significant increase in the dryout heat flux was observed. The experiments have been analyzed by using the MEWA-2D code. Models which include explicit consideration of gas–liquid friction were used in the calculations in order to realistically capture the lateral flow configuration.

© 2010 Elsevier B.V. All rights reserved.

### 1. Introduction

The flooding of the lower drywell of the reactor containment is a key part of severe accident management strategy at the Finnish boiling water reactors at Olkiluoto. If the reactor pressure vessel fails during an accident, the molten core material is discharged from the pressure vessel into a deep water pool in the lower drywell. The corium is fragmented during the discharge into the water and it is expected to form a porous particle bed on the pedestal floor of the drywell. On the other hand, coolability of a porous bed in the lower head of the pressure vessel is an important issue for reactor types in which the accident management relies on in-vessel melt retention. In both ex-vessel and in-vessel cases, the decay heat has to be removed from the solidified bed in order to thermally stabilize the material and prevent possible re-melting. In these cases, the heat removal is based on boiling and replacing the evaporated liquid from the surrounding pool so that cooling water is available in the bed interior (i.e. the bed is in a coolable condition).

The coolability of porous beds consisting of irregular particles has been studied at VTT within the frame of the STYX test programme. The first STYX tests were conducted in 2001 and the latest

in 2008 (Lindholm et al., 2006; Holmström et al., 2008). In the tests, the objective is to measure the dryout power (surface heat flux) which leads to a local dryout within the porous bed. The test bed consists of relatively small irregular alumina particles arranged in a cylindrical configuration that is 30 cm in diameter and has a height of 60 cm in the basic test configuration. The particle size distribution was originally chosen on the basis of various experiments investigating the debris bed formation (Lindholm et al., 2006). The bed depth and the pressure range at which the tests were conducted characterize the conditions expected at the Olkiluoto containments during a severe accident. The decay heat is simulated by resistance heating.

The effects of particle size stratification, particle bed height and pressure on the dryout heat flux were studied in the test series 1–9. These tests address evenly distributed beds with top flooding configuration in which the counter-current flow limitation (CCFL) restricts water flow into the bed interior at a point when a high enough vapor flux is generated by the heated particle bed. However, in realistic accident scenarios the debris bed, which is the result of a complex fragmentation process, might not be evenly distributed on the pedestal floor of the containment. Instead, according to recent experiments investigating the bed formation, a heap-like geometry with high porosity which allows coolant inflows from the sides of the bed is a possible configuration (Kudinov et al., 2007; Karbojian et al., 2007). Usually, the steam flux generated in the bed before reaching a point in which the access of liquid is locally prevented is significantly higher for bottom or lateral flooding cases in

\* Corresponding author at: VTT Technical Research Centre of Finland, PO Box 1000, 02044 VTT, Espoo, Finland. Tel.: +358 20 722 5015; fax: +358 20 722 5000.  
E-mail address: [eveliina.takasuo@vtt.fi](mailto:eveliina.takasuo@vtt.fi) (E. Takasuo).

### Nomenclature

$e$	specific internal energy (J/kg)
$F$	volumetric drag force (N/m <sup>3</sup> )
$h$	specific enthalpy (J/kg)
$j$	superficial velocity (m/s)
$k$	heat conductivity (W/mK)
$K$	permeability (m <sup>2</sup> )
$K_r$	relative permeability
$p$	pressure (Pa)
$Q$	volumetric heat flux (W/m <sup>3</sup> )
$T$	temperature (K)

### Greek symbols

$\alpha$	void fraction
$\Gamma$	phase change rate (kg/m <sup>2</sup> /s)
$\varepsilon$	porosity
$\mu$	viscosity (Pa s)
$\eta$	passability (m)
$\eta_r$	relative passability
$\rho$	density (kg/m <sup>3</sup> )

### Subscripts

$g$	gas
$i$	interface
$l$	liquid
$p$	particle (solid)
$sat$	saturated

### Superscript

$eff$	effective
-------	-----------

which co-current flows of steam and water are possible. This results in increased dryout power and improved coolability compared to cases with top flooding only (Schmidt, 2004; Bürger et al., 2006).

In the present study, the focus is on the test series STYX 10–13 in which the effect of lateral flooding on the dryout behavior was investigated. The lateral coolant inflow was achieved by using three downcomer tubes that connect the water pool above the test bed to inlets near the bottom of the test rig (Holmström et al., 2008). In this configuration, the top surface is also open for liquid infiltration which means that, here, lateral flow (or combined lateral and top flooding) refers to an additional inflow that is imposed on the STYX set-up. The lateral flow is driven by a type of natural circulation induced by the heat generation.

Both homogenous and vertically stratified beds have been studied using the STYX facility. The stratified bed represents the outcome of a scenario in which very fine particles have been formed as a result of fuel-coolant interactions. The fine particles are settled on top of the bed. The particle size stratification reduces coolability because of increased particle-fluid friction in the fine layer and capillary forces that tend to hold liquid in the fine layer preventing water from infiltrating the main bed below.

Various analytical and numerical methods exist to predict the dryout heat flux ranging from simple empirical correlations to models that take into account the complex multi-dimensional nature of the two-phase flow. Previous studies (e.g. Lindholm et al., 2006) show that correlations such as the one formulated by Theofanous and Saito (1981) and simple models such as the zero-dimensional model by Lipinski (1982) are capable of predicting the dryout heat flux under top flooding conditions with good accuracy. In order to capture the effect of the lateral flooding provided by the downcomers, these approaches are not adequate, and multi-dimensional analysis is required. The severe accident analysis code MEWA-2D

developed at the IKE institute at Stuttgart University, Germany, has been utilized in analyzing the lateral flooding tests. The solution method in MEWA-2D is based on well-known approaches for simulating porous media (Bürger et al., 2006). The simulations aim at evaluating the capability of the code to reproduce the measured dryout heat fluxes and identifying the possible mechanisms behind the differences in the behavior of the experimental and simulated debris beds.

## 2. The STYX experiments

The main components of the STYX test rig are the feed water system including a feed water tank, a pump and a pre-heater, the pressure vessel, the test bed with the heating elements, a steam line, a condenser and the process control and measurement systems. The principal measured test parameters are temperature, pressure, and the input power of the heating elements. The heating arrangement consists of resistance wire elements that are distributed within the 600 mm test bed in nine horizontal levels, at 67 mm distance from each other. The lowest level is located 33 mm from the bottom of the test bed and the topmost level is 33 mm below the top surface of the bed. There are ten thermocouple levels located between the heating element levels. In order to determine the dryout location accurately in the horizontal direction, each of the levels contains four to eight sensors. In addition, thermocouples are placed on the inner and outer pressure vessel walls and in the water reservoir above the bed. Two pressure gauges are used: one for pressure control and one for pressure monitoring. A water level gauge controls the water level on top of the test bed. The schematic of the particle bed inside the pressure vessel with the heating element and thermocouple levels is illustrated in Fig. 1. Fig. 2 shows the inner cylinder with the 8 mm downcomer tubes connected to its sides.

The total power of the heating elements is recorded from a calibrated three-phase power meter. The inputs to the device are

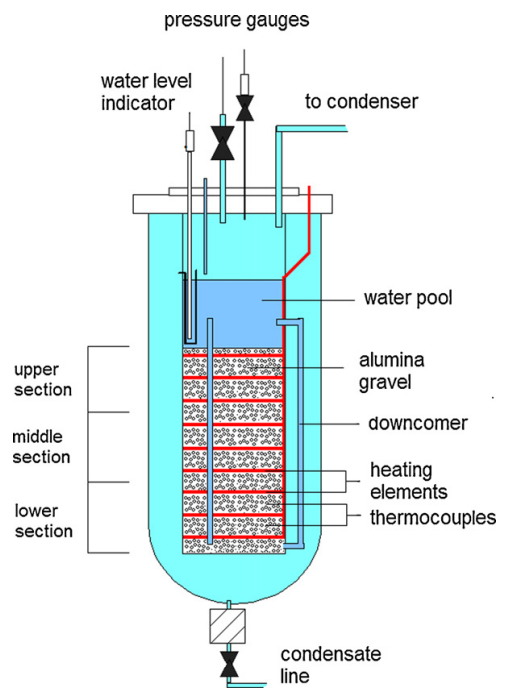


Fig. 1. The schematic of the STYX particle bed inside the pressure vessel.



Fig. 2. The inner cylinder of the test rig including the 8 mm downcomer tubes.

the line voltages and currents. The currents are measured with measurement transformers that are incorporated in the calibration set-up and the voltages are measured directly from each phase. The dryout power values are read from the power meter at the time of power increment, and the mean power values are calculated from online data.

Prior to each experiment, the test bed is heated up so that steady-state saturated conditions at the respective pressure are reached. After this, dryout power is searched by stepwise increases of the heating power. The magnitude of the power increments is selected depending on the experiment. The maximum accuracy of the power control is approximately 1 kW. A nominal holding time of 25 min is applied between the power increments to allow time for the dryout development after the critical power level has been exceeded. A dryout is considered to be reached in a location where the temperature sensor reading is 5 °C higher than the saturation temperature at the actual pressure. This temperature margin is used to eliminate possible false dryout indications due to fluctuations in the pressure and sensor offsets. It was found during

the start-up phase of the STYX programme when different holding times were tested that 25 min is adequately long for detecting dryout considering the accuracies of the power values and the locations of temperature increase. A longer waiting time would only reveal power differences smaller than 1 kW. Typically, a power step of 2 kW is adequate to reach 5–10% accuracy in the dryout power.

An important difference in the STYX set-up compared to a realistic corium bed is the local heating configuration. The decay heat in corium is generated in the whole volume of the debris bed but in the test set-up the power profile is discontinuous in the axial direction. Alumina gravel has low heat conductivity, and the conduction within the gravel bed between the heating element levels is not expected to be very effective. However, it is expected that steam that is generated near the heating wires is evenly distributed into the gravel-filled space between the heater levels. Thus, it is also assumed that the void profile in the bed with a constant power level approximates the profile in a bed with uniform volumetric heating with reasonable accuracy. In the previous studies by Lindholm et al. (2006) it was concluded that the test set-up is valid for coolability investigations based on the agreements of the measured dryout heat flux and location (for homogenous beds) with the predictions by the Lipinski's models. Also, scoping calculations using MEWA-2D suggest that local heating results in locally higher temperatures but this has no notable effect on the dryout heat flux.

### 2.1. Lateral flooding test series

The experiments including lateral flooding consist of four separate test series (Holmström et al., 2008). The downcomer test matrix and the reference cases without downcomers are presented in Table 1. In the first tests, STYX-10, three downcomer tubes of 5 mm inner diameter installed at 120° divisions were used. The STYX-11 tests were performed with plugged downcomers for the purpose of verifying that the new test results were comparable to the older ones, and that no changes had occurred in the bed properties during storage and transportation that was done during the installation work of the downcomer tubes. It was found that the previous tests were fully comparable to the new tests. In the test series STYX-12 and STYX-13, the inner diameter of the downcomers was increased to 8 mm. The STYX-10, STYX-11 and STYX-12 test series were conducted with a stratified bed and the STYX-13 with a homogenous test bed. Thus, the STYX-11 test series serves as reference to the STYX-10 and -12 tests. The STYX-13 series is compared to the data obtained from the STYX-8 tests in which the 600 mm homogenous bed without downcomers was investigated (Holmström et al., 2005).

In addition, measurements of water volume flow through the downcomers to an unheated bed were conducted after the experiments in order to verify that each downcomer was open and thus could maintain the lateral flooding. The total capacities of the downcomers measured this way were 92 ml/s for the 8 mm tubes and 35 ml/s for the 5 mm tubes with a level difference of 900 mm. It was observed that one of the three 5 mm downcomers was partially blocked with a flow rate of about 40% of the other 5 mm downcomers. The rest of the 5 mm and 8 mm downcomers performed normally. For the 8 mm tubes, an additional wire net was used at the

Table 1

The dryout heat flux experiments with and without downcomers.

Test code	Bed height and type	Pressure [bar]	Downcomer diameter [mm]
STYX-8	600 mm homogenous	2, 5, 7	–
STYX-10	600 mm with 60 mm stratification layer	2, 5, 7	5
STYX-11	600 mm with 60 mm stratification layer	2, 5, 7	–
STYX-12	600 mm with 60 mm stratification layer	2, 5, 7	8
STYX-13	600 mm homogenous	2, 5, 7	8

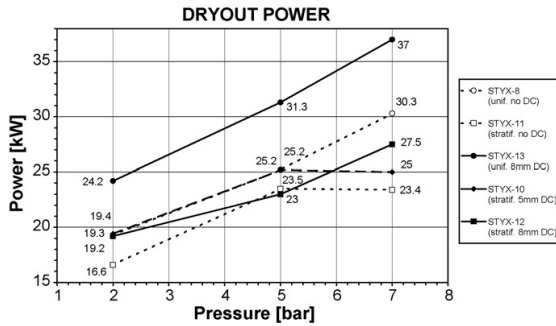


Fig. 3. The measured dryout power in the stratified and homogenous particle beds with and without downcomers.

downcomer bottom connections to further ensure that the alumina gravel would not block the downcomer inlets.

The size range of the particles in the homogenous bed is 0.25–10 mm with the mass-averaged diameter of 3.46 mm. However, single-phase flow-through measurements of the bed material have revealed that the effective hydrodynamic particle diameter is only 0.8 mm according to the Ergun equation. In the fine stratification layer the particle diameter range is 0.25–0.4 mm. The porosity of the bed is between 0.34 and 0.37 which was estimated from particle samples and flooding the bed with water (Lindholm et al., 2006). The pressure levels at which the tests were conducted were 2 bar, 5 bar and 7 bar which is a representative range of the containment pressure expected during a severe accident.

## 2.2. Lateral flooding results

The measured dryout power values for the stratified bed and the homogenous bed with the 5 mm and 8 mm downcomers and the comparison to the cases with no downcomers are presented in Fig. 3. In the homogenous test bed (STYX-13), a clear and consistent effect of the lateral flooding is seen. The measured dryout power for the cases with the 8 mm downcomers is 22–25% greater than that of top flooding only for all the pressure levels. The maximum dryout power, 37 kW, is obtained for the 7 bar case. The corresponding heat flux, obtained by dividing the test bed bottom (top) surface area by dryout power, is 523 kW/m<sup>2</sup>.

Dryout was first observed near the top of the bed at 533 mm level in the STYX-13 tests. In the homogenous bed experiment without downcomers (STYX-8), dryout occurred in the lowermost

parts of the 60-cm-deep test bed. These observations are in accordance with theoretical expectations and earlier results concerning the development of saturation distribution in the bed (Hofmann, 1987; Schmidt, 2004). Counter-current flow limitation restricts the coolant inflow via the top surface in top flooding conditions. In the combination of top and lateral flooding present in the STYX-13 tests, it may be assumed that co-current flow of water and steam is formed at least in parts of the bed interior. In the co-current mode, dryout results after a high enough steam flux has been generated to fill the pore volume in the particle bed cross-section which is likely to occur in the top sections of the test bed, provided that the dryout power is only slightly exceeded. Thus, the location of the initial dryout is transferred to the topmost parts of the bed and overall coolability is increased compared to the tests with top flooding only. However, the location is more complicated to predict in the present case of combined top and lateral flooding as will be explained in Section 3.1.1. The dryout locations are summarized in Table 2 along with the dryout heat fluxes that correspond the measured dryout power values in Fig. 3. The division of the test bed depth to different sections for dryout location analysis is indicated in Fig. 1.

The increase of dryout power for the stratified bed as compared to the cases with no downcomers was rather small, and the results are not as consistent as in the homogenous cases. The 2 bar tests in STYX-10 and STYX-12 series show 16–17% increase in the dryout power compared to STYX-11. At 5 bar pressure, STYX-10 shows a 10% increase and STYX-12 with the larger capacity, a small decrease. In the 7 bar experiment using the larger capacity downcomers (STYX-12), an increase of 18% was seen while, for the smaller capacity downcomers (STYX-10), the increase remained below 10%. The relative magnitude of the power increments in the experiments was 5–20%. An increment of 5% was applied in the 7 bar test which indicates that the observed 18% increase in dryout power is reliable but, for the other experiments, the dryout power differences compared to the tests with no lateral flooding are of the same order as the uncertainty.

The stratified bed experiments show variable dryout locations. In the STYX-10 tests, dryout was observed in the middle section of the test bed. With the larger capacity downcomers, a dryout was first seen near the lowermost levels and at the 267 mm level. It is also seen that in the stratified bed the dryout power is 10–30% lower than in the homogenous bed by comparing the cases STYX-11 and STYX-8, and STYX-12 and STYX-13. Additionally, it appears that the coolability benefit obtained from a higher pressure level could be partially lost in the presence of the stratification layer. Earlier experiments show a similar trend with a 40-cm-deep test bed (Holmström et al., 2005). The reason to this curious behavior is beyond the scope of the present analysis.

Table 2

The measured dryout heat fluxes and the locations of the incipient dryout from the particle bed bottom (i.e. the height of the thermocouple level that first indicated dryout).

Test code	Pressure [bar]	Experimental dryout heat flux [kW/m <sup>2</sup> ]	Experimental dryout location [mm]
STYX-8	2	273	
	5	357	133 (lower section)
	7	429	
STYX-10	2	274	200 (lower section)
	5	357	267 (middle section)
	7	354	400 (middle section)
STYX-11	2	235	
	5	332	133 (lower section)
	7	331	267 (middle section)
STYX-12	2	275	17 (bottommost sensor level)
	5	325	
	7	389	267 (middle section)
STYX-13	2	342	
	5	443	
	7	523	533 (upper section)

### 3. Modeling of the downcomer tests

The MEWA-2D code is developed as a module in the German integral severe accident code ATHLET-CD. Here, a stand-alone application for analyzing the particle bed behavior is used. The code includes a 2D porous media model which solves the momentum and mass conservation equations for the fluid phases and the energy equation for the liquid, gas and solid phases (Bürger et al., 2006). The fluid flow is governed by friction between the three phases, buoyancy and pressure gradient. The conservation equations of mass, momentum and energy for the gas and liquid phases are of the following form:

$$\frac{\partial}{\partial t} \varepsilon \alpha \rho_g + \nabla \rho_g \vec{j}_g = \Gamma \quad (1)$$

$$\frac{\partial}{\partial t} \varepsilon (1 - \alpha) \rho_l + \nabla \rho_l \vec{j}_l = -\Gamma \quad (2)$$

$$-\nabla p_g = \rho_g \vec{g} + \frac{\vec{F}_{pg}}{\varepsilon \alpha} + \frac{\vec{F}_i}{\varepsilon \alpha} \quad (3)$$

$$-\nabla p_l = \rho_l \vec{g} + \frac{\vec{F}_{pl}}{\varepsilon (1 - \alpha)} + \frac{\vec{F}_i}{\varepsilon (1 - \alpha)} \quad (4)$$

$$\frac{\partial}{\partial t} \varepsilon \alpha \rho_g e_g + \nabla (\rho_g \vec{j}_g h_g) = \nabla (k_g^{\text{eff}} \nabla T_g) + Q_{p,g} - Q_{g,\text{sat}} + \Gamma h_{g,\text{sat}} \quad (5)$$

$$\frac{\partial}{\partial t} \varepsilon (1 - \alpha) \rho_l e_l + \nabla (\rho_l \vec{j}_l h_l) = \nabla (k_l^{\text{eff}} \nabla T_l) + Q_{p,l} - Q_{l,\text{sat}} - \Gamma h_{l,\text{sat}} \quad (6)$$

The indices  $s$ ,  $l$  and  $g$  denote the solid, liquid and gas phases. Porosity is denoted by  $\varepsilon$ ,  $j$  is superficial velocity and  $\alpha$  is the gas fraction in the pores (void). The source term  $\Gamma$  in the mass conservation equations, Eqs. (1) and (2), is the liquid evaporation (condensation) rate. The friction forces  $\vec{F}$  in the momentum equations, Eqs. (3) and (4), are determined according to friction models most of which are based on well-known approaches for estimating pressure loss in porous media. The classical Ergun model is extended to treat the two-phase flow by using relative permeability  $K_r$  and passability  $\eta_r$ . The forces  $\vec{F}$  without an explicit consideration of the gas–liquid friction are

$$\vec{F}_{pg} = \varepsilon \alpha \left( \frac{\mu_g}{KK_{rg}} \vec{j}_g + \frac{\rho_g}{\eta \eta_{rg}} \cdot |\vec{j}_g| \vec{j}_g \right) \quad (7)$$

$$K_{rg} = \alpha^n, \quad \eta_{rg} = \alpha^m$$

$$\vec{F}_{pl} = \varepsilon (1 - \alpha) \left( \frac{\mu_l}{KK_{rl}} \vec{j}_l + \frac{\rho_l}{\eta \eta_{rl}} \cdot |\vec{j}_l| \vec{j}_l \right) \quad (8)$$

$$K_{rl} = (1 - \alpha)^n, \quad \eta_{rl} = (1 - \alpha)^m$$

According to the Reed friction model,  $n$  and  $m$  are taken to be 3 and 5, respectively. The parameters  $K$  and  $\eta$  are single-phase permeability and passability. The Reed model is applied in simulating the experiments in which the downcomers were not active. It is well-established, e.g. by Tutu et al. (1984) that an explicit model of gas–liquid drag is required to predict the pressure gradient inside the boiling bed correctly and to capture the effect of multi-dimensional flow on coolability. For this purpose, the modified Tung and Dhir (1988) friction model is used in modeling the lateral flooding tests including the downcomer flow loop. This approach contains separate expressions for the relative permeability and passability for the flow regimes of bubbly, slug and annular flow. Compared to the original model, the flow regime boundaries have been adjusted in the modified model to better fit for small particles sizes (<5.8 mm). Details of the original model can be found in Tung and Dhir (1988) and for the modifications, see Schmidt (2004).

Heat transfer in the porous configuration is dominated by boiling in the steady-state coolable conditions in which the generated

decay heat is transferred directly to the phase change. A transient that disturbs the steady-state saturation distribution results when the dryout heat flux is exceeded. The boil-off of liquid in the bed interior will lead to local or global dryout, and the decrease of saturation near to zero means that convection from solid to gas plays a slightly increased role in the overall heat transfer process. The steam mass flux is reduced correspondingly to the expansion of the dried-out zones. Here, however, the focus is on the pre-dryout phase. Also, conduction inside the solid matrix does not usually limit heat transfer from the particulate material.

The evaporation rate is calculated by the sum of the heat fluxes  $Q$  directed at the interface of gas and liquid divided by the latent heat of evaporation:

$$\Gamma = \frac{Q_{s,\text{sat}} + Q_{g,\text{sat}} + Q_{l,\text{sat}}}{h_{g,\text{sat}} - h_{l,\text{sat}}} \quad (9)$$

The boiling curve model in MEWA-2D takes into account the regimes of pool boiling and film boiling and the transition between the two modes. The Rohsenow correlation is used for pool boiling up to the critical heat flux and the Lienhard correlation for film boiling.

A simple 2D cylindrical grid is generated for each calculation case. A grid size of  $38 \times 131$  is used for the homogenous bed and  $38 \times 144$  for the stratified bed in the reference calculation set-up. Because the 2D modeling does not allow a detailed representation of the downcomer tubes, they are scaled to the computational domain and the capacity of the tubes is adjusted by particle size, porosity and downcomer size. The outer radial cells in the grid are used for the downcomers and the wall area that separates the downcomer from the particle bed. (These areas are seen in the model of Fig. 8.) Because the simplified form of the momentum equations is based on the friction forces between the three phases, the flow resistance in the tubes as well as in other volumes that contain single-phase fluid and no particles, has to be set up by means of the porous medium parameters (i.e. particle size and porosity). The discretization is done by a finite volume method. An approach similar to the SIMPLE algorithm is used for solving the system of equations. The solution time step size is controlled by the code depending on the convergence criteria given in the code input.

For the homogenous particle bed, the effective particle diameter of 0.8 mm and porosity of 0.37 are applied as a reference set-up in the calculations. The analysis presented by Lindholm et al. (2006) as well as more recent scoping calculations show that the results obtained by this choice of parameters are in good agreement with the experimental results. In the fine particle layer, a diameter of 0.4 mm is assumed. The homogenous part of the stratified bed below the fine particle layer has the same properties as the “normal” homogenous bed. The transition from 0.8 mm to 0.4 mm is done using a specific cell zone with a gradual decrease of particle size to avoid numerical problems deriving from too sharp changes in the cell properties. In the reference set-up, capillary pressure is not taken into account. Heat generation is taken to be uniform inside the solid material.

#### 3.1. Simulation results

In general, the simulated dryout heat fluxes for homogenous particle beds are in good agreement with the experimental ones. The comparison of the dryout power in the experiments and the calculations without downcomers is presented in Fig. 4. The corresponding comparison for the downcomer cases is seen in Fig. 5. The dryout heat fluxes and the locations of the incipient dryout in the simulations are presented in Table 3.

For the stratified bed cases, the simulations show underestimated dryout power. The calculated dryout power is approximately 50% of the measured power. This result may be explained by dif-

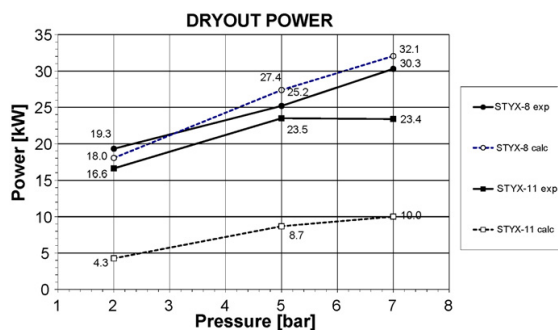


Fig. 4. The experimental and calculated dryout power for the stratified and homogeneous particle beds without downcomers (top flooding only).

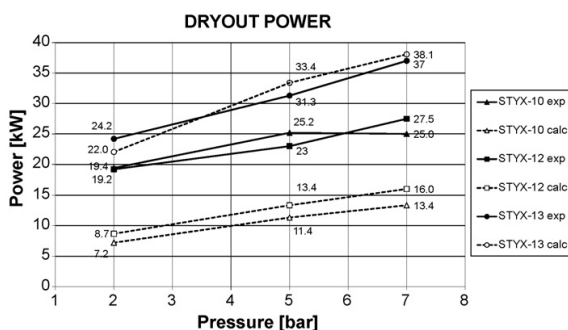


Fig. 5. The experimental and calculated dryout power for the stratified and homogeneous particle beds including downcomers (combined top and lateral flooding).

ferences in the simulated and experimental conditions: A stable 6 mm layer of fine particles is assumed to stay on top of the particle bed throughout the simulations. In this case, the decrease of particle size effectively increases friction, thus hindering water from infiltrating through the fine layer into the coarser “main” particle bed and preventing steam from escaping the bed interior. During the experiment, the fine particles most likely started to float in the steam flow which is not taken into account in the simulations. This “fluidization” allows steam to escape through the top fine layer with

Table 3

The calculated dryout heat fluxes and the approximate axial locations of the incipient dryout from the bottom of the particle bed in the simulations.

Test code	Pressure [bar]	Simulated dryout heat flux [kW/m <sup>2</sup> ]	Simulated dryout location [mm]
STYX-8	2	255	
	5	387	30 (in the bottom)
	7	454	
STYX-10	2	102	
	5	161	540 (upper section)
	7	189	
STYX-11	2	60	
	5	123	150 (lower section)
	7	142	
STYX-12	2	123	
	5	189	520 (upper section)
	7	227	
STYX-13	2	312	
	5	473	300 (middle section)
	7	539	

significantly less frictional resistance than with a stable stratification layer, resulting in a higher dryout heat flux. The fluidization can be treated as a reduction in the effective thickness of the fine particle layer.

The capillary effect that, in the case of stratified beds, tends to hold liquid in the fine particle layer is not considered in the results. Parameter variations show that the bed tolerates even less heating power before reaching dryout if the pressure difference between the phases is accounted for, the power being the order of 10–15% of the measured power. The validity of this simulation result is supported by experiments that showed a significant reduction in the dryout heat flux in the presence of horizontal phase boundaries (Hofmann and Barleon, 1986). This presumes that the boundary is stable and does not involve instabilities such as the floating particles in the STYX tests.

### 3.1.1. Analysis of the saturation development

The difference in the calculated flow patterns between the lateral and top flooding cases as well as between the stratified and homogeneous cases during the pre-dryout transient is distinguished in the development of the saturation profiles. During the experiments, it was not possible to measure the saturation (or void fraction) inside the gravel bed. The detailed flow patterns inside the bed during the process that leads to dryout are not known. Nevertheless, it is of interest to examine the simulated saturation profiles and compare the calculated dryout locations to the experimental ones. Equivalent dryout powers and locations in both cases would strongly indicate that the main features of the experiments and the simulations are similar, and no significant disturbance is caused by, e.g. the local heating method of the test facility.

The vertical saturation profiles for the four different flow configurations at different simulation times from the onset of the transient to the incipient dryout are shown in Fig. 6. The saturation values are taken from the radial position of 0.75 cm near the axis of the particle bed. The figures represent conditions at 5 bar pressure. The saturation development, however, is similar in all the simulation cases with similar flooding arrangement, independently of the ambient pressure. The simplest case is the homogeneous bed with top flooding only which is illustrated in Fig. 6(a). In this case, dryout is reached near the bottom of the test bed after a development during which the liquid reservoir in the bed evaporates and the point of minimum saturation progresses downwards inside the bed cross-section in an essentially one-dimensional configuration. Saturation first decreases in the top section due to liquid flow lower in the bed interior.

The stratified bed case with top flooding only is seen in Fig. 6(b). Again, the flow configuration is one-dimensional (i.e. no fluid flow is expected in the radial direction). Unlike to the homogeneous case, the transient is characterized by a rapid formation of a low-saturation zone below the fine layer due to the flow resistance of the fine layer that causes steam to accumulate just below the layer boundary. This zone is then transferred downwards until dryout is reached near the bottom of the computational domain in a rather similar manner as in the homogeneous case. Due to the reduced boiling steam mass flux in the low-saturation zone, liquid from above infiltrates these areas which causes the progress towards dryout to gradually slow down as seen in Fig. 6(a) and (b).

Fig. 6(c) and (d) shows the saturation profiles in the two test beds with lateral flooding achieved by the 8 mm downcomers. In the homogeneous case, Fig. 6(c), dryout is reached in the middle section of the test bed. The exact location of dryout is dependent on the coolant mass flow available through the downcomers. The flow through the top surface tends to move the incipient dryout towards the bottom while the lateral bottom flow opposes this effect, resulting in a “downcomer-specific” dryout location in the centre section of the particle bed. Sensitivity studies reveal that if the flow resis-

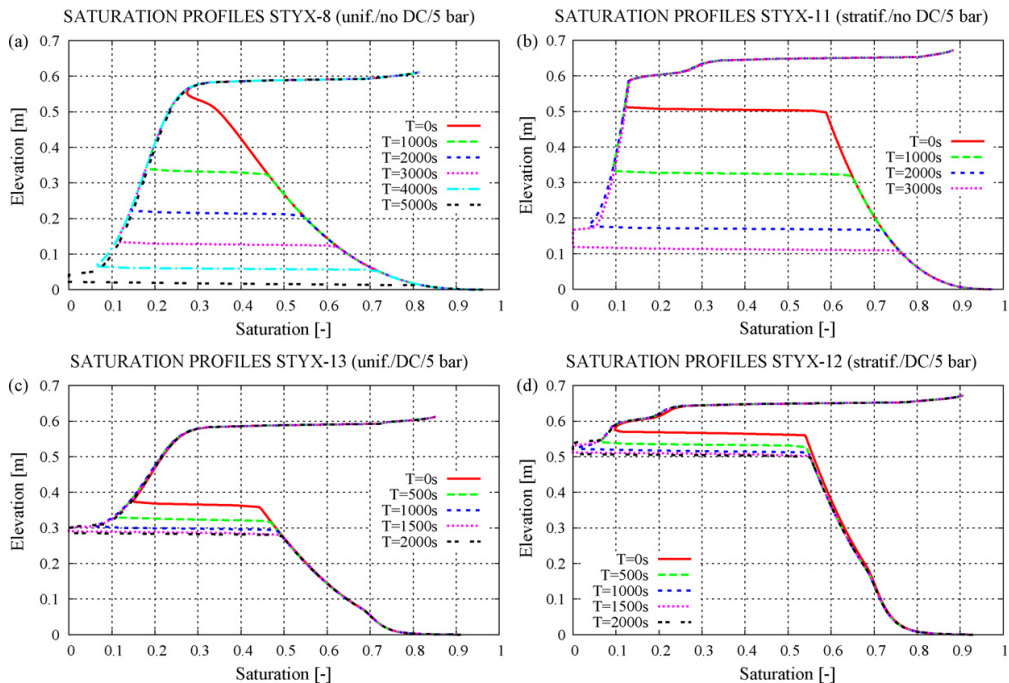


**Fig. 6.** Saturation profiles during the boil-off transient leading to dryout with 1000 s or 500 s time intervals: (a) STYX-8 with homogenous bed and top flooding, (b) STYX-11 with stratified bed and top flooding, (c) STYX-13 with homogenous bed and combined top and lateral flooding and (d) STYX-12 with stratified bed and combined top and lateral flooding. The dryout power levels are given in Figs. 4 and 5.

tance in the downcomer model is changed in such a way that the capacity of the downcomer is increased to a value where the maximum coolability benefit is reached, the incipient dryout is transferred to the topmost section of the bed. This development is demonstrated in Fig. 7(a). The corresponding particle temperature field in the end of the simulation ( $T = 10,000$  s) is presented in Fig. 7(b). In this case, the steady-state downcomer flow rate is higher than in the 8 mm downcomer base case by a ratio of 2.5.

The most complex flow conditions can be found in the STYX-12 series in Fig. 6(d) in which the flow field is modified by both the effect of the stratification layer and the inflow provided by the downcomers. However, the onset of dryout near the top of the bed can be rather well rationalized. The formation of the low-saturation, high steam content zone in the upper section caused by the fine layer (and the steam generation accordingly to the constant heating power) makes this zone prone to dryout when, simultaneously, the bottom section is fed with water which ensures coolant availability in the lowermost sections. This prevents the saturation minimum from moving deeper in the bed while steam is accumulating with an upwards increasing concentration. Then, a dryout results similarly as in co-current flow conditions. The 5 mm downcomer case (STYX-10) is a variation of the same flow configuration with a smaller downcomer to top flow ratio than with the 8 mm downcomers. Thus, no separate analysis is conducted for that case.

In summary, the general saturation profile development in the different simulation cases is in accordance with theoretical knowledge of the dryout behavior of porous beds. Comparing the predicted dryout locations in Fig. 6 and Table 3 to the experimental locations given in Table 2, the following observations are made:

- In the case of homogenous particle bed with top flooding only (STYX-8), the experimental and calculated dryout heat fluxes and

locations are in good agreement. This implies that also the overall dryout developments are similar.

- In the case of stratified particle bed and top flooding only (STYX-11), the calculated dryout locations are in agreement with the experimental locations but the calculated dryout heat fluxes are underestimated due to the high frictional resistance in the stable fine particle layer as explained in the previous section. The presence of the fine layer has no significant effect on the dryout location in case the dryout heat flux is just exceeded, and no lateral flows are present.
- In the case of homogenous particle bed including lateral flooding (STYX-13) the calculated dryout heat fluxes are in good agreement with those of experiments but the calculations predict incipient dryout in the middle of the bed, instead of upper section. The reasons for dryout location shifting towards the bed surface may be increased lateral flooding compared to top flooding and/or an exceeded power value from the actual dryout power level. The discrepancy in locations is a curious observation but, taking into account the limited knowledge of the particle bed behavior during the test and possible inaccuracy in the experimentally detected dryout location, it is not possible to detect the exact cause of this small inconsistency.
- In the case of stratified particle bed including lateral flooding (STYX-12 and STYX-10), the calculated and experimental dryout heat fluxes and locations do not agree. Dryout heat fluxes are greater in the experiments and dryout occurs in the lower or middle section of the bed similarly as in the stratified bed with no downcomers in STYX-11, instead of the simulated upper section. Dryout in the lower section in the experiments is probably caused by the unstable fine layer: there is no boundary below which steam would accumulate. The location is also a possible indication of very limited downcomer flow.

(a) SATURATION PROFILES STYX-13 (unif./DC variation/5 bar)

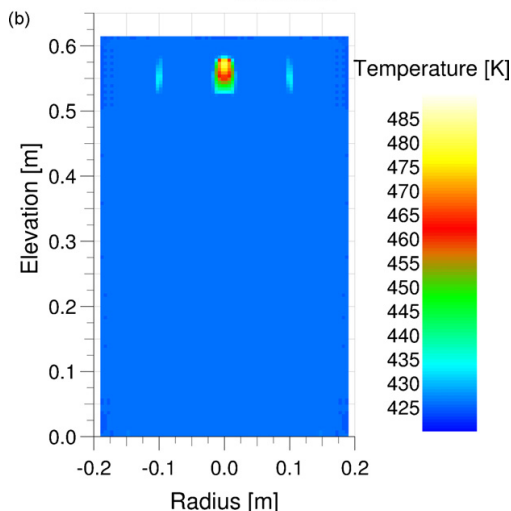
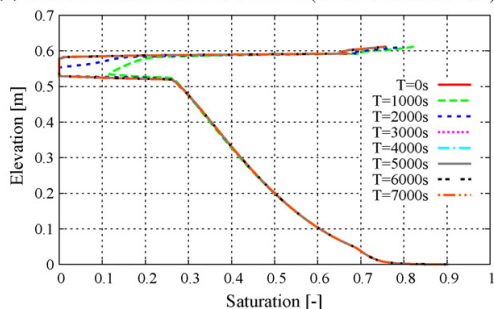


Fig. 7. A homogenous particle bed simulation with maximum lateral flooding rate obtained by varying the downcomer flow resistance: (a) saturation profile development and (b) temperature field graph at  $T=10,000$  s.

Based on the simulation results, transfer of the dryout location to the upper section can be considered to be a clear indication of the effect of the downcomers, independently whether the configuration is stratified or not. Especially, the systematically observed lower or middle section dryout in the stratified particle beds of STYX-10 and STYX-12 clearly indicates that the performance of the downcomers was questionable in the experimental conditions. This is in agreement with the main result of the stratified bed experiments: very small difference in the dryout power between the downcomer cases and top flooding only.

3.1.2. Post-dryout conditions

An example of post-dryout saturation in the STYX-12 case (stratified bed with the 8 mm downcomers) at 5 bar pressure is illustrated in Fig. 8(a). The solid temperature at the corresponding simulation time is shown in Fig. 8(b). A relatively large zero-saturation area has been developed below the fine particle layer. The dryout starts at the height of approximately 52 cm as seen in Fig. 6(d). No boiling occurs at the particle surface in the dried-out area from which heat is transferred by convection from solid to the gas phase, and the particle temperature has increased from the saturation temperature up to about 250 °C. The condition depicted in the figures is transient, i.e. the temperature is increasing and the dried-out zone still continues to grow. Post-dryout transient conditions are observed in all the cases simulating the experiments with the downcomer tubes of 5 mm and 8 mm. An exception to this is the situation represented by the simulation case in Fig. 7. With the increased downcomer capacity, dryout first occurs in the top section of the particle bed but, unlike in the other simulations, the zero-saturation zone quickly stabilizes between the 50 cm and 60 cm level in the bed. In addition, it is located near the central axis of the grid, showing a clear two-dimensional behavior. This is in contrast to the case in Fig. 8 and the other cases in which the dryout is nearly global (covers the full cross-section of the bed) even in the downcomer cases. The post-dryout development is not included in detail in the current analysis but the simulation results lead to the following preliminary conclusions:

- In the case of 5 mm and 8 mm downcomers, the solid temperature may increase unlimitedly as the heat-up of the zero-saturation zone is not stabilized by coolant infiltration.

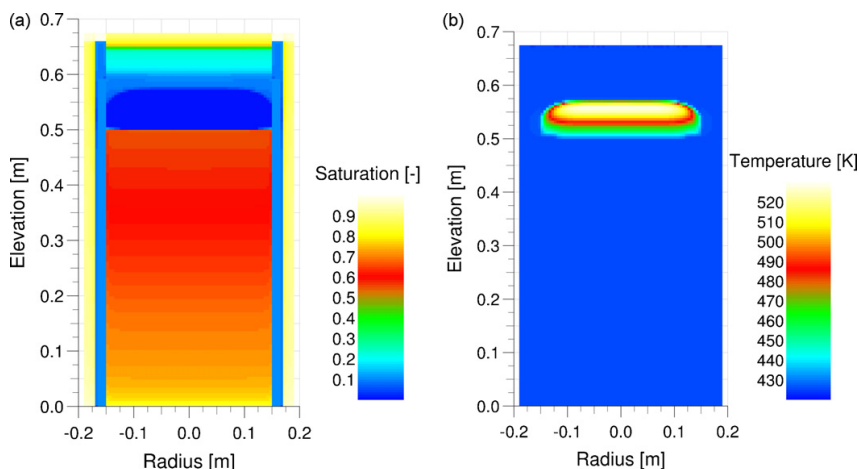


Fig. 8. (a) Liquid saturation and (b) solid temperature field approximately 4000 s after the initial dryout in the stratified bed with the 8 mm downcomers (STYX-12). The outer cell columns (radius > 0.15 m) seen in (a) represent the downcomers and the impermeable wall between the downcomer area and the particle bed.

- The increase of downcomer capacity enhances the contribution of the lateral flooding to the overall flow configuration so that the expansion of the dryout zone and the temperature excursion is restricted to a level clearly below the re-melting temperature which provides additional coolability benefits.

#### 4. Discussion

Several experiments including lateral flooding with and without a stratification layer of fine particles on top of the porous bed have been performed, and the experimental results are compared to simulation results given by a 2D porous media model. Next, the experimental configuration is evaluated from the point of view of realistic reactor scenarios and the significance of the simulation results is summarized.

##### 4.1. Power plant scenario considerations

Based on the early STYX experiments 1–3, it was estimated that the homogenous particle bed would maintain coolable conditions under the decay heat flux expected in the case of Olkiluoto containment at pressure above 2 bar (Lindholm et al., 2006). In the present configuration, the coolability margin in the combined top and lateral flooding would be improved by a modest 22–25%. It is important to note that this result is specific to the used geometry, particle size and downcomer configuration and might be further improved by using larger capacity downcomers. It is also expected that a bed consisting of larger particles would show a more pronounced “downcomer effect” because of greater effect of gas–liquid friction in the pores of the bed. The original STYX geometry without downcomers is a conservative design in the sense that only top flooding is allowed. The current tests including downcomers serve as scoping studies of the effect of lateral flooding in a bed that consists of irregularly shaped particles and as such they do not represent a general reactor scenario.

One of the main open questions in the research area is the representativeness of the experimental set-ups for reactor scenarios. The properties of the solidified debris depend on the bed formation process which is difficult to predict. Experiments in the DEFOR programme suggest that debris porosity may be as high as 60–70% in some cases and that the particle bed may be highly non-homogenous (Kudinov et al., 2007; Karbojian et al., 2007). On the other hand, numerical studies suggest that even “micro-inhomogeneities” that do not contribute to the average properties of the debris can have a significant effect on the overall coolability (Ma and Dinh, 2010). In this light, the cylindrical geometry and the 37% porosity of the STYX facility are not representative. In order to investigate the effect of bed geometry and to extend the current investigations concerning multi-dimensional flows, experiments involving a heap-like particle bed are planned at VTT in the future.

##### 4.2. Remarks on experimental and simulation results

The presented MEWA-2D results show that the main features of the effect of downcomers in the homogenous test bed are captured in the calculations even though the two-dimensional model is not capable of simulating possible three-dimensional effects in the test configuration. The effect of the fine layer appears a more challenging question since there is no experimental data of the extent of the fluidization. The dislocation of the fine surface particles due to floating was verified in post-test visual inspections of the test bed and predicted by scoping calculations already in the earliest experiments. Due to the floating, the measured dryout power in the stratified particle bed was 20–30% lower than in the homogenous bed in the early STYX test series 1–3 which was a smaller difference than expected (Lindholm et al., 2006). In the new tests, similar results were obtained. This difference is larger in

the MEWA-2D results because, similarly as in the simpler models used by Lindholm et al. (2006), the model does not take the floating particles into account and under-predicts dryout power.

The stratified bed experiments including downcomers show somewhat inconsistent results, and no clear increase in the dryout power compared to the experiments without downcomers is seen, except at 7 bar pressure with the 8 mm downcomer tubes. In the simulations, the presence of stratification layer promotes flow through the downcomers. An increase in the dryout heat flux by the ratio of 1.5–2 is seen between the stratified cases without and with downcomers (STYX-11 and STYX-12 in Table 3). In addition to the under-predicted dryout power, this is another major discrepancy between the experiments and calculations. In the stratified bed experiments, the combination of the effects caused by the fine layer and lateral flooding which both include significant uncertainties (the fluidization and possible local effects of the downcomers and heating elements) is not reproduced in the simulations. Thus, the simulations provide only a limited insight into the role of lateral flooding in the stratified particle bed experiments.

Finally, it should be noticed that the magnitude of the power increment has an effect on the dryout location. In case the measured power exceeds the exact dryout power (to some extent, this is the case in all the tests since it is not possible to reach the exact value experimentally) the location differs from the location that corresponds to the power level at which the dryout is just reached. This difference depends on the deviance from the actual dryout power. It is important that the power increments during the tests are kept small enough and the waiting time long enough to obtain accurate values for the dryout power and location. In this study, the uncertainty related to the power increments, i.e. the difference between the coolable and dryout power levels was within 5–10% in most of the tests. The corresponding accuracy in the simulations, the “window” between the two power levels, was taken to be 4–8%.

#### 5. Conclusions

The effect of lateral bottom flooding on the coolability of irregular core debris beds has been investigated using the STYX test facility. For this purpose, three downcomer tubes with the inner diameters of 5 mm and 8 mm have been installed on the outside of the cylindrical test bed that consist of irregularly shaped and sized alumina particles. Compared to the tests without downcomers, the lateral flooding in connection with simultaneous top flooding increased the dryout heat flux and the coolability by 22–25% for a homogeneously distributed test bed. For a stratified bed, which contains a layer of very fine particles on top of the coarse main bed, no significant improvement in coolability was observed in the present conditions using the relatively small downcomers.

The tests were simulated using a porous media model with explicit consideration of gas–liquid friction incorporated into the MEWA-2D severe accident simulation code. The simulation results of the homogenous particle bed are in good agreement with the test results. More deviation from the test results is seen in the simulations of the stratified beds in which the flow configuration is more complex due to floating fine particles that are not taken into account in the modeling. This leads to overly conservative predictions of dryout power by the code. Issues still to be resolved in future studies are the behavior of the fine layer and its modeling, as well as selecting a representative particle bed based on predictions of the type of debris configurations that may be formed in realistic accident scenarios.

#### Acknowledgments

The STYX tests and analysis have been conducted within the framework of the SAFIR2010 Finnish National Research Programme

on Nuclear Power Plant Safety. The support received from the European Union Project SARNET-2 is gratefully acknowledged.

## References

- Bürger, M., Buck, M., Schmidt, W., Widmann, W., 2006. Validation and application of the WABE code: investigations of constitutive laws and 2D effects on debris coolability. *Nuclear Engineering and Design* 236, 2164–2188.
- Hofmann, G., 1987. Dryout in very deep particulate beds. *Nuclear Engineering and Design* 99, 177–185.
- Hofmann, G., Barleon, L., 1986. Reduced coolability of particle beds as a result of capillary effects at horizontal phase boundaries. In: *International ANS/ENS Topical Meeting on Thermal Reactor Safety*, San Diego, CA, USA, February 1986.
- Holmström, S., Kinnunen, T., Pankakoski, P., Hosio, E., December 2008. STYX dry-out heat flux testing with lateral coolant inflow. In: *Research Report, VTT-R-06910-08*. VTT Technical Research Centre of Finland.
- Holmström, S., Pankakoski, P., Hosio, E., 2005. STYX dry-out heat flux testing with different test bed thicknesses. Part II. Homogenous and stratified tests with 600 mm and 400 mm test beds. In: *Research Report, BTU074-051381*. VTT Technical Research Centre of Finland.
- Karbojian, A., Ma, W., Kudinov, P., Davydov, M., Dinh, T.N., 2007. A scoping study of debris formation in DEFOR experimental facility. In: *Proceedings of the 15th International Conference on Nuclear Engineering*, Nagoya, Japan, April 22–26, 2007, ICONE15-10620.
- Kudinov, P., Karbojian, A., Ma, W., Davydov, M., Dinh, T.N., 2007. A study of ex-vessel debris formation in a LWR severe accident. In: *Proceedings of ICAPP 2007*, Nice, France, May 13–18, 2007, Paper 7512.
- Lindholm, I., Holmström, S., Miettinen, J., Lestinen, V., Hyvärinen, J., Pankakoski, P., Sjövall, H., 2006. Dryout heat flux experiments with deep heterogeneous particle bed. *Nuclear Engineering and Design* 236, 2060–2074.
- Lipinski, R.J., 1982. A Model for Boiling and Dryout in Particle Beds, NUREG/CR-2646, SAND82-0765. US Nuclear Regulatory Committee.
- Ma, W., Dinh, T.-N., 2010. The effect of debris bed's prototypical characteristics on corium coolability in a LWR severe accident. *Nuclear Engineering and Design* 240, 598–608.
- Schmidt, W., 2004. Influence of Multidimensionality and Interfacial Friction on the Coolability of Fragmented Corium. Doctoral Thesis. Institut für Kernenergetik und Energiesysteme, Universität Stuttgart.
- Theofanous, T.G., Saito, M., 1981. An assessment of class 9 (core-melt) accidents for PWR dry-containment systems. *Nuclear Engineering and Design* 66, 301–332.
- Tung, V.X., Dhir, V.K., 1988. A hydrodynamic model for two-phase flow through porous media. *International Journal of Multiphase Flow* 14 (1), 47–65.
- Tutu, N., Ginsberg, T., Chen, J., 1984. Interfacial drag for two-phase flow through high permeability porous beds. *Journal of Heat Transfer* 106, 865–870.

PUBLICATION II

**The COOLOCE experiments  
investigating the dryout power in  
debris beds of heap-like  
and cylindrical geometries**

Nuclear Engineering and Design (250), 687–700.

Copyright 2012 Elsevier B.V.

Reprinted with permission from the publisher.



## The COOLOCE experiments investigating the dryout power in debris beds of heap-like and cylindrical geometries

Eveliina Takasuo\*, Stefan Holmström, Tuomo Kinnunen, Pekka H. Pankakoski

VTT Technical Research Centre of Finland, P.O. Box 1000, 02044 VTT, Espoo, Finland

### HIGHLIGHTS

- We investigate the effect of geometry on the coolability of porous core debris beds.
- Dryout power is measured for a heap-like (conical) and a cylindrical debris bed.
- The coolability of the cylindrical bed is better due to the lower height of the configuration.

### ARTICLE INFO

#### Article history:

Received 13 January 2012

Received in revised form 22 May 2012

Accepted 5 June 2012

### ABSTRACT

The COOLOCE test facility has been used for experimental investigations of the coolability of porous core debris beds with different geometries. The main objective of the experiments was to compare the dryout behavior of conical (heap-like) and top-flooded cylindrical (evenly distributed) debris bed configurations in order to investigate the effect of geometry on the coolability of the debris bed. The experimental debris beds simulate the possible outcomes of melt discharge from the reactor pressure vessel and the formation of a core debris bed in a deep water pool during a severe accident. The results suggest that if the two debris bed configurations have equal height, the coolability of the conical bed is improved compared to the cylindrical bed due to the multi-dimensional infiltration of water through the surface of the cone. However, in case the conical and cylindrical debris beds have equal diameter and volume, the dryout power density of the conical configuration is lower than that of the cylindrical configuration by approximately 50%. This is due to the greater height of the conical configuration which leads to increased heat flux in the upper parts of the conical debris bed. According to the present results, the effect of the increased debris bed height is greater than the effect of multi-dimensional flooding. Simulations show the differences between the two-phase flow behavior of the two geometries, and the resulting difference in dryout development.

© 2012 Elsevier B.V. All rights reserved.

### 1. Introduction

At the Nordic boiling water reactors, the coolability of a core debris bed in the flooded lower drywell of the containment is an important issue in the severe accident management strategy. In the course of a core melt accident, corium is expected to be discharged from the reactor pressure vessel into a deep water pool in the lower drywell of the containment. Corium is fragmented and settles to the bottom of the pool as solidified particles to form a porous debris bed. Decay heat must be removed from the debris in order to prevent re-melting of the material and the resulting threat to the integrity of the containment structures. Boiling and water infiltration into the debris bed interior play key roles in the decay heat removal. Experimental studies that aim for the verification of

the debris coolability have focused on measuring the dryout heat flux, or power density, that results in the loss of coolant and dryout in the bed interior.

The effects of pressure, particle size stratification, particle bed depth and downcomers for cylindrical beds consisting of irregular particles have been examined at VTT in the STYX experiments (Lindholm et al., 2006, Takasuo et al., 2011). The basic experimental configuration was flooded through the top surface and it was based on the assumption that the debris bed is evenly distributed against the walls of the spreading area below the reactor pressure vessel, forming a layer of about 0.6 m in height. The diameter and the height of the STYX test bed were 0.3 and 0.6 m, respectively. The pressure range in the STYX experiments, 2–7 bar, characterized the conditions expected at the Finnish Olkiluoto 1 and 2 containments during a core melt accident.

In realistic accident scenarios, however, the debris bed may not be evenly distributed in the containment. Experimental data of the bed characteristics have been obtained from fuel-coolant

\* Corresponding author. Tel.: +358 20 722 5015; fax: +358 20 722 5000.  
E-mail address: [eveliina.takasuo@vtt.fi](mailto:eveliina.takasuo@vtt.fi) (E. Takasuo).

### Nomenclature

$a$	area (m <sup>2</sup> )
$h$	height (m)
$P$	power (W)
$q''$	heat flux (W/m <sup>2</sup> )
$q'''$	power density (volumetric heat flux) (W/m <sup>3</sup> )
$V$	volume (m <sup>3</sup> )

### Subscripts

c	comparison
exp	experimental
tot	total

interaction (FCI) studies with corium (Spencer et al., 1994; Magallon, 2006) and from the DEFOR program which focuses specifically on the debris bed formation and the underlying physical mechanisms that determine the debris bed properties (Karbojian et al., 2007; Kudinov et al., 2008). The studies suggest that irregular bed geometries with high porosity and complex particle morphology are possible. Multi-dimensional flooding of coolant is typical for debris beds with irregular geometry and non-homogenous internal structure. Here, we use “multi-dimensional flooding” to describe all modes of coolant infiltration driven by lateral pressure differences and not restricted to the horizontal top surface of the geometry, such as flooding through vertical surfaces and the combination of downcomers and top flooding which was applied in the latest STYX experiments. Multi-dimensional flooding tends to increase the dryout heat flux and improve coolability. For instance, increases up to twice the dryout heat flux of top-flooded configurations have been measured for bottom flooding (Hofmann, 1984; Rashid et al., 2011). Increases of 22–25% were measured in the STYX experiments with small downcomers that were used in addition to top flooding (Takasuo et al., 2011). These increases of dryout heat flux have been measured for a column of simulant particles with different downcomer set-ups to facilitate the bottom or lateral flooding. It is important to notice that a realistic debris bed geometry may be heap-like (conical) or mound-like, rather than cylindrical since the pouring of granular material – in this case, the solidified melt particles – onto a horizontal surface is expected to form a conical heap.

In order to investigate the effect of the bed geometry on dryout power and to explicitly compare conical and cylindrical geometries, a new test facility named COOLOCE (coolability of cone) was designed and built. The COOLOCE facility replaces the STYX facility and utilizes some of the components of the old facility, mainly the feed water and steam removal systems. The aim in the design was to create a well-controlled laboratory-scale test environment specifically for distinguishing the effect of the particle bed shape, taking into account the limitations of the existing power source and laboratory facilities. Series of experiments have been conducted with both conical and cylindrical debris beds.

An important goal of the work is to produce data useful for simulation code validation and development. The experimental data can be used to estimate the capabilities of codes to predict debris coolability in different reactor scenarios. In this paper, we present a brief comparison of the experimental and simulation results obtained by the MEWA 2D code (Bürger et al., 2006) to demonstrate the differences in the dryout process between the cylindrical and conical debris bed configurations. The comparison shows a reasonably good agreement between the experimental and simulation results. The progress of the extensive validation of the MEWA code against the experiments has been presented in Takasuo et al. (2012a). Also, preliminary 3D simulations of the two-phase flows in the debris bed

and the water pool using the PORFLO code have been performed (Hovi and Ilvonen, 2011; Takasuo et al., 2012a,b).

## 2. Problem definition

The two-phase flow configuration explains the improved coolability related to the multi-dimensional flooding in simple debris bed geometries. In a cylindrical top-flooded configuration, counter-current flow of water and steam is present. The limit of coolability in this kind of configuration is reached at a point when the vapor flux is high enough to prevent the liquid flow from reaching the bottom of the debris bed (counter-current flow limitation is met). In a configuration with multi-dimensional flooding, the water and steam flow is typically co-current. The limit for coolability is encountered when the vapor flux is high enough to replace water in an entire cross-section of the particle bed. The difference in the geometries and flow principles between top flooding (cylinder) and multi-dimensional flooding (cone) is illustrated in Fig. 1.

On the other hand, a heap-like debris bed which allows multi-dimensional flooding is higher than a cylindrical bed of the same volume and radius. This implies that, in order to exit from the debris bed, steam has to travel a longer distance in the bed interior near the center of the heap-like bed. In a geometry which has a uniform power generation (homogenous heating), the heat flux per cross-sectional area (W/m<sup>2</sup>) increases along with the height of the cross-section. Heat flux is the power generated by the volume below the examined cross-section divided by the area of the cross-section, which equals to the power density (W/m<sup>3</sup>) multiplied by the height of the cross-section. It follows that dryout is seen in the upper parts of geometries with multi-dimensional water infiltration. For geometries that are comparatively high, the conditions for the onset of dryout might be met at a lower power level than for top-flooded, flat-shaped geometries, regardless of the multi-dimensional flooding.

In the assessment of power plant scenarios, comparisons of these types of configurations are necessary because they take into account the spatial dimensions of the possible debris beds. In the case of Olkiluoto 1 and 2, the assumption that the debris is evenly distributed against the walls and has a conservative porosity (34–40%) results in a wide but a rather shallow cylinder. The height of the cylinder is approximately 0.6 m. If the same amount of debris settles in a conical configuration so that the bottom of the cone is spread against the walls of the drywell, i.e. covers the entire basemat of the spreading area, the cone is 1.8 m in height (three times higher than the cylinder). The present study aims to clarify how significant is the effect of multi-dimensional flooding compared to the effect of the debris bed height, and what is the significance to the overall coolability of the debris. We consider the formation of the first dry zone to be the coolability limit for both geometries. The post-dryout behavior is not studied even though it is expected that the multi-dimensional flooding may help to maintain comparatively low temperatures even after local dryout has occurred.

## 3. The experimental facility

The main components of the COOLOCE test facility are the pressure vessel that houses the particle bed section with its heating arrangement, the feed water system and the steam removal system. The schematic of the test facility (with the conical test bed) is presented in Fig. 2. The test vessel has a volume of 270 dm<sup>3</sup> with the outer diameter of 613 mm and a design pressure of 7 bar overpressure. The pressure vessel bottom plate with the full particle bed section can be removed for maintenance work, e.g. for changing the test bed configuration. The pressure vessel is equipped with

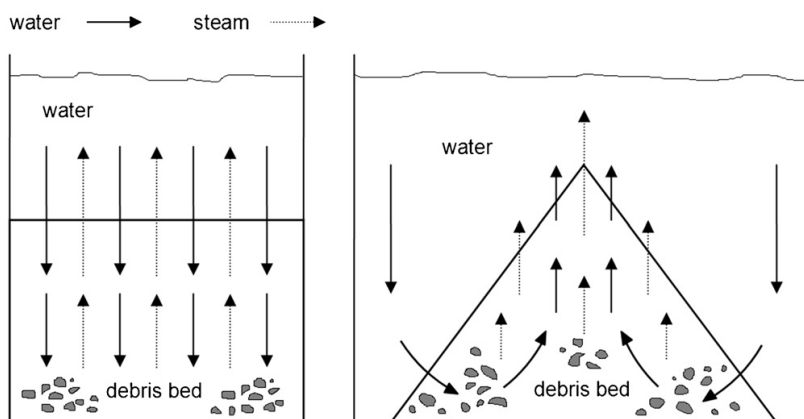


**Fig. 1.** The conceptual difference in the flow configuration between an evenly distributed cylindrical particle bed (left) and a heap-like particle bed (right) submerged in water. Solid and dashed lines indicate the directions of liquid and vapor flow, respectively.

sightglasses that can be used for visual observations of boiling in the fluid volume (by a video recorder). The decay heat is simulated by electrical resistance heaters arranged in a vertical configuration which aims for a volumetrically uniform power distribution within the test bed.

The determination of dryout time and location is done by thermocouples which are distributed between the heaters so that the full volume of the particle bed is covered. In pre-dryout conditions, the test facility is in saturated, or nearly saturated, state. A stable increase from the saturation temperature shown by one or more thermocouples during a test run indicates that dryout occurs in the bed interior. An increase of  $5^{\circ}\text{C}$  from the saturation temperature was systematically used as the dryout criterion in the STYX experiments. In the COOLOCE experiments, we have applied a more flexible criterion because it was found that the temperature readings are very stable in pre-dryout conditions at constant pressure. The increase of  $2\text{--}3^{\circ}\text{C}$  is already considered a good indication of dryout. However, in all the experiments selected for the comparison analysis (test series 3–5 and 6 and 7) in Section 4.1, dryout was indicated by a significant increase (typically more than  $50^{\circ}\text{C}$ ) from the saturation temperature which eliminates any question about the presence of dryout.

The test runs consist of series of stepwise power increases with a holding time of 20–30 min between each of the power increases. The holding time is necessary in order to see whether the particle bed stabilizes to a coolable steady-state or dryout is developed. Discussion of the sufficient length of the holding time for cylindrical test beds is found in Takasuo et al. (2011). (For the conical test bed, the time for the detection of dryout after exceeding the dryout power level is expected to be shorter due to different flow configuration but the same holding time is applied for both test beds.) The electrical heaters of the test bed are divided in three different groups according to electrical phase. The power of the facility is controlled by manually controlling the output voltage of a purpose-tailored power transformer with the maximum output of 63 kW. In practice, the maximum heating power of the arrangement is lower than the nominal outputs of the transformer and the heaters (about 50 kW). The power control has an accuracy of around 0.2 kW.

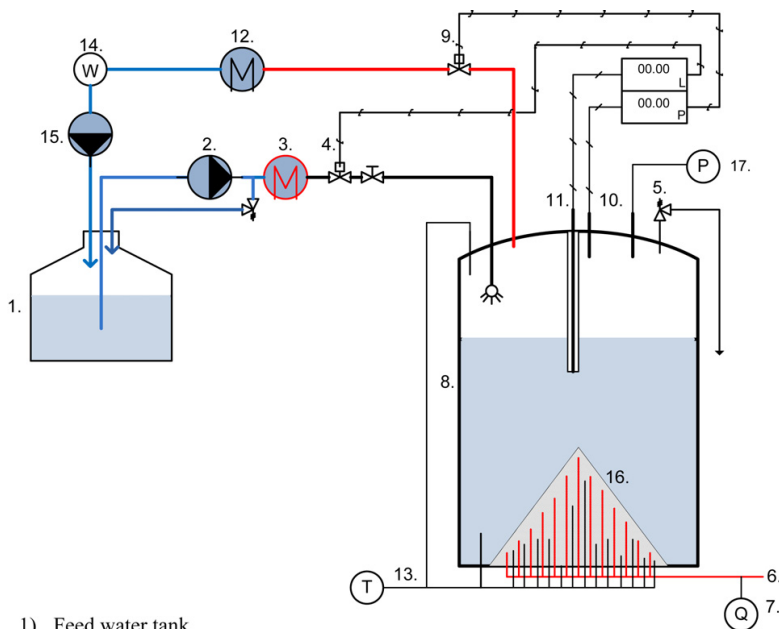
Each test sequence begins with a heat-up sequence during which the temperature of the test bed and the pool is increased to the saturation temperature. This is done by the test bed heaters at power levels clearly below the expected dryout power. The duration of the heat-up sequence is test-specific and depends on the

pressure of the experiment. During the experiments and the heat-up sequence, the feed water into the pressure vessel is pre-heated by a 3 kW pre-heater which is capable of increasing the feed water temperature to  $70\text{--}90^{\circ}\text{C}$ . As a result, the increase to saturation temperature has to be done by the particle bed heaters and a small amount of subcooled water is continuously mixed into the saturated water in the test vessel.

The steam is discharged from the pressure vessel to a condenser through a control valve which is also used for controlling the vessel pressure. The mass flow rate of the condensate is measured on-line by a scale that has the accuracy of 50 g. The power that is consumed by boiling is estimated by comparing the heating power (power output of the transformer) to the power calculated based on the mass flow rate measurements. The calculation assumes that the water which is collected to the scale per unit of time is equal to the mass flow evaporated by the heated test bed. We refer to the heating power as the *control power* and the power based on condensate mass flow measurements as the *calculated power*. Comparisons of the two power values are conducted mainly for verification purposes and to estimate the heat losses from the facility.

### 3.1. The conical debris bed

The heating arrangement of the conical particle bed consists of 137 purpose-tailored cartridge heaters of different lengths. The heaters have constant surface power density, i.e. the power of each heater depends on length. The nominal maximum power is 175 W for the shortest heater (45 mm heated length) and 950 W for the tallest heater (220 mm heated length). The total maximum power of the heaters is approximately 55 kW and they are divided into three different groups in such a way that the share of each group is 1/3 of the total power, yielding a practically uniform power distribution. The tallest heaters in the center of the conical bed are contained in one group with 29 heaters and the two other groups have 54 heaters each. The heaters are installed into the bottom plate of the pressure vessel into a “square mesh” in which the distance of the heaters from each other is 30 mm. The heaters ( $\varnothing 6\text{ mm}$ ) occupy about 2% of the volume of the conical bed. For dryout detection, there are 68 type K thermocouples installed between the heaters at different vertical positions. The distribution of the thermocouples takes into account that dryout is expected in the upper parts of the cone. One of the thermocouples near the center has multiple measuring points, i.e. the total number of measuring points in the test bed is 77.



- 1) Feed water tank
- 2) Feed water pump
- 3) Feed water pre-heater
- 4) Feed water control valve
- 5) Safety valve
- 6) Resistance heaters of the test bed
- 7) Power input and measurement
- 8) Pressure vessel
- 9) Steam line control valve (pressure control)
- 10) Pressure measurement (control)
- 11) Water level measurement (feed water control)
- 12) Condenser
- 13) Temperature measurements
- 14) Bench scale for condensate mass measurement
- 15) Water circulation pump
- 16) Test bed (conical)
- 17) Pressure measurement

Fig. 2. The schematic of the COOLOCE test facility.

The test debris bed ( $\varnothing 500$  mm) is composed of highly corrosion-resistant ceramic beads (zirconia/silica) with the diameter of 0.8–1.0 mm according to the manufacturer. An image analysis of a sample of the beads, however, suggests that the particles are slightly larger, 0.82–1.13 mm. The height of the test bed is 270 mm and it is held in conical shape by a wire net. The volume of the bed is approximately 17.5 l. The heating arrangement and the packing of the conical test bed with the spherical beads are shown in Fig. 3. It should be noticed that in a realistic debris bed, the particles are not constrained and dislocation of the particles may occur as well as leveling of the bed as a result of floating of the light particles in the steam flow that exits the bed. However, since the present study concerns the effects of a high, heap-like geometry of the porous bed and not the settling of realistic particles after the bed formation, it is necessary to prevent the particles from leaving the original configuration.

The conical test bed was modified after the first series of experiments because damage was observed in the central heaters in the dryout phase of the first experiments. The steel sheaths of

the central heaters were deteriorated causing the heater insulation to fail, apparently because of overtemperature and possible high-temperature corrosion caused by the steam-water environment. After the problem was detected, the central heaters of the conical set-up were replaced by heaters with Incoloy (Inconel alloy) outer sheaths. Three of the new central heaters were equipped with built-in thermocouples to monitor the heater sheath temperature. After the latest experiments, it was seen that the modifications did not completely remove the problem of possible overheating even though dryout was successfully measured for several pressure levels.

### 3.2. The cylindrical debris bed

The heating and sensor arrangement of the cylindrical test bed contains 69 heaters and 70 measuring points for temperature (20 measuring points in two multi-point thermocouples and 50 single-point thermocouples). Similarly to the conical bed and in order to approximate the decay heat generation, the heater arrangement

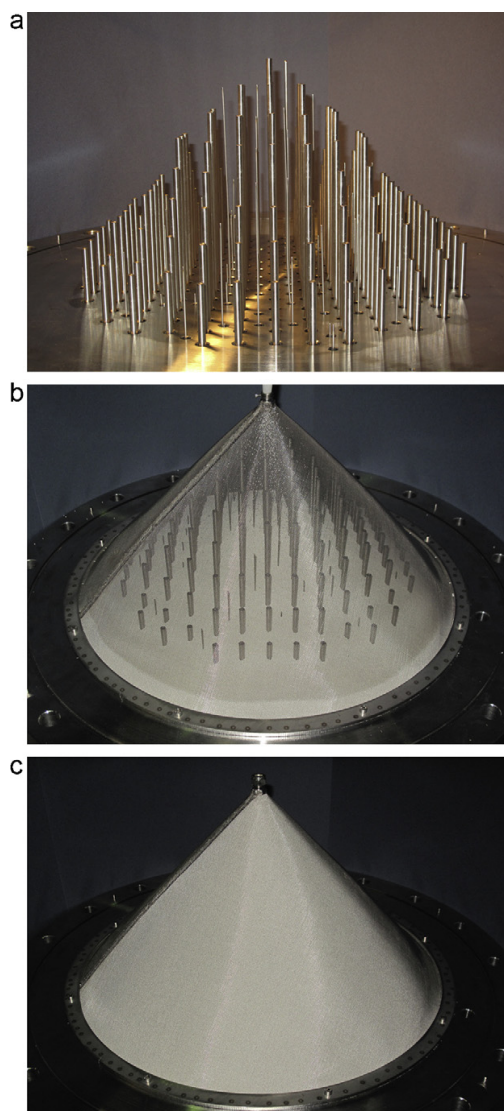


**Fig. 3.** (a) The heating arrangement of the conical test bed, (b) the filling of the bed with particles and (c) the ready conical bed before the experiments. The thin rods between the larger heaters are temperature sensors.

aims at volumetrically uniform power generation within the test bed. All the heaters in the cylindrical bed have equal length of 220 mm (this is the heated part inside the pressure vessel and the test bed) and the nominal maximum power of 1012 W. Thus, the total maximum power of the heaters is 70 kW but this is not presently achievable due to restrictions of the power transformer and the limited durability of the heaters in the test conditions. Since the heaters have equal power, the division to three groups according to electrical phase is done by assigning 23 heaters to each group.

The diameter of the cylindrical test bed is 310 mm and the height is 270 mm. This yields a volume of 20.4 l. The same ceramic beads are used for the particle material as in the conical test bed. A steel cylinder inside the pressure vessel holds the bed in the cylindrical

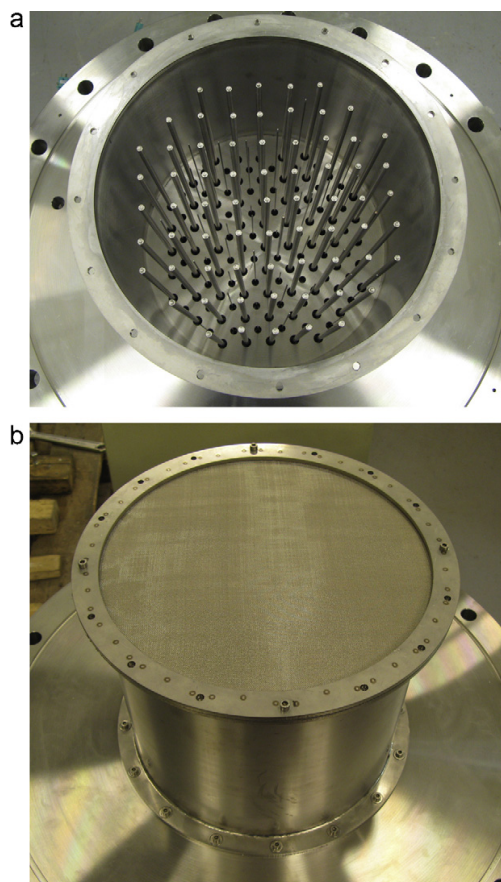


**Fig. 4.** (a) The heating arrangement of the cylindrical test bed and (b) the ready cylindrical bed. The test bed is contained in a steel cylinder.

shape. The top of the cylinder is open to facilitate top flooding but covered with a wire mesh to prevent floating of particles out of the bed. The cylindrical test bed before and after the fill with particles is shown in Fig. 4.

The average porosity of the cylindrical test bed was estimated to be about 0.38 by filling the test bed with water after the experiments. A low power was applied to evaporate the liquid in the test bed before the measurement. For the conical test bed, no such measurement has been done because it would be relatively difficult to perform due to the geometry and the permeable surface net of the cone. In the following analysis, it is assumed that the porosity of the conical bed does not significantly deviate from that of the cylindrical bed. A vibratory screening machine was used in the build-up of both test beds in order to reach the maximum packing density (minimum porosity) possible for the present configuration in which the spherical particles are packed against the pressure vessel structures, the wire net and the heater and thermocouple arrangement.

The dimensions of the particle bed of both geometries have been selected to be as large as possible considering the maximum power output of the facility. Dryout has to be reached within the available power range. MEWA calculations have been conducted to help the selection of the bed dimensions and particle size. With these calculations, predictions of limiting particle sizes were made by fixing

the dryout power to technically feasible levels and assuming porosity close to a value corresponding to the maximum packing density of spherical particles ( $\sim 0.63$ ). A smaller bed volume, and thus a smaller total dryout power, would give a better margin for ensuring that dryout can be reached with the test set-up. However, the test bed cannot be very small in order to avoid the effects of bed boundaries which may distort the results if the bed is not deep or wide enough. Also, the sensors and heaters have to be incorporated into the test bed in such a way that they do not occupy an unreasonably large volume of the test bed.

The limitation of the power output is also the reason why the cylindrical test bed cannot have the same radius and volume as the conical test bed since this would result in a very shallow bed ( $<100$  mm) with a very low surface heat flux at a fixed power level compared to a taller cylinder. This would mean that the total dryout power corresponding to the dryout heat flux would become too high, i.e. greater than the maximum output of the test facility according to calculations. Because of this, the experimental results have to be translated for the cylinders of different dimensions by a simple scaling analysis that uses the measured dryout heat flux. This procedure is explained in detail in Section 4. Technical reasons also explain the difference in the volumes of the 17.5 l conical bed and the 20.4 l cylindrical bed; the heaters are installed into a type of square lattice into the bottom lid of the pressure vessel and, as a result, the radius of the test bed cannot be chosen arbitrarily.

All the heaters of the cylindrical test bed have outer sheaths made of Incoloy since the cylindrical bed experiments were performed after the first series of the conical bed experiments. No overheating or remarkable damage to the heaters was seen during the experiments. This could be due to the evenly distributed loading of the heaters and the generally lower power levels required for the cylindrical test set-up to reach dryout. However, after the experiments and the removal of the particle material, some surface damage was visible on the sheath of the heaters near dryout locations.

#### 4. Results

Dryout experiments that provide comparison data for the conical and cylindrical geometries were conducted for the pressure range of 1–3 bar absolute. The maximum pressure level in the experiments was 7 bar which was reached with the cylindrical test bed. The full test matrix consisting of the test series COOLOCE-1–7, the measured dryout power and the corresponding power density (power divided by the total volume of the porous bed) are presented in Table 1. The dryout power is given according to the control power of the facility. The calculated power based on estimating the condensate mass flow rate is discussed in Section 4.2. The test series are named (numbered) according to their chronological order.

The experiment COOLOCE-0 was a preliminary experiment performed in order to verify that the instrumentation was working as required. The COOLOCE-1 and -2 experiments were conducted with a conical test bed, followed by the COOLOCE-3–5 experiments with a cylindrical test bed. Between the first conical bed experiments and the cylindrical bed experiments, improvements were made in order to make the heating configuration more robust to resist overheating and possible high-temperature corrosion caused by the contact of the heater sheath to saturated liquid and steam. The last two experiments COOLOCE-6–7 were performed with the improved conical set-up. The letters *a–d* in the test series denotes the different pressure levels and *R* denotes repeatability experiments which were conducted for selected pressure levels after a shut down and restart from a cold state.

The maximum pressure level reached for the conical test bed was 3.0 bar. No attempts for pressure increase beyond this were

**Table 1**

The test matrix of the COOLOCE experiments and the measured dryout power and power density.

Experiment	Pressure (bar abs)	Dryout results	
		Control power (kW)	Power density (kW/m <sup>3</sup> )
Conical test bed (1)			
COOLOCE-0 (preliminary test)	2.0	–	–
COOLOCE-1	1.9	46.2	2326
COOLOCE-2	1.6	43.8	2206
Cylindrical test bed			
COOLOCE-3	1.1	19.0	932
COOLOCE-3R	1.1	20.4	1001
COOLOCE-4a	1.6	23.4	1148
COOLOCE-4b	1.9	26.1	1281
COOLOCE-4bR	1.95	26.2	1286
COOLOCE-5a	3.0	31.9	1565
COOLOCE-5b	4.0	34.6	1698
COOLOCE-5c	4.95	37.2	1825
COOLOCE-5d	6.95	42.3	2076
Conical test bed (2)			
COOLOCE-6	1.1	26.0	1488
COOLOCE-7a	1.6	31.8	1820
COOLOCE-7b	2.0	36.0	2060
COOLOCE-7c	3.0	42.9	2455

made because of suspected heater overtemperature during the dryout power step at this pressure level. For the cylindrical test bed, dryout was measured for pressures up to 7 bar. For the Finnish BWRs, this represents the upper limit of the pressure expected in a severe accident scenario because filtered venting starts to reduce the containment pressure at approximately 6 bar. The test data for the higher pressure levels (4–7 bar) may be used to verify (i) earlier experiments concerning the pressure dependence of dryout and (ii) the applicability of the present set-up against the STYX experiments which utilized the same pressure range.

It is seen directly from the measurements that the dryout power for the conical configuration (test series 6 and 7) is greater than for the cylindrical configuration (test series 3–5) by 48–60%. This is explained by the infiltration of water through the surface of the cone which improves coolability compared to the cylinder which is as high as the cone and cooled only by infiltration through the top surface. Based on the first test series with the conical bed (1 and 2), the difference between the two geometries is as high as 81–92% because the dryout power measured in the first test series with the conical bed was higher than in the second series (6 and 7). The reason to the difference between the two conical test arrangements is somewhat unclear. However, we take the results of the second series (6 and 7) to be more reliable than the first series (1 and 2), and use the results of the second series for the analysis and comparisons in the following Sections. This is because of the following reasons:

- (1) The measured dryout was accompanied by a clear and consistent temperature increase at least the order of 50 °C from saturation temperature for all the measured pressure levels and it was typically indicated by several thermocouples. In the test 1, the temperature increase was significant but not in test 2 which may be related to the failure of the central heater or heaters mentioned in Section 3.1.
- (2) The test facility was modified after the test series 1 and 2 for the following experiments with the cylindrical and conical test beds. Thus, the results of the test series 6 and 7 provide a better reference for the cylindrical bed experiments (test series 3–5).
- (3) The pressure range achieved for the modified conical test bed of the test series 6 and 7 is more comprehensive.

**Table 2**

Dryout locations in the experiments (in mm from the bottom of the test bed), the number of sensors (measuring points) that indicated dryout and the approximate volume of the dryout zone.

Experiment	Pressure (bar abs)	Dryout zone		
		Height (mm)	Number of sensors in dryout	Dryout zone volume (dl)
Conical test bed (1)				
COOLOCE-1	1.9	140–170	4	2.8
COOLOCE-2	1.6	170	1	0.7
Cylindrical test bed				
COOLOCE-3	1.1	120–170	3	2.9
COOLOCE-3R	1.1	110–150	3	2.9
COOLOCE-4a	1.6	110–150	3	2.9
COOLOCE-4b	1.9	110–150	3	2.9
COOLOCE-4bR	1.95	110–120	2	1.9
COOLOCE-5a	3.0	110	2	1.9
COOLOCE-5b	4.0	110	2	1.9
COOLOCE-5c	4.95	110	1	1.0
COOLOCE-5d	6.95	110	1	1.0
Conical test bed (2)				
COOLOCE-6	1.1	140–170	4	2.8
COOLOCE-7a	1.6	140–180 <sup>a</sup>	5 <sup>a</sup>	3.5
COOLOCE-7b	2.0	115–120 <sup>a</sup>	3 <sup>a</sup>	2.1
COOLOCE-7c	3.0	120–170	2	1.4

<sup>a</sup> Measured at a power level one step (2 kW) above the minimum dryout power. At the minimum dryout power, one sensor at 170 mm indicated dryout.

- (4) With the dryout power being lower in test series 6 and 7 than in the first series, the results of the series 6 and 7 are more conservative and cannot be disregarded in the safety assessment.

The dryout zone in the conical bed experiments was consistently located in the upper and central parts of the cone. Also in the cylindrical bed, the incipient dryout occurred in the central parts of the test bed, in both horizontal and vertical directions. The dryout locations in the experiments are presented in Table 2. The vertical location is given simply as the height range of the sensors which indicated dryout in the experiment. The spreading of dryout in lateral direction may be described by the horizontal distance of the thermocouple rods which indicated dryout. In all the experiments which showed dryout in more than a single thermocouple rod (with single or multiple measuring points), dryout spread to one of the neighboring rods at the maximum lateral distance of 42.4 mm. The locations and distances are indicative; interpolation of the possible interfaces of dryout/wetted zones based on the sensor locations has not been conducted.

In the conical bed experiments, dryout was indicated by four innermost thermocouple rods installed around the center point of the test bed, one of which was the multi-point thermocouple. In the cylindrical bed experiments, dryout was almost always indicated by two of the four innermost thermocouple rods, arranged in a similar manner as in the conical test bed. An exception to the centrally located dryout is the COOLOCE-5b test run with cylindrical test bed in which dryout was located slightly farther away from the center of the arrangement. The dryout zone did not show significant spreading in any of the experiments during the time between the incipient dryout and the power shutdown. This is an expected result for the conical bed with multi-dimensional flooding and co-current flow. For the cylindrical bed, some vertical spreading was seen but no lateral spreading which is not typical to top-flooded configurations. This may be caused by the internal inhomogeneity of the cylindrical test bed. (Here, it should be noticed that it was not possible to conform to a pre-defined waiting time in post-dryout conditions in order to avoid overheating. The time between incipient dryout and power shutdown was generally short, about 5–20 min.)



Fig. 5. Steam bubbles near the surface of the conical particle bed.

Discussion of the flow patterns in the two test beds given in Section 4.3 provides clarification to the experimental observations. The uncertainty related to the inhomogeneity and representativeness of the test beds is considered in Section 5.

One method for estimating the dryout zone volume is based on the average volume covered by the temperature sensors in the test beds in regions where dryout was observed. In the conical debris bed, the “sensor density” near the symmetry axis is about 1 sensor/69 cm<sup>3</sup>. The average sensor density near center of the cylindrical test bed is 1 sensor/97 cm<sup>3</sup>. Multiplication of the number of sensors with the sensor density for each test shows that the approximate size of the dryout zone in the experiments varied from 70 to 350 cm<sup>3</sup> (0.7–3.5 dl) as presented in Table 2. As percentage of the test bed volume, this is 4–20% for the conical test bed and 5–14% for the cylindrical test bed.

Steam bubbles rising from the particle beds indicating vigorous boiling in the test bed interior were observed during the experiments. It was seen that the bubbles were dragged into a steam column near the center of the test bed for both geometries. For the conical bed, this is expected due to the flow circulation and greater steam generation in the center of the geometry but also for the cylindrical bed, the steam bubbles than exited the test bed near the perimeter were clearly drawn into a column in the center of the top surface. Since the convective two-phase flow in the water pool may have significant influence on the coolability because of e.g. its capability to float smaller particles it would be of interest to gain more data of the flow field. At the moment, this is beyond the scope of the study and the capabilities of the experimental set-up. An example of steam bubbles in the fluid volume photographed through a sightglass is presented in Fig. 5.

#### 4.1. The effect of geometry

In this section, the evaluation of the effects of the particle bed geometry is presented. As explained before, due to technical reasons the conical and cylindrical particle beds have different diameters and slightly different volumes. In a power plant scenario, however, the top-flooded cylindrical particle bed is assumed to be distributed against the walls of containment lower drywell area. In this case, a corresponding heap-like, or conical, bed cannot be larger in diameter than the cylindrical bed. Assuming that the two particle beds have the same volume and diameter, the cone is three times higher than the cylinder. Note that we also assume that porosities are equal in both cases.

In order to transform the present experimental data comparable for this kind of spreading scenario, we have to transform the cylindrical bed results to correspond to those of a cylinder that has the same diameter as the cone in the experiments. This can

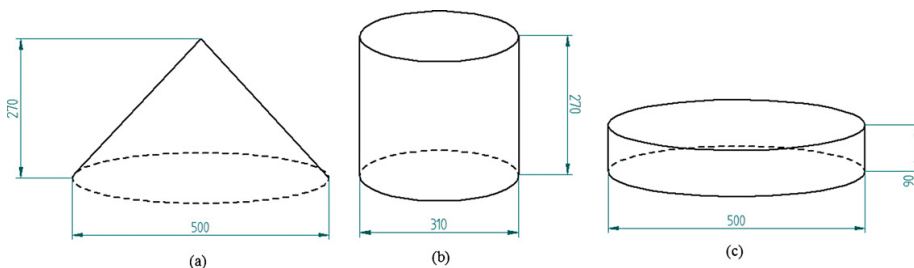


Fig. 6. The dimensions of the (a) experimental cone, (b) experimental cylinder and (c) comparison cylinder.

be done fairly easily because the coolability of the cylindrical configurations is determined by the dryout heat flux (total power per cross-sectional area) which is independent of height for deep beds. The dryout heat flux measured for one top-flooded homogeneously heated cylinder can be converted to total power or power density for cylinders of various dimensions. Once the heat flux has been measured for the experimental cylinder, the power and power density required for dryout in a cylinder of different height and diameter is calculated based on the constant heat flux. The heat flux for the experimental cylinder  $q''_{exp}$  is defined as

$$q''_{exp} = \frac{P_{exp}}{a_{exp}} \quad (1)$$

where  $P_{exp}$  is the experimental total power and  $a_{exp}$  is the area of the experimental cylinder. The total power  $P_c$  for a cylinder with a new area  $a_c$  is

$$P_c = q''_{exp} \times a_c \quad (2)$$

We call this cylinder with the experimental heat flux and a calculated total power the *comparison cylinder*. Note that the simple calculation is applicable only if no other parameter (aside from the geometrical dimensions) is presumed to change in the scaling process. The comparison cylinder with the experimental cone and cylinder are illustrated in Fig. 6.

For a cylinder whose radius equals the base radius of the COOLOCE cone, the comparison power is 2.6 times greater than the experimental dryout power. For example, in the COOLOCE-3R experiment, the dryout power was 20.4 kW. The surface area of the experimental cylinder is 0.0755 m<sup>2</sup>. The surface area of the comparison cylinder is 0.196 m<sup>2</sup>. For the dryout heat flux, this yields 270.2 kW/m<sup>2</sup>. The value of the comparison power is 53.0 kW. The physical interpretation of the increased total power is that the steam mass flux density (kg/m<sup>2</sup>/s) exiting the low, flat-shaped cylinder is very small compared to a tall narrow cylinder. This allows easier water infiltration into the bottom of the bed.

The comparison power may be converted to power density by dividing it by volume, either by the total volume of the porous bed or the solid volume. The latter yields a value independent of porosity which is directly connected to the decay heat generation of the solidified mass. Here, we use power density instead of total power for the comparisons due to the slightly different volumes of the test beds, specifically, the dryout power divided by the total volume of the debris bed:

$$q''' = \frac{P}{V_{tot}} = \frac{q''}{h} \quad (3)$$

The comparison of the dryout power densities of the experimental cone and cylinder and the comparison cylinder is presented in Fig. 7.

It is seen that the dryout power density for the comparison cylinder is greater than for the conical configuration by 47–51%. The difference appears to be independent of pressure. The result

is contrary to the directly measured dryout power density for the tall cylinder which was roughly 35% smaller than the dryout power of the conical test bed. The results are explained by examining the key mechanisms that have an effect on the dryout power. As already mentioned in Section 2, the coolability is affected by the following:

- (1) The conical configuration is cooled by multi-dimensional flooding throughout the surface of the cone which increases the dryout power density compared to configurations that have the same height and top flooding only.
- (2) The maximum height of the cone is greater than the cylinder which means that the heat flux, or the accumulated mass flux of steam, near the top of the cone is higher than the one that exits the cylinder through the top surface. This “geometry effect” decreases the coolability of the cone compared to the cylindrical configuration. Specifically, the upper parts of the cone are problematic due to the high thermal loading.

The dryout power density is greater for the experimental cone than for the experimental cylinder because of mechanism 1. It is well known that multi-dimensional flooding increases coolability compared to top-flooding only. In some early studies, the top-flooded cylinder has been taken as the most conservative case due to the lack of multi-dimensional water infiltration. However, these traditional analyses have not included cases in which porous beds that have equal volumes are distributed in different spatial configurations and the geometry differences have to be accounted for.

Mechanism 2 is important in the evaluation of the experimental cone and the comparison cylinder: the dryout power for the comparison cylinder is greater due to the flat geometry and large surface area of the cylinder. The large surface area allows a greater power generation of the debris bed at the same critical heat flux as in a taller debris bed with a smaller surface area. The heat flux in the conical bed (as defined per horizontal cross-section of the cone) is proportional to the change in the height of the examined cross-section as seen from Eq. (3). For a cone and a cylinder with equal volumes and radii, the cone is three times higher than the cylinder. This gives an idea of the ratio of the heat fluxes at the top of a cylinder and at the top of a cone. In order for the lateral flooding to be more significant than the increased height, the increase of dryout heat flux would have to be close to three times the dryout heat flux for top flooding.

#### 4.2. The role of heat losses and pressure dependence

In the COOLOCE experiments, the heating power directed to boiling was estimated based on the mass of condensate measured by a scale connected to the outlet of the heat exchanger. The purpose of the measurement was to estimate the heat losses from the facility and to reduce the uncertainties related to the

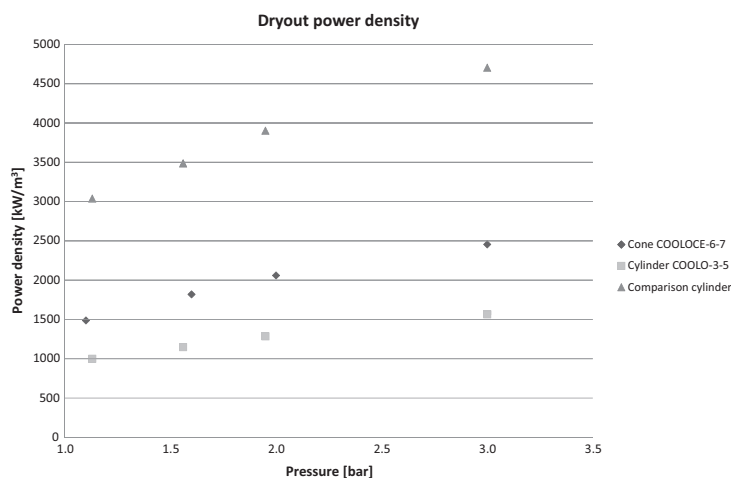


Fig. 7. Dryout power density comparison for the conical and cylindrical debris beds.

measured dryout power. The calculated power is the average condensate mass flow rate multiplied by the latent heat of evaporation during the power step that leads to dryout. The calculation assumes that the water which is collected at the condenser outlet is equal to the mass that has been evaporated by the heated test bed. The comparisons of the control power (electrical output power) and the calculated power for the conical and cylindrical test beds are presented in Figs. 8 and 9, respectively.

It is seen that the control power differs from the calculated power by roughly 2–8 kW (7–20%). The heat losses that contribute to this difference consist of (i) the power required to increase the feed water temperature to the saturation temperature and (ii) the heat losses through the bottom plate and the walls of the pressure vessel. The greater relative difference between the control power and calculated power at higher pressure levels is mainly caused by the fact that the power consumed by the feed water heat-up is greater for higher than lower pressures. This is due to the greater feed water mass flow rate and the greater difference between the

feed water temperature and saturation temperature. According to the average condensate mass flow rates, the power required to increase the feed water temperature could be as high as 6 kW, while at the lowest power levels it is below 1 kW.

Remaining uncertainties in the value of the calculated power are possible direct contact condensation in the vessel when the cooler feed water that is mixed into the water pool is in contact with the evaporating steam and wall condensation which might occur in the steam volume and at the inlet of the steam line. These condensation mechanisms may reduce the evaporating mass flux and the condensate mass flow rate. These uncertainties cannot be reliably estimated with the present test arrangement and we consider them to be negligible in the analysis of the effect of the debris bed geometry. However, the authors wish to point out that in general the effect of pool subcooling on coolability may not be straightforward due to mixing and condensation. The feed water heat-up is expected to reduce the power directed to phase change but this does not necessarily mean that the dryout power density in the debris bed is reduced.

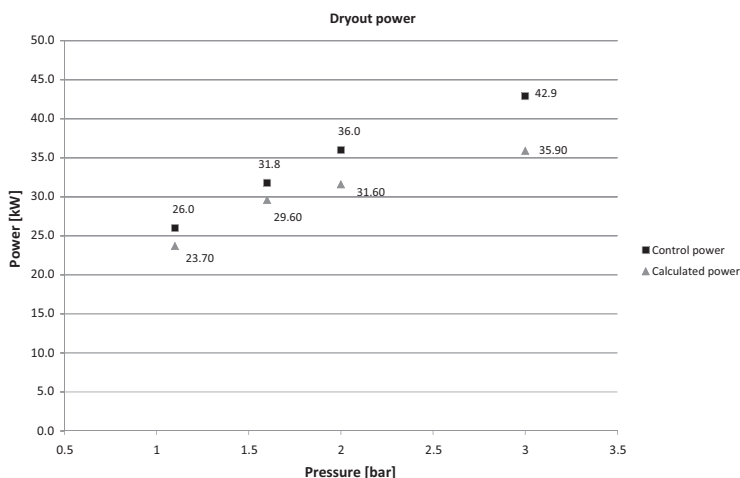


Fig. 8. Control power and the power calculated based on condensate flow in the conical bed experiments.

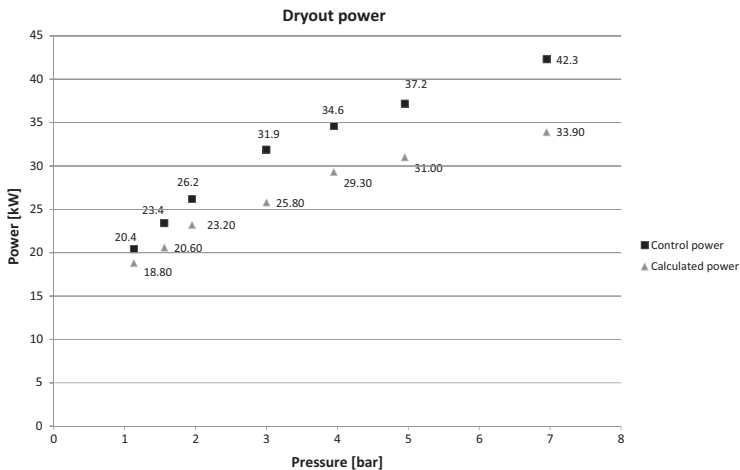


Fig. 9. Control power and the power calculated based on condensate flow in the cylindrical bed experiments.

The control power curve for the cylindrical debris bed in Fig. 9 clearly shows the power increase as a function of pressure for the range relevant to the Nordic BWRs. The increased dryout power is caused by the increase in steam density: steam occupies a smaller volume in the debris bed interior. As a result, a higher mass flux of steam – generated by a greater heating power – may escape the debris bed at the point at which counter-current flow limitation is reached in the case of the cylindrical bed. Numerical simulations (Takasuo et al., 2012a) and the results of the STYX experiments with a deep cylindrical bed (Takasuo et al., 2011) show similar pressure dependence as the control power of the COOLOCE cylindrical bed experiments. For the conical bed, CCFL does not limit the coolability but the smaller steam volume allows more volume for the liquid flow (lower void fraction) also for co-current flow. Again, this increases dryout power. The pressure dependence of the conical bed is close to that of the cylindrical bed based on the range for

which experimental data of both geometries is available (1–3 bar and four dryout power measurements). The pressure dependence of the STYX-8 test series is compared to the COOLOCE results in Fig. 10 which shows the dryout power density for the different experiments. The STYX-8 test series addressed a homogenous test bed of irregular particles as originally reported in Takasuo et al. (2011).

4.3. Evaluation against simulation results

The dryout process is in principle different in the conical and cylindrical debris beds as a result of differences in flow configuration. In the cylindrical debris bed, counter-current flow limitation determines whether liquid water reaches the bottom of the bed before it is evaporated, and a type of steam cushion is formed in the bottom of the bed. In the conical debris bed, the two-phase

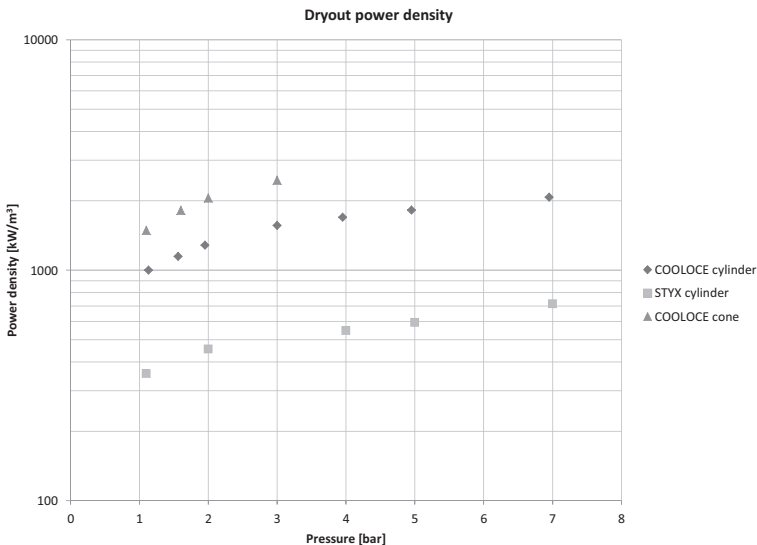


Fig. 10. Power density in the STYX-8 and COOLOCE test series. The dependence of dryout power (power density) on pressure is relatively similar in the different experiments.

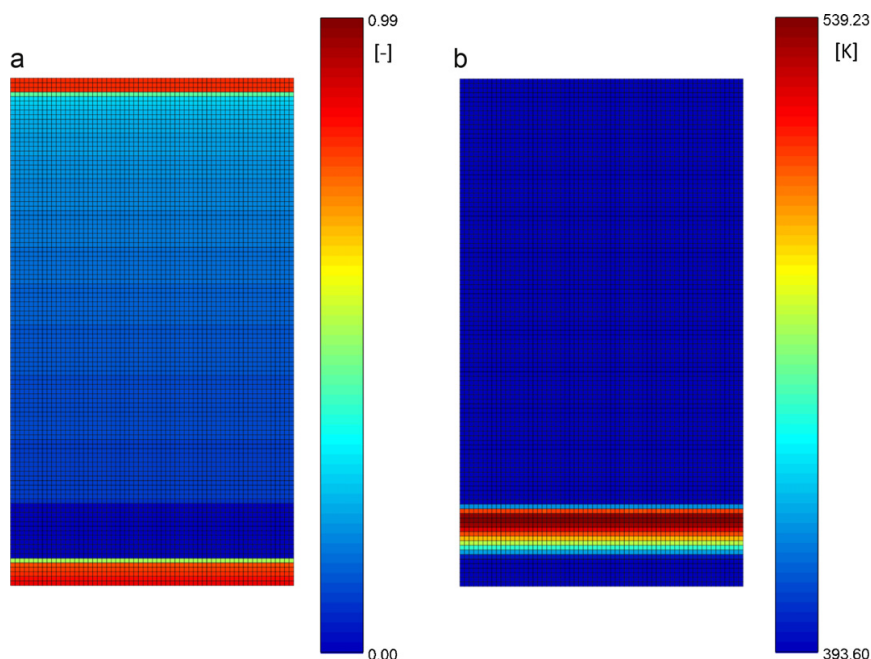


Fig. 11. (a) Post-dryout saturation and (b) solid temperature in the 2.0 bar cylindrical bed experiment (COOLOCE-4b).

circulation (co-current flow of steam and water) cools the bottom regions of the test bed and dryout is formed in the upper parts of the configuration. Next, we use MEWA calculations to demonstrate the dryout process in the two geometries and present a comparison of the experimental and simulation results.

The MEWA code has been developed by the IKE institute at Stuttgart University (Bürger et al., 2006) and it has been used in predicting dryout in several earlier studies (e.g. Takasuo et al., 2011; Ma and Dinh, 2010; Bürger et al., 2010). The code solves the basic two-phase flow conservation equations for mass, momentum and energy. Friction models based on the two-phase extension of the Ergun's equation (Ergun, 1952) are applied to model the friction between the fluid, solid and gas phases. The present approach utilizes a simple Cartesian 2D grid with the grid cell size of 2.5 mm. It has been chosen to use homogenous heating and constant porosity (38%) and particle size (0.9 mm) in the calculation. The interfacial friction models applied in the simulations are the Tung and Dhir (1988) model for the conical bed and the Reed model (1982) for the cylindrical bed. Previous studies suggest that these are the most suitable of the available models for predicting dryout power in the present flow conditions. See the discussion of the models e.g. in Schmidt (2004). The MEWA code utilizes an approach similar to the SIMPLE algorithm in the numerical solution. The simulation time step is controlled by the code depending on given convergence criteria. Initially, saturated conditions are assumed and no heat losses from the system are taken into account.

The post-dryout saturation (fraction of liquid in the pores) and solid temperature maps for the cylindrical bed simulation are illustrated in Fig. 11. The pressure in the simulation is 2.0 bar, i.e. the simulated experiments is COOLOCE-4b. In the top flooded cylindrical debris bed, the detection of dryout in experiments is straightforward at least in a theoretical sense. In dryout conditions, water does not reach the bottom of the debris bed and steam flow is stagnant in the dryout zone due to the lack of boiling. This leads to the formation of a relatively large dried-out zone and a

rapid increase of solid temperature as seen in Fig. 11. The dryout behavior is effectively one-dimensional. The power level in the cylindrical bed simulation – which is also the minimum power leading to dryout – is 25.0 kW. This is close to the experimental value of approximately 26 kW. In the cylindrical bed experiments, however, no significant spreading of dryout in horizontal direction was seen. The type of dryout behavior seen in the simulations would be extremely difficult to reproduce experimentally since the heating arrangement causes inhomogeneity in the local power distribution and porosity. The probable reasons to the differences in the dryout location in the experiments and simulation are (i) the vertical heaters that cause some channeling in the debris bed, (ii) heat losses through the bottom of the test vessel and (iii) the measured dryout power tends to be slightly above the exact critical power.

The post-dryout saturation and solid temperature maps for the conical bed simulation of the COOLOCE-7b experiment (2.0 bar) are illustrated in Fig. 12. In this case, dryout is formed in the upper part of the bed; above the height at which the heat flux in the bed cross-section becomes larger than the heat flux for a top flooded cylinder of equal height. Because of this and the cooling effect of the multi-dimensional flooding, the dryout zone in the conical case is expected to be very small compared to the cylindrical case. The power level in the simulation is 36.0 kW which is the same as the experimentally detected dryout power. At this power level, the dryout zone is located somewhat higher in the cone than in the experiment but the size of the dryout zone is roughly the same. The deviation in the simulated and experimental dryout location may be explained by the heating arrangement: even though the heaters are uniformly arranged in the test bed volume, the local power generation is not comparable to a debris bed with heat-generating particles. There is internal channeling and the heaters do not reach the test bed surface. (In addition, the thermocouple locations affect the accuracy of dryout detection in the experiments even though the design aims for a good coverage of the test bed.)

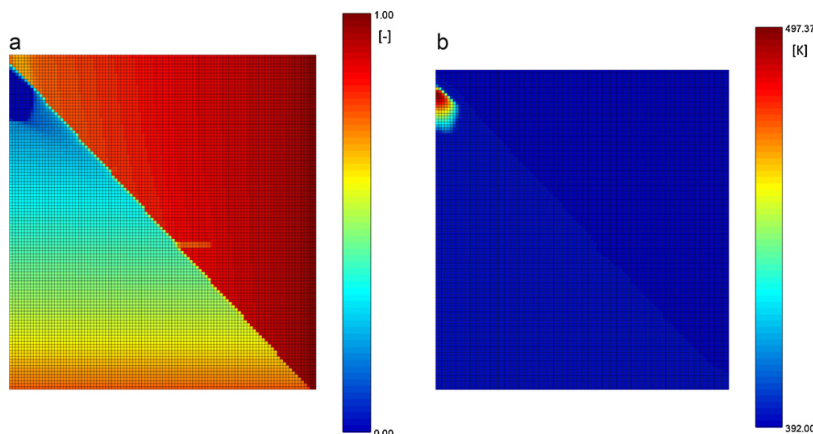


Fig. 12. (a) Post-dryout saturation and (b) solid temperature in the 2.0 bar conical bed experiment (COOLOCE-7b).

The minimum dryout power in COOLOCE-7b according to the simulation is 32.0 kW. Saturation and phase temperature were examined at different post-dryout power levels and, indeed, it was seen that the incipient dryout occurs in an extremely small region near the tip of the cone. It would be difficult to detect such a small zone in the experiments because of limited coverage of the thermocouples. For the top-flooded cylinder, the situation is different because a large dryout zone can be detected by evenly distributed thermocouples with relative ease. In addition, increase of dryout zone size (spreading) in the conical bed simulation is only observed in connection with the power increases, correspondingly to the increase in the boiling mass flux of steam and higher void in the bed interior. It also appears that post-dryout steady-states may be formed in the case of the conical bed due to the cooling effect of the steam flow. This may limit the solid temperature increase compared to the cylindrical cases and help to maintain coolability.

In general, both geometries show some discrepancy between the experimental and simulation results in the location of dryout. However, the good agreement between the experimental and simulated dryout power for both geometries increase the confidence that the test design can be used for reliable measurements of dryout power. A set of validation calculations for the full pressure range of the experiments including simulations of the flat-shaped comparison cylinder is presented in Takasuo et al. (2012a).

#### 4.4. Error estimation and uncertainties

One of the main sources of error related to the experimental procedure is the power increase scheme. Due to practical reasons, the power increases have been kept at 2 kW which means that the maximum deviation of the dryout power is about 2 kW below the measured value. (The correct dryout power value cannot be above the measured value since the temperature excursion determines dryout.) This corresponds to a relative error of 5–11% depending on the pressure.

Inaccuracies related to instrumentation are also present in the experiments, specifically in the power measurement. These include calibration error of the power analyzer, voltage conversion error and the possible inaccuracy of the data logging system. All the inaccuracies in the power measurement chain are not known but it is estimated that the maximum error contributed by the voltage conversion and the calibration inaccuracy is approximately  $\pm 0.3$  kW for power levels below 42 kW. For the power level of

50 kW, the inaccuracy is about  $\pm 0.6$  kW. The maximum relative error is approximately 2%.

During experiments, the test vessel pressure fluctuates due to the insertion of the cooler feed water which is done according to the water level measurement. The accuracy of the pressure control is about  $\pm 0.1$  bar. The nominal accuracy of the temperature sensors is  $\pm 1.5$  °C. The sensor-specific accuracy against the saturation temperature can be checked during test runs, and the fluctuations have been very small (a few tenths of °C). The temperature fluctuations follow the fluctuations in pressure as the saturation temperature is slightly changed. The performance of the temperature sensors is not expected to affect the dryout power results since dryout is generally noted after a significant temperature increase (the order of tens of °C).

In some experiments, clearly erroneous single point values (peaks) were recorded by the output module of the power analyzer. These peaks were not detectable from the power analyzer display and were clearly output signal disturbances. These values were removed from the final data, and the display of the power analyzer was continuously followed in order to verify the input power level. In addition, it should be noticed that the input power does not remain completely stable throughout the experiments: there are power fluctuations of at most a few hundred watts which depend on e.g. the temperature dependence of the heater resistivity. The reported values are power step averages that have been cross-checked against the values shown by the power analyzer display.

Inherently to the test arrangement, the accuracy of dryout detection is limited by the distribution of temperature sensors. It is possible that the incipient dryout is formed in a location between the thermocouples and remain undetected. Due to the aforementioned difference in the flow configurations, the risk for such a condition is greater for the conical debris bed in which the dryout does not spread effectively as already seen in the simulation results. In this analysis, we resort to limit the definition of dryout to a dryout *large enough to be detected* by the test arrangement, rather than attempt to evaluate the contribution of the uncertain location to the inaccuracy of the measured dryout power. In the simulations, obviously, this is not an issue since the results can be examined on the level allowed by the resolution of the computational grid.

The same 2 kW power steps have been applied in the simulations which yields the same 5–11% accuracy window as in the experiments. There are other uncertainties related to the simulation parameters such as the selection of particle diameter and

porosity. The representative (effective) particle diameter considering the pressure drop in the porous medium has not been estimated for the COOLOCE experiments. However, it is expected that the uncertainty in the modeling parameters does not have an effect on the relative coolability of the conical and cylindrical geometries in the simulations, i.e. the effect of particle size and porosity variation is similar for both geometries. The verification of the representative parameters has been planned to be included in future experiments which aim to reduce the different remaining uncertainties in debris bed coolability.

## 5. Discussion

The experimental results suggest that the effect of increased height is greater than the effect of the multi-dimensional flooding, yielding a reduced dryout power for the conical bed compared to the flat-shaped cylindrical bed. This result is supported by the preliminary calculations used in the design of the test arrangement and recent simulations conducted by the authors and other researchers (Takasuo et al., 2012a; Ma, 2011). It appears clear that the heap-like geometry cannot be taken as the most conservative case when the formation of the first dry zone is taken as the coolability limit. In case of the heap-like geometry, this criterion for the coolability may be questionable due to the possible formation of post-dryout steady-states as seen in the simulation of the conical debris bed. The steam flow might improve coolability but a detailed investigation of this is beyond the scope of the work.

The present experiments aim at distinguishing the difference in coolability between two well-defined geometries. Thus, the experimental conditions are not “prototypic” for power plant scale assessment. Nevertheless, the COOLOCE results imply that more investigations are needed to verify the coolability of the conical bed and other comparatively high configurations. The probability of the formation of high heaps of debris should be evaluated in reactor scenarios. Based on the latest knowledge of the debris bed formation process, limiting geometries for detailed coolability assessment could be derived. In power plant scenarios, the mechanisms that affect the debris coolability are complex and include uncertainties. In addition to the spatial distribution, the coolability of the debris bed depends on the porosity and the size, morphology and the distribution of particles. These are dependent on the melt discharge (e.g. the amount and rate of the melt poured into the water pool), i.e. the progress of the accident scenario. It is also important to notice the possible capability of the boiling in the bed interior and the resulting natural convection in the water pool to shift the particles. The debris bed may deform by the floating of particles, i.e. the shape of the debris bed might be transient even after the initial settling.

Further studies have been planned for the purpose of verifying the experimental results and reducing the uncertainties related to the test facility. One of the main differences of the experimental set-up compared to realistic corium is that the electrical heaters cannot reproduce the internal heat generation of debris, and the vertical heater arrangement might cause some artificial channeling which may increase coolability in the cylindrical test bed (compared to a cylindrical bed with uniform power distribution). This is because the packing of the particle material forms a type of boundary layer with increased porosity next to the heaters. The fact that dryout did not spread in lateral direction in the cylindrical bed experiments may suggest that a non-representative condition has been formed due to the vertical heaters. On the other hand, when any method of resistance heating is applied (cartridge heater, resistive wires, etc.) non-uniform heating, at least to some extent, cannot be avoided since the particles have no internal heat-generation, and additional structures are present in the test bed interior. For instance, behavior suggesting local effects was observed in the STYX experiments in

which horizontal wire heaters and a more realistic bulk of irregular particles were used (Lindholm et al., 2006; Takasuo et al., 2011). In top-flooded cases such as most of the STYX experiments, the theoretically expected behavior would be dryout covering the full horizontal cross-section near the bottom of the test bed. In the case of COOLOCE, the effect of non-homogeneity and the magnitude of uncertainties related to the heating arrangement and the used particles remain somewhat unclear. Further measurements with irregular particles and the comparison of the results to those obtained by the STYX facility will clarify the effect of the heating systems in the test set-ups as compared to reactor scenarios with uniform heating.

## 6. Conclusions

Experimental facility used for investigating the coolability of porous core debris beds of different geometries has been built. Experiments have been performed that aim to clarify the difference in coolability between cylindrical (evenly distributed) and conical (heap-like) ex-vessel debris beds. The cylindrical configuration was cooled by top flooding through the upper surface of the test cylinder while the surface of the test cone was open to lateral infiltration of coolant, resulting in a multi-dimensional flow configuration. The coolability was evaluated by measuring dryout power for the two geometries in the pressure range of 1–3 bar (abs.) and converting the results to power densities. Because, for technical reasons, the cylindrical test bed has different dimensions as those needed in the comparison analysis of a flat-shaped cylinder and a cone of equal volume and diameter, a scaling analysis based on the measured dryout heat flux for the cylinder was done. The measured power levels in the experiments were verified by collecting the condensed water from the steam line of the test facility and estimating the heat flow directed to boiling from the average condensate mass flow rates at the dryout power levels.

The results suggest that the coolability of a conical debris bed is reduced by 47–51% compared to a cylindrical debris bed of equal diameter and volume. This is explained by the greater height of the conical debris bed configuration. In a homogeneously heated debris bed, the heat flux through a cross-sectional plane increases with increasing height causing dryout in the upper part of the geometry when a critical steam flux (high enough to fully replace water) is reached. In case the height difference between the heap-like and the flat-shaped cylindrical configurations is great enough, the heap-like configuration reaches dryout at a lower power (or power density) than the flat-shaped geometry, regardless of the multi-dimensional flooding which is expected to increase coolability compared to top flooding. Indeed, the experiments also suggest that if the two debris beds have equal height, the coolability of the cone is better by 48–60% compared to the cylinder.

The location of the dryout zone was in the upper central parts of the conical test bed. In the cylindrical test bed, dryout was seen in the center of the test bed in both vertical and horizontal directions. The locations are reasonable considering the previous experience and understanding of the debris bed dryout process. In addition, it was seen that the pressure dependence of coolability is similar for both test bed geometries.

The experiments have produced new data which is used for the validation of simulation codes applied in the safety assessment of power plant scale. Also, the results highlight the need of further investigations which take into account the latest knowledge of realistic debris bed configurations and finding the possible limiting geometries based on this knowledge.

## Acknowledgments

The experiments and analysis have been conducted within the framework of the SAFIR2014 Finnish National Research Programme on Nuclear Power Plant Safety. The authors wish to thank everyone involved in the different stages of the experimental programme for their extremely valuable help in both technical and analytical issues, especially the scientists Mr. Mikko Ilvonen and Mr. Ville Hovi.

## References

- Bürger, M., Buck, M., Schmidt, W., Widmann, W., 2006. Validation and application of the WABE code: Investigations of constitutive laws and 2D effects on debris coolability. *Nucl. Eng. Des.* 236, 2164–2188.
- Bürger, M., Buck, M., Rahman, S., Kulenovic, R., Fichot, F., Ma, W.M., Miettinen, J., Lindholm, I., Atkhen, K., 2010. Coolability of particulate beds in severe accidents: Status and remaining uncertainties. *Prog. Nucl. Energy* 52, 61–75.
- Ergun, S., 1952. Fluid flow through packed columns. *Chem. Eng. Prog.* 48, 89–94.
- Hofmann, G., 1984. On the location and mechanisms of dryout in top-fed and bottom-fed particulate beds. *Nucl. Technol.* 65, 36–45.
- Hovi, V., Ilvonen, M., 2011. The 3D two-phase porous medium flow solver POR-FLO and its applications to VVER SG and EPR RPV. SAFIR 2010 Final Report. VTT Research Notes 2571. Helsinki, Finland, pp. 160–170. ISBN 978-951-38-7689-0.
- Karbojian, A., Ma, W., Kudinov, P., Davydov, M., Dinh, T.N., 2007. A scoping study of debris formation in DEFOR experimental facility. In: Proceedings of the 15th International Conference on Nuclear Engineering, Nagoya, Japan, April 22–26, 2007 (ICONE15-10620).
- Kudinov, P., Karbojian, A., Ma, W., Dinh, T.N., 2008. An experimental study on debris formation with corium simulant materials. In: Proceedings of ICAPP'08, Anaheim, CA, USA, June 8–12, 2008 (Paper 8390).
- Lindholm, I., Holmström, S., Miettinen, J., Lestinen, V., Hyvärinen, J., Pankakoski, P., Sjövall, H., 2006. Dryout heat flux experiments with deep heterogeneous particle bed. *Nucl. Eng. Des.* 236, 2060–2074.
- Ma, W., 2011. Prediction of dryout heat flux of volumetrically heated particulate beds packed with multi-sized particles. In: 14th International Topical Meeting on Nuclear Reactor Thermal Hydraulics (NURETH-14), paper 199, Ontario, Canada, September 25–29, 2011.
- Ma, W., Dinh, T.-N., 2010. The effect of debris bed's prototypical characteristics on corium coolability in a LWR severe accident. *Nucl. Eng. Des.* 240, 598–608.
- Magallon, D., 2006. Characteristics of corium debris bed generated in large-scale fuel-coolant interaction experiments. *Nucl. Eng. Des.* 236, 1998–2009.
- Rashid, M., Kulenovic, R., Laurien, E., Nayak, A.K., 2011. Experimental results on the coolability of a debris bed with multidimensional cooling effects. *Nucl. Eng. Des.* 241, 4537–4543.
- Reed, A.W., 1982. The effect of channeling on the dryout of heated particulate beds immersed in a liquid pool. Doctoral Thesis, Department of Mechanical Engineering, Massachusetts Institute of Technology.
- Schmidt, W., 2004. Influence of Multidimensionality and Interfacial Friction on the Coolability of Fragmented Corium. Doctoral Thesis. Institut für Kernenergetik und Energiesysteme, Universität Stuttgart.
- Spencer, B.W., Wand, K., Blomquist, C.A., McUmber, L.M., Schneider, J.P., 1994. Fragmentation and Quench Behavior of Corium Melt Streams in Water. NUREG/CR-6133, ANL-93/32. Argonne National Laboratory.
- Takasuo, E., Holmström, S., Kinnunen, T., Pankakoski, P.H., Hosio, E., Lindholm, I., 2011. The effect of lateral flooding on the coolability of irregular core debris beds. *Nucl. Eng. Des.* 241, 1196–1205.
- Takasuo, E., Hovi, V., Ilvonen, M., Holmström, S., 2012a. Modeling of dryout in core debris beds of conical and cylindrical geometries. In: Proceedings of the 20th International Conference on Nuclear Engineering, Anaheim, California, USA, July 30–August 3, 2012 (ICONE20-54159), submitted.
- Takasuo, E., Hovi, V., Ilvonen, M., 2012b. Applications and development of the POR-FLO 3D code in nuclear power plant thermal hydraulics. In: Proceedings of the 20th International Conference on Nuclear Engineering, Anaheim, California, USA, July 30–August 3, 2012 (ICONE20-54161), submitted.
- Tung, V.X., Dhir, V.K., 1988. A hydrodynamic model for two-phase flow through porous media. *Int. J. Multiphase Flow* 14 (No. 1), 47–65.

PUBLICATION III

# **Modeling of Dryout in Core Debris Beds of Conical and Cylindrical Geometries**

20th International Conference on Nuclear Engineering  
collocated with the ASME 2012 Power Conference.

July 30 – August 3, 2012, Anaheim, California, USA.

ICONE20-POWER2012-54159. 10 p.

Copyright 2012 ASME.

Reprinted with permission from the publisher.

## MODELING OF DRYOUT IN CORE DEBRIS BEDS OF CONICAL AND CYLINDRICAL GEOMETRIES

**Eveliina Takasuo**

VTT Technical Research Centre of Finland  
Espoo, Finland

**Ville Hovi**

VTT Technical Research Centre of Finland  
Espoo, Finland

**Mikko Ilvonen**

VTT Technical Research Centre of Finland  
Espoo, Finland

**Stefan Holmström**

VTT Technical Research Centre of Finland  
Espoo, Finland

### ABSTRACT

A porous particle bed consisting of core debris may be formed as a result of a core melt accident in a nuclear power plant. The coolability of conical (heap-like) and cylindrical (evenly-distributed) ex-vessel debris beds have been investigated in the COOLOCE experiments at VTT. The experiments have been modeled by using the MEWA severe accident analysis code. The main objectives of the modeling were (1) to validate the simulation results against the experiments by comparing the dryout power density predicted by the code to the experimental results and (2) to evaluate the effect of geometry on the coolability by examining the flow field and the development of dryout in the two geometries. In addition to the MEWA simulations, 3D demonstration calculations of the particle bed dryout process have been performed using the in-house code PORFLO. It was found that the simulation and experimental results are in a relatively good agreement. The results suggest that the coolability of the conical debris bed is poorer than that of the cylindrical bed due to the greater height of the conical configuration.

### INTRODUCTION

A porous debris bed that consists of quenched and solidified corium may be formed as a result of a core melt accident in a nuclear power reactor. Depending on the design of the reactor, such a debris bed may be formed in the containment in a deep water pool (ex-vessel) or inside the pressure vessel. In the Nordic boiling water reactors, the coolability of the ex-vessel debris bed plays an important role in the severe accident management strategy. In order to ensure the coolability of the core debris and to prevent dryout and possible re-melting of the material, decay heat has to be removed by boiling and two-

phase flow circulation. The objective is to prevent significant thermal loads to the structures and the possible loss of containment integrity.

The COOLOCE test facility has been used to experimentally investigate the coolability of porous debris beds of different geometries. The aim of the experiments was to compare the dryout power of a conical (heap-like) debris bed configuration to that of a cylindrical (evenly-distributed) configuration [1 - 4]. Even though a lot of attention has been paid to investigations of dryout heat flux for different debris bed parameters and flow conditions, few previous coolability studies have evaluated the effect of the possible bed geometries. In a heap-like configuration, multi-dimensional flooding through the surface of the heap (or cone) is expected to increase dryout power while the height of the configuration can reduce it, and thus decrease coolability compared to cylindrical, top-flooded geometries. Here, we use the traditional approach in which the coolability is determined by the formation of the first dry zone in the debris bed. For the conical bed configuration, the issue is more complicated because post-dryout steady-states which help to maintain coolability even after the formation of the first dry zone might be formed.

An important goal of the work is to obtain data for simulation code validation and development. The coolability analyses in reactor scale are done by severe accident simulation codes. In the present work, the MEWA 2D code has been used to model the COOLOCE experiments. The capabilities of the code are evaluated against the experimental results by comparing the simulated and experimental dryout power. In addition, 3D scoping calculations of the dryout process using the two-phase flow solver PORFLO have been conducted for the purposes of gaining an in-depth understanding of the flow

behavior in the debris bed and estimating the possible effect of the heating arrangement on the experimental results.

The MEWA code has been developed by the IKE institute at Stuttgart University specifically for severe accident analysis [5]. The code has been used in several previous studies [6 - 8]. The application of the PORFLO code to model debris bed coolability is a more recent research topic. PORFLO has been developed at VTT as a general-purpose code for nuclear power plant thermal hydraulics but, instead of structure-fitted grids, it utilizes porous medium models for complex geometries (see e.g. [6]). The solution principles in both codes are similar: The basic two-phase flow and energy conservation equations are solved with closure models suitable for flows in porous media.

## EXPERIMENTAL FACILITY

The COOLOCE test facility consists of a debris bed test section housed in a 270 dm<sup>3</sup> pressure vessel which is filled with water during the experiments. Presently, there are two different test section geometries available: a conical bed and a top-flooded cylindrical bed. The test beds are heated by resistance heaters arranged in a vertical configuration that aims for a uniform power distribution within the simulant debris. The heating and thermocouple arrangement for the conical test bed is illustrated in Figure 1.

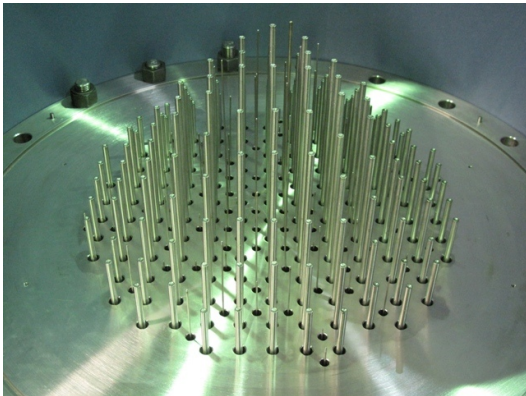


**Figure 1.** The heating and thermocouple arrangement of the conical test bed (Ø 500 mm). Heater diameter is 6.3 mm.

K type thermocouples are used to detect dryout (temperature excursion) somewhere in the bed interior. The thermocouple arrangement is designed to cover as much volume as possible in the test bed. The thermocouple distribution is densest in the upper part of the conical test bed because this is the expected dryout location. The search for dryout is done by stepwise power increases. The debris beds consist of corrosion-resistant ceramic beads with the diameter of 0.8-1.0 mm. The conical test bed is held in place by a dense wire net which prevents the particles from leaving the conical configuration. The cylindrical configuration has a steel cylinder to prevent lateral flooding, and the top surface of the cylinder is

covered by a wire net. It should be noticed that in reactor scenarios, the particles may be floated around in the steam flow, and the heap-like debris bed may lose its shape, but this kind of transient bed is beyond the scope of the study and the test bed geometry has to be retained by the wire net. The diameter of the wire has been selected to be small (Ø 0.25 mm) in order to avoid any significant additional flow resistance by the net.

The conical debris bed in the pressure vessel before the experiments is shown in Figure 2 (photographed through a sightglass). The volumes of the conical and cylindrical test beds are approximately 17.5 dm<sup>3</sup> and 20.4 dm<sup>3</sup>, respectively. The two test beds are equal in height (270 mm). The porosity of the cylindrical test bed has been estimated to be about 38% by filling the bed with water. This value was also used in the calculations for both geometries (no similar measurement for the conical test bed has been done because it would be technically difficult). Before the experiments, the beds were packed as dense as possible with the help of a vibratory screening machine.

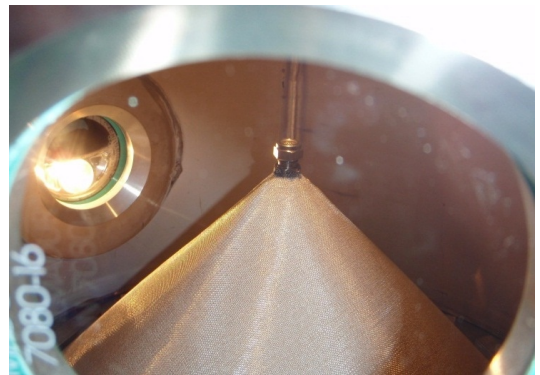


**Figure 2.** The conical test bed inside the pressure vessel before experiments (dry bed).

Steam generated by the test bed is led to a condenser which is connected to a bench scale for the purpose of estimating the mass flow rate of the condensed water. This gives an estimate of the heat flux directed to boiling and helps to estimate the heat losses from the facility. The water level in the test vessel is kept constant by feed water flow which is controlled according to a water level measurement.

## CYLINDRICAL BED HEAT FLUX

In order to be able to compare the two different geometries, it is important that the test bed parameters and internal structure are equal in the experiments. This is relatively easy to achieve by utilizing a same type of heating system and the same particle material in both cases. Because it is not technically possible to easily change the heating arrangement between the experiments, investigations on the effect of geometry are more or less restricted to a few representative variations of the geometry.

For a top-flooded bed, it is known that the dryout heat flux ( $\text{kW/m}^2$ ) is independent of the bed dimensions. This assumes that the internal heat generation is uniform and that the bed height is great enough to avoid boundary effects at the interface of the water pool and the debris bed [9]. The heat flux  $q$  ( $\text{W/m}^2$ ) through a horizontal cross-section of the internally heated bed at the height  $h$  (m) is the volumetric heat generation or power density  $Q$  ( $\text{W/m}^3$ ) multiplied by height:

$$q = Qh \quad (1)$$

The maximum heat flux is reached at the top of the debris bed. This heat flux equals to the dryout heat flux when the conditions for the formation of dryout are met. Based on the heat flux being independent of height, it is possible to measure the dryout heat flux for one cylindrical debris bed, and to calculate the dryout power density for other top-flooded beds with different dimensions (assuming that no other bed parameter or condition is changed in the process). From the definition of heat flux

$$q = \frac{P}{a} \quad (2)$$

it is also seen that the total power  $P$  (kW) of the bed is proportional to the bed surface area  $a$  ( $\text{m}^2$ ). For constant heat flux, the total power increases with increasing area because a greater amount of steam escapes through the larger cross-section. This also means that for a wide bed with greater surface area, a greater total power is allowed before the critical heat flux required for the onset of dryout is reached. In the COOLOCE experiments, the dryout power in the cylindrical test bed was measured for the pressure range of 1–7 bar which characterizes the containment pressure expected during a severe accident. The results are presented in Figure 3 which shows the dryout power converted to heat flux (according to Eq. 2) as a function of pressure.

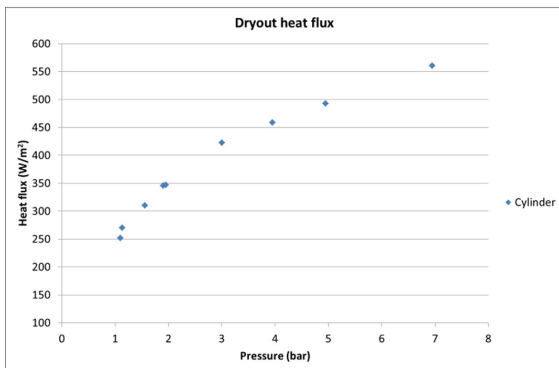


**Figure 3.** Dryout heat flux for the cylindrical test bed in the COOLOCE experiments.

It is seen that the dryout heat flux increases along with the pressure increase from approximately  $250 \text{ kW/m}^2$  at 1.1 bar up to  $560 \text{ kW/m}^2$  at 7 bar. This is an expected result since it is well-known that the dryout heat flux is pressure-dependent mainly due to the increase of steam density. When the pressure is increased, a greater mass flux of steam (and energy in the form of latent heat of evaporation) escapes the debris bed in the same volume as previously.

Concerning the debris bed geometry, it is of particular interest to compare conical and cylindrical beds with equal diameter since this is a limiting case in reactor scenarios; the heap-like and cylindrical debris beds are assumed to spread to cover the entire basemat of the flooded drywell. In this case, the conical bed is three times higher than the cylindrical bed since the two beds also have equal volumes. Thus, the analysis that will be presented in the following Chapter includes the comparison of the simulated dryout power density to the experimental dryout power density of 1) conical bed, 2) cylindrical bed and 3) flat-shaped cylindrical bed, i.e. *comparison cylinder* with  $1/3$  of the height of the experimental cylinder and cone ( $1/3 \cdot 270 \text{ mm} = 90 \text{ mm}$ ). The exact dimensions can be seen in Figure 4 which shows the MEWA grids for the simulations.

## MEWA SIMULATIONS

The main objective of the simulations was to predict the dryout power. This is done by finding out the minimum power level that leads to dryout and the maximum power level at which the particle bed just stays in a coolable steady-state. In principle this is the same procedure as the one in the experiments. A stepwise power increase is conducted in order to see whether the configuration stabilizes to a steady-state or dryout is reached.

2D grids which utilize the cylindrical symmetry of the cases have been generated for both test beds and the flat comparison cylinder. The three grids are illustrated in Figure 4 and the simulation set-up is given in Table 1.

**Table 1.** MEWA simulation set-up.

Particle diameter	0.9 mm
Porosity	0.38
Material density	$4000 \text{ kg/m}^3$
Thermal conductivity	$2.0 \text{ W/mK}$
Specific heat capacity	$775 \text{ J/kgK}$
Grid cell size	2.5 mm
Time step size	Controlled by the code
Heating method	Constant power density
Pressure	1-3 bar cone / 1-7 bar cylinder
Boundary conditions (top)	Pressure, saturated liquid inflow
Boundary conditions (side and bottom)	Adiabatic, no flow-through

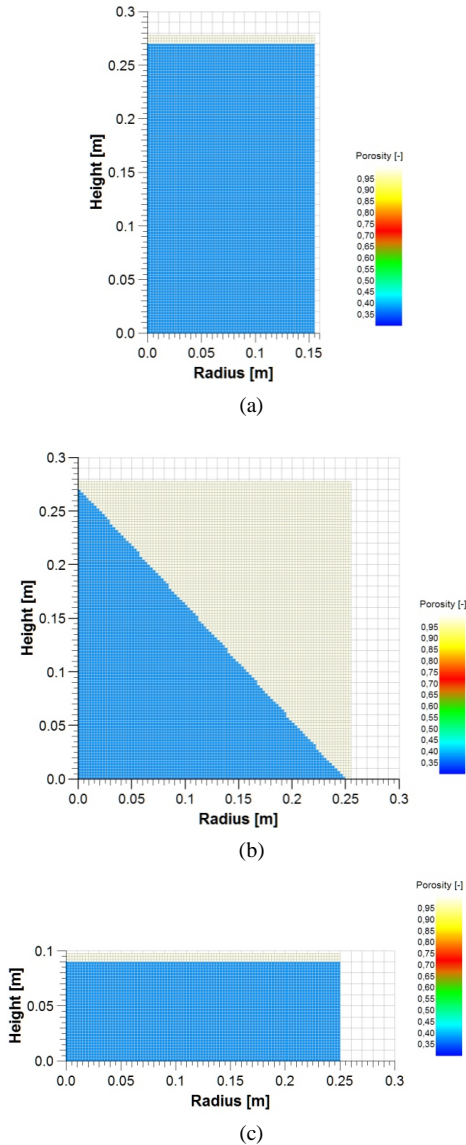


**Figure 4.** The computational grids for the MEWA simulations: (a) cylinder, (b) cone and (c) comparison cylinder.

The material properties of the particles in Table 1 are from their manufacturer. Since the exact particle size distribution is not known, a uniform size distribution is assumed between 0.8-1.0 mm, yielding the average of 0.9 mm. Similarly to a typical plant scale assessment, uniform power distribution (homogenous heating) is assumed because it would be difficult

to create a representative model of the heating system in 2D. The possible effect of the heating system is considered in the PORFLO simulations in the following Chapter.

The Reed model [10] is applied to model the particle bed friction in the case of cylindrical bed. The modified Tung and Dhir model [9, 11] with the explicit consideration of gas-liquid friction is used for the conical beds. Other options are available but these models have been shown to be the most suitable for the flow conditions and the particle size range of the experiments. The models are summarized in [9]. Several heat transfer models are included in the code to model the various heat transfer processes between the liquid, gas and solid phases [12]. Here, we use the same heat transfer models in both cylindrical and conical cases. The pool region is not modeled in a mechanistic manner. Instead, the water pool in which the debris bed is submerged is treated as a type of high-porosity porous medium that serves as a water reservoir from which the evaporated liquid is replaced.

### MEWA results

The comparison of the experimental and simulated dryout power density for the conical debris bed is presented in Figure 5. The comparison for the cylindrical debris beds is shown in Figure 6 (CYLI1 denotes the 270 mm experimental cylinder and CYLI2 is the 90 mm comparison cylinder).

The measured dryout power densities for the conical debris bed vary between 1500-2500 kW/m<sup>3</sup>. For the cylindrical bed, the range is between 1000 kW/m<sup>3</sup> and 2100 kW/m<sup>3</sup>. For the comparison cylinder, the corresponding power density range is 3000-6200 kW/m<sup>3</sup>. This is calculated by dividing the geometry-independent dryout heat flux in Figure 3 by the bed height, 0.09 m. It is seen that the experimental and simulation results are in a good agreement for the cylindrical debris beds (within 13%). The pressure dependence appears to be slightly steeper in the simulations than in the experiments. For the conical debris bed, the simulated dryout power density is lower than that of the experiments by fairly constant 220-290 kW/m<sup>3</sup> (10-24%).

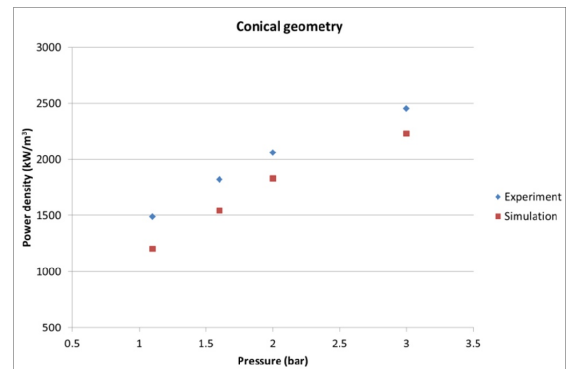


**Figure 5.** The experimental and simulated dryout power density for the conical debris bed.

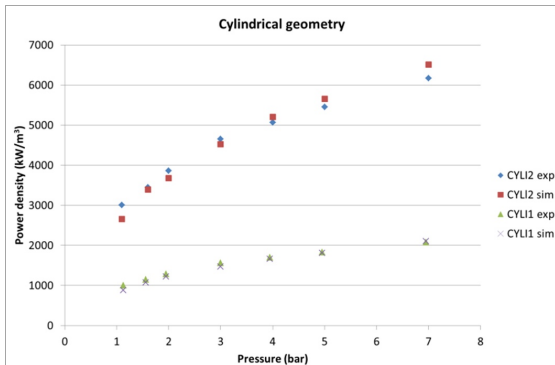


**Figure 6.** The experimental and simulated dryout power density for the cylindrical debris beds.

According to the experiments, the dryout power density for the conical debris bed was 50-60% greater than for the cylindrical bed. This is explained by the capability of multi-dimensional flooding to increase coolability compared to top flooding. The comparison of the 270 mm conical test bed and the 90 mm comparison cylinder, however, shows that, in this case, the coolability of the conical configuration is reduced by about 50%. Here, the effect of the increased bed height is greater than the effect of the multi-dimensional flooding, and the coolability is reversed for the geometries. Since the power generation occurs homogeneously within the modeled debris bed, the heat flux through a cross section increases with height (as stated by Eq. 1) in both cylindrical and conical geometries. This corresponds to increase in the mass flux of steam at the examined cross-section. The flat-shaped cylinder is not high enough for reaching dryout at the same power density, or total power, which causes the highest part of the conical geometry to be filled with steam due to greater local heat flux.

In the simulations, the increase of dryout power for the conical bed compared to the cylindrical bed of equal height is 15-30%. Correspondingly, the reduction for the 270 mm conical bed in comparison to the 90 mm flat-shaped cylinder is 50-55%. This means that the same conclusions can be made based on both the experimental and simulation results: the coolability of the conical bed is reduced compared to the cylindrical bed, presuming that the same total volume of debris (including solid and pore volume) is spread over a similar area.

### Flow field comparisons

The difference in the flow configurations between the cylindrical and conical geometries is clearly distinguished in the simulations. The solid temperature and saturation (liquid fraction in the pores) in post-dryout conditions (at the minimum dryout power density) for the conical bed and the two cylindrical beds at 3 bar pressure level are illustrated in Figure 7 (next page).

The vectors of superficial liquid and gas velocity are also shown in the images; liquid velocity is imposed on the saturation map and the gas velocity on the temperature map. Some of the values in the vector illustrations have been blanked to improve the readability of the images. Note also that we present only one illustration of each simulated configuration since the dryout behavior, in general, is independent of pressure.

It is seen that the incipient dryout in the conical debris bed is located in an extremely small region near the tip of the cone where saturation first reaches zero. A small increase in the particle temperature accompanies the dryout. According to the simulations, no spreading of dryout occurs until the heating power is further increased. This suggests that a type of post-dryout steady-state state in which the dry zone is cooled by steam flow is formed.

For both cylindrical debris beds, a full horizontal cross-section near the bottom of the test bed reaches dryout when the dryout power density is exceeded. This is typical for homogenous top-flooded beds. There are no radial changes in the flow field, and a 1D model would be adequate to describe the conditions in the debris bed.

As seen in the liquid and gas velocity for the cylindrical bed, the two-phase flow is clearly counter-current throughout the porous bed. In the case of the conical bed, liquid infiltrates the debris bed through the surface of the cone and travels more or less laterally towards the center of the geometry. The general direction of gas flow is upwards even though some entrainment of gas by the liquid flow is seen at the surface of the cone (interface of debris bed and the pool area). The circulation in which the liquid flows down near the outer parts of the geometry and upwards and out of the conical debris bed near the center (co-current with gas) is clearly seen in Figure 7(a). The present model does not include a mechanistic approach to model the pool flows but it is expected that this type of circulation is formed also in realistic scenarios.

Another difference between the configurations is that dryout in the cylindrical bed occurs after a saturation transient as already shown in the early studies by Hofmann [13]. This is illustrated in Figure 8 which shows the saturation profiles at the symmetry axis of the cylindrical and conical debris beds at different simulation times. When the heating power is increased to the level of the dryout heat flux, boiling rate in the upper parts of the cylindrical bed (at the location of the minimum saturation in coolable steady-state) is reduced due to the loss of liquid. It follows that the liquid from the top of the debris bed infiltrates the upper parts of the bed with less resistance than before. The location of minimum saturation is transferred downwards in the bed. At this point the evaporation rate is greater than the water infiltration rate, and the water "reservoir" in the debris bed slowly boils off. During the transient the reducing boiling rate allows water to infiltrate deeper in the bed until, finally, all the liquid is evaporated in the bottom of the bed. Then, the heat transfer from the solid phase is reduced when only the gas phase is in contact with the solid.

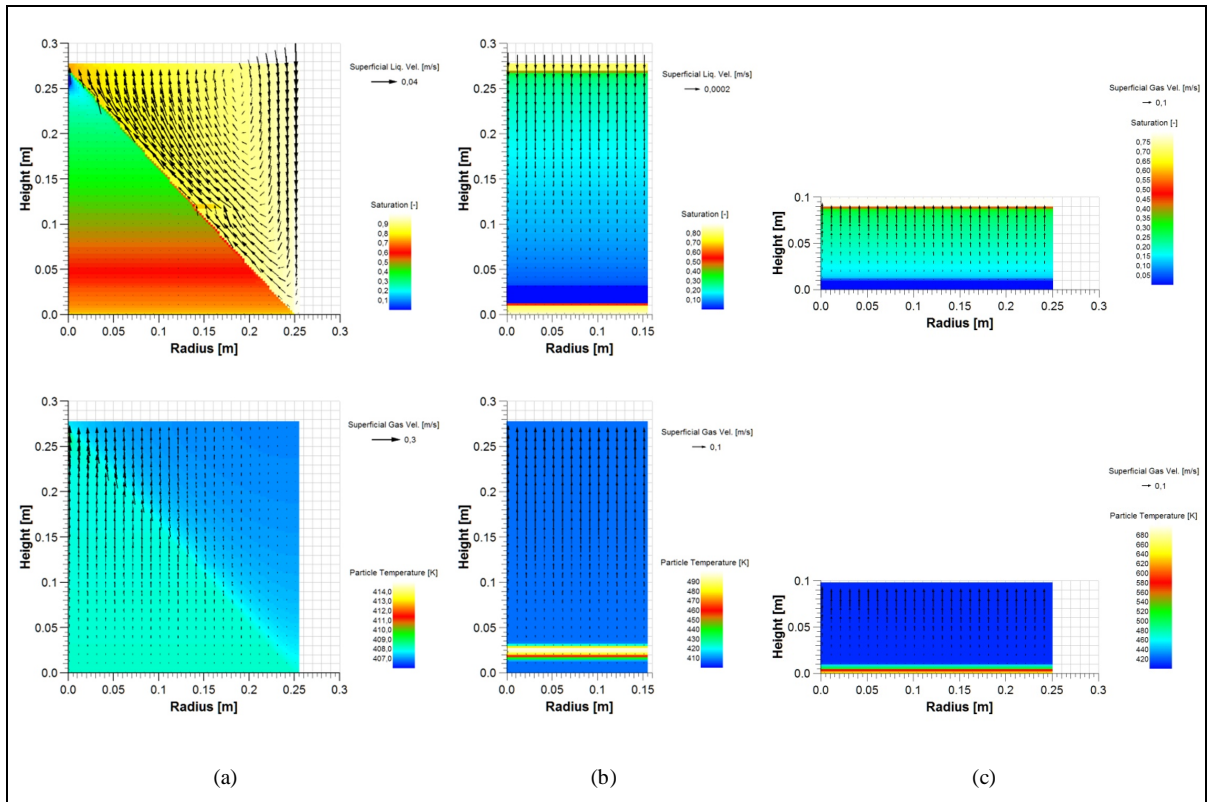


**Figure 7.** Post-dryout saturation (top) and solid temperature (bottom) in the MEWA simulations: (a) conical debris bed, heating power  $2232 \text{ kW/m}^3$ , (b) 270 mm cylindrical bed, heating power  $1472 \text{ kW/m}^3$  and (c) 90 mm cylindrical debris bed, heating power  $4584 \text{ kW/m}^3$ .

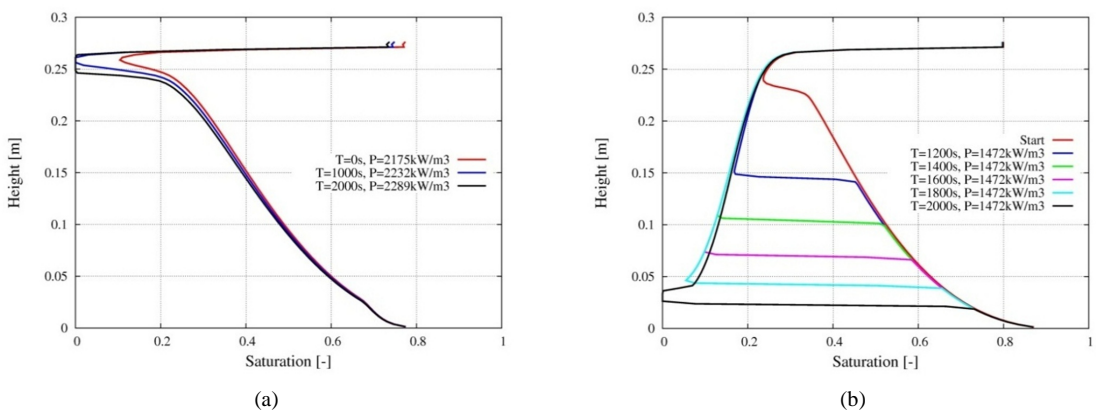


**Figure 8.** Vertical saturation profiles in the MEWA simulations for (a) the conical bed and (b) the cylindrical bed. The profiles are taken from the cell row at the symmetry axis (constant heating power for the cylindrical bed and three-step increase for the conical bed).

The simulations suggest no significant saturation transient for the conical bed. The bottom of the debris bed remains coolable because of the lateral flooding. Throughout the simulations, the point of minimum saturation is located in the topmost part of the cone as seen in Figure 8(a). Here, the heat flux increases according to Eq. 1 until the corresponding mass flux density is enough to fully replace water near the top of the conical bed. The system settles into a new steady-state soon after this. According to the simulations, the temperature increase connected to the dryout zone is rather modest compared to the cylindrical case. As seen in the temperature map of Figure 7(a), the temperature increase from saturation temperature is only 7 K at the minimum dryout power density.

The small dryout zone in the case of the conical bed explains the observed under-prediction of dryout power density seen in Figure 5. The locations of the thermocouples obviously limit the accuracy of dryout detection in the experiments. It is unlikely that a very small (and comparatively cool) dryout zone first formed in the tip of the cone would be detected by the experimental apparatus. But, when the power is increased from the critical level, the dryout zone covers a larger volume which is more easily detected by thermocouples. In addition, the exact mechanism of dryout is expected to differ from that of the “ideal” homogeneously heated bed in the simulations due to the vertical heating arrangement (seen in Figure 1). The dryout power in cylindrical beds is less sensitive to the limitations of the test facility because dryout is expected to occur in a larger volume.

## PORFLO SIMULATIONS

Heat transfer and friction models appropriate for solving two-phase flow in porous debris beds have been incorporated into the PORFLO code and 3D simulations have been run. A description of the code development and current status can be found in another paper in these Proceedings [14]. The PORFLO debris bed simulations consist of the following cases:

- 1) Homogenous conical bed (41 x 41 x 58 cells)
- 2) Non-homogenous, locally heated conical bed (41 x 41 x 58 cells)
- 3) Homogenous cylindrical bed (41 x 41 x 58 cells)
- 4) Non-homogenous, locally heated cylindrical bed (21 x 21 x 34).

Structured, Cartesian grids are utilized in the PORFLO simulations. The grid generation is performed by a routine that calculates average porosity for each cell based on the geometry information given by the user. As a result, the boundaries of the structures are automatically “smoothed” on the Cartesian grid. In the non-homogenous cases, the grid generation routine accounts for the vertical heaters of the test facility shown in Figure 1 and calculates local porosity variations with the accuracy allowed by the density of the specified grid. In the homogenous cases, a uniform porosity and power distribution is forced on the debris bed. This approach is somewhat close to that of the MEWA grid generation in which the porosity of each

cell is (in principle) given separately in the input. The grid cell size in all the PORFLO simulations was 15 mm.

Due to the modeling history, the volume of the non-homogenous cylinder (case 4) differs from the other simulated debris beds. We want to emphasize that the simulations conducted thus far serve as demonstrations of the 3D dryout behavior. The focus is on examining the dryout location and general development for the purpose of gaining a better understanding of the dryout process and to identify possible deficiencies in the 2D approach, and to estimate the effect of the localized heating in the experiments. Systematic efforts to validate the code for coolability predictions have not yet been done. Because of this, only atmospheric pressure is addressed in the simulations and the modeling parameters are slightly different than the ones used in the MEWA calculations. This means that no direct comparison to the MEWA simulations can yet be made.

The PORFLO simulation set-up is summarized in Table 2. The closure models for friction and heat transfer and the boundary condition settings closely follow the ones used in MEWA, e.g. the Reed model is used for the cylindrical beds and the modified Tung and Dhir model for the conical beds.

**Table 2.** PORFLO simulation set-up.

Particle diameter	0.8 mm
Porosity	0.37 (homog.) / 0.32-0.37 (non-homog.)
Material density	2700 kg/m <sup>3</sup>
Thermal conductivity	1.0 W/mK
Specific heat capacity	1090 J/kgK
Grid cell size	15 mm
Time step size	0.01 s
Pressure	1 bar
Boundary conditions (top)	Pressure, saturated liquid inflow
Boundary conditions (other)	Adiabatic, no flow-through

One of the main differences between the MEWA and PORFLO models is that a large part of the pool volume is accounted for in the PORFLO calculations. The height of the model is 825 mm which accounts for a free-flow volume close to the one in the COOLOCE test vessel for the 41 x 41 x 58 grids. However, similarly to the MEWA code, the pool is not modeled in detail in the present code version. No wall friction or turbulence models for the free flow region have been applied. Instead, the debris bed friction models with high porosity and a large particle size are used in the pool area to give some resistance to the flow, and to allow the water to infiltrate the debris bed. As a part of the general-purpose code development, the programming of wall friction and turbulence models is already on-going. In the future, this facilitates a more realistic modeling of the pool flows which could be used for investigating the effect of the pool flows on coolability.

**PORFLO results**

The post-dryout saturation predicted by the PORFLO model for the homogenous and non-homogenous conical beds is illustrated in Figure 9. The homogenous model correctly predicts the formation of dryout near the tip of the cone (indicated by the dark blue region in Figure 9). The saturation development with increasing heating power is generally similar as the process in Figure 8(a), taking into account the limitations of the coarser grid of the PORFLO simulations.

In the case of the non-homogenous conical bed, dryout is formed in the uppermost part of the cone but there is a clear difference compared to the homogenous model: channels with low saturation are formed to the vertical cell rows to which the heating is focused and to which dryout is formed. The non-homogenous case reaches local dryout clearly before the homogenous case. In this example, the dryout power density is 2571 kW/m<sup>3</sup> for the homogenous case and 429 kW/m<sup>3</sup> for the non-homogenous case. Note that the latter value is the average power density calculated as the total dryout power *P* per debris bed volume and not the local power density of the cells in dryout.

The high power density in the heater cells actually causes the difference in the dryout power. The steam generation is focused in these areas and, consequently, a higher maximum void corresponding to a total heating power level is present in these cells (since the general direction of gas flow is upwards). In the non-homogenous model, it is also seen how the gas flow continues directly upwards above heater cells. With a more realistic pool model, a different pattern would likely be seen due to turbulent mixing.

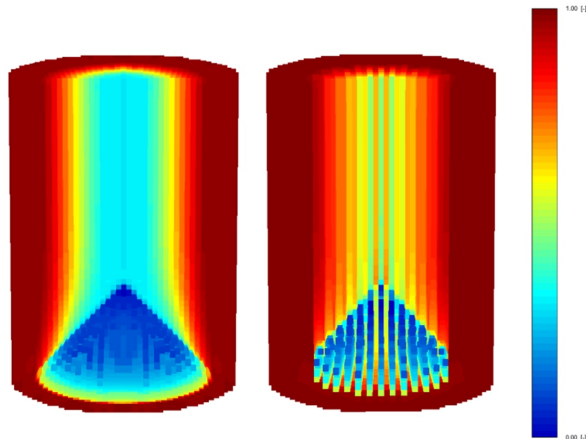


**Figure 9.** Saturation in post-dryout conditions in the PORFLO simulation of the conical debris bed: homogenous model (left) and non-homogenous model (right).

The post-dryout saturation for the homogenous and non-homogenous cylindrical beds (270 mm in height) is shown in

Figure 10. In the non-homogenous model (Figure 10 on the right) the vertical heaters are contained in every other cell column (one heater per column) with the cell size of 15 x 15 mm. This yields an average porosity of 0.32 for the heater cells while the porosity between the heater cells is 0.37. The comparison of liquid velocities for the homogenous and non-homogenous cylinders is seen in Figure 11 which shows the velocity vectors mapped on a vertical cross-section in the center of the modeled bed.

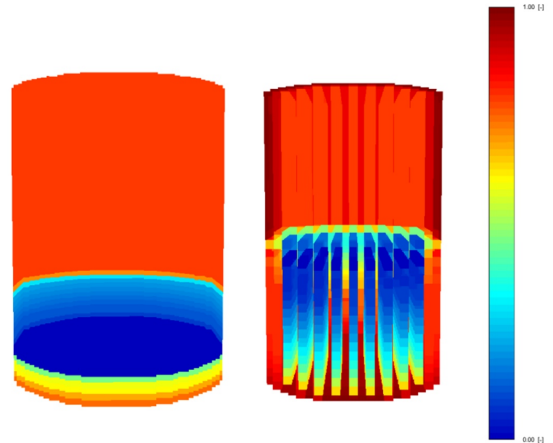


**Figure 10.** Saturation in post-dryout conditions in the PORFLO simulation of the 270 mm cylindrical debris bed: homogenous model (left) and non-homogenous model (right). The size of the geometries in the image is not to scale.

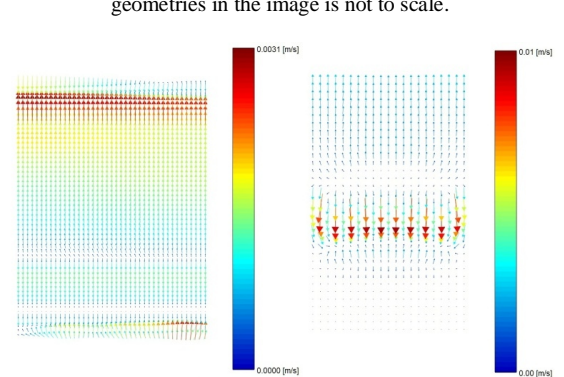


**Figure 11.** Vectors of liquid velocity in the PORFLO simulations of the homogenous (left) and non-homogenous (right) cylindrical debris beds in post-dryout conditions.

For the homogenous cylinder, the dryout development is reasonably similar to the MEWA simulations, and the saturation profile during the dryout transient approximates the one seen in Figure 8(b). Dryout generally occurs in the lower part of the

geometry and covers the full horizontal area of the debris bed. However, in the simulation in Figure 10 the location of the incipient dryout is above the bottom, at the height of 11 cm (dark blue region in Figure 10 on the left). This indicates that the heating power in the simulation is somewhat above the critical power. The horizontal cross-section at which all the liquid has been evaporated is found upper in the bed because of the greater boiling rate in regions where liquid is still available.

In the non-homogenous case, the non-uniform power distribution is clearly seen in the saturation field as was the case for the conical beds. However, in the cylindrical bed, the difference between the homogenous and non-homogenous cases is even more pronounced. It is seen that the localized heating causes a type of channeling effect which is seen as the vertical columns in Figure 10 (right). This effect transfers the dryout location into the upper parts of the bed, specifically, into the topmost cells of the heater regions. Steam flows upwards in the grid cells which contain the heaters until the mass flux of steam becomes high enough to displace water in the cells at the top of the heaters. The bottom of the geometry is cooled after dryout has been reached in the upper region because liquid flows down with less resistance between the heaters where there is no significant steam generation to counter the liquid flow. The formation of dryout is in principle closer to that of multi-dimensionally flooded configurations rather than the top-flooded, homogenous cylinder. Curiously, the 3D model of the homogenous cylinder also shows some asymmetric behavior as observed in Figure 11 near the top and bottom regions of the velocity field but not to the extent of the non-homogenous model. This might be due to a convergence problem in the homogenous model.

In the case of the non-homogenous cylinder, the multi-dimensional flow configuration caused by the channeling does *not* increase overall coolability because of the high local power density at the heater cells. The average dryout power density for the non-homogenous bed is  $368 \text{ kW/m}^3$ . For the homogenous bed, it is  $1250 \text{ kW/m}^3$ .

### Discussion of the PORFLO results

It is difficult to evaluate the simulation results of the non-homogenous debris beds against the experiments because no data is available of possible local dryout next to the heaters, not to mention void fraction. The main interest in the experiments was to obtain data of dryout in the particle material between the heaters and this is where the temperature sensors are located in the test beds. The good agreement between the measured dryout power and the MEWA results considering homogenous debris beds suggests that the heating arrangement does not cause significant disturbances to the measurement of the overall coolability.

However, this does not rule out the possibility of channeling in the test bed interior and local effects caused by the vertical heating system. A gas film might be present at the heater surfaces during the experiments and the flow field might be non-homogenous in a similar manner as in the PORFLO simulations. In reactor assessment, non-uniform heating is not

an issue but non-uniform porosity and a variable particle size may be important because the debris bed may have a highly irregular internal structure. The analysis of realistic non-homogenous debris beds supports the extension of the modeling approach to 3D.

Regardless of the modestly different modeling parameters, preliminary conclusions of the results can be made. The dryout power densities in the PORFLO simulations suggest that the present model over-estimates the coolability, e.g.  $1250 \text{ kW/m}^3$  was predicted for the cylindrical bed by PORFLO while the MEWA simulation and the experiment at 1 bar indicated  $883 \text{ kW/m}^3$  and  $1000 \text{ kW/m}^3$ , respectively. The reason to the discrepancy is presently unknown. Nevertheless, it has been demonstrated that the main processes of the dryout development are captured by the code. Efforts to develop the code to a more mature level will be continued by further verification and validation. Specific development targets include the implementation of a turbulence model, the possibility for an unstructured grid and the improvement of the calculation time by parallelization.

### CONCLUSIONS

The COOLOCE experiments that investigate the coolability of core debris beds of different geometries have been modeled by using the MEWA severe accident analysis code. It was seen that the 2D code is capable of capturing the dryout power density measured in the experiments with a very good accuracy for a cylindrical, evenly-distributed debris bed. For a conical (heap-like) debris bed, the dryout power density predicted by the code was slightly smaller than in the experiments but the differences are reasonable considering the different dryout process for the conical debris bed. The simulations clearly demonstrate the difference in the flow configurations between the two geometries. In the case of the conical bed, steam flow may help to maintain post-dryout steady-states with limited temperature increase.

According to both experimental and simulation results, the conical debris bed reaches dryout at a lower power density than the cylindrical bed in case the debris material is distributed over an equal area and the conical bed is three times higher than the cylindrical bed. This is observed even though the cylindrical geometry is cooled by top-flooding only.

Friction and heat transfer models suitable for porous debris beds have been incorporated into the PORFLO 3D code, and demonstration simulations of the dryout behavior have been run. The simulations suggest that the main processes of dryout development are correctly captured by the code. However, the capability of the code to predict dryout power in various situations has not yet been demonstrated. The systematic verification and validation of the code as well as further development of e.g. the pool model are topics for future studies.

### ACKNOWLEDGMENTS

The experimental and analytical work has been conducted within the framework of the SAFIR2014 Finnish Research Programme on Nuclear Power Plant Safety and its predecessor

SAFIR2010. The MEWA support received from IKE/Stuttgart University is gratefully acknowledged.

## REFERENCES

- [1] Takasuo, E., Kinnunen, T. Pankakoski P.H., Holmström, S. Description of the COOLOCE test facility – Conical particle bed. Research Report VTT-R-08956-10. Espoo, 2010. 18 p.
- [2] Takasuo, E., Kinnunen, T. Pankakoski P.H., Holmström, S. The COOLOCE-2 coolability experiment with a conical particle bed. Research Report VTT-R-02427-11. Espoo, 2011. 15 p.
- [3] Takasuo, E., Kinnunen, T. Pankakoski P.H., Holmström, S. The COOLOCE particle bed coolability experiments with a cylindrical geometry: Test series 3–5. Research Report VTT-R-07099-11. Espoo, 2011. 27 p.
- [4] Takasuo, E., Kinnunen, T. Pankakoski P.H., Holmström, S. The COOLOCE particle bed coolability experiments with a conical geometry: Test series 6–7. Research Report VTT-R-07097-11. Espoo, 2011. 26 p.
- [5] Bürger, M., Buck, M., Schmidt, W., Widmann, W. Validation and application of the WABE code: Investigations of constitutive laws and 2D effects on debris coolability. Nuclear Engineering and Design 236 (2006), p. 2164–2188.
- [6] Takasuo, E., Hovi, V., Ilvonen, M. PORFLO modelling of the coolability of porous particle beds. Research Report VTT-R-09376-10. Espoo, 2011. 41 p.
- [7] Takasuo, E., Holmström, S., Kinnunen, T., Pankakoski, P.H., Hosio, E., Lindholm, I. The effect of lateral flooding on the coolability of irregular core debris beds. Nuclear Engineering and Design 241 (2011), p. 1196–1205.
- [8] Ma, W. Dinh, T-N. The effect of debris bed's prototypical characteristics on corium coolability in a LWR severe accident. Nuclear Engineering and Design 240 (2010), 598-608.
- [9] Schmidt, W. Influence of Multidimensionality and Interfacial Friction on the Coolability of Fragmented Corium. Doctoral Thesis, Institut für Kernenergetik und Energiesysteme, Universität Stuttgart, 2004.
- [10] Reed, A.W. The effect of channeling on the dryout of heated particulate beds immersed in a liquid pool. Doctoral Thesis, Department of Mechanical Engineering, Massachusetts Institute of Technology, 1982.
- [11] Tung, V.X., Dhir, V.K. A Hydrodynamic Model for Two-Phase Flow through Porous Media. International Journal of Multiphase Flow 14 (1988), 47-65.
- [12] Buck, M., Pohlner, G., Rahman, S. Documentation of the MEWA code. IKE, Stuttgart University, August 2009, p. 18-24.
- [13] Hofmann, G. On the location and mechanisms of dryout in top-fed and bottom-fed particulate beds. Nuclear Technology 65 (1984), 36-45.
- [14] Takasuo, E., Hovi, V., Ilvonen, M. Applications and development of the PORFLO 3D code in nuclear power plant thermal hydraulics. Proceedings of the 20<sup>th</sup> International Conference on Nuclear Engineering, July 30 – August 3, 2012, Anaheim, California, USA. ICONE20-54161.

PUBLICATION IV

**Applications and Development  
of the PORFLO 3D Code  
in Nuclear Power Plant  
Thermal Hydraulics**

20th International Conference on Nuclear Engineering  
collocated with the ASME 2012 Power Conference.  
July 30 – August 3, 2012, Anaheim, California, USA.  
ICONE20-POWER2012-54161. 10 p.  
Copyright 2012 ASME.  
Reprinted with permission from the publisher.

ICONE20-54161

APPLICATIONS AND DEVELOPMENT OF THE PORFLO 3D CODE IN NUCLEAR  
 POWER PLANT THERMAL HYDRAULICS

**Eveliina Takasuo**  
 VTT Technical Research Centre  
 of Finland  
 Espoo, Finland

**Ville Hovi**  
 VTT Technical Research Centre  
 of Finland  
 Espoo, Finland

**Mikko Ilvonen**  
 VTT Technical Research Centre  
 of Finland  
 Espoo, Finland

**ABSTRACT**

PORFLO is a 3D two-phase flow simulation code which utilizes porous medium approach in the modeling of complex geometries. The code has been developed specifically for investigating various problems encountered in thermal hydraulic safety analysis of nuclear power plants. The code solution is based on the basic two-phase flow conservation equations with application-specific closure models for pressure loss, interfacial friction and heat transfer. The current main applications of the code include the simulations of flows in the horizontal steam generators of the Loviisa VVER-440 reactors and in the EPR reactor pressure vessel (RPV), and the modeling of the dryout behavior of porous core debris beds in the area of severe accident analysis. In the present work, the status of the code development, the main applications and the simulation results are summarized. In the case of the horizontal steam generator, the PORFLO simulation results are compared to the results obtained by the FLUENT CFD software. In the case of the core debris bed, comparisons to experimental data are also made.

**NOMENCLATURE**

$F$	volumetric friction force	[N/m <sup>3</sup> ]
$g$	acceleration of gravity	[m/s <sup>2</sup> ]
$h$	enthalpy	[J/kg]
$p$	pressure	[Pa]
$s_E$	energy source term	[W/m <sup>3</sup> ]
$s_M$	momentum source term	[N/m <sup>3</sup> ]
$s_{Mass}$	mass source term	[kg/m <sup>3</sup> s]
$t$	time	[s]
$v$	velocity	[m/s]

**Greek**

$\alpha$	volume fraction	[-]
$\varepsilon$	porosity	[-]

$\rho$	density	[kg/m <sup>3</sup> ]
$\tau$	stress tensor	[N/m <sup>2</sup> ]

**Subscripts**

$D$	associated to porous matrix
$p$	phase index for interphase drag
$q$	phase index
$I$	associated to phase change

**INTRODUCTION**

The PORFLO code is a two-phase flow simulation tool based on the solution of the basic conservation equations for the liquid and gas phases in three dimensions. As the name implies, the code utilizes porous medium approach for the geometry models. It is mainly targeted at applications where 3D phenomena may be significant but geometrical complexity does not allow for a CFD-style structure-fitted grid such as fuel bundles and other internal structures of reactor pressure vessels, steam generators and heat exchangers in general.

The basic features of PORFLO include staggered Cartesian grid and iterative solution of pressure and phase velocities using the phase-coupled SIMPLE algorithm (Semi-Implicit Method for Pressure-Linked Equations) [1]. In addition, the version currently being developed and tested includes two major development steps: the possibility for collocated structure-fitted grids and parallel computation on Open MPI (Message Passing Interface). The code has been under active development at VTT within the framework of the recent and on-going Finnish public research programmes on nuclear power plant safety, SAFIR2010 and SAFIR2014 [2]. In this paper, we focus on the following code applications:

- Modeling of the flow field in the secondary side of the horizontal steam generators (SGs) of VVER-440 reactors

- Demonstration calculations of the flow field in the pressure vessel and the core of the EPR (European Pressurized Water Reactor)
- Modeling of the coolability and dryout processes of porous ex-vessel core debris beds

Each of the applications is of importance in the safety analysis of operating power plants, or at the EPR which is currently under construction in Olkiluoto, Finland. The details of the two-phase flow field in the secondary side of horizontal or vertical steam generators are not well known due to the lack of experimental data and the difficulties related to measurements in operating nuclear power plants. However, this type of information would be useful in accident assessment and the life time management of steam generators. Knowledge of the flow field and void fraction distribution is needed e.g. for prediction of structural vibrations and locations of the accumulation of deposits. As velocities and void fractions are very difficult to measure in the SG, one has to resort to simulations.

In addition to PORFLO, steam generator simulations have been conducted using the APROS system code and the commercial FLUENT computational fluid dynamics code [3, 4]. In this work, the PORFLO simulations are evaluated against the FLUENT results. The long-term goal of the SG modeling is to develop extensively validated simulation tools and methodologies for the needs of the nuclear power industry.

The EPR reactor has an open core design which allows cross-flows between the fuel assemblies. In the currently operating power plants in Finland, this is not the case and channel boxes enclose the fuel elements. Thus, the “traditional” focus of calculations has been on 1D modeling of the flows in fuel bundles. However, in the case of EPR, 1D models may be overly conservative because the cross-flows are expected to reduce the probability of the formation of local hot-spots and improve the margin for DNB (departure from nucleate boiling). In order to realistically capture the effect of 3D transverse mixing between the subchannels and fuel elements, mechanistic models have to be used instead of artificial mixing terms. The long-term goal of being able to realistically predict the effect of the cross-flows motivated the development of an in-house model of the reactor pressure vessel (RPV) and core. Here, the first stages of the development, i.e. the grid generation and demonstration calculations with which the grid model was tested and the general flow behavior examined, are presented.

The third PORFLO application investigates the thermal hydraulics of severe accidents. During a core melt accident, a debris bed consisting of solidified melt particles may be formed in the cavity below the reactor pressure vessel, or inside the pressure vessel. The severe accident management at the Nordic BWRs relies on the coolability of such a debris bed in a deep water pool in the flooded lower drywell of the containment. This application differs from the two other code applications in the sense that the simulated debris bed is a “true” porous medium whose internal structure is known only in an averaged

manner. Debris bed dryout experiments which examine the effect of bed geometry on coolability and produce data for code validation have been performed at VTT [5]. In this paper, a brief comparison of the experimental and simulation results is provided. Code validation is a crucial issue in this research area since the plant-scale assessment aiming to verify coolability is done by severe accident simulation codes.

The past applications of the code include a model of an isolation condenser [6] and the BWR fuel bundle for the calculation of one of the BFBT (BWR Full-size Fine-mesh Bundle Tests) benchmark exercises [7, 8]. The isolation condenser (passive heat exchanger) model has not been further developed and validated during recent years but, since passive heat exchanger systems are expected to play an important role in the design of future power reactors, re-application of PORFLO to simulate these types of systems is included in the code development plans. In the discussion of the research needs following the Fukushima accident, the importance of the development of passive safety systems is even more pronounced than previously.

## SOLUTION PRINCIPLES

PORFLO utilizes the well-known Euler-Euler two-phase flow model, also known as the six-equation model, which solves the conservation equations of mass, momentum and energy for the liquid and gas phases [9]. The mass conservation equation for the phases is of the form:

$$\frac{\partial}{\partial t}(\varepsilon\alpha_q\rho_q) + \nabla \cdot (\varepsilon\alpha_q\rho_q\mathbf{v}_q) = s_{\text{Mass},q} \quad (1)$$

where  $\varepsilon$  is porosity,  $\alpha_q$  is the volume fraction of phase  $q$ ,  $\mathbf{v}_q$  is the phase velocity and  $s_{\text{Mass},q}$  is the mass source to phase  $q$ . The momentum equations have the form:

$$\frac{\partial}{\partial t}(\varepsilon\alpha_q\rho_q\mathbf{v}_q) + \nabla \cdot (\varepsilon\alpha_q\rho_q\mathbf{v}_q\mathbf{v}_q) = \mathbf{s}_{\text{M},q} \quad (2)$$

The source term of momentum  $\mathbf{s}_{\text{M},q}$  is formulated as

$$\mathbf{s}_{\text{M},q} = -\varepsilon\alpha_q\nabla p + \varepsilon\alpha_q\rho_q\mathbf{g} + \nabla \cdot (\varepsilon\alpha_q\boldsymbol{\tau}_q) + \varepsilon(\mathbf{F}_{pq} + \mathbf{F}_{r,q} + \mathbf{F}_{D,q}) \quad (3)$$

where the terms  $\mathbf{F}_{pq}$ ,  $\mathbf{F}_{r,q}$  and  $\mathbf{F}_{D,q}$  are the interphase drag, momentum source due to phase change and the drag cause by the porous medium to the phase  $q$ , respectively, and  $\boldsymbol{\tau}_q$  is the stress-strain tensor of phase  $q$ . The energy equations have the following form:

$$\frac{\partial}{\partial t}(\varepsilon\alpha_q\rho_q h_q) + \nabla \cdot (\varepsilon\alpha_q\rho_q\mathbf{v}_q h_q) = s_{\text{E},q} \quad (4)$$

where  $s_{\text{E},q}$  denotes the source terms of energy to phase  $q$  which consist of the energy of the phase change and the application-specific heat sources.

The closure models for the pressure loss, interfacial friction and heat transfer depend on the application. A selection of interfacial drag force and heat transfer models between the phases has been incorporated into the code for the different cases. The implementation of a turbulence model is an on-going task: the widely used  $k-\epsilon$  model has been included in the code and it has been tested with single-phase flow calculations. The iterative solution process of the PORFLO six-equation model is presented in Figure 1.

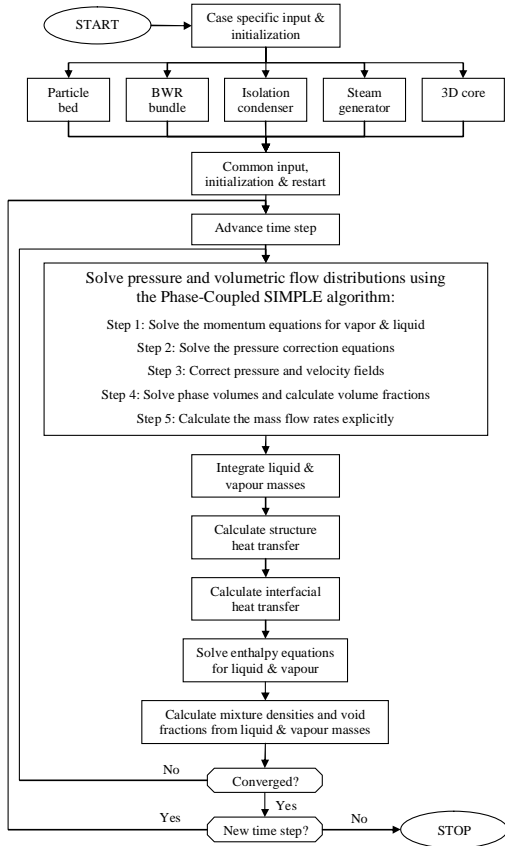


**Figure 1.** The solution procedure of the PORFLO six-equation model.

The pressure-velocity solution is based on the SIMPLE algorithm originally developed by Patankar [1]. Several numerical models are available for the discretization of the phase fraction, velocity and temperature. The grid generation in PORFLO is performed by a subroutine that calculates the porosity information for any given regular grid during the initialization of a simulation. This is done based on the geometrical dimensions of the case given as user input.

## HORIZONTAL STEAM GENERATOR

Horizontal steam generators are used in the VVER power reactors (a Russian type of pressurized water reactor) while most western PWRs use vertical SGs to transfer the heat from the primary circuit to produce steam in the secondary circuit. The VVER-440 power plants at Loviisa, Finland, have six horizontal SGs with the inner diameter of approximately 3 m and the length of 12 m. The internal geometry of the SGs is rather complex: a single SG contains 5536 heat transfer tubes in U tube form, their support plates and the hot and cold leg collectors.

All the internal structures are modeled using the porous medium approach with no detailed geometry information carried over to the calculation. A Cartesian grid with  $109 \times 30 \times 30$  cells has been generated for the simulations. The grid is illustrated in Figure 2 and Figure 3 which show the porosity mapped on the longitudinal cross-sections of the model. The boundary conditions for the simulation, i.e. the temperatures of the outer surface of the heat transfer tubes, were taken from an APROS calculation (one-way coupling of the codes) [3].

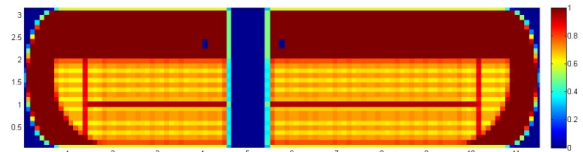


**Figure 2.** Porosity of the steam generator model (xz plane,  $y=2.0$  m).

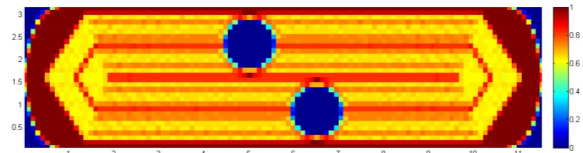


**Figure 3.** Porosity of the steam generator model (xy plane,  $z=1.5$  m).

The SG model of PORFLO utilizes the interfacial drag correlation by Simovic et al. [10]. The first part of the correlation, valid for bubbly flow regime ( $\alpha < 0.3$ ), has been adopted from Ishii and Zuber [11] which includes a minor modification to the original model. Also, the calculation of the drag force caused by the tube bundles is based on the presentation of Simovic et al. [10] for equilateral in-line tube arrangement. The Dittus-Boelter correlation (presented in [12], p. 491) is used for the calculation of the convective heat transfer processes and the Thom pool boiling correlation [13] for the phase change rate. A more detailed description of the models and their implementation can be found in [3].

### Steam generator simulation results

The calculations were run with fixed boundary conditions until a steady-state simulating the normal operating conditions was reached. A similar calculation has been performed using FLUENT [4], against which the PORFLO results can be compared. The calculation utilizes the Euler-Euler approach with the same closure laws for heat transfer and friction as the ones used in PORFLO, included in the FLUENT calculation as user-defined functions. The main differences in the two calculations are the grid model and the modeling of turbulence. The FLUENT calculation is based on a non-structured collocated grid. However, the density of the grid was chosen to be close to that of the PORFLO model. The standard k- $\epsilon$  turbulence model was used in the FLUENT calculations for the full computational domain while the PORFLO calculation did not include a turbulence model.

The resulting flow fields are compared in Figure 4 - Figure 8. The void fraction according to the PORFLO simulation in a vertical cross-section of the model is presented in Figure 4 and the void fraction at the corresponding cross-section in the FLUENT simulation in Figure 5.

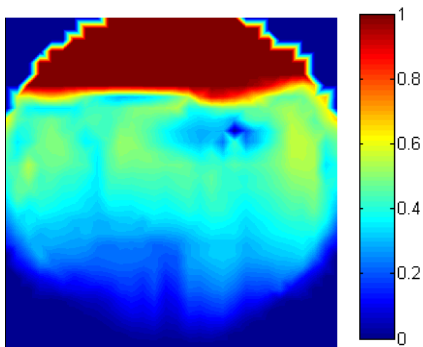


**Figure 4.** Void fraction in the PORFLO simulation (yz plane at  $x=2.83$  m).

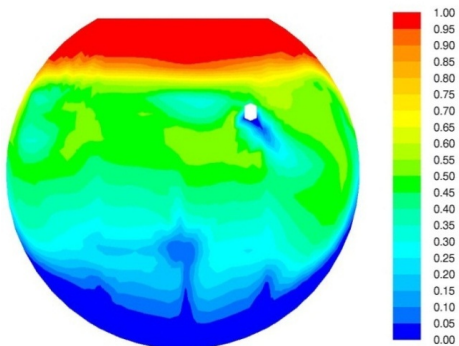


**Figure 5.** Void fraction in the FLUENT simulation (yz plane at  $x=2.83$  m).

It is seen that the general outlooks of the two void fraction distributions are similar: smaller void fractions are located near the bottom and the feedwater injection line and at the gaps between the tube sections. A difference is seen in the direction of the feedwater flow near the injection line. The FLUENT simulations suggest that the feedwater flow is directed downwards into the section occupied by the primary tubes, whereas the PORFLO simulations would suggest that the colder feedwater mainly stays on top of the tube bundles and moves to the middle section of the steam generator.

This can be explained in part by the differences in the boundary conditions between the two cases. In the FLUENT simulations, the feed water is injected downwards with a source term for the liquid momentum. In PORFLO, the liquid is injected as a mass source without a source term for momentum. Appropriate momentum sources could be included in PORFLO as well but in the absence of detailed data concerning the liquid velocity at the nozzles of the feedwater injection line, the momentum source terms were not taken into account.

Another difference between the results is that the shape of the water level is different; there is a distinct dip in the water level predicted by PORFLO directly above the feedwater injection line that is absent in the FLUENT results. These two differences between the results may be connected. In FLUENT, the feedwater flow is directed further downwards and in PORFLO the cold feedwater is located directly below the dip in the surface level. The presence of cold feedwater near the surface may have a profound effect on the surface level through increased condensation. However, it must be noted that on such coarse grids it is difficult to capture the surface level accurately.

The void fraction distributions on the horizontal cross-sections have more dissimilarity than the cross-sections on the vertical plane. This is seen by comparing the void fraction maps given in Figure 6 for the PORFLO simulations and in Figure 7 for the FLUENT simulations.

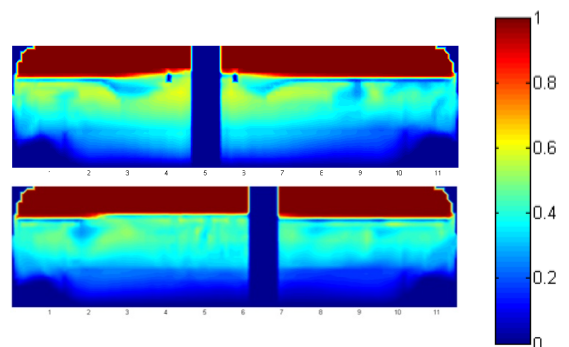


**Figure 6.** Void fractions in the PORFLO simulation: cross-sections at xz plane,  $y=2.0$  m (top) and  $y=1.21$  m (bottom).

The “broad strokes” are similar in both cases; higher void fractions appear on the hot side (upper of the two pictures), especially near the hot collector, and void fraction is increased with height when moving up from the bottom of the steam generator. The details that can be seen in both cases, however, are few. Generally, the distribution seems to be more uniform in the FLUENT simulations than what is seen in PORFLO results. The numerous small pockets of higher void fractions seen in Figure 6 below the surface level stand out in particular.

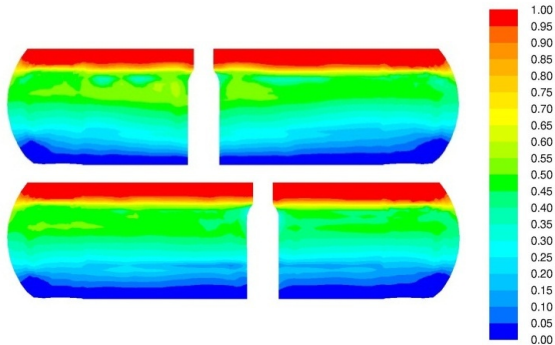


**Figure 7.** Void fraction in the FLUENT simulation: cross section at xz plane, y=2.0 m (top) and y=1.21 m (bottom).

The vectors of liquid and vapor velocity at the yz-plane at z=2.83 m in the PORFLO simulation (corresponding to the void fraction in Figure 4) are presented in Figure 8. The velocity field in the simulation indicates that the liquid flow is directed upwards in the primary tube region and downwards near the outer shell of the SG. Strong vortices are seen near both ends of the geometry. The main direction of the vapor flow is upwards with the exception of the region near the inlet tube and the vortices where the flow is diverted downwards with the liquid flow.

It is seen that the liquid velocities are large at the water surface level. This might be caused by pressure gradients normal to the free liquid surface or this could be an artifact of the staggered grid: the averaging procedure might distort the results because the volume fraction of one of the phases approaches zero above the surface.

In general, it can be said that the simulation results of the two codes are in a rather good agreement. The simulated flow behavior is close to what would be expected in a steam generator during normal operation. The most distinct differences between the results of the two codes, e.g. the non-monotonicity of the void fraction distribution near the water surface predicted by PORFLO, pointed out some aspects of the code that need further development. (Of course, this does not necessarily mean that the FLUENT results are an accurate reproduction of the flows present in the steam generator. Due to lack of measured data, this would be difficult to estimate.)

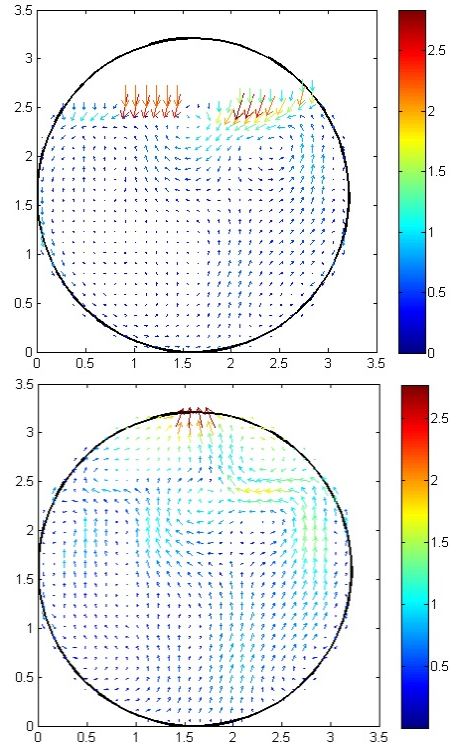


**Figure 8.** Velocity field for liquid (top) and vapor (bottom) in the PORFLO simulation (yz plane at x=2.83 m).

## EPR PRESSURE VESSEL

The EPR core consists of 241 fuel assemblies. Each of the assemblies contains 265 fuel rods and 24 control rod guide tube locations in a 17 x 17 array. The reactor core is open, i.e. there are no channel boxes enclosing the fuel assemblies. The interesting question from the safety point of view is to what extent the flow in each fuel element proceeds straight upwards and to what extent there is transverse mixing between the subchannels and the fuel assemblies. Correct prediction of transverse mixing is important in inherently 3D transients such as the introduction of boron-diluted or cold water into a part of the core. Such transients are dynamic in nature and should ultimately be simulated with coupled neutronics. Generally, in any case in which the state of a part of the core in the radial direction differs from the rest of the core, it is important to apply 3D thermal-hydraulic models as mechanistic as possible.

The first part of the modeling work was the spatial discretization of the pressure vessel geometry to the regular grid, followed by demonstration simulations used for investigating the possibilities of the structured grid approach. A

3D model of the EPR pressure vessel which consists of  $23 \times 23 \times 55$  grid cells has been generated. The grid is illustrated in Figure 9. The cell width in the horizontal directions is 0.215 m accordingly to the width of the fuel assemblies. In vertical direction, the fuel assemblies (active fuel length of 4.2 m) are divided to 20 cells. The grid is adjusted to account for the lower and upper support plates.

At the time of the model testing, the available models for calculating the pressure loss consisted of the tube bundle correlation by Simovic et al. [10] and the Ergun's equation [14] based models for porous debris beds. The modeling approach in the simulation utilized the Simovic model for the section with the fuel assemblies coupled to a somewhat artificial background friction terms for the free flow regions of the model (as there is no wall friction model in the code at the moment). Simulations were performed with the system pressure of 15.8 MPa, total heating power of 4291 MW, the inlet temperature of 296°C and mass flow rate of 23141 kg/s. The values correspond to the nominal thermal-hydraulic operation of the EPR.

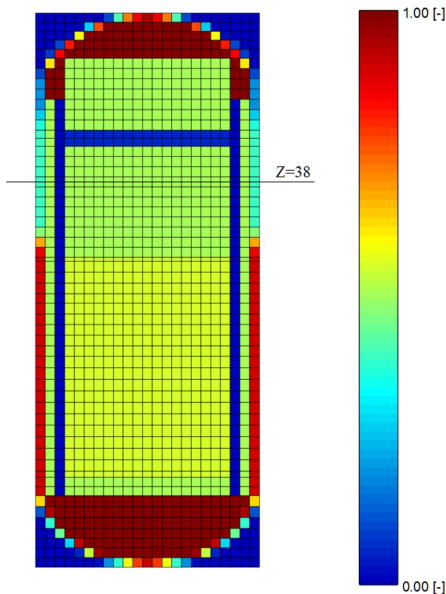


**Figure 9.** Porosity of the PORFLO model of the EPR pressure vessel (yz plane, centerline). Z=38 is the inlet/outlet level.

### EPR simulation results

The simulations were run until a converged steady-state was reached. The vectors of liquid velocity in a vertical cross-section at the centerline are shown in Figure 10 and at the horizontal cross-section at the hot and cold leg connections in Figure 11. The liquid temperature is shown in Figure 12 (maximum intensity projection).

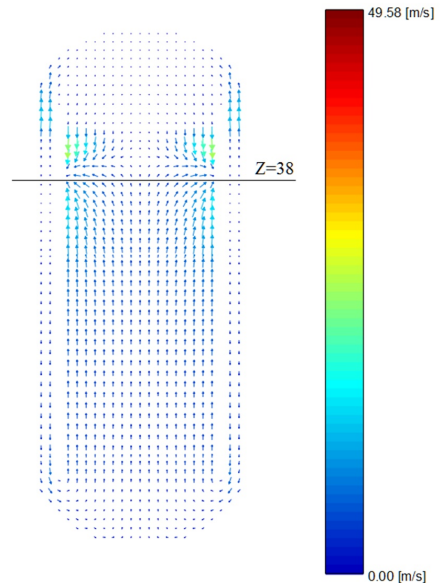


**Figure 10.** Liquid velocity in the EPR pressure vessel simulation (xz plane, centerline). Z=38 is the inlet/outlet level.

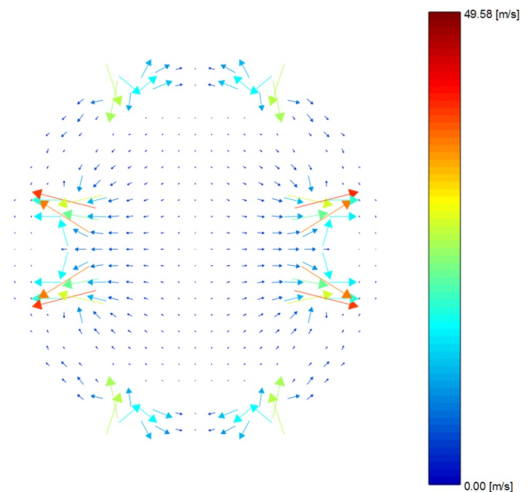


**Figure 11.** Liquid velocity in the EPR pressure vessel simulation, xy plane at the hot and cold leg connections (inlet and outlet), Z=38.

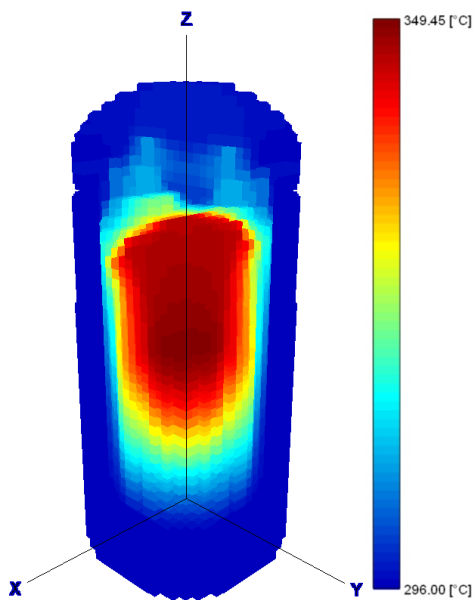


**Figure 12.** Liquid temperature in the EPR pressure vessel simulation.

It is seen that the flow direction is generally correct. Liquid flows up through the fuel and control rod guide assembly regions and down between the core barrel and the RPV wall. The outflow of hot liquid and the inflow of cold liquid are clearly distinguished in Figure 11. The region of highest liquid temperature is formed in the upper part of the active core and directly above it. A small amount of steam is generated in the topmost parts of the fuel assemblies, resulting in a void fraction of 15% at most. This suggests that the preliminary model is rather conservative: such a void fraction is not expected during normal operation.

The lateral flow and mixing in the core region can be examined by the relative mass flow rates in the axial and lateral directions in each computational cell. Averaged over the fuel bundles, the fraction of the lateral flow of the total mass flow rate through the cell faces is approximately 11%. The result appears reasonable but, due to lack of experimental or numerical 3D comparison data, the results have not yet been further evaluated. A review of the drag force models in order to find the most suitable models for the core region should also be done.

A difficulty with the present approach is the porosity distribution near the curved walls and other structures. The information of the exact locations of the walls is lost in the grid generation routine which evens out the discontinuities of porosity at the walls. The result is a checkerboard-like pattern of variable porosity in adjacent cells seen e.g. in the lower and

upper heads of the pressure vessel in Figure 9. Because of this, the flow next to the walls is not captured in a realistic manner. This may have an adverse effect on modeling of mixing phenomena. The issue could be solved by the implementation of an unstructured grid with the fuel assemblies modeled as a separate porous zone. In this case, models for wall friction and turbulence should be incorporated in order to avoid the use of artificial friction terms. Finally, the model should be validated by code-to-code comparisons (since there are no EPRs yet operating anywhere in the world and no measurement data is available).

### CORE DEBRIS BED

The severe accident management concept at the Nordic BWRs relies on the coolability of the solidified corium in a deep water pool (>10 m) in the containment. The core debris bed is cooled by two-phase flow circulation. The capability of liquid water from the pool to infiltrate the debris bed to replace evaporated water plays a key role in ensuring the removal of decay heat, and the coolability of the debris bed. The fluid flow in the debris bed interior is governed by frictional forces between the solid, liquid and gas phases. The coolability which is determined by the dryout power density is strongly dependent on porosity and particle size as well as the homogeneity and geometry of the bed.

Traditionally, in the assessment of debris coolability, critical heat flux correlations as well as 0D and 1D models have been applied. In recent years, steps towards CFD style approaches have been taken as the main focus has been on 2D models. These models are capable of predicting the pressure gradient in case of multi-dimensional water infiltration into the debris bed. This facilitates the modeling of realistic (heap-like) bed geometries. The PORFLO model of the porous debris bed is the first attempt known to the authors to simulate the flows in the debris bed in 3D. Thus, in its own specific field of study, the modeling approach has considerable novelty value.

As a first task, the friction and heat transfer models suitable for two-phase flows in porous beds were incorporated into the code [15]. In this work, the documentation of the MEWA severe accident analysis code [16] was used as a guideline along with the original publications by the model developers. The assessment of the MEWA code against the COOLOCE (Coolability of Cone) experiments conducted at VTT is addressed in another paper in these Proceedings [17]. The COOLOCE experiments focused on comparing the coolability of conical (heap-like) and cylindrical (evenly-distributed) debris beds. This is also the main goal of the simulations. The drag force models used in the simulations are based on the Ergun's equation [14] for pressure loss in porous media. An extensive summary of the heat transfer and drag models for debris beds can be found in [18].

3D grids for both debris bed geometries were generated for the calculation. First, the model was tested with a coarse grid of  $21 \times 21 \times 28$  computational cells yielding 3 cm cell size. After it was found that the dryout process (the increase in void fraction and the directions of the phase velocities) was

approximated correctly - and convergent results had been obtained - the density of the grid was increased to  $41 \times 41 \times 55$  cells (1.5 cm cell size).

Two variations of the dense grid were made: a uniform bed and a non-uniform bed that accounts for the effect of the heaters of the experimental debris bed. The uniform conical and cylindrical debris beds with the 1.5 cm cell size are illustrated in Figure 13 which shows porosity mapped on the vertical 2D cross-section in the center of the grid. A total of six simulation cases have been run which help to evaluate the performance of the code and also increase the basic understanding of the dryout processes of the different debris bed geometries and flow configurations.

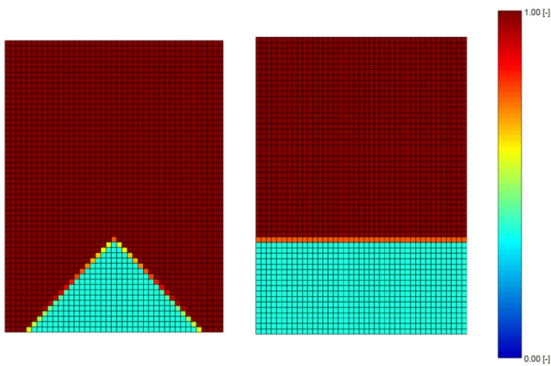


**Figure 13.** Porosity of the conical (left) and the cylindrical (right) debris beds (vertical cross-section in the center of the model,  $x=0.3$  m).

### Debris bed simulation results

In the simulations, the power generation distributed into the debris bed was used as input while the aim was to pin-point the dryout power level by simulations with stepwise power increases. The criterion of dryout (a non-coolable state) was the formation of the first dry zone (void fraction equal to 1.0) somewhere in the debris bed interior. The void fraction in dryout conditions for the conical and cylindrical debris beds are illustrated in Figure 14 and Figure 15, respectively.

The incipient dryout is formed in the upper part of the geometry in case of the conical bed. This is because the bottom of the debris bed is cooled by multi-dimensional infiltration of water through the surface of the cone. The two-phase flow in the debris bed is co-current. In this type of flow configuration, the mass flux of steam has to be great enough so that it replaces water in an entire (horizontal) cross-section of the bed in order for the geometry to reach dryout. The dryout power density in the simulation is  $2570 \text{ kW/m}^3$ .

In Figure 14, again a pattern resembling a checkerboard is seen in the void fraction distribution near the surface of the cone where some cells have a distinctly high void. This might be an artifact caused by the still relatively coarse grid and an

uneven distribution of porosity at the interface of the debris bed and the pool volume surrounding it. This issue could possibly be solved by improving the computational grid.

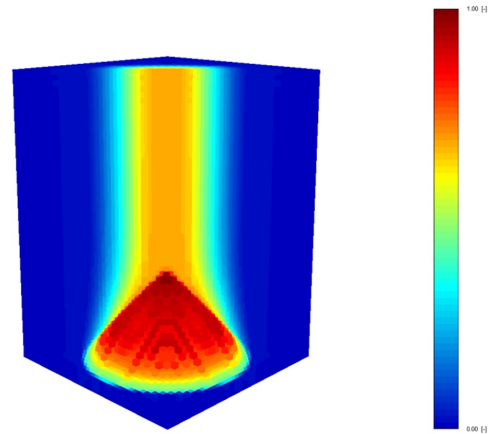


**Figure 14.** Post-dryout void fraction in the conical debris bed.

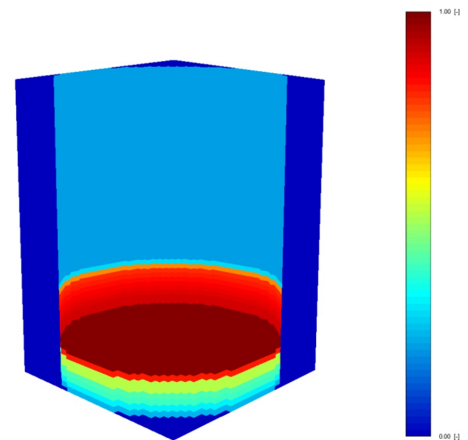


**Figure 15.** Post-dryout void fraction in the cylindrical debris bed.

Dryout is seen in the central and lower parts of the geometry in the case of the cylindrical bed. In this case, the void fraction is constant in radial direction, i.e. the dryout behavior is effectively one-dimensional, and a relatively large volume has dried-out. The dryout is followed by a rather drastic temperature increase compared to the conical in which only a small dryout zone, partially cooled by the heavy steam, flow is observed. This type of dryout development is in accordance with theoretical knowledge of dryout in top-flooded debris beds. However, because dryout occurs somewhat above the

bottom of the bed in the simulation, the power may be slightly exaggerated (greater than the minimum dryout power). The dryout power density in the simulation is  $1250 \text{ kW/m}^3$ .

The results suggest that the main features of the dryout development in both geometries are captured by the code. According to the results, the dryout power density of the conical debris bed is about twice the corresponding value of the cylindrical bed. In the light of previous studies, the relative difference is reasonably accurate. However, this result is valid only for debris beds of equal height. If the debris beds of different geometries are spread with equal radius and volume, the dryout power density of the cylindrical bed is actually smaller as explained in [17].

The dryout power measured in the experiments at near-atmospheric pressure (1.1 bar) was approximately  $1400 \text{ kW/m}^3$  for the conical test bed and  $1000 \text{ kW/m}^3$  for the cylindrical test bed. Compared to these results (described in detail in [5] and [17]), the present model tends to over-predict the dryout power by 25-80%. The possible reasons for the discrepancy are the rather coarse grid model or the implementation of the porous media friction models which will be verified in future simulations. Nevertheless, the simulations suggest that 3D approach could be feasible in the analyses of debris bed coolability. More simulations of the COOLOCE experiments can be found in [17] in which the effect of the heaters and MEWA code validation is discussed.

## FUTURE PERSPECTIVE

A problem common to all the three applications presented above is the loss of exact knowledge of walls – even those which could be represented with a reasonable number of mesh cells. In areas of fine detail, like the numerous fuel pins in the core, the only option is some kind of porous medium description. On the other hand, the large pressure vessel structures such as the inner walls of the SG shell or the COOLOCE experimental vessel and the downcomer and lower plenum of the reactor could well be fitted with the mesh. Now when the walls are ‘blurred’ in the Cartesian grid, we cannot have realistic wall friction and source of turbulence there. Wall friction has to be represented by more global pressure losses. These shortcomings affect both the resolved flow field and mixing phenomena. Other problems, traced to the fact that velocities are staggered at the faces of the pressure cells, were encountered with void fractions at the free water surface in the SG application.

Recently, a major overhaul of the PORFLO code was initiated. The main change is the introduction of general collocated, unstructured (i.e. structure-fitted) grids that can be generated using available meshing tools and read by PORFLO from a CGNS (CFD General Notation System) file. Then it is possible to fit the grid to those structures that can be represented by an affordable number of cells, and use variable porosity elsewhere when needed. As the change is big enough to be described as rewriting of the code, parallelization based on domain decomposition using Open MPI library at the level

of linear solvers was programmed at the same time. Other current and future developments include

- “libraries” of closure laws
- different types of boundary conditions
- further improvement of calculation speed by both algorithmic and coding developments
- robustness by e.g. gradient reconstruction methods
- turbulence modeling with two phases in a porous medium
- improved steam tables
- solution strategy for transients with changing pressure and density of steam
- division of phases into fields (like continuous liquid and droplets)
- interfacial area transport (IAT)
- coupling issues with neutronics and system codes

PORFLO has been developed over several years but only with small resources. However, the work will continue and it is envisioned that in the long-term future PORFLO will be an in-house tool for all safety-related thermal-hydraulic transients which may be encountered in Finland’s NPPs (two VVERs and two BWRs in operation, an EPR under construction and two future plants) and in which a 3D simulation approach could be beneficial. Examples of components for 3D modeling - in addition to the already discussed reactor pressure vessel, steam generator and core debris bed - are spent fuel storage and various passive safety systems with heat exchangers e.g. an isolation condenser.

Finally, we point out the main benefits seen in in-house code development: In comparison with FLUENT or other commercial codes, the complete source code is available and well-known to developers. On the other hand, in comparison with OpenFOAM or other open source code projects, the code was written from the start with the specific goal of nuclear applications and coupling to other nuclear-specific codes.

## CONCLUDING REMARKS

The PORFLO code has been developed for solving two-phase flow problems related to nuclear power plant safety analysis. Three of the modeling applications of the code from different areas of thermal hydraulics have been summarized in this paper. The presented models were the VVER steam generator, the EPR pressure vessel and the core debris bed. The first two models deal with the normal operation conditions of a nuclear power plant but the final application considers the porous, ex-vessel debris bed formed in the case of a severe accident. For all the modeled cases, the geometry of the modeled component has been discretized to a regular 3D grid. Various calculations with application-specific drag and heat transfer models have been performed.

The code to code comparison of the PORFLO and FLUENT simulations of the horizontal steam generator suggests a relatively good agreement. Some code development

targets, however, were identified. According to the debris bed simulations, it appears that the PORFLO model is capable of capturing the main processes of dryout development. The EPR RPV simulation also shows reasonable flow behavior but no comparisons to other codes or model review have yet been done. The development of the code will continue on several different topics with the long-term goal of developing a general-purpose CFD code applicable for 3D thermal hydraulics and safety assessment.

#### ACKNOWLEDGMENTS

The PORFLO development and simulations have been financed by the SAFIR2014 Finnish Research Programme on Nuclear Power Plant Safety and its predecessor SAFIR2010.

#### REFERENCES

1. Patankar, S.V. 1980. Numerical Heat Transfer and Fluid Flow. New York, Hemisphere Publishing Corporation. 197 p. ISBN 0-89116-552-3.
2. Hovi, V., Ilvonen, M. 2011. The 3D two-phase porous medium flow solver PORFLO and its applications to VVER SG and EPR RPV. SAFIR2010 Final Report. VTT Research Notes 2571. Helsinki, Finland, 2011. Pp. 160-170. ISBN 978-951-38-7689-0.
3. Hovi V., Ilvonen, M. 2010. 3D PORFLO simulations of Loviisa steam generator. AER Symposium, September 20-24, 2010, Espoo, Finland.
4. Pättikängas, T.J.H., Niemi, J., Hovi, V., Toppila, T., Rämä, T. 2010. Three-Dimensional Porous Media Model of a Horizontal Steam Generator. In: CFD for Nuclear Reactor Safety Applications (CFD4NRS-3) Workshop. Bethesda, MD, 14-16 September 2010.
5. Takasuo, E., Kinnunen, T., Pankakoski, P.H., Holmström, S. 2011. The COOLOCE coolability experiments with a conical geometry: Test series 6-7. Research Report VTT-R-07097-11. Espoo, 2011. 26 p.
6. Miettinen, J., Karppinen, I. 2003. A Porous Media Calculation Applications for the Isolation Condenser Heat Transfer and Circulation. The 10th International Topical Meeting on Nuclear Reactor Thermal Hydraulics (NURETH-10). Seoul, Korea, October 5-9, 2003.
7. Neykov, B., Aydogan, F., Hochreiter, L., Ivanov, K. Utsuno, H., Kasahara, F., Sartori, E., Martin, M. 2005. NUPEC BWR Full-size Fine-mesh Bundle Test (BFBT) Benchmark. Volume I: Specifications. NEA/NSC/DOC(2005)5. OECD Nuclear Energy Agency, 2006. ISBN 92-64-01088-2.
8. Ilvonen, M., Hovi, V. 2009. The porous medium model PORFLO for 3D two-phase flow and its application to BWR fuel bundle simulations. SAFIR2010 Interim Report. VTT Research Notes 2466. Helsinki, Finland, 2009. Pp. 231-141. ISBN 978-951-38-7266-3.
9. Hovi, V. 2008. Calculations of Boiling Two-Phase Flow Using a Porous Media Model. Master's Thesis. Lappeenranta University of Technology. 112 p.
10. Simovic, Z. R., Ocoolkjic S. and Stevanovic V. D. 2007. Interfacial friction correlations for the two-phase flow across tube bundle. International Journal of Multiphase Flow, Vol. 33, pp. 217-226.
11. Ishii, M. and Zuber, N. 1979. Drag coefficient and relative velocity in bubbly, droplet or particulate flows. American Institute of Chemical Engineers Journal, Vol. 25, Issue 5, pp. 843-855.
12. Incropera, F. P., DeWitt, D. P. 2002. Fundamentals of Heat and Mass Transfer, 5<sup>th</sup> edition. John Wiley & Sons, Inc. 981 p. ISBN 0-471-38650-2.
13. Groeneveld, D. C., Snoek, C. W. 1986. A Comprehensive Examination of Heat Transfer Correlations Suitable for Reactor Safety Analysis. In: Hewitt, G. F., Delhaye, J. M., Zuber, N. Multiphase Science and Technology, Vol. 2. Hemisphere. pp. 181-274. ISBN 0-89116-283-8.
14. Ergun, S. 1952. Fluid flow through packed columns. Chemical Engineering Progress 48, 89-94.
15. Takasuo, E. Hovi, V., Ilvonen, M. 2011. PORFLO modelling of the coolability of porous particle beds. Research Report VTT-R-09376-10. Espoo, 2011. 41 p.
16. Bürger, M., Buck, M., Schmidt, W., Widmann, W. 2006. Validation and application of the WABE code: Investigations of constitutive laws and 2D effects on debris coolability. Nuclear Engineering and Design, 236, pp. 2164-2188.
17. Takasuo, E., Hovi, V., Ilvonen, M., Holmström, S. 2012. Modeling of dryout in core debris beds of conical and cylindrical geometries. Proceedings of the 20th International Conference on Nuclear Engineering, July 30 – August 3, 2012, Anaheim, California, USA. ICONE20-54159.
18. Schmidt, W. 2004. Influence of Multidimensionality and Interfacial Friction on the Coolability of Fragmented Corium. Doctoral Thesis, Institut für Kernenergetik und Energiesysteme, Universität Stuttgart.
19. Takasuo, E., Holmström, S. Kinnunen, T., Pankakoski, P.H., Hosio, E., Lindholm, I. 2011. The effect of lateral flooding on the coolability of irregular core debris beds. Nuclear Engineering and Design 241, pp. 1196-1205.

PUBLICATION V

**Evaluation of an effective diameter  
to study quenching and dry-out  
of complex debris bed**

Annals of Nuclear Energy (74), 24–41.  
Copyright 2014 Elsevier Ltd.  
Reprinted with permission from the publisher.



ELSEVIER

Contents lists available at ScienceDirect

## Annals of Nuclear Energy

journal homepage: [www.elsevier.com/locate/anucene](http://www.elsevier.com/locate/anucene)

# Evaluation of an effective diameter to study quenching and dry-out of complex debris bed<sup>☆</sup>



N. Chikhi<sup>a,\*</sup>, O. Coindreau<sup>a</sup>, L.X. Li<sup>b</sup>, W.M. Ma<sup>b</sup>, V. Taivassalo<sup>c</sup>, E. Takasuo<sup>c</sup>, S. Leininger<sup>d</sup>, R. Kulenovic<sup>d</sup>, E. Laurien<sup>d</sup>

<sup>a</sup> Institut de Radioprotection et de Sûreté Nucléaire (IRSN), Cadarache, France

<sup>b</sup> Royal Institute of Technology (KTH), Stockholm, Sweden

<sup>c</sup> Technical Research Centre of Finland (VTT), Espoo, Finland

<sup>d</sup> Institute of Nuclear Technology and Energy Systems (IKE), University of Stuttgart, Germany

## ARTICLE INFO

## Article history:

Received 12 December 2013

Accepted 6 May 2014

Available online 13 June 2014

## Keywords:

Debris bed coolability

Quenching

Dry-out

Effective diameter

## ABSTRACT

Many of the current research works performed in the SARNET-2 WP5 deal with the study of the coolability of debris beds in case of severe nuclear power plant accidents. One of the difficulties for modeling and transposition of experimental results to the real scale and geometry of a debris bed in a reactor is the difficulty to perform experiments with debris beds that are representative for reactor situations. Therefore, many experimental programs have been performed using beds made of multi-diameter spheres or non-spherical particles to study the physical phenomena involved in debris bed coolability and to evaluate an effective diameter. This paper first establishes the ranges of porosity and particle size distribution that might be expected for in-core debris beds and ex-vessel debris beds. Then, the results of pressure drop and dry-out heat flux (DHF) measurements obtained in various experimental setups, POMECA, DEBRIS, COOLOCE/STYX and CALIDE/PRELUDE, are presented. The issues of particle size distribution and non-sphericity are also investigated. It is shown that the experimental data obtained in “simple” debris beds are relevant to describe the behavior of more complex beds. Indeed, for several configurations, it is possible to define an “effective” diameter suitable for evaluating (with the porosity) some model parameters as well as correlations for the pressure drop across the bed, the steam flow rate during quenching and the DHF.

© 2014 Elsevier Ltd. All rights reserved.

## 1. Introduction

It is acknowledged that in the late stages of a severe accident in a nuclear reactor core, accumulations of fuel and structure materials, commonly called debris beds, may be formed. Such debris beds may be formed in the core after collapse of the fuel rods or in the lower plenum of the reactor pressure vessel after melt–water interaction. Both configurations have been observed in the TMI-2 reactor (Broughton et al., 1989). Similarly, a debris bed may form in the reactor pit when it is filled with water, after failure of the vessel and melt–water interaction.

The NEA/SARNET2 Workshop on “In-vessel coolability” (Amri and Clement, 2009) and the SARNET-SARP group (Schwings

et al., 2010) considered the question of debris coolability to be a high priority issue. Many of the current research works performed in the SARNET-2 WP5 deal with the study of the coolability of such debris beds. One of the difficulties for modeling is the transposition of experimental results to the real scale and geometry of a debris bed in a reactor. First, processes of debris formation are very complex and make it very difficult to manufacture similar debris for an experiment. Secondly, even if it would be possible to manufacture realistic debris, the bed itself results from a stochastic collapse of particles of various sizes, and there are infinite possible debris bed configurations, that could result from a sample initial damaged geometry. Therefore, any modeling must use some assumptions and extrapolations in order to use experimental data obtained with a set of particular debris beds in models that can be applied to any debris bed.

The question arises whether the complex debris bed can be characterized by only few parameters that are used in the constitutive laws. Especially, is it possible to describe a complex debris bed with only one diameter, i.e. an effective diameter?

<sup>☆</sup> 6th European Review Meeting on Severe Accident Research (ERMSAR-2013) Avignon (France), Palais des Papes, 2–4 October, 2013.

\* Corresponding author. Tel.: +33 4 42 19 97 79.

E-mail address: [nourdine.chikhi@irsn.fr](mailto:nourdine.chikhi@irsn.fr) (N. Chikhi).

Two approaches have been used up to now. The first step consists in measuring some characteristics of the debris bed such as the pressure drop across the bed or the Dry-out Heat Flux (DHF) (Lindholm et al., 2006; Takasuo et al., 2011; Rashid et al., 2008; Rashid et al., 2011, 2012). In this first approach, a model (as Lipinski (1982) for the DHF model) involving an equivalent diameter is needed. The equivalent diameter that gives the best agreement between the model and the experiment is considered as the effective diameter (Kulkarni et al., 2010). In the second approach, the results (the DHF or the quenching velocity for example) obtained in realistic configurations are compared with results obtained in monodisperse beds of various sizes. The diameter of the monodisperse bed that is the most suitable to represent the realistic bed is considered as the effective diameter.

This paper first establishes the ranges of porosity and particle size distribution that might be expected for in-core debris beds and ex-vessel debris beds. Then, the results obtained in various experimental setups, POMECO, DEBRIS, COOLOCE/STYX and CALIDE/PRELUDE, are presented and analyzed. The issues of particle size distribution and non-sphericity are also investigated. Finally, the knowledge gained from the experimental works and the common findings are drawn.

## 2. Typical particle distribution and porosity ranges for realistic debris beds

### 2.1. In core debris bed

Debris could form in the reactor core of a PWR in case of water injection to slow down a core meltdown accident transient. Several observations indicate that this phenomenon occurred during the TMI-2 accident (Akers et al., 1986; McCardell et al., 1990) and in severe fuel degradation experiments like LOFT (Coryell et al., 1994; Hobbins and McPherson, 1990), PBF (Petti et al., 1989) and PHEBUS.

The examination of the debris bed formed in the TMI-2 core by ten debris grab samples analysis (Akers et al., 1986) have shown that the samples can be divided in three parts. In the first part, the largest amount of material is in the greater than 4 mm fraction. In the second part, 80–86 wt% of the sample material is larger than 1 mm in size with the 1.68–4 mm particle size containing the most material. For the third part, the fraction of the sample material larger than 1 mm is less than 75 wt%. There is a bimodal distribution of particles with the major peak lying at the 1.68–4 mm size fraction and a minor peak at the 0.3–0.71 mm size fraction. For these samples, located in the depth of the debris bed, settling of the fine material and/or washout of the fine material from the upper layers has probably occurred. This analysis has shown us that the particles in the TMI-2 core are mostly millimeter-sized.

Concerning fuel particles, it was observed in the rubble beds formed in the upper part of the bundle in the LOFT LP-FP-2 (Coryell et al., 1994; Hobbins and McPherson, 1990) and in the PBF-SFD (Petti et al., 1989) that their size is set primarily by the crack distribution prior to the transient. Indeed, the pellet cracking occurs right from the beginning of the reactor operation as consequence of differential expansion between the centre of the pellet and the periphery. The final number of radial fragments ranges from 10 (Walton and Husser, 1983) to 16 (Oguma, 1983) leading to a minimum equivalent fuel diameter ( $d_{\text{sauter}}$ , see Section 3.1) of 2 mm for fuel pellet of 13.5 mm height and 8.2 mm diameter according to (Coindreau et al., 2013). Under accident conditions, additional fuel cracking could occur with very highly irradiated fuel (Kolstad et al., 2011). This has been attributed to the formation of the High Burn-Up Structure (HBS) in the periphery of PWR fuel  $\text{UO}_2$  pellet beyond 40 GW d/t<sub>U</sub>. If fine particles from the HBS struc-

ture, whose size can reach around 30  $\mu\text{m}$  (Hiernaut et al., 2008) are considered, it can contribute to a significant decrease of the mean diameter of fuel particles. The occurrence of this phenomenon for moderately to highly irradiated fuel is not proven but it is not excluded that fine particles could come from the most irradiated fuel assemblies of the reactor core. Concerning cladding particles, they are millimetre-sized. It can be computed that their equivalent diameter ( $d_{\text{sauter}}$ , see Section 3.1) ranges between 1.1 and 1.7 mm for an inner cladding diameter of 8.36 mm and a thickness of 570  $\mu\text{m}$  (Coindreau et al., 2013). It is more difficult to evaluate the size of prior molten material particles.

The porosity of the debris bed formed during the TMI-2 accident can be deduced from measurements of the bulk tap density of the core debris grabbed samples that ranges between 3.5 and 5.5  $\text{g cm}^{-3}$  (Akers et al., 1986). This corresponds to a porosity ranging between 0.35 and 0.4 (depending on the assumption about the material composition) for the denser sample to a porosity higher than 0.55 for the less dense material. The 0.37–0.4 range corresponds to the porosity of an unarranged configuration of mono-sized spheres (Dias et al., 2005). For mixed spherical particles, the porosity can be lower, depending on the size distribution. If fine particles coming from the HBS structure are mixed with coarse particle, it was computed that a minimum theoretical value of 0.35 could be reached for fuel with a burn-up of 60 GW d/t<sub>U</sub> (Coindreau et al., 2013). For moderately irradiated fuel, the average porosity of 0.4, usually used in coolability analyses for instance in Bürger et al. (2006), consequently seems to be reasonable.

### 2.2. Ex-vessel and lower plenum debris bed

If the damaged core cannot be cooled, the molten corium will relocate downwards, and finally fall into the water pool in the lower plenum. The melt fragments in the coolant, and a debris bed is expected to form on the pool bottom. If the debris is not coolable there either, it will re-melt. Ultimately, the vessel will fail under the aggressive attack of the molten corium in the lower plenum, and the melt jet ejected into the cavity under beneath the RPV. In case the cavity is flooded (as a strategy of severe accident management or a result of containment spray), the melt jet will breakup and the debris will settle down on the floor.

In order to obtain the characteristics (porosity, particle morphology and size distribution, etc.) of so-formed debris beds for coolability study, a good number of fuel-coolant interaction (FCI) experiments has been carried out during the past two decades. The debris bed of interest is formed because of the corium fragmentation and settlement in the coolant. Thus, the first question of coolability significance is how the debris bed looks like. Among them are the well-known FCI tests CCM, KROTOS, FARO, TROI and COTELS programs, as well as the DEFOR tests dedicated to debris bed formation.

Corium-Coolant Mixing (CCM) tests were performed in Argonne National Laboratory to investigate the phenomena associated with molten fuel-coolant interaction (Spencer et al., 1994). Molten corium (60%  $\text{UO}_2$ , 16%  $\text{ZrO}_2$ , 24% SS at  $\sim 2800^\circ\text{C}$ ) fell through a water pool around one meter in depth. Table 1 shows the initial conditions and some debris characteristics of the series of 6 CCM tests.

The CCM-1 test had mass of 2.15 kg, and the formed debris bed was heap-like with loosely bound and sintered particles. All sizes and shapes of particles were present, with many spheroidal and ellipsoidal fragments. Typical particle diameter is 3 mm, with fragments having diameters of over 10 mm. A large number of the particles were hollow shells. CCM-3 was similar to CCM-1 except for a higher water temperature near saturation and a higher porosity. CCM-4 test was identical to CCM-1 except a larger melt mass and ejection diameter. Similar debris bed was obtained with a higher porosity. Interestingly, it was found that the variation in

**Table 1**  
Initial conditions and porosity of CCM tests (Spencer et al., 1994).

Parameter	Test					
	CCM-1	CCM-2	CCM-3	CCM-4	CCM-5	CCM-6
Corium mass (kg)	2.15	11.15	3.43	9.24	11.34	12.79
Jet diameter (mm)	25.4	4 × 20.2	25.4	50.8	50.8	50.8
Water pool depth (m)	1.06	0.63	1.1	1.07	1.07	1.07
Vessel diameter (m)	0.21	0.21	0.21	0.21	0.76	0.76
Water temperature (°C)	57.4	99.0	100.3	63.3	55.4	100.8
Initial pressure (bar)	1.1	1.75	3.15	3.55	1.34	2.01
Free fall (mm)	454	435	412.8	447.7	339.7	339.7
Debris bed height (mm)	15.9–27	45	19–38	n/a	0–42	0–40
Mean particle size (mm)	2.3	0.8	4.0	1.0	5.0	3.5
Porosity (%)	53	68	65	63	67	63

mean particle size appeared little effect on the porosity. For instance, the mean particle size of CCM-5 was 5 times that of CCM-4, but they had almost the same porosity. By arithmetic average, (Lindholm, 2002) took the average particle size of all CCM test as 2.7 mm. For a bed packed with spherical particles at such a diameter, the mean porosity is ~0.39 (Schmidt, 2004), which is much less than average porosity obtained in the CCM tests.

The old KROTOS tests (Huhtiniemi et al., 1997; Huhtiniemi and Magallon, 1999) were conducted at JRC-Ispra to study energetic fuel-coolant interaction (steam explosion) with corium composition of 80% UO<sub>2</sub>–20% ZrO<sub>2</sub>, and an external trigger. Although steam explosion was not obtained with corium melt poured into highly subcooled or near-saturated water pool, the average particle sizes (varied from 1.0 to 1.7 mm) were much smaller than those of the CCM tests.

The FARO tests (Magallon and Huhtiniemi, 2001; Magallon et al., 1999), also performed at JRC-Ispra, employed much more mass to investigate corium jet breakup and quench during the penetration of molten corium into the water pool. Altogether 12 tests were performed in FARO program, with most tests having more than 100 kg mixture of 80% UO<sub>2</sub>–20% ZrO<sub>2</sub>. One of the findings of the FARO tests was the formation of cakes which are solid chunks of corium without breakup. The worst case is L-19 where the cake mass is up to 50% of the total discharge of corium. Even for the test L-29 with low temperature and high subcooled water pool, no loose particle debris was found, and all debris were agglomerated to cake (Magallon and Huhtiniemi, 2001). In the FARO tests, the diameter of water pool is around 0.7 m. Yet, the debris did not uniformly spread on the bottom, and heap-like debris beds were obtained. Various particle shapes were observed, with the size varying between 0.25 and 11 mm. The mean particle sizes for some tests are from 2.5 mm to 4.8 mm, which are obviously larger than those of the KROTOS tests.

The COTELS tests (Kato and Nagasaka et al., 1999) in Japan were carried out to investigate energetic corium water interaction, but no violent steam explosion was observed. The corium was 60 kg mixture of 55% UO<sub>2</sub>–25% Zr–5% ZrO<sub>2</sub>–15% SS, supposed to simulate BWR corium composition. Most of poured corium was broken up and only a small amount of ingot corium (cake) was found on the pool bottom. The sizes of corium particles were ranging from a few hundred microns to more than 10 mm. The shape was spherical in middle size, while it was irregular in both small and large sizes. Particles had many pores not only on their surfaces but also inside.

The TROI tests (Song and et al., 2003) were performed at KAERI to investigate the probability of energetic steam explosion. Among the large number of tests are TROI-13, TROI-14 and TROI-15 which had steam explosion. TROI-13 and TROI-14 used corium of 69% UO<sub>2</sub>–30% ZrO<sub>2</sub>–1% Zr, while TROI-15 used 99% ZrO<sub>2</sub>–1% Zr. The main finding of the TROI tests in term of debris characteristics is the large amount of fine particles (<0.7 mm). The result of TROI-

15 indicates there is also a strong effect from the material composition. Among various debris shapes are hollow-shell zirconia debris and solid corium debris.

The DEFOR tests (Karbojian and Ma, 2009; Kudinov et al., 2010) were performed at KTH to investigate study of debris bed formation in severe core melt accident of a light water reactor (LWR), using different corium simulant materials CaO–B<sub>2</sub>O<sub>3</sub>, WO<sub>3</sub>–CaO, WO<sub>3</sub>–Bi<sub>2</sub>O<sub>3</sub> or MnO–TiO<sub>2</sub>. The test results revealed a strong dependence of the resulting debris bed characteristics on water subcooling and pool depth. As the pool depth decreases, the debris may reach the bed in a liquid state, rendering agglomeration and even cake formation. With the decreased water subcooling, intense evaporation and mixing occurred, leading to a more uniform spreading of melt/debris over a larger floor area. The DEFOR experiments showed that the coolant subcooling influences not only jet breakup, but also particle sizes distribution and bed formation. The porosity of the resulting debris beds is higher (up to 60%) than the traditionally assumed value of 40% obtained from packed bed of spherical particles. Debris agglomeration and cake formation were also observed in the DEFOR tests, contingent upon the pool's depth, water subcooling, and melt superheating. The porosity of the bed with cake formation is still relatively high (45%), but largely due to the internal encapsulated porosity. The size distribution and morphology of debris particles are similar to those observed in the above tests carried with prototypical material. Notably, the porosity of the debris bed obtained after the melt-coolant interactions is fairly insensitive to the melt composition materials.

When confronted with the FCI fragments which are non-spherical and/or have a broad size distribution in a debris bed, a natural question is what is the equivalent particle diameter suitable for coolability analysis of the debris bed? In paragraph 3, the definition of different equivalent and mean diameters is recalled. The computation of the equivalent and mean diameters only relies on the number, the size and the shape of the particles. Several of these diameters, including area mean and mass mean diameters, have been seen in coolability studies and thus considered as the effective diameters. The determination of the effective diameter and the identification of the equivalent diameter which is the closest to him is the subject of paragraph 4.

### 3. Bed and two-phase flow description

#### 3.1. Bed description

When considering a system of unequally-sized spherical particles, a useful parameter is the mean diameter that can be defined as:

$$d_{p,q} = \left( \frac{\sum n_i d_i^q}{\sum n_i d_i^1} \right)^{1/p-q} \quad (1)$$

With  $n_i$  the number of particles of diameter  $d_i$ . Weight fractions ( $w_i$ ) can also be used with the following relationship if all particles have the same density:

$$w_i = \frac{n_i d_i^3}{\sum n_i d_i^3} \quad (2)$$

Table 2 summarizes some mean diameters that will be used in this paper.

If the particles are irregularly shaped, it is convenient for modelling purpose to represent the particles by equivalent spherical particles. If  $V$  is the volume of the irregularly shaped objects and  $A$  their surface area, three equivalent diameters can be defined. The equivalent spherical particles exhibit one identical property to that of the non-spherical particles. In case of for spherical particles, it is worth mentioning that the Sauter diameter and the surface mean diameter are equal.

The sphericity coefficient (also named shape factor) can also be introduced in the study of non-spherical particles:

$$\Psi = \frac{\pi^{1/3} (6V)^{2/3}}{A} \quad (3)$$

The  $\Psi$  factor is equal to the square of the ratio between  $d_v$  and  $d_s$  and is equal to 1 for spherical particles.

### 3.2. Two-phase flow description

Single-phase flow in porous media is generally modeled using the Forchheimer's equation (Forchheimer, 1914) which includes a term to the Darcy's law (Darcy, 1856) to account for inertial effects:

$$-\frac{dp}{dz} = \rho g + \frac{\mu}{K} J + \frac{\rho}{\eta} |J| \times J \quad (4)$$

where  $dp/dz$  is the pressure gradient,  $\mu$  the dynamic viscosity,  $J$  the superficial velocity (flow rate per unit of total cross section of the bed),  $\rho$  the fluid density,  $K$  the permeability and  $\eta$  the passability.

The above equation contains two unknown coefficients: the permeability and the passability.

A lot of studies were devoted to predict the  $K$  and  $\eta$  parameters by measuring the pressure drop for a single-phase flow in a porous medium. In case of bed packed with single size spherical particles, one of the mostly used is the well known Kozeny–Carman's equation for the permeability  $K$  and the Ergun's law (Ergun, 1952) for the passability  $\eta$ :

$$K = \frac{\varepsilon^3 d^2}{36k_0 \tau^2 (1 - \varepsilon)^2} = \frac{\varepsilon^3 d^2}{A(1 - \varepsilon)^2} \quad (5)$$

$$\eta = \frac{\varepsilon^3 d}{B(1 - \varepsilon)} \quad (6)$$

With  $\varepsilon$  the porosity of the medium,  $k_0$  a shape parameter,  $\tau$  the tortuosity and  $d$  the mean particle diameter.

Different values for the parameters  $A$  and  $B$  were determined: Ergun proposed in 1952  $A = 150$  and  $B = 1.75$  and Macdonald et al., 1979  $A = 180$  and  $B = 1.8$  (Macdonald et al., 1979). It remains an unknown parameter, the mean particle diameter  $d$ . It is defined as the diameter of a hypothetical sphere with the same specific surface area as the porous medium.

In the case of beds packed with multi-diameter spherical or non-spherical particles, it is doubtful whether the Ergun law can still be used. If yes, what should be the equivalent diameter of such beds?

To access the relative contribution of the passability term with respect to the permeability, it is convenient to introduce the Reynolds number in porous media  $Re_p$  (Rhodes, 1989). It leads to the following equations if Eqs. (5) and (6) are used for the permeability and the passability:

$$\frac{\text{passability\_term}}{\text{permeability\_term}} = \frac{\rho K}{\eta \mu} J = Re_p \frac{B}{A} \quad (7)$$

with

$$Re_p = \frac{\rho J d}{\mu(1 - \varepsilon)} \quad (8)$$

The above-mentioned values for the  $A$  and  $B$  parameters give a Reynolds number ranging between 85 (for  $A = 150$  and  $B = 1.75$ ) and 100 (for  $A = 180$  and  $B = 1.8$ ) for an equal contribution of viscous and inertial forces. For  $Re_p < 85$ , the flow can be considered as laminar with viscous forces prevailing. For  $Re_p > 100$  the contribution of the passability prevails.

It is important to notice that the Reynolds number depends on the particle size. Therefore, for a same flow rate, the dominant term can be either the permeability or the passability depending on the particle size. Regarding the data range expected during debris bed cooling (in/ex vessel) for the fluid velocity ( $0 \text{ cm/s} < v_l < 4 \text{ cm/s}$ ,  $0 \text{ m/s} < v_g < 10 \text{ m/s}$ ), the porosity ( $0.4 < \varepsilon < 0.8$ ) and the particle size ( $1 \text{ mm} < d < 8 \text{ mm}$ ), the Reynolds numbers expected during reflow/dryout are as follows:  $0 < Re_p < 600$ . Thus, one can conclude that both regimes (laminar and turbulent) must be considered in the study of debris bed coolability.

The modeling of two-phase flow in porous media is based on the generalization of the Forchheimer's equation for the two fluids (Buchlin and Stubos, 1987):

$$-\frac{dp_g}{dz} = \rho_g g + \frac{\mu_g}{K_{rg}} J_g + \frac{\rho_g}{\eta_{rg} \times \eta} |J_g| \times J_g \quad (9)$$

$$-\frac{dp_l}{dz} = \rho_l g + \frac{\mu_l}{K_{rl}} J_l + \frac{\rho_l}{\eta_{rl} \times \eta} |J_l| \times J_l \quad (10)$$

with subscript standing either for the gas (g) or the liquid (l) phase.

The above equations contain four unknown coefficients in addition to the permeability and the passability: the relative permeabilities ( $K_{rg}$ ,  $K_{rl}$ ) and the relative passabilities ( $\eta_{rg}$ ,  $\eta_{rl}$ ). In other models (Schulenberg and Müller, 1987; Tung and Dhir, 1988),

**Table 2**  
Definition of mean diameters for a distribution of unequally-sized spherical particles.

Symbol	Name	$p, q$ values	Expression	Properties conserved
$d_{(n)}$	Count mean diameter	$p = 1, q = 0$	$\frac{\sum n_i d_i}{\sum n_i} = \frac{\sum w_i d_i^{-2}}{\sum w_i d_i^{-4}}$	Number length
$d_{(l)}$	Length mean diameter	$p = 2, q = 1$	$\frac{\sum n_i d_i^2}{\sum n_i d_i} = \frac{\sum w_i d_i^{-1}}{\sum w_i d_i^{-2}}$	Length surface area
$d_{(s)}$	Surface mean diameter	$p = 3, q = 2$	$\frac{\sum n_i d_i^3}{\sum n_i d_i^2} = \frac{\sum w_i}{\sum w_i d_i^{-1}}$	Surface area volume
$d_{(v)}$	Volume mean diameter	$p = 4, q = 3$	$\frac{\sum n_i d_i^4}{\sum n_i d_i^3} = \frac{\sum w_i d_i}{\sum w_i}$	Volume

there is an additional term for the interfacial drag between vapor–liquid phases, yielding to a total of seven unknown parameters.

For the relative permeabilities and passabilities, some authors suggest that both coefficients are equal for each fluid (Lipinski, 1982; Saez and Carbone, 1985; Lee and Catton, 1984). Powers of the void fractions ( $\alpha$ ) are usually used, an increase of the exponent resulting in an increased friction. Table 4 summarizes commonly used formulations.

In problems related to the cooling of a debris bed after an accident in a nuclear power plant, two-phase flow Eqs. (9) and (10) have been used to establish DHF models. In these models, it is usually considered that the DHF corresponds to the counter-current flooding limit. According to these models, DHF is reached at the maximum gas flux, determined by the integrated steam flux that can be counterbalanced by the water inflow. In these theoretical models, the DHF is a combination of the above-mentioned parameters. For instance, the expression obtained by Lipinski in his zero-dimensional coolability model (Lipinski, 1982) is:

$$\Phi_{\text{DHF}} = \frac{h_{lv} \sqrt{\rho_g (\rho_l - \rho_g) g \eta (1 + \frac{\lambda_c}{H})}}{\left(1 + \left(\frac{\rho_g}{\rho_l}\right)^{1/4}\right)^2} \quad (11)$$

with

$$\lambda_c = \frac{\sigma \sqrt{\frac{k}{K}}}{\sqrt{5}(\rho_l - \rho_g)g} \quad (12)$$

$\sigma$  stands for the surface tension,  $H$  the height of the debris and  $h_{lv}$  for the latent heat. The DHF depends on the correlations chosen for the (relative) permeability and passability.

### 3.3. Different approaches to identify the effective diameter

In the context of debris coolability, the objective is to represent the debris bed, which may form in the core or in the lower plenum, by a bed made of single-sized spherical particles (see Fig. 1). The diameter of the single-sized spherical particles that are the most suitable to represent the real debris bed, is named the effective diameter. If a real debris bed can be described by its porosity and an effective diameter, the prediction of its coolability is easier. Indeed, models developed for simple packed beds can be used with the parameters of the real beds and then makes it possible to

**Table 3**  
Definition of equivalent diameters for irregularly shaped particles of volume  $V$  and surface area  $A$ .

Symbol	Name	Expression	Property conserved
$d_v$	Equivalent sphere in volume	$\left(\frac{6V}{\pi}\right)^{1/3}$	Volume
$d_s$	Equivalent sphere in surface	$\left(\frac{A}{\pi}\right)^{1/2}$	Surface area
$d_{\text{sauter}}$	Equivalent sphere in specific surface (Sauter diameter)	$\frac{6V}{A}$	Volume-to-surface-area ratio

**Table 4**

Summary of commonly used formulations for the relative permeabilities and passabilities (where  $\alpha$  is the void fraction or the relative gas volume fraction in the fluid).

	$K_{rl}$	$\eta_{rl}$	$K_{rg}$	$\eta_{rg}$
Lipinski (1982)	$(1 - \alpha)^3$	$(1 - \alpha)^3$	$\alpha^3$	$\alpha^2$
Reed (1982)	$(1 - \alpha)^3$	$(1 - \alpha)^5$	$\alpha^3$	$\alpha^5$
Hu and Theofanous (1991)	$(1 - \alpha)^3$	$(1 - \alpha)^6$	$\alpha^3$	$\alpha^6$

compute the quenching front velocity under reflooding, the dryout heat flux, etc. To determine this effective diameter, different approaches have been adopted. The first step consists in measuring the characteristics of the debris bed. This can be the single-phase pressure drop along the bed height, the quench front velocity or the steam flow rate produced during the reflooding or the dryout heat flux. The second step consists in identifying the effective diameter of the debris bed from the experimental data. Two approaches can be used in this context (see Fig. 2):

- In the first approach, the use of a model is needed for the identification of the effective diameter. The effective diameter is an analytically calculated diameter, which shows the best agreement between the model and the experiment. For instance, Kozeny–Carman's and Ergun's equations are used to retrieve the effective diameter from the measurement of the single-phase pressure drop inside the bed. One must keep in mind that the effective diameter is linked to the pre-supposed modeling. Consequently, different modeling of the same phenomena gives different effective diameters. This is especially the case for DHF models.
- The second approach consists in comparing the results obtained from studied debris bed with results obtained with single-sized spherical particles. No model assumption is needed for this approach. However, a lot of experiments can be necessary to find out which single-sized spherical particles are the most suitable to represent the studied debris bed. In addition, the effective diameter is not necessarily the same depending on the investigated property of the debris bed.

## 4. Results and preliminary conclusions

### 4.1. POMECO-FL experiments

To identify the effective particle diameter for a particulate bed under well-controlled conditions (i.e., to isolate other influential factors), three types of particles were selected for experimental studies at KTH: (i) spheres with varied size distributions; (ii) non-spherical particles with known geometries (e.g., cylinders, hollow spheres with through holes); (iii) irregular particles with variations in both sizes and shapes (e.g., gravels). The first approach in Section 3.3 was employed to determine the effective particle diameter, by assuming that Ergun equation is valid for fluid flow through the particulate beds.

The POMECO-FL test facility was employed to accommodate the particulate beds under investigation (Li and Ma, 2011a, 2011b, 2012a). The effective particle diameters are obtained from the measured pressure gradients of air/water single-phase flow in the particulate beds with various combinations of particles, based on the Kozeny–Carman and Ergun equations. The effective particle diameters are also applied to predict the dryout heat flux obtained in the POMECO-HT experiment (Li et al., 2012b) for coolability study.

#### 4.1.1. Particulate beds packed with spherical particles

Table 5 shows the particulate beds investigated on the POMECO-FL facility and the experimental results for the effective particle diameters ( $d_e$ ). For the purpose of comparison, the table also includes the corresponding count mean diameter, length mean diameter, surface mean diameter and volume mean diameter, calculated by the equations in Table 1. Water is used as the working fluid during all the tests. Bed-4 is packed with multi-diameter spheres whose sizes are varied from 0.7 mm to 10 mm. The size distribution of the particles in Bed-4 is illustrated in Fig. 3, which is chosen in such a way that it is similar to the particle size



Fig. 1. Evaluating an equivalent diameter.

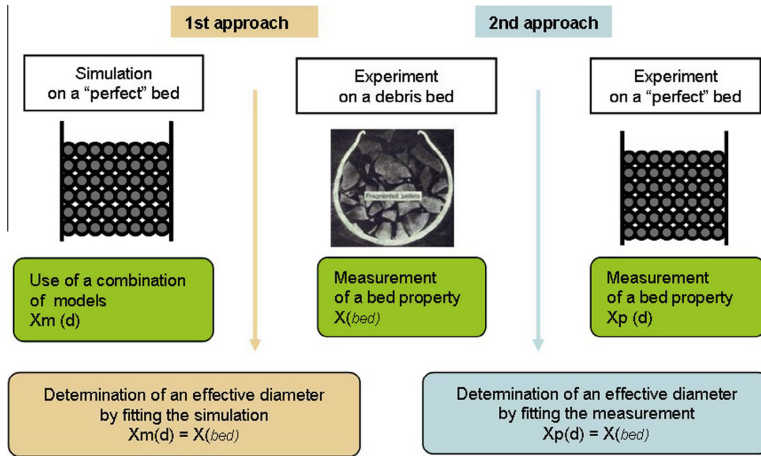


Fig. 2. Determination of an effective diameter.

Table 5  
Data of Bed-1 to Bed-4.

Bed	Diameter (mm)	Mass ratio (%)	$\varepsilon$	$d_{(m)}$ (mm)	$d_{(l)}$ (mm)	$d_{(s)}$ (mm)	$d_{(v)}$ (mm)	$Re_p$	$d_e$ (mm)
1	1.5/3	1/1	0.34	1.67	1.8	2	2.25	<7	1.98
2	1.5/6	4/1	0.33	1.52	1.57	1.76	2.4	>7	1.82
3	1.5/3/6	1/1/1	0.3	1.73	2	2.57	3.5	<7	1.77
4	0.7–10	See Fig. 3	0.34	0.9	1.18	2.12	3.97	>7	1.58
								<7	2.5
								>7	1.9
								<7	1.82
								>7	1.22



distributions in FCI tests with real corium (Lindholm, 2002; Magallon, 2006).

The modified Reynolds number ( $Re_p$ ) is obtained by using the superficial velocity of the fluid and the Sauter mean diameter of the spheres in the bed. The measured pressure gradients for Bed-1 are as depicted in Fig. 4, which includes the values predicted by Ergun’s equation using different mean particle diameters of  $d_{(v)}$ ,  $d_{(s)}$ ,  $d_{(l)}$  and  $d_{(m)}$  as shown in Table 5. From Fig. 4 and the data in Table 5, one may conclude that at low Reynolds number ( $Re_p < 7$ ) the effective particle diameter is close to the surface mean diameter of the spherical particles, while at high Reynolds number

( $Re_p > 7$ ) it is close to the length mean diameter (Li and Ma, 2011a). Nevertheless, when the coolability of the particulate bed is concerned, only the surface mean diameter is sufficient to predict by the Reed model the dryout heat flux of the bed under top-flooding condition (Li et al., 2012b).

4.1.2. Particulate beds packed with non-spherical particles

Two types of non-spherical particles were investigated in our study (Li and Ma, 2011b): cylinders and hollow spheres separately (see the pictures in Tables 6 and 7). The hollow spheres have holes made through the solid balls concentrically. It was found that the

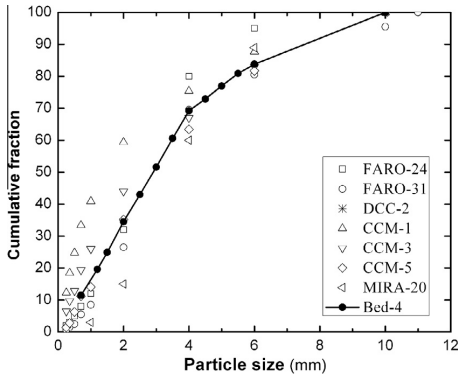


Fig. 3. Particle size distributions of Bed-4 and debris beds from FCI tests.

pressure drops in the packed beds with hollow spheres and cylindrical particles are much higher than the predictions of the Ergun equation if the Sauter mean diameters of the hollow spheres and cylinders are employed in the equation. By introducing an equivalent diameter of the particles in each bed, which is the product of Sauter mean diameter and the shape factor ( $\Psi$ ) of the particles, the flow frictional resistance in the packed beds can be predicted by the Ergun equation in the whole flowrate range. This is illustrated in Figs. 5 and 6 where the measured pressure drops and the pressure drops predicted by using Sauter mean diameter ( $d_{st}$ ) are also plotted.

4.1.3. Particulate beds packed with sand particles

Bed-9 is a particulate bed packed with sand particles whose size distribution is listed in Table 8. The shapes of the particles are as

shown in Table 9 where the different mean diameters of the particles in the bed are also presented.

If the particles in each span of Table 8 are assumed to be represented by its arithmetic diameter, it can be estimated that the count mean diameter is 0.94 mm, the length mean diameter is 1.2 mm, and the surface mean diameter is 2 mm, which are all less than the volume mean diameter (3.7 mm). The effective diameter ( $d_{eff}$ ) of the sand particles is 1.1 mm, derived from the measured pressure gradients and the Ergun equation. Obviously, the equivalent diameter of the sand particles is the length mean diameter.

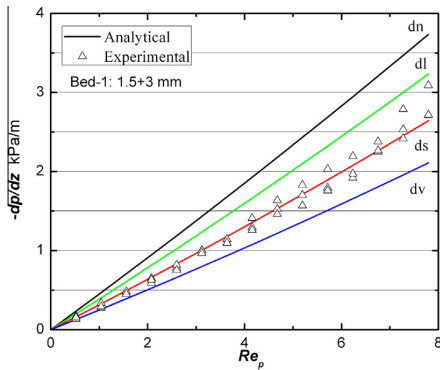
4.2. COOLOCE experiments

4.2.1. COOLOCE program

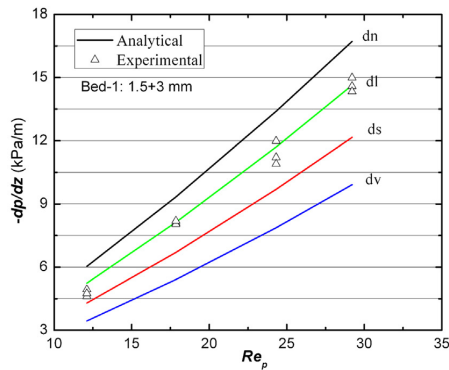
The COOLOCE (Coolability of Core Debris) test facility at VTT was designed for follow-up studies after the STYX experiments were completed (Lindholm, 2002; Magallon, 2006). The motivation of the experiments was to investigate the coolability in debris beds of different geometries (conical and cylindrical), and apply the results in simulation code and model validation.

Concerning the question of finding an equivalent particle diameter, the cylindrical bed experiments with top flooding are of interest. The cylindrical test bed of the COOLOCE facility has been used to measure dryout heat flux for two materials: spherical ceramic beads and alumina gravel consisting of irregularly sized and shaped particles. The latter material was used also in the STYX experiments, and its size distribution was originally adjusted based on older FCI experiments to be a “realistic” one (Magallon, 2006; Spencer et al., 1994; Haraldsson and Sehgal, 1999).

Here, we present the estimation of the effective particle diameter by two methods which both utilize the commonly-used models described in Chapter 3.2. The method used for the estimation of the effective diameter with the COOLOCE test facility is based on the



(a) at low  $Re_p$



(b) at high  $Re_p$

Fig. 4. Pressure gradients of water flow through Bed-1 at different Reynolds number.

Table 6  
Data for Bed-5 and Bed-6 with cylindrical particles.

Bed	a/b (mm)	$\epsilon$	$\psi$	$d_{st}$ (mm)	$d_{eq}$ (mm)	$d_e$ (mm)
5	3/3	0.34	0.874	3	2.6	2.6
6	3/6	0.37	0.832	3.6	3	3



**Table 7**

Data for Bed-7 and Bed-8 with hollow spheres.

Bed	a/b (mm)	$\epsilon$	$\psi$	$d_{st}$ (mm)	$d_{eq}$ (mm)	$d_p$ (mm)
7	1/6	0.39	0.845	5	4.2	4.2
8	3/6	0.56	0.577	3	1.7	1.8

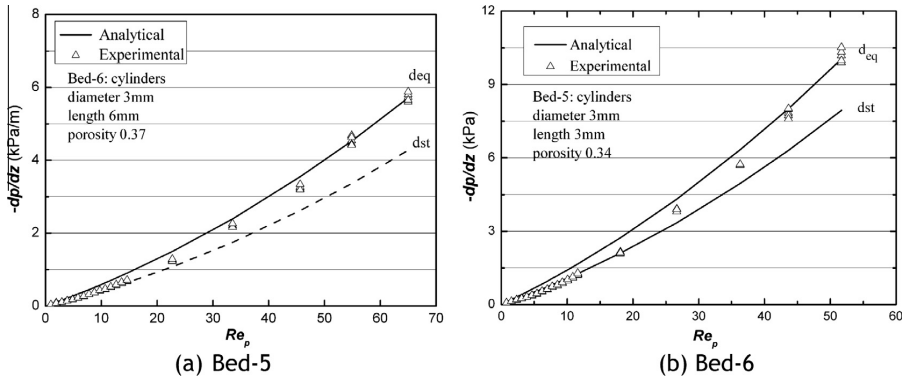


**Fig. 5.** Pressure gradients of water flow through bed with cylindrical particles.

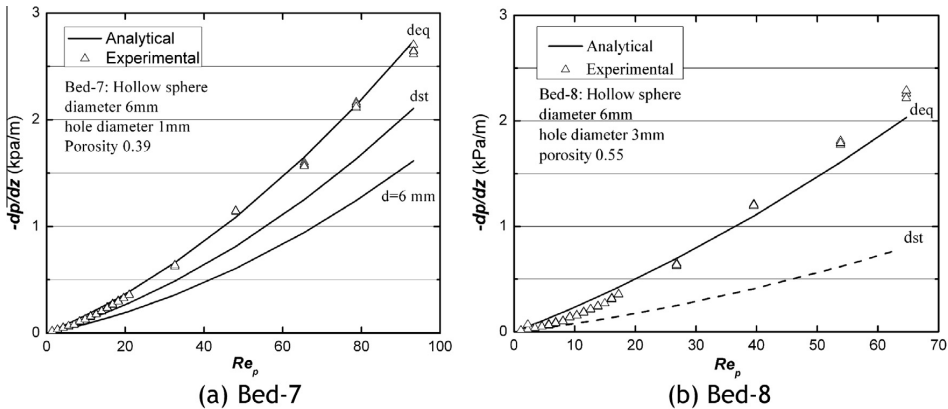


**Fig. 6.** Pressure gradients of water flow through bed with hollow spheres.

measured dryout heat flux. For obtaining the particle diameter from DHF, several two-phase flow modeling assumptions are necessary. We have adopted the Reed formulation (Reed, 1982) for the relative permeability and passability as a basic case, and applied the MEWA code (Bürger et al., 2006) to calculate DHF with several particle diameters (used as input for the models) to find out the particle diameter which produces the best agreement with the experimental data. In order to produce reliable results with this approach, porosity has to be well-known and the drag force model has to be able to yield correct predictions for DHF. With the objective of clarifying the uncertainty related to the results, the DHF in 1D case has been solved analytically with particle size and porosity variations and some error estimates have been provided.

The second approach consists of single-phase pressure loss measurements which were conducted by KTH using the POM-ECO-FL facility for both particle materials used at VTT. The effective particle diameter was estimated based on the (single-phase) Ergun’s equation and measured porosity. The effective particle sizes are compared to the average sizes calculated from the particle size distributions.

4.2.2. Particle size assessment

Spherical particles (grinding beads consisting of zirconia/silica) were used in the test series COOLOCE-3-5. The spherical particles are not uniform in diameter: according to a sample of about 1000 particles analyzed with image processing, the size range is

**Table 8**  
Size distribution of Bed-9.

Particle size (mm)	Accumulative fraction
0.5–1	14.1
1–1.2	17.5
1.2–1.4	21.3
1.4–1.7	28
1.7–2	34.5
2–2.4	41
2.4–2.8	48.5
2.8–3.4	58.1
3.4–4	69.1
4–5.6	81.2
5.6–8	87.1
8.0–12	100

**Table 9**  
Mean diameter of Bed-9 packed with sands particles.

Method	Size (mm)	Porosity
Count mean	0.94	0.38
Length mean	1.2	
Surface mean	2	
Volume mean	3.7	
Effective diameter	1.1	



0.815–1.126 mm. The distribution is rather uniform which means that the different mean diameters are close to each other. The calculated mean diameters and the diameters that produce the best agreement based on the measured pressure loss and DHF (effective diameters) are listed in Table 10.

Because the DHF simulation and the pressure loss based measurement rely on the Ergun's law in which porosity is a significant contributor to the pressure loss, porosity is also given. It should be noted that in these cases, specifically in the DHF simulation, combinations of porosity and particle diameter may yield similar results for the pressure loss/DHF, e.g. if the porosity is decreased, a certain increase in particle diameter "cancels out" the effect of increased friction by the decreased porosity.

Aluminum oxide gravel consisting of irregularly shaped particles with the size distribution between 0.25 and 10 mm was used in COOLOCE-8. A sieve analysis has been conducted to the material to find out the size distribution, and the mean diameter can be

**Table 10**  
Mean diameters of the spherical particles and effective diameters obtained by measurements.

Method	Size (mm)	Porosity
Count mean	0.970	–
Length mean	0.974	–
Surface mean	0.978	–
Volume mean	0.983	–
Effective diam. (pressure loss)	0.8	0.4
Effective diam. (DHF)	0.97	0.37



expressed as averages calculated from the weight fractions ( $w_i$ ) of the different particle size classes (see Table 2). The average diameters and the effective diameters based on the measured DHF and pressure loss, along with a sample image of the material, are shown in Table 11.

In the COOLOCE experiments, DHF was measured for a range of pressures, 1–7 bar (absolute). This is considered as a reasonable interval for the Finnish boiling water reactors. The dryout heat fluxes as a function of pressure for the spherical and irregular particles are plotted in Fig. 7 which shows the comparisons of the experimental results and the MEWA simulation results with variations of particle size and porosity. As default, the void fraction powers of Reed are used. A variation is included for the gravel particle simulation set in which one of the simulations has been run with the Hu and Theofanous model (Hu and Theofanous, 1991) and the effective diameter based on the pressure loss measurement as input.

It is seen that the pressure dependency predicted by the simulation models does not exactly correspond to the measured one. This is especially true in the case of gravel particles in which the experimental highest pressure DHF at 7 bar is very close to the DHF measured at 5 bar. For the pressure of 1–2 bar, the agreement between the experiment and the simulation with  $\varepsilon = 0.408$ ,  $dp = 0.65$  mm is good. This porosity and particle diameter are also in agreement with the single-phase pressure loss measurement. This suggests that the effective diameter is comparatively small; the closest mean diameter is the count mean. For higher pressures, the Hu and Theofanous drag force model (Hu and Theofanous, 1991) appears to give somewhat better agreement than the Reed model, however, the use of the Hu and Theofanous model is not very well established in the light of previous studies (Yakush et al., 2013).

For the spherical particles, the simulated DHF at atmospheric pressure is slightly lower than the experimental DHF but, starting from 2 bar, the experimental and simulation results are in a good agreement for the cases of  $\varepsilon = 0.4$ ,  $dp = 0.8$  mm and  $\varepsilon = 0.37$ ,  $dp = 0.97$  mm. The values of  $\varepsilon = 0.4$ ,  $dp = 0.8$  mm were also obtained from the single-phase pressure loss measurements. However, it is of interest to notice that the diameter of 0.8 mm is close to the lowest limit of the size distribution, being even slightly smaller than the minimum diameter obtained from the size distribution estimates. The adjustment of particle diameter in the simulation to the arithmetic mean of 0.97 mm yields the same DHF if porosity is decreased to 0.37. Based on filling the test bed with water and the weight of the particles in the test bed, the porosity of the cylindrical test bed is 38–40%. The conditions in the COOLOCE test bed may not be exactly repeated in the single-phase measurement of the effective particle diameter. However, it can be deduced that the most representative particle diameter for the true porosity of the bed filled with the spherical particles is between 0.8 and 0.97 mm (lower half of the size distribution).

**Table 11**  
Mean diameters of the irregular particles (weight-based evaluation) and effective diameters obtained by measurements.

Method	Size (mm)	Porosity (–)
Mass mean	3.32	–
Count mean	0.725	–
Length mean	0.969	–
Surface mean	1.77	–
Effective diam. (pressure loss)	0.65	0.408
Effective diam. (DHF)	0.65	0.408



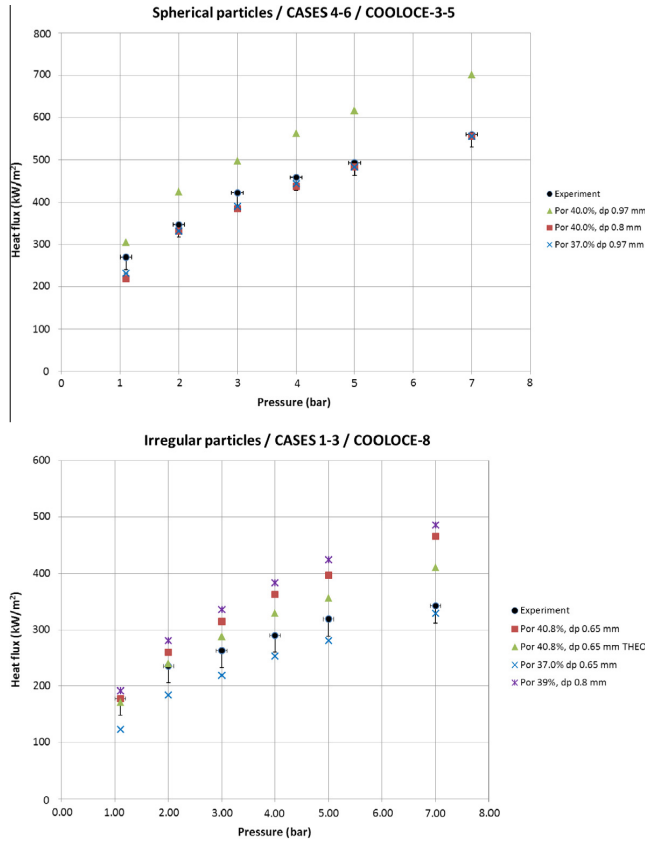


Fig. 7. MEWA simulation results with different particle diameters and porosities compared to the experimental dryout heat flux for spherical particles (top) and irregular particles (bottom).

Concerning the gravel particles, the porosity can be considered as more uncertain. The gravel bed was built by carefully mixing the particles of different sizes to simulate a bed formed by the pouring of mixed-size particles, with no intention to reach the maximum packing density of the gravel. Thus, it is possible that the gravel bed has been shifted toward a denser packing during the test runs which may explain the low DHFs in the higher pressures (almost all the test runs from lower to higher pressures were made in consecutive order). Currently, final conclusions of this cannot be made because we have not conducted repeatability experiments.

4.2.3. Error estimation and uncertainties

The predictions of the dryout heat flux are sensitive to model parameters as well as physical parameters with the particle size and porosity being the most important ones. Instead of the common method of predicting DHF based on known (fixed) values of particle size and porosity, the aforementioned studies with the COOLOCE facility focus on predicting the particle diameter based on known experimental DHF and porosity. In this type of “reverse” analysis, the accuracy of the determination of the effective particle diameter depends on the validity of the interpretation model, the representativeness of the used porosity value and the accuracy at which the DHF is measured.

To further clarify the uncertainty present in the results, the possible error in the particle diameter was evaluated by using the algebraic solution to the 1D dryout heat flux equation for

homogeneously heated debris beds with different values of porosity. The DHF as a function of particle diameter for the porosities of 0.37, 0.39 and 0.41 is shown in Fig. 8 (left). The relative permeability and passability are, again, chosen according to the Reed model (Reed, 1982) and atmospheric pressure is presumed.

The accuracy of the experimental DHF measurement is about 30 kW/m<sup>2</sup> (Takasuo et al., 2012). The inaccuracy in DHF is mainly due to the 2 kW power step used in the experiments for the dryout determination. Another contributor is the inaccuracy in the power control which is about ±3 kW/m<sup>2</sup>. As the power step related inaccuracy cannot be above the measured DHF in the applied method of defining the dryout power, the actual DHF can deviate +3 ... -33 kW/m<sup>2</sup> from the measured value (error bars seen in Fig. 7 [above DHF vs. pressure]). The effect of the DHF uncertainty on the particle diameter is illustrated in Fig. 8 (right) in which the highlighted area represents the range of variation.

As Fig. 8 depicts, the particle diameter is quite sensitive to the possible errors in DHF and porosity. The error of ±0.02 in porosity corresponds to an inaccuracy of approximately ±0.1 mm in particle diameter. The potential uncertainty caused by the uncertain DHF is not symmetric but biased towards negative values due to the dryout determination method: the error in particle diameter is about +0.01 ... -0.1 mm. The total uncertainty is demonstrated in Fig. 8 (left) where the shaded area near the center represents the range of particle diameters for the DHF range of 237–273 kW/m<sup>2</sup> (measured DHF for the spherical particles at about 1.1 bars) and the

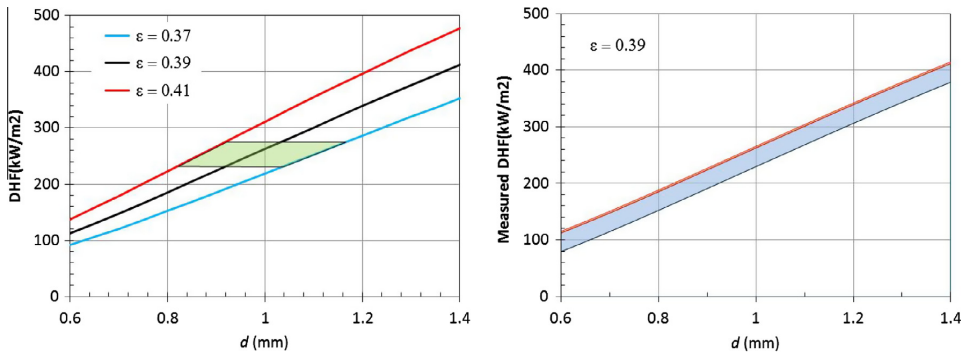


Fig. 8. Dryout heat flux as a function of particle diameter according to the Reed model for different porosities (left) and the uncertainty in the experimental DHF for 0.39 porosity (right).

porosity range of 0.37–0.41. The range obtained for the effective particle diameter in this case is 0.83–1.18 mm. This range largely overlaps the particle size distribution of 0.815–0.126 mm.

Based on this, it can be concluded that the accuracy of the equivalent particle size determination is of the same order of magnitude as the size range of the spherical particles, i.e. the effective particle size may not be identified within the size distribution because this would require a very precise measurement. In addition, the sphericity tolerance of the particles is not known; some of the particles in the samples were slightly elliptical which may have an effect on their measured size. It is questionable whether the uncertainty is crucial from the coolability point of view since the realistic debris bed can have a much wider size distribution. For the gravel particles in the experiments, the size distribution and the range of weighted averages is considerably larger than for the spherical particles and, taking the uncertainty into account, the count mean is closest to the effective diameter.

In the analysis above, the influence of the model parameter selection is not taken into account. It has been assumed that the Reed model is applicable to model the experiments in question for the purpose of scoping the magnitude of the potential error, regardless of the fact that an exact fit between the experimental and simulation data has not been found. Furthermore, the fundamental assumption required for the presented analysis is that the test facility which, in reality, is not a homogeneously heated 1D configuration is capable of reproducing the DHF in the postulated 1D configuration with adequate accuracy.

#### 4.3. DEBRIS air/water loop

##### 4.3.1. Test set-up

At IKE an air/water test set-up is applied to determine effective particle diameters of particle beds. In this one-dimensional set-up a single-phase (water) or two-phase (water/air) flow can be established.

The set-up consists of a transparent polycarbonate tube with an inner diameter of 100 mm, which is filled with well mixed particles with a height of approximately 500 mm. Water and/or air can be supplied from the bottom and exhausted at the top. Along the bed height, four pressure taps are uniformly distributed in 100 mm intervals. Each pressure tap is connected to the particle bed via six holes in the polycarbonate tube. Two differential pressure transducers (100 mbar, class 0.1) measure the pressure differences between two of the four pressure taps as it can be seen in

Fig. 9.

Water is injected by a frequency-controlled pump, and its flow rate is measured by an electromagnetic flow meter. In order to reduce uncertainties regarding the temperature depending properties of water the water temperature is measured inside the particle bed. To establish a co-current two-phase flow inside the bed also air can be injected in the bed. The air flow rate is measured and controlled by a thermal flow meter.

##### 4.3.2. Investigated particle beds

In previous studies at IKE the boiling, dry-out and quench behavior of mono- and polydispersed spherical particle beds but also of irregularly shaped aluminum-oxide particles from PRE-MIX-experiments were investigated (Rashid et al., 2012, 2013). Ongoing experiments are focused on particle beds, which are more complex than monodispersed particle beds but have a well-defined geometry. Such particles are for instance cylinders and screws (see Fig. 10), which are investigated in this work. Additionally, a mixture of these cylinders and screws and a polydispersed particle bed made of spheres is investigated.

In order to determine different equivalent diameters for monodispersed particles, the particle surface and volume should be well-known. For cylindrical particles, length and diameter can readily be measured. For screws, the surface area is calculated by using the dimensions given in the ISO-standard. The volume is calculated by weighing the particles and dividing the weight by the

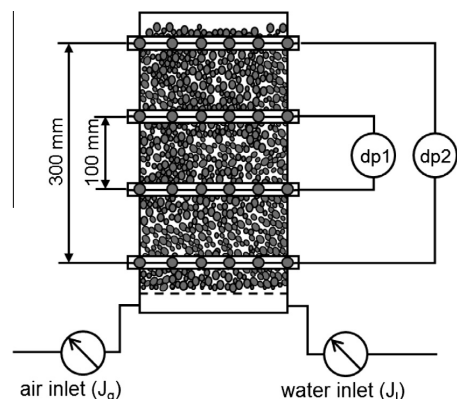


Fig. 9. DEBRIS air-/water test set-up.

density. For the surface calculation the screw thread is neglected, otherwise the surface area would be significantly higher. It is assumed that the fine structure of the thread has no influence on the effective particle diameter. In addition, the effective particle diameter  $d_{eff}$  is calculated by fitting the experimental data with the Ergun's equation. For calculating the Reynolds numbers the respective diameters were applied (e. g. the effective particle diameter for experimental data).

The equivalent particle diameters for polydispersed beds were calculated according to Table 13. In the formulas from Table 2, the effective particle diameters were used, not any calculated equivalent diameter from Table 3. Otherwise the estimated errors would be higher. As for monodispersed particle beds the Reynolds numbers and pressure gradients were calculated using the respective diameters.

#### 4.3.3. Results

In Figs. 11 and 12, the pressure gradients from experiments and calculated predictions by Ergun's equation for the investigated particle beds at single-phase flow conditions are plotted. For all beds, one representative case was chosen and only the results for pressure transducer dp2 are given. Due to fluctuations of pressure gradient, the given values are averaged over a period of one minute. The corresponding error bars indicate the experimental uncertainties from pressure drop, fluid velocity, porosity, dimensions of particles and properties of water.

For monodispersed beds (Fig. 11) it can be seen, that the Sauter mean diameter fits the experimental data best. Contrastingly the volume and surface averaged particle diameter are too large compared to the effective particle diameter (see Table 12), so that the experimental pressure gradients are significantly underpredicted.

The error bars of the calculated data indicate that for the screws (bed 2, 3 and 5) the uncertainties are relatively high. This is due to uncertainties regarding the volume and surface of the screws. This effect is more prominent for the Sauter diameter, because here both volume and surface area yield the Sauter mean diameter.

For polydispersed beds (Fig. 12) also three different equivalent diameters were applied. For both beds it can be seen, that the length mean diameter fits the experimental results best. This finding agrees well with the experiments performed by Li and Ma (Li and Ma, 2011a). They already showed that for high Reynolds numbers ( $Re_p > 7$ ) the length mean diameter is the most suitable one for representing the effective particle diameter. Whereas, for smaller Reynolds numbers the surface mean diameter fits the experimental data best.

Regarding the calculation of equivalent particle diameters, there are two remaining uncertainties. It was shown that it is difficult to calculate the surface area and volume of complex particles like screws. Especially for the calculation of Sauter mean diameters, the uncertainties are quite large. This uncertainty should be reduced to yield more accurate results. The second uncertainty is regarding the "surface roughness" such as the thread of a screw. In case of real debris, it will also be a decisive question, which surface roughness should be considered and which can be neglected.

#### 4.4. CALIDE/PRELUDE experiments

##### 4.4.1. CALIDE and PRELUDE facilities

To reduce the uncertainty in the assessment of debris coolability following a core melt accident, the CALIDE program has been launched at IRSN. Its purpose is to characterize the pressure losses in any porous medium for single- and two-phase flow (air/water,



Fig. 10. Particle beds investigated at IKE.

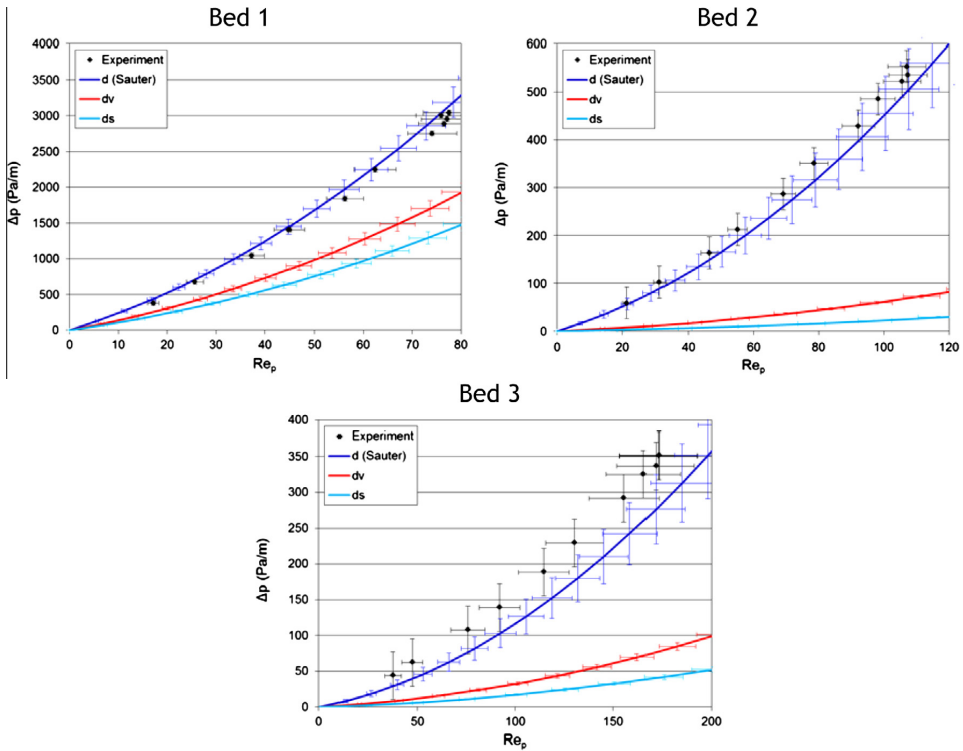


Fig. 11. Pressure drop vs.  $Re_p$  for monodispersed beds 1, 2 and 3 (irregularly shaped particles).

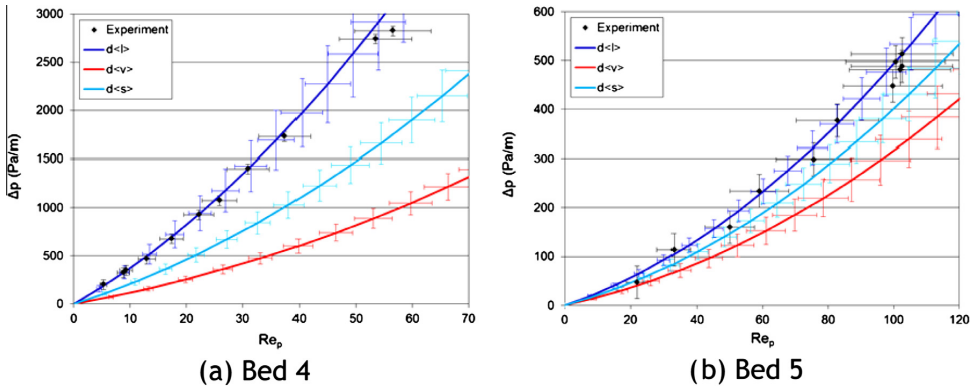


Fig. 12. Pressure drop vs.  $Re_p$  for polydispersed bed 4 (unequally-sized spherical particles) and 5 (irregularly shaped particles).

Table 12  
Data for monodispersed particle beds.

Bed	Composition	$\varepsilon$	Surface area (mm <sup>2</sup> )	Volume (mm <sup>3</sup> )	$d_v$ (mm)	$d_s$ (mm)	$d_{Sauter}$ (mm)	$d_{eff}$ (mm)
1	Cylinders ( $3 \times 5.75$ mm)	0.35	68.33	40.64	4.27	4.66	3.57	3.64
2	Cylindrical screws/bolts (M3 $\times$ 10 ISO 1207)	0.59	185.12	87.44	5.51	7.67	2.83	2.72
3	Hexagonal screws/bolts (M6 $\times$ 10 ISO 4017)	0.50	479.71	519.53	9.97	12.36	6.50	5.93

**Table 13**

Data for polydispersed particle beds.

Bed	Composition	Mass ratio (%)	$\epsilon$	$d_{(n)}$ (mm)	$d_{(l)}$ (mm)	$d_{(s)}$ (mm)	$d_{(v)}$ (mm)	$d_{eff}$ (mm)
4	Spheres (2/3/6 mm)	20/30/50	0.37	2.53	2.91	3.53	4.30	2.96
5	Irregular particles (bed 1/2/3)	20/45/35	0.54	3.35	3.54	3.79	4.10	3.60

Fig. 13. The test facility containing the bed is made of a Plexiglas pipe (500 mm in height and 94 mm in diameter) which allows flow visualization. Air is supplied from the bottom and flows-up through the bed, while water can flood the bed either by the top or the bottom providing co-current flow and counter-current flow.

The fluid flow rates are measured and controlled by five high precision Bronkhorst® flowmeters (nominal accuracy 0.1% full scale +0.5% of reading) with specific measuring ranges. Pressure drops are measured by two Rosemount-3051® differential pressure sensors (nominal accuracy ±0.0047 mbar + 0.4% of reading). A thermocouple is mounted at the top of the test section for fluid viscosity and density calculation.

To build the debris bed, the following particles have been used: glass spheres (diameter: 1.5/2/3/4/8 mm), cylinders and prisms. The ratio between the particle size and the test section diameter is lower than 0.1 so that the wall effect can be neglected.

The PRELUDE facility has been designed to perform reflood experiment on debris bed made of spherical stainless steel particles (Fig. 14; see Repetto et al., 2013). It includes:

- A water tank with water flow rate measurement.
- A test section varying from Ø110 mm to Ø290 mm containing a debris bed instrumented with thermocouples and pressure sensors.
- An induction furnace (coil around the test device).
- A downstream heated vertical tube to remove steam from test section, including temperature and steam mass flow rate measurements.
- The debris bed is inserted inside a quartz tube with various possible configurations (Fig. 14):
- Debris bed ( $\epsilon = 0.400 \pm 0.003$ ) with stainless steel balls ( $\varnothing = 1, 2, 4, \text{ or } 8 \text{ mm}$ ),
- Mixed particules (2/4 mm, 4/8 mm, etc.) to decrease the porosity ( $\epsilon = 0.376 \pm 0.006$ ).

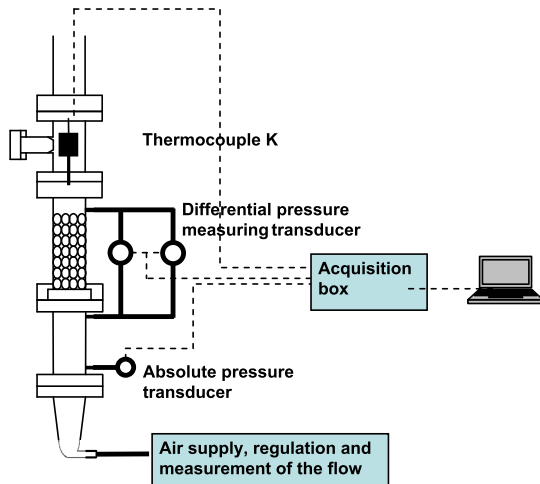


Fig. 13. Schematic view of the CALIDE facility.

4.4.2. CALIDE results: single phase pressure drop

Pressure drop has been measured for air flow through beds packed with multi-diameter spheres and non-spherical particles (Chikhi et al., 2013). The effective diameter  $d_{eff}$  has been determined by fitting the experimental data with the Ergun law, for low Reynolds numbers  $Re_p < 8$ . The Reynolds number is calculated using the Sauter diameter.

Measurements of pressure drops through beds packed with multi-diameter glass spheres (Beds no. 1, no. 2, no. 3) have been performed and compared to the Ergun’s equation. Four mean diameters ( $d_{(v)}$ ,  $d_{(s)}$ ,  $d_{(l)}$ ,  $d_{(n)}$ ) have been tested in this equation. The bed characteristics are given in Table 14. The results are presented in Fig. 15 together with the uncertainty associated to the measurements concerning the pressure drop, the fluid velocity, the porosity, the particle size. The particle size, surface and volume have been measured carefully, by sampling, using image/pics analyses. It is worth noticing that the Reynolds number uncertainty directly depends on the porosity and on the particle size. It has been shown that the experimental results can be accurately reproduced using the surface mean diameter as the effective diameter.

The experience has been repeated with beds packed with non-spherical particles. Five beds have been tested using three types of cylinders (Beds no. 4, no. 5, and no. 6) and two types of prisms (Beds no. 7, no. 8). Their characteristics are given in Tables 15 and 16. The Ergun’s equation has been assessed using several equivalent diameters ( $d_v, d_s, d_{Sauter}$ ). It is illustrated on Figs. 16 and 17. The Sauter diameter gives the best prediction.

4.4.3. PRELUDE results: reflood tests

First reflood tests on polydispersed debris bed have been performed (Repetto et al., 2013) in the PRELUDE facility with the same thermalhydraulic conditions for different beds: B1: 1 mm-mono-disperse, B2: 2 mm-mono-disperse, B4: 2 mm-mono-disperse, B4321: polydisperse bed made of 1 mm, 2 mm, and 4 mm glass balls. Several mean diameter corresponds to the bed B4321:  $d_{(n-v)} = 2.1 \text{ mm}$ ,  $d_{(l)} = 2.4 \text{ mm}$ ,  $d_{(v)} = 3.1 \text{ mm}$ ,  $d_{(s)} = 2.8 \text{ mm} = \text{Sauter diameter}$ . At moderate water flow rate ( $J = 5 \text{ m/h}$ ) and temperature ( $T_{ini} = 400 \text{ }^\circ\text{C}$ ), the analysis of the steam flow rate during the reflood (Fig. 18) shows that the B4321 polydispersed bed (mixture of 4, 3, 2 and 1 mm) behaves as a monodispersed debris bed of around Ø2 mm close to  $d_{(n)}$ . Repeatability tests have to be done to confirm this result.

5. Synthesis and recommendations for the evaluation of an effective diameter

5.1. Most adequate equivalent diameter

5.1.1. Approach 1

5.1.1.1. Pressure drop measurement. The Ergun law has been used to characterize the pressure drop in the debris bed and to identify the effective diameter by fitting the experimental results. The effect of particle morphology and size distribution has been investigated. The common finding of the experiments carried out in CALIDE, DEBRIS and POMECA-FL facilities is that the Sauter diameter can be considered as the effective diameter to describe pressure drop at low or high Reynolds numbers in particulate beds packed with non-spherical particles. If the non-sphericity of the particles is

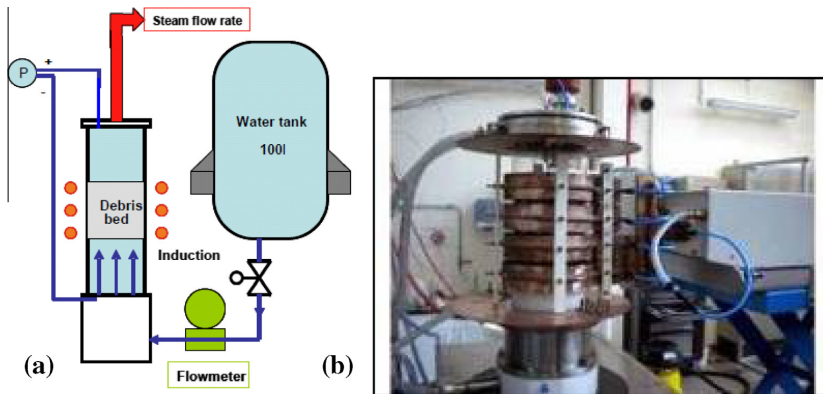


Fig. 14. View of the PRELUDE facility.

Table 14

Data for polydisperse beds no. 1, 2 and 3 made of glass balls.

Bed	Diameter (mm)	Mass ratio (%)	Porosity	$d_{(n)}$ (mm)	$d_{(l)}$ (mm)	$d_{(s)}$ (mm)	$d_{(v)}$ (mm)	$d_e$ (mm)
1	1.5/3/4	60/28/12	0.34	1.703	1.811	2.000	2.285	2.055
2	1.5/4/8	69/21/10	0.34	1.634	1.728	2.002	2.749	2.187
3	2/4/8	45/40/15	0.34	2.338	2.568	3.002	3.750	3.051

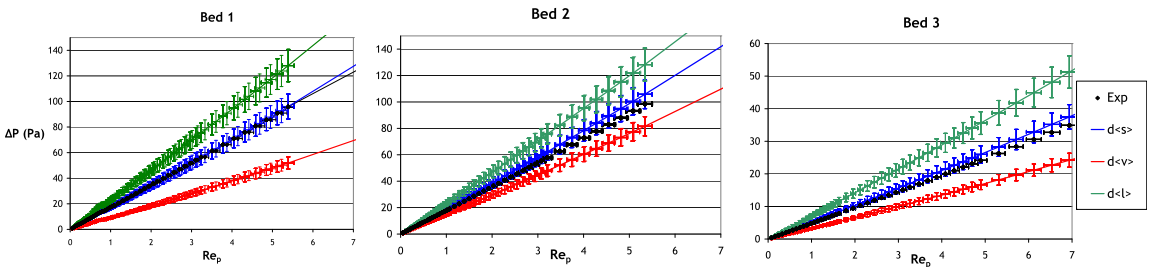
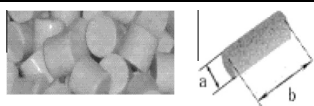

Fig. 15. Pressure drop vs.  $Re_p$  for polydispersed beds no. 1, 2 and 3 (unequally-sized spherical particles).

Table 15

Data for monodispersed beds no. 4, 5 and 6 made of cylinders.

Bed	$a/b$ (mm)	Porosity	$d_s$ (mm)	$d_e$ (mm)	min ( $a/b$ ) (mm)	max ( $a/b$ ) (mm)	$d_{\text{Sauter}}$ (mm)	$d_e$ (mm)
4	5/5	0.35	5.718	6.027	4.526	5.128	5.147	5.129
5	5/8	0.37	6.449	6.917	4.859	7.389	5.606	5.287
6	8/12	0.39	10.32	11.00	7.986	11.165	9.077	8.105



high, the Sauter diameter must be weighted by the shape factor to give the effective diameter. In case of particulate beds packed with spherical particles, it was found that at low Reynolds numbers ( $Re_p < 8$ ), the surface mean diameter ( $d_{(s)}$ ) which is equal to the Sauter diameter for a mixture of spheres can be considered as the effective diameter. For higher Reynolds numbers (i.e. when the turbulence effect is no longer negligible), it seems that the length mean diameter ( $d_{(l)}$ ) permits to predict precisely the pressure drop through a debris bed. Therefore, it can be concluded that the

friction in a debris bed can be deduced knowing the particle size distribution and the bed porosity. Moreover, using the Sauter diameter allows to predict with a precision of  $\pm 15\%$  the pressure drop for all flow regime and any bed. The Sauter diameter preserves the surface and the volume of the bed (see Table 1).

**5.1.1.2. DHF measurement.** The effective particle diameters for two types of materials have been estimated based on (1) DHF measured with the COOLOCE test facility and (2) single-phase pressure loss

**Table 16**

Data for monodispersed beds no. 7 and 8 made of prisms.

Bed	a/b (mm)	Porosity	$d_v$ (mm)	$d_s$ (mm)	min (a;b) (mm)	max (a;b) (mm)	$d_{\text{Sauter}}$ (mm)	$d_e$ (mm)
7	4/4	0.36	4.297	4.715	3.835	4.148	3.569	3.583
5	5/8	0.37	6.449	6.917	4.859	7.389	5.606	5.287

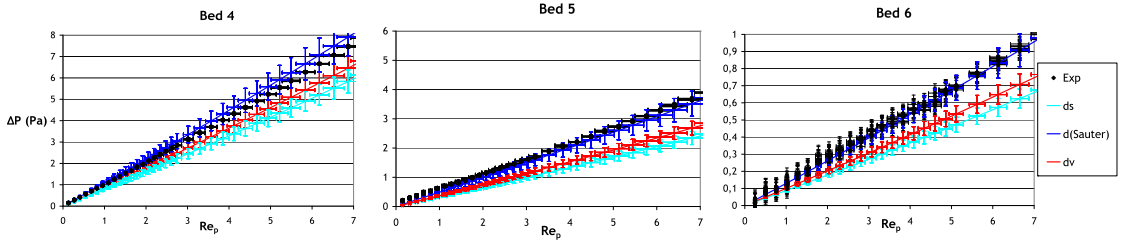
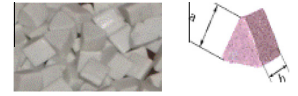


**Fig. 16.** Pressure drop vs.  $Re_p$  for monodispersed beds no. 4, 5 and 6 (irregularly shaped particles).

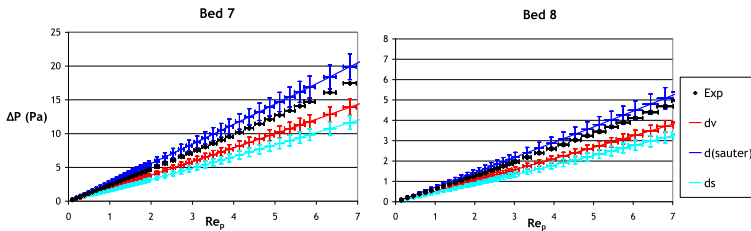


**Fig. 17.** Pressure drop vs.  $Re_p$  for monodispersed beds no. 7 and 8 (irregularly shaped particles).

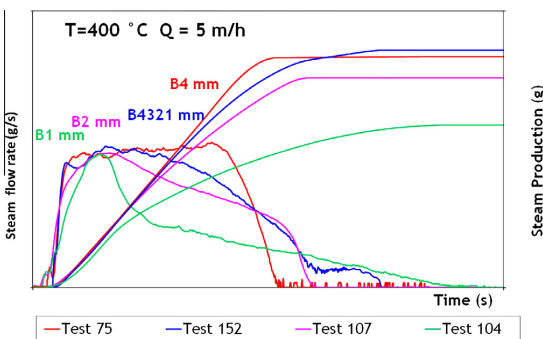


**Fig. 18.** Effect of particle size (Ø4, Ø2 and Ø1 mm particles and mixture Ø4–3–2–1 mm) on steam flow rate during quenching.

measured with the POMECO-FL facility. The drag force model that is used in both approaches to calculate the particle diameter is based on the Ergun’s law, or its two-phase extension. The results obtained with the two methods are in a reasonably good agreement.

In the case of the gravel bed, the effective diameter based on DHF and pressure loss measurements is not in the range of the particle mean diameters calculated by different weighting methods

directly from the size distribution. Only the count and length mean diameters are reasonably close to the effective diameter fitting to the predictions of the Ergun’s law and the measured DHF. The mass averaged mean and even the surface mean are too large and would yield overestimated coolability for realistic values of test bed porosity. A similar conclusion was previously made in the STYX experiments (Lindholm et al., 2006; Takasuo, 2013).

In the case of the bed consisting of spherical particles, it was estimated that the effective particle diameter cannot be accurately determined because its size distribution is too narrow considering the current uncertainty in the measurements of porosity and DHF. For a porosity of 37%, the mean diameter of 0.97 yields a good agreement with the experimental DHF, in addition to the values obtained from single-phase pressure loss measurements. Improvements of the accuracy could be achieved by a very careful determination of porosity and a higher precision of DHF measurement. There is also some unclarity concerning porosity and the pressure-dependent results in the experiments. In the experiments with gravel, the test bed might have been somewhat shifted towards denser packing. This makes it difficult to correctly identify the effective particle diameter for the full pressure range due to the sensitivity to porosity.

5.1.2. Approach 2

5.1.2.1. Steamflow rate measurement. Reflood experiments have been performed in the PRELUDE facility using either “perfect” monodisperse beds or polydisperse beds. The comparison of the

steam flow rate measurements shows that it is suitable to use an effective diameter to represent a polydisperse bed. The effective diameter is nearly equal to the count diameter  $d_{(n)}$ , i.e. in the lower range of the particle size distribution.

## 5.2. Remaining issues and uncertainties

The modeling of the debris bed is a key point in order to study its coolability (in/ex-vessel). In the framework of safety assessment using severe accident codes, significant improvements would be done if the bed could be described by a single monodispersed bed made of spheres, i.e. by an **effective diameter**. With such an objective, the main limit is that the effective diameter depends on the considered physical phenomena. In the case of reflood, the physical phenomena involved are the **pressure drop** (which limits the flow rate through the bed) and the **heat transfer** (CHF especially). In the case of ex-vessel cooling, the relevant phenomena are again the pressure drop (counter current limit flow) and the heat transfer (DHF).

The results presented in the previous section have shown that the *single phase pressure drop* through a debris bed can be calculated using the Ergun law and introducing the Sauter diameter. It requires a good knowledge of the debris bed particle porosity and size distribution. A lot of data are now available (see Section 2).

The attempts to find an effective diameter to estimate the heat transfer have been limited by the uncertainties associated *the two-phase flow pressure drop models* and the DHF/CHF models. A first step can be reached by using a generalization of Ergun law for two-phase flows introducing relative permeability and passability and keeping the Sauter diameter as an effective diameter. For the modeling of heat transfer (Lipinski or other) a second “effective” diameter should be introduced. According to COOLOCE/STYX experiment, the effective diameter should be lower than the Sauter diameter (at least in the lower range of the distribution size  $d_{(n)}$  or  $d_{(q)}$ ). This effective diameter is different from the one obtained in the pressure drop measurement experiments. But the results from PRELUDE experiments show that the steam flow rate during quenching (which is an integral evaluation of heat transfer) can be calculated with the mean diameter  $d_{(n)}$ .

Thus, it is shown that at least two effective diameters should be used in order to take into account the mechanical (pressure drop) and the thermal (DHF/CHF) properties of the bed. Moreover, the Sauter diameter can be used as the mechanical effective diameter.

## 6. Conclusions

This paper proposes a large review of the attempts to describe a debris bed with an effective diameter in the framework of the study of debris bed coolability.

First, the typical particle distribution and porosity ranges expected during a severe accident (in core, ex-vessel and in the lower plenum) have been presented showing that the mean part of a bed is made of millimeter particles with a porosity varying from 0.3 to 0.8. Then, various approaches that have been used in order to identify an effective diameter have been classified into two groups: the first approach implies the use of a model to identify an effective diameter; the second approach consists in a direct comparison of experiments performed with single-sized spherical particle bed and more complex ones.

The results obtained in POMECA, COOLOCE/STYX, DEBRIS, CALIDE/PRELUDE facilities have been presented. It indicates that the experimental data obtained in “simple” debris beds are relevant to describe the behavior of more complex beds. Indeed, for several configurations, it is possible to define an “effective” diameter suitable for evaluating (with the porosity) some model

parameters as well as correlations for the pressure drop across the bed, the steam flow rate during quenching and the DHF. For some configurations, the definition of an effective diameter appears less obvious but it may be due to the uncertainties of the model used for the identification.

As a conclusion, it is reasonable to propose at least two effective diameters to study the coolability of debris bed. The first one corresponds to the **mechanical properties** of the bed and it has been seen that the Sauter diameter can be used. The second one deals with the **thermal properties** of the bed and should be taken in the lower range of the particle size distribution.

## Acknowledgements

Florian Fichot (from IRSN) is gratefully thanked for initiating this paper and for fruitful discussions.

Most of this R&D work was performed within the framework of the SARNET2 Network of Excellence of the 7th European Framework Program. In parts, this work was also supported by the German Federal Ministry of Economics and Technology (BMWi-project FKZ 1501312) monitored by GRS, Cologne.

## References

- Akers, D.W., Carlson, E.R., Cook, B.A., Ploger, S.A., Carlson, J.O., 1986. TMI-2 core debris grab samples- Examination and analysis, Sandia National Laboratory, GEND-INF-075.
- Amri, B., Clement, 2009. Joint OECD/NEA-EC/SARNET2 Workshop In-vessel Coolability (CDROM), Issy-les-Moulineaux, France, 12–14 October.
- Broughton, J., Kuan, P., Petti, D., Tolman, E., 1989. A scenario of the Three Mile Island unit 2 accident. Nucl. Technol. 87, 34–53.
- Buchlin, J.M., Stubos, A., 1987. Phase change phenomena at liquid saturated self heated particulate beds. In: Bear, J., Buchlin, J.M. (Eds.), Modeling and Applications of Transport Phenomena in Porous Media. Kluwer Acad. Pub..
- Bürger, M., Buck, M., Schmidt, W., Widmann, W., 2006. Validation and application of the WABE code: investigations of constitutive laws and 2D effects on debris coolability. Nucl. Eng. Des. 236, 2164–2188.
- Chikhi, N., Lenoir, B., Garcin, T., 2013. Reflooding a damaged core: characteristics of a debris bed. In: Proceedings of NURETH-15 Conference, Pisa, Italy, 12–17 May.
- Coindreau, O., Fichot, F., Fleurot, J., 2013. Nuclear fuel rod fragmentation under accidental conditions. Nucl. Eng. Des. 255, 68–76.
- Coryell, E.W., Akers, D.W., Allison, C.M., Carboneau, M.L., Hobbins, R.R., Hohorst, J.K., Jensen, S.M., Modro, S.M., 1994. Summary of Important Results and SCDA/P/RELAP5 Analysis for OECD LOFT Experiment LP-FP-2, U.S. Nuclear Regulatory Commission, NUREG/CR-6160, EGG-2721.
- Darcy, H., 1856. Les fontaines publiques de la ville de Dijon, Dalmont.
- Dias, R., Mota, M., Teixeira, J.A., Yelshin, A., 2005. Study of ternary glass spherical particle beds: porosity, tortuosity and permeability. Filtration 5 (1), 68–75.
- Ergun, S., 1952. Fluid flow through packed columns. Chem. Eng. Prog. 48 (2), 89–94.
- Forchheimer, P., 1914. Chap. 15 in Hydraulik, Teubner.
- Haraldsson, H.O., Sehgal, B.R., 1999. Breakup of high temperature oxide jet in water. In: Proceedings of the Ninth International Topical Meeting on Nuclear Reactor Thermal Hydraulics (NURETH-9), San Francisco, California, USA, 3–8 October.
- Hiernaut, J.P., Wiss, T., Colle, J.-Y., Thiele, H., Walker, C.T., Goll, W., Konings, R.J.M., 2008. Fission product release and microstructure changes during laboratory annealing of a very high burn-up fuel specimen. J. Nucl. Mater. 377, 313–324.
- Hobbins, R.R., McPherson, G.D., 1990. A Summary of results from the LOFT LP-FP-2 test and their relationship to other studies at the Power Burst Facility and of the Three Mile Island Unit 2 accident. In: Proceedings of LOFT Open Forum, Madrid (Spain).
- Hu, K., Theofanous, T.G., 1991. On the measurement of dryout in volumetrically heated coarse particle beds. Int. J. Multiphase Flow 17 (4), 519–532.
- Huhtiniemi, Magallon, D., 1999. Insight into Steam Explosions with Corium Melts in KROTOS. In: Proc. of the 9th Int. Topical Meeting on Nuclear Reactor Thermal-Hydraulics (NURETH-9), San Francisco (USA).
- Huhtiniemi, Magallon, D., Hohmann, H., 1997. Results of recent KROTOS FCI tests: alumina vs. corium melts. In: Proc. of OECD/CSNI Specialists Meeting on Fuel-Coolant Interactions, Tokai-Mura (Japan).
- Karbojian, A., Ma, W.M., Kudinov, P., Dinh, T.N., 2009. A scoping study of debris bed formation in the DEFOR test facility. Nucl. Eng. Des. 239 (9), 1653–1659.
- Kato, M., Nagasaka, H., et al., 1999. Fuel coolant interaction tests under ex-vessel conditions. In: Proc. of the OECD Workshop on Ex-vessel Debris Coolability, Karlsruhe (Germany).
- Kolstad, E., Wiesenack, W., Oberlander, B., Tverberg, T., 2011. High Burn-up Fuel Behaviour under LOCA Conditions as Observed in Halden Experiments, IAEA Technical Meeting on Fuel Behaviour and Modelling Under Severe Transient and LOCA Conditions, Mito (Japan).

- Kudinov, P., Karbojian, A., Ma, W.M., Dinh, T.N., 2010. The DEFOR-S experimental study of debris formation with corium simulant materials. *Nucl. Technol.* 170, 219–230.
- Kulkarni, P.P., Rashid, M., Kulenovic, R., Nayak, A.K., 2010. Assessment of capability of models for prediction of pressure drop and dryout heat flux in a heat generating particulate debris bed. *Nucl. Eng. Des.* 240, 3067–3077.
- Lee, H.S., Catton, I., 1984. Two-phase flow in stratified porous media. In: 6th Information Exchange Meeting on Debris Coolability, Los Angeles.
- Li, L.X., Ma, W.M., 2011a. Experimental characterization of the effective particle diameter of a particulate bed packed with multi-diameter spheres. *Nucl. Eng. Des.* 241 (5), 1736–1745.
- Li, L.X., Ma, W.M., 2011b. Experimental study on the effective particle diameter of a packed bed with non-spherical particles. *Transp. Porous Media* 89, 35–48.
- Li, L.X., Gong, S.J., Ma, W.M., 2012a. Experimental study of two-phase flow regime and pressure drop in a particulate bed packed with multidiameter particles. *Nucl. Technol.* 177, 107–118.
- Li, L.X., Ma, W.M., Thakre, S., 2012b. An experimental study on pressure drop and dryout heat flux of two-phase flow in packed beds of multi-sized and irregular particles. *Nucl. Eng. Des.* 242, 369–378.
- Lindholm, 2002. A Review of Dryout Heat Fluxes and Coolability of Particle Beds, SKI Report 02:17.
- Lindholm, S., Holmström, J., Miettinen, V., Lestinen, J., Hyvärinen, P., Pankakoski, Sjövall, H., 2006. Dryout heatflux experiments with deep heterogeneous particle bed. *Nucl. Eng. Des.* 236, 2060–2074.
- Lipinski, R.J., 1982. A model for boiling and dryout in particle beds, Sandia National Laboratories. NUREG/CR-2646, SAND82-0765.
- Macdonald, I.F., El-Sayed, M.S., Mow, K., Dullien, F.A.L., 1979. Flow through porous media—the Ergun equation revisited. *Ind. Eng. Chem. Fundam.* 18 (3), 199–208.
- Magallon, D., 2006. Characteristics of corium debris bed generated in large scale fuel coolant interaction experiments. *Nucl. Eng. Des.* 236, 1998–2009.
- Magallon, D., Huhtiniemi, I., 2001. Corium melt quenching tests at low pressure and subcooling water in FARO. *Nucl. Eng. Des.* 204, 369–376.
- Magallon, D., Huhtiniemi, I., Hohmann, H., 1999. Lessons learnt from FARO/TERMOS corium melt quenching experiments. *Nucl. Eng. Des.* 189, 223–238.
- McCardell, R.K., Russell, M.L., Akers, D.W., Olsen, C.S., 1990. Summary of TMI-2 core sample examinations. *Nucl. Eng. Des.* 118, 441–449.
- Oguma, M., 1983. Cracking and relocation behaviour of nuclear fuel pellet during rise to power. *Nucl. Eng. Des.* 76, 35–45.
- Petti, D.A., Martinson, Z.R., Hobbins, R.R., Allison, C.M., Carlson, E.R., Hagman, D.L., Cheng, T.C., Hartwell, J.K., Vinjamuri, K., Seifken, L.J., 1989. Power Burst Facility (PBF) Severe Fuel Damage Test 1–4 Test Results Report. U.S. Nuclear Regulatory Commission, NUREG/CR-5163, EGG-2542.
- Rashid, M., Chen, Y., Kulenovic, R., Laurien, E., 2008. Experiments on the Coolability of a Volumetrically Heated Particle Bed with Irregularly Shaped Particles, NUTHOS-7: The 7th International Topical Meeting on Nuclear Reactor Thermal Hydraulics, Operation and Safety, Seoul, Korea, 5–9 October.
- Rashid, M., Kulenovic, R., Laurien, E., Nayak, A.K., 2011. Experimental results on the coolability of a debris bed with multidimensional cooling effects. *Nucl. Eng. Des.* 241 (11), 4537–4543.
- Rashid, M., Kulenovic, R., Laurien, E., 2012. Experimental results on the coolability of a debris bed with down comer configurations. *Nucl. Eng. Des.* 249, 104–110.
- Rashid, M., Rahman, S., Kulenovic, R., Bürger, M., Laurien, E., 2013. Quenching experiments: coolability of debris bed. *Nucl. Technol.* 181, 208–215.
- Reed, W., 1982. The Effect of Channeling on the Dryout of Heated Particulate Beds Immersed in a Liquid Pool, Ph.D. Thesis, Massachusetts Institute of Technology, Cambridge, USA.
- Repetto, G., Garcin, T., Eymery, S., New insights in the Thermal Hydraulics behaviour of a high temperature debris bed during reflooding. In: Proceedings of NURETH-15 Conference, Pisa, Italy, 12–17 May.
- Rhodes, M., 1989. Introduction to Particle Technology. Wiley.
- Saez, A.E., Carbone, R.G., 1985. Hydrodynamic parameters for gas-liquid concurrent flow in packed beds. *AIChE J.* 31, 52–62.
- Schmidt, W., 2004. Influence of Multidimensionality and Interfacial Friction on the Coolability of Fragmented Corium, Ph.D. Thesis of University of Stuttgart (Germany).
- Schulenberg, T., Müller, U., 1987. An improved model for two-phase flow through beds of coarse particles. *Int. J. Multiphase Flow* 13, 87–97.
- Schwinges, B., Journeau, C., Haste, T., Meyer, L., Tromm, W., Trambauer, K., 2010. Ranking of severe accident research priorities. *Prog. Nucl. Energy* 52, 11–118.
- Song, J.H. et al., 2003. Insights from the recent steam explosion experiments in TROL. *J. Nucl. Sci. Technol.* 40 (10), 783–795.
- Spencer, B.W., Wang, K., Blomquist, C.A., McUmber, L.M., Schneider, J.P., 1994. Fragmentation and Quench Behaviour of Corium Melt Streams in Water. US Nuclear Regulatory Commission, NUREG/CR-6133, ANL-93/32.
- Takasuo, E., 2013. Debris Coolability Simulations with Different Particle Materials and Comparisons to COOLOCE Experiments. VTT Research Report VTT-R-00257-13, Espoo, Finland.
- Takasuo, E., Holmström, S., Kinnunen, T., Pankakoski, P.H., Hosio, E., Lindholm, I., 2011. The effect of lateral flooding on the coolability of irregular core debris beds. *Nucl. Eng. Des.* 241, 1196–1205.
- Takasuo, E., Holmström, S., Kinnunen, T., Pankakoski, P.H., 2012. The COOLOCE experiments investigating the dryout power in debris beds of heap-like and cylindrical geometries. *Nucl. Eng. Des.* 250, 687–700.
- Tung, V.X., Dhir, V.K., 1988. A hydro-dynamic model for two-phase flow through porous media. *Int. J. Multiphase Flow* 14 (1), 47–65.
- Walton, L.A., Husser, D.L., 1983. Fuel Pellet Fracture and Relocation, in Water Reactor Fuel Element Performance Computer Modelling. Applied Sciences Publishers, London.
- Yakush, S.E., Kudinov, P., Lubchenko, N.T., 2013. Coolability of heat releasing debris bed. Part 1: Sensitivity analysis and model calibration. *Ann. Nucl. Energy* 52, 59–71.

Title	<b>Coolability of porous core debris beds</b> Effects of bed geometry and multi-dimensional flooding
Author(s)	Eveliina Takasuo
Abstract	<p>This thesis addresses the coolability of porous debris beds in the context of severe accident management of nuclear power reactors. In a hypothetical severe accident at a Nordic-type boiling water reactor, the lower drywell of the containment is flooded, for the purpose of cooling the core melt discharged from the reactor pressure vessel in a water pool. The melt is fragmented and solidified in the pool, ultimately forming a porous debris bed that generates decay heat. The properties of the bed determine the limiting value for the heat flux that can be removed from the debris to the surrounding water without the risk of re-melting.</p> <p>The coolability of porous debris beds has been investigated experimentally by measuring the dryout power in electrically heated test beds that have different geometries. The geometries represent the debris bed shapes that may form in an accident scenario. The focus is especially on heap-like, realistic geometries which facilitate the multi-dimensional infiltration (flooding) of coolant into the bed. Spherical and irregular particles have been used to simulate the debris. The experiments have been modeled using 2D and 3D simulation codes applicable to fluid flow and heat transfer in porous media. Based on the experimental and simulation results, an interpretation of the dryout behavior in complex debris bed geometries is presented, and the validity of the codes and models for dryout predictions is evaluated.</p> <p>According to the experimental and simulation results, the coolability of the debris bed depends on both the flooding mode and the height of the bed. In the experiments, it was found that multi-dimensional flooding increases the dryout heat flux and coolability in a heap-shaped debris bed by 47–58% compared to the dryout heat flux of a classical, top-flooded bed of the same height. However, heap-like beds are higher than flat, top-flooded beds, which results in the formation of larger steam flux at the top of the bed. This counteracts the effect of the multi-dimensional flooding. Based on the measured dryout heat fluxes, the maximum height of a heap-like bed can only be about 1.5 times the height of a top-flooded, cylindrical bed in order to preserve the direct benefit from the multi-dimensional flooding.</p> <p>In addition, studies were conducted to evaluate the hydrodynamically representative effective particle diameter, which is applied in simulation models to describe debris beds that consist of irregular particles with considerable size variation. The results suggest that the effective diameter is small, closest to the mean diameter based on the number or length of particles.</p>
ISBN, ISSN, URN	ISBN 978-951-38-8344-7 (Soft back ed.) ISBN 978-951-38-8345-4 (URL: <a href="http://www.vttresearch.com/impact/publications">http://www.vttresearch.com/impact/publications</a> ) ISSN-L 2242-119X ISSN 2242-119X (Print) ISSN 2242-1203 (Online) <a href="http://urn.fi/URN:ISBN:978-951-38-8345-4">http://urn.fi/URN:ISBN:978-951-38-8345-4</a>
Date	October 2015
Language	English, Finnish abstract
Pages	112 p. + app. 72 p.
Name of the project	
Commissioned by	
Keywords	nuclear energy, severe accident, corium coolability, debris bed, two-phase flow, thermal-hydraulic experiment, porous medium, numerical modeling
Publisher	VTT Technical Research Centre of Finland Ltd P.O. Box 1000, FI-02044 VTT, Finland, Tel. 020 722 111

Nimeke	<b>Huokoisen sydänromukeon jäädytettävyyys</b> Tutkimus keon muodon ja moniulotteisen virtauksen vaikutuksista
Tekijä(t)	Eveliina Takasuo
Tiivistelmä	<p>Tämä väitöskirja käsittelee sydänmateriaalin jäädytettävyyttä vakavien ydinvoimalaitosonnettomuuksien hallinnassa. Pohjoismaisten kiehutusvesilaitosten suojarakennuksen alakuivatiila tulvitetaan reaktorisydämen sulamiseen johtavassa onnettomuustilanteessa. Toimenpiteen tavoitteena on muodostaa vesiallas, minne sydänsula fragmentoituu ja jäähtyy reaktoripainesäiliön rikkoutumisen jälkeen. Vesialtaaseen muodostuu huokoinen, sydänromusta koostuva partikkelipeti, joka tuottaa fissiotuotteiden hajoamisesta aiheutuvaa jälkilämpötehoa, joka poistuu petiä ympäröivään vesialtaaseen. Huokoisen pedin virtaus- ja lämmönsiirto-ominaisuudet määräävät, kuinka suuri jälkilämpöteho on mahdollista poistaa, jotta materiaalin uudelleen sulaminen estyisi.</p> <p>Työssä on tutkittu huokoisen partikkelipedin jäädytettävyyttä kokeellisesti mittaamalla kuivumiseen johtava lämpöteho erilaisissa partikkelipetigeometrioissa, jotka edustavat sulapurkauksessa muodostuvia huokoisen pedin muotoja. Erityisesti kekomaiset, realistiset partikkelipedit, joissa jäädytteen virtaus petiin on selkeästi moniulotteinen, on otettu huomioon. Kokeet on mallinnettu käyttämällä kaksi- ja kolmiulotteisia laskentamalleja, jotka simuloivat kaksifaasivirtausta huokoisessa väliaineessa. Koe- ja mallinnustulosten avulla esitetään tulkinta partikkelipetien kuivumiskäyttäytymisestä sekä arvioidaan mallien soveltuvuutta jäädytettävyyssarviointiin.</p> <p>Kokeiden ja laskentamallien tulosten mukaan kuivumislämpövoima riippuu virtausmekanismista ja pedin korkeudesta. Kokeissa havaittiin, että moniulotteinen virtaus parantaa kekomaisen petien jäädytettävyyttä. Kuivumislämpövoima on 47–58 % suurempi kuin päältä jäädytettävässä pedissä. Kekomainen peti on kuitenkin korkeampi kuin tilavuudeltaan vastaava tasaisesti jakautunut, päältä jäädytettävä peti, mikä kasvattaa höyryvuota kekomaisen pedin yläosassa ja huonontaa jäädytettävyyttä. Kuivumislämpövoiman perusteella pedin korkeus saa olla vain noin puolitoistakertainen tasaisesti jakautuneeseen petiin verrattuna, jotta moniulotteisesta virtauksesta saatava suora hyöty säilyisi.</p> <p>Lisäksi työssä arvioitiin hydrodynaamisesti edustavaa efektiivistä partikkelikokoa, jota mallinnuksessa sovelletaan kuvaamaan epäsuunnollisista ja vaihtelevan kokoisista partikkeleista koostuvaa petiä. Tulokset viittaavat siihen, että efektiivinen koko tulee valita kokojakauman pienempien partikkelien joukosta, mahdollisesti käyttäen partikkelien lukumäärän tai pituuden mukaan painotettua keskikokoa.</p>
ISBN, ISSN, URN	ISBN 978-951-38-8344-7 (nid.) ISBN 978-951-38-8345-4 (URL: <a href="http://www.vtt.fi/julkaisut">http://www.vtt.fi/julkaisut</a> ) ISSN-L 2242-119X ISSN 2242-119X (Painettu) ISSN 2242-1203 (Verkkojulkaisu) <a href="http://urn.fi/URN:ISBN:978-951-38-8345-4">http://urn.fi/URN:ISBN:978-951-38-8345-4</a>
Julkaisu-aika	Lokakuu 2015
Kieli	Englanti, suomenkielinen tiivistelmä
Sivumäärä	112 s. + liitt. 72 s.
Projektin nimi	
Rahoittajat	
Avainsanat	ydinenergia, vakava ydinvoimalaitosonnettomuus, jäädytettävyyys, huokoinen aine, partikkelipeti, kokeellinen termohydrauliikka, kaksifaasivirtaus, laskentamalli
Julkaisija	Teknologian tutkimuskeskus VTT Oy PL 1000, 02044 VTT, puh. 020 722 111

## Coolability of porous core debris beds

### Effects of bed geometry and multi-dimensional flooding

The utilization of nuclear energy for power generation is a safety critical activity due to the large amount of radioactive materials contained in the nuclear reactor core. In the design of modern power reactors, the possibility of a severe accident that results in damage to the reactor core, or even melting, has to be taken into account. One of the main questions in the management and mitigation of the consequences of a severe accident is how to cool and stabilize the molten corium heated by decay heat. In this thesis, stabilizing the corium in the form of a debris bed is investigated. The focus is on heap-like, realistic debris beds which facilitate multi-dimensional infiltration (flooding) of coolant into the bed. Both experimental and numerical methods are utilized in the study, aiming to describe the characteristics of the coolability and dryout behavior of debris beds with complex geometries. Since it is not possible to conduct experiments on a realistic scale, safety assessment is performed using simulation codes that aim to capture the complicated physical mechanisms governing the debris coolability. The new experimental data presented in this work serve as a basis for code validation, necessary for verifying the reliability of the simulation codes in reactor safety studies.

ISBN 978-951-38-8344-7 (Soft back ed.)  
ISBN 978-951-38-8345-4 (URL: <http://www.vttresearch.com/impact/publications>)  
ISSN-L 2242-119X  
ISSN 2242-119X (Print)  
ISSN 2242-1203 (Online)  
<http://urn.fi/URN:ISBN:978-951-38-8345-4>

